Quand la théorie des perturbations devient non-perturbative : applications aux systèmes fortement corrélés.

Renaud Garioud

INSTITUT POLYTECHNIQUE DE PARIS

NNT : 2023IPPAX052

Thèse de doctorat

ÉCOLE POLYTECHNIQUE

IP PARIS

When perturbation theory becomes non-perturbative: applications to strongly-correlated systems

Thèse de doctorat de l'Institut Polytechnique de Paris
préparée à l'École polytechnique

École doctorale n°626 École doctorale de l'Institut Polytechnique de Paris (EDIPP)
Spécialité de doctorat : Physique

Thèse présentée et soutenue à Paris, le 4 Juillet 2023, par

RENAUD GARIOUD

Composition du Jury :

Marco Schiro Chargé de recherche, Collège de France	Rapporteur
Fabien Alet Directeur de recherche, Université Paul Sabatier à Toulouse (IRSAMC)	Rapporteur
Laura Messio Maîtresse de conférences, Sorbonne Uinversité (LPTMC)	Examinatrice
Nicolas Dupuis Directeur de recherche, Sorbonne Université (LPTMC)	Président Examinateur
Antoine Georges Professeur, Collège de France	Co-directeur de thèse
Michel Ferrero Chargé de recherche, CPHT Ecole polytechnque et Collège de France	Co-directeur de thèse

Acknowledgment

I want to begin by expressing my gratitude to Michel Ferrero and Antoine Georges, my PhD directors, for putting their trust in me for this thesis. I am very thankful to you for giving me the opportunity to work in your team at Collège de France and École polytechnique. I would like to thank you for finding time to manage my projects and to create a team cohesion even during these years marked by the pandemic and the associated long-time confinement. I am extremely grateful for the opportunity I was given to attend to the summer schools held in Saas-Fee and at the Flatiron institute in New York. These two events were a turning point in my PhD journey.

Thank you Antoine for finding time to discuss physics despite your extremely busy schedule. It was a tremendous chance to be able to learn from your knowledge in our field.

Thank you Michel for your inspired and comprehensive management of my projects. It was a blessing to have such an accessible and attentive director and to exchange with you about your experience as an academic researcher. Thanks a lot for spending hours debugging my code, discussing physics around a coffee and answering my numerous questions, even at crazy hours in the middle of the night.

I am especially grateful to Fedor Šimkovic who has been managing my project for two years. Thanks a lot for sharing with me your coding and methodological skills. It was a huge relief to be able to count on you for all my technical questions. Thank you for having accompanied me through these complicated two years of work.

I would like to thank my collaborators on the two projects that I have been working on during my PhD. First, I would like to thank Fedor Šimkovic and Riccardo Rossi who have been developing the Fast Feynman Diagram library which I have been extensively using through these three years. Thanks a lot for always being available for ensuring the after sales service of your very efficient library. Thank you Félix Werner for the many discussions and advice. Your exhaustive theoretical understanding of our projects facilitated deeply my work. I also would like to thank Thomas Schäfer, Gabriele Spada, Kris Van Houcke and Jason Kyle for their helpful collaboration. Many thanks go to the IT support team of CPHT laboratory which provided the high performance computing resources used for my work.

I had the chance to be part of an amazing team during these three years at Collège de France. Fedor, Thomas, Liam, Hanhim, Sidhartha, Alfred, Andrea, Françoise, it was a great pleasure to share the office with you and all of the lunch and coffee break. Pauline, it was an amazing support to share every step of this PHD with you, thanks a lot !

These PHD years were also dedicated to teaching at École polytechnique in the experimental course dedicated to high-temperature superconductivity. Thank you Yannis for this opportunity and for the nice teaching environment. Thanks a lot to my fellow teaching assistants Benjamin, Aurélien, Liam and Samy.

Enfin, mes plus chaleureux remerciements vont à ma famille et à mes amis sans qui tout ce travail aurait peu de sens. Merci Maman, Papa, Gauthier pour votre soutien sans faille tout au long de mes études.

Un grand merci à la team lunch Maxime, Flavien, Léa, Victor, Théo : la meilleure équipe de soutien moral aux doctorants. Car il n'y a rien de mieux qu'un doctorant en physique pour en comprendre un autre. Merci à Maxime, Théo, Martin, Alice, Camille, Samuel pour avoir réussi à adoucir les longues périodes de confinement. Merci à Marie et Théo pour votre soutien au quotidien et dans les moments les plus intenses et stressants de ces trois années. Et bien sûr mille mercis Annaïg, pour ton soutien extrêmement précieux pour mettre un point final à ce travail.

Abstract

Strongly correlated materials reveal remarkable physical phenomena at low temperatures. Depending on external parameters, they exhibit extremely different electronic phases, ranging from insulating magnetic orders to strong superconductivity with infinite electrical conductivity. The richness of these physical phenomena takes its roots in the strong interactions that impact heavily the behaviour of electrons. These materials can not be understood by an effective one-body treatment. To accurately describe these properties, one must solve the quantum many-body problem of interacting particles. This is a complex problem that requires numerical approaches to obtain quantitatively accurate results. In this thesis, we focus on the development of new algorithms to address strongly interacting fermionic systems.

After introducing strongly interacting systems, we show that the perturbation theory framework is a powerful tool for studying the many-body problem. By considering electronic interactions as a perturbation to the non-interacting system, we focus on computing efficiently, and up to high orders, the perturbation series, which can be expressed as sums of Feynman diagrams. We present the CDet (Connected Determinants) state-of-the-art algorithm which allows us to reach high perturbation orders. We overcome one of the main limitations of perturbation theory by introducing a novel chemical potential shift that breaks a symmetry. We show that this approach allows us to describe perturbatively the physics of ordered phases in the thermodynamic limit. We apply this new algorithm to the cubic half-filled Hubbard model and provide a quantitative description of the Néel order both near the phase transition and at low temperature up to the high coupling regime. This study enables us to detail the limitations to our method and to present the numerical tools that ensure an efficient implementation of the CDet algorithm and an accurate resummation of the resulting perturbative series. The attractive counterpart of this model shows a superconducting phase that can also be described by adapting our symmetry-breaking approach.

In the last chapter of this thesis we turn our attention to out-of- equilibrium interacting systems. The non-equilibrium interacting problem in real materials is extraordinarily difficult to solve exactly, and we rely on a diagrammatic approximation : the Non-Crossing-Approximation. We implement an efficient and fast impurity solver by alternating between the real-time and frequency domains in the steady-state limit. This solver allows us to compute transport properties in systems that are driven out-of-equilibrium by an external electric field.

Résumé

Les matériaux fortement corrélés révèlent des phénomènes physiques remarquables à basse température. Selon les paramètres externes, ils peuvent présenter des phases électroniques extrêmement différentes, allant d'ordres magnétiques isolants à une phase supraconductrice présentant une résistance électrique nulle. La richesse de ces phénomènes physiques prend ses racines dans les interactions fortes qui impactent le comportement des électrons. Ces matériaux ne peuvent pas être compris par un traitement effectif à un seul corps. Pour décrire avec précision leurs propriétés, il faut prendre en compte les corrélations entre électrons et résoudre le problème quantique à N corps. Il s'agit d'un problème complexe sans solution analytique exacte. Ce problème nécessite des approches numériques efficaces pour obtenir des résultats quantitativement précis. Dans cette thèse, nous abordons le développement de nouveaux algorithmes pour étudier les propriétés à l'équilibre et hors d'équilibre, des systèmes fermioniques à fortes interactions.

Après avoir introduit les systèmes électroniques à fortes interactions, nous présentons le modèle fermionique de Hubbard. Ce modèle microscopique minimaliste nous permet de décrire la physique des matériaux dont les électrons interagissent fortement. Nous montrons ensuite que la théorie des perturbations est un outil puissant pour étudier ce modèle, et de manière générale pour étudier le problème à N corps quantique. En considérant les interactions électroniques comme une perturbation du système sans interaction, nous exposons comment calculer de manière efficace, et jusqu'à des ordres élevés, la série perturbative qui peut être exprimée comme une somme de diagrammes de Feynman. Nous présentons l'algorithme CDet (Connected Determinants) qui nous permet d'atteindre des ordres de perturbation élevés en effectuant en un nombre d'étapes exponentiel, la somme d'une quantité factorielle de diagrammes. Nous dépassons l'une des principales limites de la théorie des perturbations en introduisant un changement de potentiel chimique qui brise une symétrie du système. Cette approche permet de décrire de façon perturbative la physique des phases ordonnées dans la limite thermodynamique des grands systèmes. Ce nouvel algorithme est appliqué au modèle de Hubbard à moitié rempli et sur un réseau cubique. Il fournit une description quantitative de la transition de phase du système vers un ordre antiferromagnétique (ordre de Néel) à basse tempárature. Ces résultats numériquement exacts sont obtenus à la fois près de la température critique, et à basse température jusqu'au régime de couplage fort. Cette étude nous permet de détailler les limites de notre méthode et de présenter les outils numériques qui assurent une mise en œuvre efficace de l'algorithme CDet et une resommation précise des séries perturbatives. La version attractive de ce modèle présente une phase supraconductrice qui est décrite en adaptant notre approche d'expansion dans une phase à symétrie brisée. Ceci nous permet

de comparer l'utilisation de notre approche perturbative pour des transitions de phase du premier ou du second ordre.

Dans le dernier chapitre de cette thèse, nous nous intéressons aux systèmes à forte interaction et hors équilibre. Le problème hors équilibre dans les matériaux fortement corrélés est exceptionnellement difficile à résoudre exactement, et nous nous appuyons sur une approximation diagrammatique NCA (Non Crossing Approximation). Cette approximation permet une évaluation analytique et auto-cohérente de la somme des diagrammes de Feynman de la série perturbative. Ceci nous conduit à implémenter un solveur d'impuretés efficace et rapide en alternant entre les domaines en temps réel et en fréquence, dans la limite du régime permanent. Ce solveur nous permet de calculer les propriétés de transport dans des systèmes qui sont maintenus hors équilibre par un champ électrique extérieur. Nous l'appliquons de manière préliminaire à l'étude des propriétés du modèle d'impureté d'Anderson.

Contents

Chapter I

Context and overview on strongly correlated systems

Contents

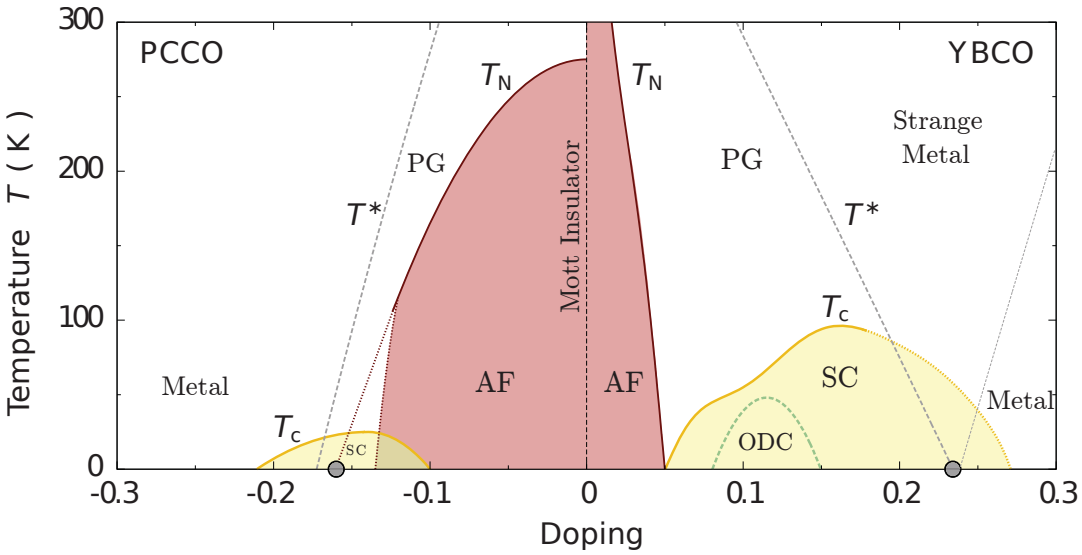

Figure I.1: Electronic phase diagram as a function of temperature and doping of hole-doped $YBa_2Cu_3O_7$ and electron-doped Pr_2CuO_4. Adapted from [76].

I.1 Physics of strongly correlated materials

The goal of condensed matter physics is to understand the properties of matter as it organizes into solid crystals at the microscopic level. Starting from the observed microscopic structure and symmetries of a piece of matter, we want to understand the macroscopic properties of a material : Is it a metal that easily conducts electricity and heat? Is it an insulator that exhibits high resistance? Does it show magnetic properties as observed in permanent magnets?

In crystals the atoms form a lattice which organizes according to spatial symmetries. The nuclei of the atoms are essentially fixed or vibrating around their equilibrium position. The electrons from the outer orbitals carry the remaining degrees of freedom that determine the physical properties of the solid. In strongly correlated materials, these electrons are not only subject to the electric field generated by the lattice of cations, but they also strongly interact with each other. This gives rise to intricate and interesting physical properties. As the temperature drops, the electronic degrees of freedom condense into new phases with very different and fascinating characteristics.

I.1.1 Phase diagram of high-temperature superconductors

The interest for strongly correlated materials hinges on the discovery of a new class of materials at the end of the 1980s called cuprates, which exhibit strong superconductivity up to extremely high temperatures in comparison to conventional metals. They hold the name of high temperature superconductors and have been shown to host fascinating physical phenomena which still remain to be understood in details.

In these materials the Coulomb repulsion between electrons is exceptionally strong such that, at zero doping, the Coulomb interaction impedes the motion of electrons and

the material is a Mott insulator. As the system is doped with adding (negative doping) or removing (positive doping) electrons, the Coulomb blocking of charge carriers vanishes and the system becomes metallic. This is shown in the phase diagram of cuprates displayed in Fig. I.1. In between these two regimes, cuprates show a wide variety of electronic phases at low temperatures with very dissimilar properties. At low temperature, and as the doping is increased, the system goes through an insulating antiferromagnetic (AF) phase, a charge density wave ordering (CDO) and superconductivity (SC) under a dome described by the critical temperature T_c. At higher temperature and under the T^* line, we find a regime called the pseudo-gap (PG) characterized by an anisotropic suppression of quasi-particles in the Brillouin zone. At higher doping, the system goes to a regime called strange metal which exhibits an enigmatic linear dependence of the resistance with respect to the temperature. For a complete review on the low temperature physics of cuprates, see [107].

The rich and intricate physics at work in these materials motivates the research on interacting electronic systems. This phase diagram shows competition between different orders which is still not fully understood theoretically.

I.1.2 Cold atoms experiments

Understanding the behaviour of strongly interacting fermions is a complicated physics problem that can be addressed experimentally. Indeed, the quantum dynamics of fermions in a material can be reproduced in cold atom experiments. They simulate the physical environment of the electrons and perform measurements of the physical properties of the system.

In experiments with cold atoms, tunable lasers are used to create periodic potentials. By superimposing light from lasers in different directions, these experiments construct an optical lattice on which individual atoms are studied. The periodic potential generated by the lasers mimics the potential generated by the solid cations in a material. The fermionic atoms interact with each other through a contact repulsion. These experiments provide highly controllable systems for studying interacting fermions in an external periodic potential, and one can vary the repulsion intensity, lattice potential, and geometry [18, 65]. They can also include time-dependent perturbations to study the out-of-equilibrium dynamics of interacting systems. Recently, cold atom experiments have been able to describe phase transitions and have shown to be able to describe antiferromagnetic ordering [43, 50, 87, 134] as well as a Mott insulator to superfluid transition [44].

However, the description of strongly correlated materials with cold atoms experiments is currently limited to relatively high temperatures ($T/t \geq 0.3$ with t the hopping term introduced in the next section). The theoretical description of these materials in conjunction with numerical techniques is therefore more than a complementary approach, as it provides an understanding of their physical properties at low temperatures.

I.2 Models for strongly interacting electrons

I.2.1 Introduction to the many-body problem

The main challenge for condensed matter physics is to be able, starting from simple quantum physics principles, to describe collective and complex phenomena happening in materials. The energy levels of a single electron in orbit around a proton is well understood from the Schrödinger equation, but what does happen when we assemble many of these hydrogen atoms together ? Because of the interactions between particles the physics of the whole system can become drastically different and richer than the one of the single body. They give rise to various electronic phases as exotic as superconductivity or spin waves orders with very dissimilar physical properties in terms of transport or excitations.

The Hamiltonian describing the degrees of freedom of N_{at} atoms and N_e electrons inside a material is easily written from the kinetic energy and coulomb interaction terms :

$$\begin{aligned}\mathcal{H} =& \sum_{i=1}^{N_{at}} \frac{\mathbf{P}_i^2}{2M_i} + \sum_{i=1}^{N_e} \frac{\mathbf{p}_i^2}{2m_i} + \frac{1}{2} \sum_{1\leq i\neq j\leq N_e} \frac{e^2}{4\pi\epsilon_0|\mathbf{r}_i - \mathbf{r}_j|} + \frac{1}{2} \sum_{1\leq i\neq j\leq N_{at}} \frac{Z_i^2}{4\pi\epsilon_0|\mathbf{R}_i - \mathbf{R}_j|} \\ & - \frac{1}{2} \sum_{i=1}^{i=N_{at}} \sum_{j=1}^{j=N_e} \frac{Z_i e^2}{4\pi\epsilon_0|\mathbf{R}_i - \mathbf{r}_j|}\end{aligned} \tag{I.1}$$

Where $\mathbf{P}_i$, M_i, $\mathbf{R}_i$ are the momentum, mass and position of the atoms with Z_i protons of charge $+e$ and $\mathbf{p}_i$, m_i, $\mathbf{r}_i$ are the momentum, mass and position of electrons of charge $-e$.

The energy levels of the material are then given by the stationary Schrödinger equation (or eigenvalue problem of the Hamiltonian) :

$$\mathcal{H}\Psi = E\Psi \tag{I.2}$$

With Ψ a stationary wave function of the system with energy E. Even though expressing this physical problem is very simple and straight forward, it is in practice impossible to solve, as for a small dice of matter, Ψ is a function of more than 10^{23} variables. This intricate problem of many particles interacting with each other is called the quantum many-body problem. It has no analytic solution for more than 3 particles and it is a strong challenge for numerical physics.

In this thesis we consider the Born-Oppenheimer approximation : the atoms having a large mass compared to the electrons and forming a crystal are supposed to be fix on a periodic lattice. This reduces drastically the number of degrees of freedom of the problem. We are left with interacting electrons in a periodic external potential created by the lattice.

The richness of the physics of strongly correlated materials lies in the various and different electronic phases that emerge when going to low temperature, such as ferromagnetism or superconductivity. As we decrease the temperature, the electronic degrees of freedom tend to order and spontaneously break a symmetry of the system. This phenomenon is called phase transition and is, at the level of electrons in a material, similar to the common experiment of solidification or liquefaction of water for instance. This is a collective thermodynamic phenomenon which tends to reduce the energy of the system at low temperature, at the expense of a higher degree of ordering and therefore a smaller entropy. It can only happen because a huge number of particles are present in the system. Therefore the understanding of phases in strongly correlated materials requires to tackle the many-body problem in the limit of infinite number of particle $N_{at}, N_e \to \infty$, called the thermodynamic limit.

I.2.2 The Hubbard model

In this section we introduce a toy model for strongly-correlated materials. It is, from the theoretical point of view, one of the simplest models to investigate correlations and phase transitions in strongly correlated materials. Starting from the Hamiltonian (I.1) rewritten in the second quantization formalism after dropping the atomic degrees of freedom we obtain the Hamiltonian :

$$\hat{\mathcal{H}} = \sum_{ij}\sum_{\sigma} t_{ij}\hat{c}^{\dagger}_{i\sigma}\hat{c}_{j\sigma} + \frac{1}{2}\sum_{i,j,k,l}\sum_{\sigma,\sigma'} U_{ijkl}\hat{c}^{\dagger}_{i\sigma}\hat{c}^{\dagger}_{j\sigma'}\hat{c}_{l\sigma'}\hat{c}_{k\sigma} \tag{I.3}$$

Where $\hat{c}^{\dagger}_{i\sigma}$ creates an electron in orbital i with spin σ, which we write $|i,\sigma\rangle$, and $\hat{c}_{i\sigma}$ annihilates and electron on orbital i with spin σ. $t_{ij} = \langle i|\hat{\mathbf{p}}^2/2m|j\rangle$ is the hopping term between orbitals i and j. $U_{ijkl} = \langle i|\langle j|\hat{V}|k\rangle|l\rangle$ the Coulomb interaction term. For a given material the t and U matrices are hard to compute and require electronic band structure computations.

As we are describing a system of electrons, the second quantization creation and annihilation operators verify the fermionic anti-commutation relations :

$$\begin{aligned}\left\{\hat{c}_{j\sigma}, \hat{c}^{\dagger}_{i\sigma'}\right\} &= \delta_{ij}\delta_{\sigma\sigma'} \\ \left\{\hat{c}^{\dagger}_{j\sigma}, \hat{c}^{\dagger}_{i\sigma'}\right\} &= 0 \\ \{\hat{c}_{j\sigma}, \hat{c}_{i\sigma'}\} &= 0\end{aligned} \tag{I.4}$$

The Hubbard Hamiltonian is obtained after imposing several approximations :

- We restrict ourselves to the single orbital case so that the system is made of a network of sites forming a lattice. Each site can be occupied by either no electron, one electron with spin up or down, or two electrons with opposite spins. Therefore there are four possible states for each site which are respectively $|0\rangle$, $|\uparrow\rangle$, $|\downarrow\rangle$ and $|\uparrow\downarrow\rangle$

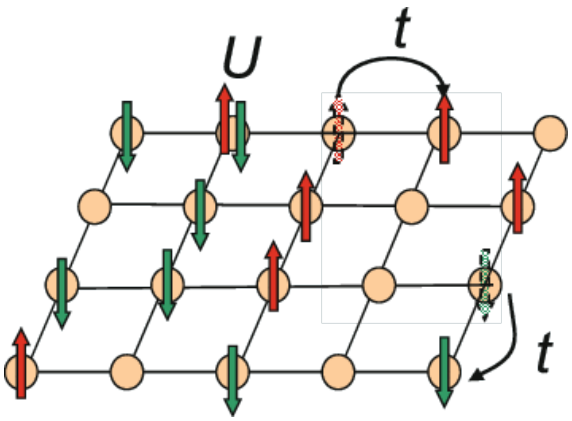

Figure I.2: Hubbard model on a two dimensional square lattice [150] with t the hopping term and U the on-site Coulomb interaction

- We only consider nearest neighbour hopping so that $t_{ij} = -t$ if i and j describe neighbouring sites of the lattice, $t_{ij} = 0$ otherwise.
- We neglect long-range Coulomb repulsion which is limited to on-site interaction : $U_{ijkl} = U$ if $i = j = k = l$ and 0 otherwise.

We obtain the Hubbard Hamiltonian [49,56,57] to which we add the chemical potential term for working in the grand canonical ensemble. The sum $\langle i, j\rangle$ runs over neighbouring sites :

$$\hat{\mathcal{H}} = -t \sum_{\langle i,j\rangle} \sum_{\sigma} \hat{c}^{\dagger}_{i\sigma} \hat{c}_{j\sigma} + U \sum_{i} \hat{n}_{i\uparrow} \hat{n}_{i\downarrow} - \mu \sum_{i} (\hat{n}_{i\uparrow} + \hat{n}_{i\downarrow}) \tag{I.5}$$

With $\hat{n}_{i\sigma} = \hat{c}^{\dagger}_{i\sigma} \hat{c}_{i\sigma}$ the occupation number operator on site i with spin σ. There are various versions of this model when considering different dimensions or lattice geometry, next-nearest neighbour or asymmetric hopping, and Coulomb repulsion between electrons on different sites. In two dimensions on a square lattice, this model is depicted in Fig. I.2.

For depicting strongly correlated materials we have $t > 0$ since atomic orbitals overlap on neighbouring sites, and $U > 0$ for the Coulomb interaction is repulsive between negatively charged electrons. Despite its apparent simplicity this model has no analytic solution in more than one dimension. It shows a competition between two terms : the kinetic energy term $\hat{\mathcal{H}}_{kin} = -t \sum_{\langle i,j\rangle} \sum_{\sigma} \hat{c}^{\dagger}_{i\sigma} \hat{c}_{j\sigma}$ which tends to delocalize electrons on the lattice, and the potential energy term $\hat{\mathcal{H}}_{pot} = U \sum_i \hat{n}_{i\uparrow} \hat{n}_{i\downarrow}$ which costs energy for doubly occupied states and therefore tends to localize electrons. For better understanding of this competition we can study two limits :

- $U = 0$: The Hubbard Hamiltonian becomes non-interacting and describes free electrons on a lattice similarly to what is obtained for tight-binding models. It is diagonal on the reciprocal lattice in $\mathbf{k}$ space and we get after performing a Fourier transformation on the lattice positions $\hat{\mathcal{H}} = \sum_{\mathbf{k}} (\epsilon_{\mathbf{k}} - \mu) \hat{c}^{\dagger}_{\mathbf{k}\sigma} \hat{c}_{\mathbf{k}\sigma}$. The dispersion

relation $\epsilon_{\mathbf{k}}$ depends on the geometry of the lattice, but it describes a band structure and the system is in a metallic state.

- $t = 0$ (or $U \to \infty$) : $\hat{\mathcal{H}} = U \sum_i \hat{n}_{i\uparrow}\hat{n}_{i\downarrow} - \mu \sum_i (\hat{n}_{i\uparrow} + \hat{n}_{i\downarrow})$ which is diagonal in the lattice basis. The system is a collection of independent atoms with no hopping. Each electron is localized on a site and no electric transport is possible. Because of overwhelming interactions the system is a Mott insulator.

In the general case, the sum of these two competing terms leads to a complex interacting problem with no easy diagonalisation. Its simple formulation associated with the intricate physics of the many-body problem make this model an ideal platform for investigating the capabilities of new algorithms before engaging in the study of actual materials. The model is also actively explored using quantum simulations in cold-atomic experiments on optical lattices [66].

The two-dimensional Hubbard model on a square lattice is believed to be especially relevant for high-temperature superconductor cuprates. It could be a minimal model for understanding the quasi two-dimensional physics of the CuO_2 planes in which the copper $3d$ orbitals form a square lattice with nearest-neighbour orbitals overlap. This model is believed to exhibit a rich phase diagram with various nontrivial phenomena which compares well with the one observed in cuprates, including metal-insulator transition, antiferromagnetism, pseudo-gap and superconductivity. For a detailed overview of the two-dimensional Hubbard model, and the properties of its ground state see [7, 109]. Recently, the ground state of the two-dimensional Hubbard model, in the absence of next-nearest-neighbour hopping, has been found to show no superconductivity in a regime of parameters relevant to cuprates [108]. The superconducting phase turns out to be in competition with a stripe order, which has been shown to prevail by very small energy scales. Nevertheless the next-nearest-neighbour hopping term is believed to be a key ingredient for the modeling of cuprates. Including this term, the Hubbard model exhibits a d-wave superconducting ground state around the optimal doping [149]. Moreover, at finite temperatures, simulations have pointed out the presence of a pseudo-gap regime with properties similar to what is observed in cuprates [83, 103, 144, 148].

In this thesis we focus on this minimal microscopic model of interacting fermions in order to understand the physics of strongly correlated materials. By developing new numerical accurate techniques we want to provide a deeper understanding of the physical phenomena observed experimentally in cuprates and provide results for guiding the development of cold atoms experiments which are currently limited to relatively high temperature of the order of $T \sim 0.3t$.

I.2.3 DMFT and the impurity problem

A first simple approach to tackle the Hubbard model would be to apply a mean-field approximation to the interacting term, approximating the Coulomb interaction by an averaged effective one body interaction term. An example of a Hartree-Fock resolution of the Hubbard model in the paramagnetic and antiferromagnetic states, useful for further

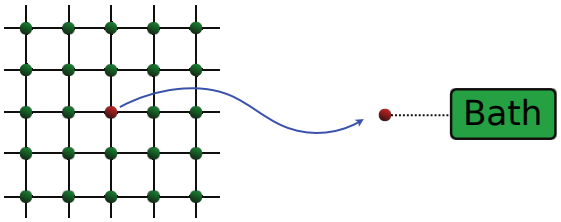

Figure I.3: Illustration of the DMFT scheme. We map a site of the lattice into an impurity embedded in a self-consistent bath. Figure adapted from [110]

developments in this thesis, can be found in the Appendix C. Nevertheless this approximation is known to be extremely rough and can not be considered satisfying for studying strongly correlated systems.

The Dynamical Mean Field Theory (DMFT) goes one step further into taking into account correlations in strongly correlated systems. It is centered on the idea that a lattice problem can be mapped to a single impurity embedded in a bath. We can take one site of the Hubbard model out of the lattice, the rest of the sites forming a bath which exchanges electrons with the impurity as shown in Fig. I.3. The DMFT approximation neglects the interactions between the electrons inside the bath, and the properties of the bath are self-consistently determined from the interacting impurities [38, 39, 67].

The DMFT approximation is formulated in the many-body Green's function formalism which we employ in the rest of this thesis. We note $\mathcal{G}_0$ the non-interacting Green's function (for $U = 0$ in the case of the Hubbard model), $\mathcal{G}$ the interacting Green's function, Σ its associated self-energy, $\mathbf{k}$ a wave vector of the reciprocal lattice, and $i\omega_n = (2n+1)\pi/\beta$ the n-th Matsubara frequency in the imaginary-time framework at equilibrium and at temperature $T = 1/\beta$. The non-interacting Green's function reads (see Appendix A) :

$$\mathcal{G}_{0\sigma}(\mathbf{k}, i\omega_n) = \frac{1}{i\omega_n - \epsilon_{\mathbf{k}\sigma} + \mu} \tag{I.6}$$

With $\epsilon_{\mathbf{k}\sigma}$ the energy dispersion of the non-interacting system, and μ the chemical potential. By definition of the self-energy the Green's function for the interacting system is given by the Dyson's equation :

$$\begin{aligned} \mathcal{G}_\sigma(\mathbf{k}, i\omega_n) &= (\mathcal{G}_{0\sigma}(\mathbf{k}, i\omega_n)^{-1} - \Sigma_\sigma(\mathbf{k}, i\omega_n))^{-1} \\ &= (i\omega_n - \epsilon_{\mathbf{k}\sigma} + \mu - \Sigma_\sigma(\mathbf{k}, i\omega_n))^{-1} \end{aligned} \tag{I.7}$$

The Green's function of the single lattice site considered as an impurity which exchanges electrons with a bath through a hybridization function $\Delta(i\omega_n)$ reads :

$$\mathcal{G}_{\mathrm{imp},\sigma}(i\omega_n) = (i\omega_n - \epsilon_d + \mu - \Delta(i\omega_n) - \Sigma_{\mathrm{imp},\sigma}(i\omega_n))^{-1} \tag{I.8}$$

So far we did not make any approximation and this last equation is a representation of the local Green's function as an impurity coupled to a bath :

$$\mathcal{G}_{\mathrm{loc},\sigma}(i\omega_n) = \sum_{\mathbf{k}} \mathcal{G}_\sigma(\mathbf{k}, i\omega_n) = \mathcal{G}_{\mathrm{imp},\sigma}(i\omega_n). \tag{I.9}$$

The DMFT approximation considers the bath to be non-interacting and self-determined by the impurity's characteristics. Formally it states that the lattice self-energy is equal to the impurity's one :

$$\Sigma_\sigma(\mathbf{k}, i\omega_n) = \Sigma_{\mathrm{imp},\sigma}(i\omega_n) \tag{I.10}$$

We neglect the $\mathbf{k}$ dependency of the self-energy but keep its dynamical properties as a function of the imaginary-time or Matsubara frequencies, hence the name of Dynamical Mean-Field Theory. Therefore this approximation neglects non-local correlations but is able to handle the different time-scales involved in the correlations encoded in the self-energy function.

Within the DMFT approximation Eq. I.10 the hybridization function Δ has to be self-determined for the local Green's function to stay equal to the impurity one. It leads to the self-consistent scheme :

i. We start from a guess for the non-interacting Green's function $\mathcal{G}_{0\sigma}(\mathbf{k}, i\omega_n)$ and determine the associated hybridization function $\Delta(i\omega_n)$.

ii. We solve the impurity problem and determine the impurity self-energy $\Sigma_{\mathrm{imp},\sigma}(i\omega_n)$ and Green's function.

iii. We apply the DMFT approximation to compute the local Green's function :

$$\mathcal{G}_{\mathrm{loc},\sigma}(i\omega_n) = \sum_{\mathbf{k}} (i\omega_n - \epsilon_{\mathbf{k}\sigma} + \mu - \Sigma_{\mathrm{imp},\sigma}(i\omega_n))^{-1} \tag{I.11}$$

iv. We obtain a new non-interacting Green's function and its associated hybridization function through :

$$\mathcal{G}_{0\sigma}(\mathbf{k}, i\omega_n) = (\mathcal{G}_\sigma(\mathbf{k}, i\omega_n)^{-1} + \Sigma_{\mathrm{imp},\sigma}(i\omega_n))^{-1} \tag{I.12}$$

v. We repeat this procedure until convergence of the hybridization and local Green's function.

This scheme stresses the importance of being able to solve efficiently an impurity problem and we will discuss some impurity solvers in Subsection I.3.2. The DMFT approximation has been shown to become exact in the limit of infinite dimension on a Bethe lattice (infinite coordination lattice) [38]. It is also exact in the limits of infinite or zero interaction ($U = 0$ or $U = \infty$). In the intermediate regime where $t \approx U$, since it approximates the self-energy by the impurity one, it becomes a good approximation in regimes with a localized self-energy.

Many extensions to this DMFT scheme have been developed in order to enhance its ability to describe accurately the physics of correlated systems. The Cellular DMFT

(CDMFT) extracts several sites of the original lattice as an impurity so that the non-local correlations are encoded in the impurity self-energy up to the size of the considered impurity. This approach becomes exact in the limit of infinite cluster size which corresponds to all the system being treated exactly. The Dynamical Cluster Approximation (DCA) is the counterpart of CDMFT on the reciprocal lattice. It separates the Brillouin zone into patches of wave vectors and distinguishes the behaviour of the self-energy on these different areas. Other expansions focus on including correlations by making approximations on different objects than the self-energy. At a heavy computational price, the Dynamical Vertex Approximation (DΓA) relies on considering purely local the fully irreducible two-fermion scattering vertex.

It is to be noted that the DMFT framework enables one to study symmetry-broken phases and phase transition. As in the plain mean-field approximation, it can allow several solutions depending on their symmetries. A comparison of the free-energy of these solutions is required to establish the phase diagram. However, as DMFT neglects spatial correlations up to some extent, it does not follow the Mermin–Wagner theorem and leads to spontaneous breaking of continuous symmetries at finite non-zero temperatures in two dimensions.

The DMFT framework can be used for computing the electronic structure of more realistic interacting materials when associated with the Density Functional Theory (DMFT + DFT approach) [52]. The DMFT is also successful for describing out-of equilibrium systems [82, 85, 102].

I.3 Computational methods to the many-body problem

Efficient computational tools are essential to understand quantitatively and solve the quantum many-body problem. Considerable progress has been achieved in this field in the last decade with the introduction of new algorithms and concepts to tackle strongly correlated systems. Since this thesis is based on algorithmic developments on this matter, we give in this section an overview on modern numerical methods which have been applied successfully in some regime of the Hubbard model. We will emphasize on equilibrium methods and address approaches for out-of-equilibrium systems in Chapter V. Recent works have put efforts into comparing quantitatively these methods in different regimes of the two dimensional Hubbard model [79, 123].

We distinguish two classes of such methods : the finite temperature methods and the zero temperature methods which focus on establishing the ground state properties.

I.3.1 Finite temperature methods

Many numerical techniques are opening the path to understanding strongly correlated materials at finite temperature $T \neq 0$ working directly on the lattice. They try to reach low temperatures starting from the equilibrium high temperature limit at which the physics of the system is well understood. They are based on a perturbative expansion of some quantity and rely on Monte Carlo techniques for computing the interacting Green's function,

or partition function. Because of the anticommutation relations that fermionic operators obey, these techniques sample stochastically a quantity with alternating sign. This is the main limitation of these methods called the sign problem. It leads to exponentially increasing statistical errors with decreasing temperature [137].

A large class of algorithms belong to the Diagrammatic Monte Carlo methods which perform an expansion in interaction of the problem directly on the lattice. They either sample connected diagrams to obtain a physical observable or correlator, or sample determinants to compute the partition function.
The Determinant Diagrammatic Monte Carlo (DDMC) [23] performs an expansion in the interaction parameter to compute stochastically the partition function. It is limited to small system sizes and it relies on universal scaling laws to extrapolate towards the thermodynamic limit (infinite lattice).
The Diagrammatic Monte Carlo (DiagMC) algorithm constructs a Markov Chain of Feynman diagrams in order to evaluate a perturbative series in the interaction parameter. The complexity of this algorithm scales badly with the maximum order of perturbation and the stochastic method suffers from a fierce sign problem. Recent developments have been made to overcome these difficulties which will be the subject of Chapters II and III.

The Auxiliary-Field Quantum Monte Carlo (AFQMC) [151] performs the imaginary-time evolution of a constrained wave function by applying the evolution operator $e^{-\beta\mathcal{H}}$ by stochastically evaluating imaginary-time path integrals. This approximate method takes advantage of symmetries and auxiliary fields introduced by a Hubbard-Stratonovich transformation [126]. It aims at taking the limit of zero temperature $\beta \to \infty$ to obtain the ground state wave function.

Recent developments have been implemented to build quantum Monte Carlo algorithms working in the real-time domain, that could be used for both equilibrium and out-of-equilibrium systems. The Inchworm algorithm [4, 25, 26] builds diagrams on the Keldysh contour to evaluate the real-time Green's function.

I.3.2 Embedding methods and impurity solver

A powerful framework to study strongly interacting systems comes from the DMFT approximation as described in I.2.3. Many extensions of this method have been developed to go further and reduce the roughness of this approximation, such as CDMFT and DCA which involve some non-local correlations in the definition of the impurity self-energy. Other extensions focus on other objects than the self-energy such as DΓA, Trilex [8, 9], Dual-Fermion [117] or Dual-Boson [118]. They are called embedding methods, and they all require to solve efficiently and accurately an impurity problem of an interacting impurity embedded in a non-interacting bath.

The Iterative Perturbation Theory (IPT) [39] or Non-Crossing Approximation (NCA) [16, 31] are performing approximations in the diagrammatic expansion of the self-energy. By removing some well-chosen terms they sum analytically the remaining diagrams and

lead to self-consistent analytic solutions. They provide impurity solvers that do not require many computational resources, but they perform a rough and uncontrolled approximation which can not be quantified. For this reason other state of the art numerically exact methods are preferred at equilibrium. They are yet employed extensively out-of-equilibrium where other methods become excessively greedy in terms of computational complexity. The use of NCA as an out-of-equilibrium impurity solver is the subject of Chapter V.

The Continuous Time Quantum Monte Carlo (CT-QMC) [46] is a group of three algorithms which have been a breakthrough in finding the exact solution of impurity models. They all rely on a perturbative expansion of the partition function and adapt the maximum perturbation order to get a fully resummed result. This expansion can either be expressed in interaction (CT-INT), in hybridization (CT-HYB) or using auxiliary fields (CT-AUX). They compute the perturbation coefficients stochastically using a Monte Carlo scheme. Their complexity scales poorly with the system size and they suffer from the sign problem at low temperatures which limits their usage. They are described in more details in Subsection I.3.2.

I.3.3 Ground state numerical approaches

An active field of research focuses on understanding the ground state properties of materials and are therefore studying the zero temperature $T = 0$ limit. These methods are by construction not perturbative in any of the system parameters. They are centered on building directly the wave function of the system which minimizes the energy.

The Exact Diagonalization (ED) directly tackles the Hamiltonian diagonalization problem. At $T = 0$ it can be associated to an iterative eigenvalue solver, like the Lanczos algorithm, in order to obtain specifically the ground state eigenvector. This method provides an exact solution of the problem when successful but it remains highly limited by the number of sites of the system. Taking advantage of symmetries an upper limit of $N = 50$ spins was recently reached [145].

The Numerical Renormalization Group (NRG) [22, 146] is an impurity solver at zero temperature. It takes advantage of the concepts of renormalization group flow introduced by Wilson to the field of condensed matter theory (Nobel prize 1982). It adds iteratively to an impurity the degrees of freedom of a non-interacting bath. The Hilbert space is truncated to keep the small energy scales of the impurity.

The Tensor Network algorithms rely on a specific representation of the wave function described by a network of tensors adapted recursively in order to minimize the energy towards the ground state. The Density Matrix Renormalization Group (DMRG) [124, 142, 143] belongs to this class of methods. It represents the wave function as a matrix product state in one dimension and truncates the Hilbert space to reduce the degrees of freedom of the ground state.

These methods have proven effective for finding the ground state of correlated systems. However they are limited by the size of the Hilbert space and struggle for addressing large

system sizes or dimensions greater than $D = 2$. Since they put effort into reducing the number of degrees of freedom of the system when constructing the ground state wave function, they suffer from limitations regarding the degree of entanglement of the ground state.

All of these techniques have extensions to study non-zero temperature systems, but they remain restricted to small system sizes and are limited by the entanglement entropy. The Minimally Entangled Typical States (METTS) method is one of these extensions. It evolves in imaginary time a typical wave function constructed as a matrix product state.

Chapter II

Perturbative approach to the many-body problem

Contents

We introduce in this chapter the perturbative theory framework for strongly correlated fermions which is at the center of the algorithmic developments provided in this thesis. It is a common idea in physics for treating systems with interaction to start from the much simpler non-interacting limit. One can then add interactions considered as a small parameter, and treat it as a perturbation to the non-interacting system. Let us take the example of the Hubbard Hamiltonian Eq.I.5 to illustrate this idea :

$$\begin{aligned}\hat{\mathcal{H}} &= -t\sum_{\langle i,j\rangle}\sum_{\sigma}\hat{c}^{\dagger}_{i\sigma}\hat{c}_{j\sigma} + U\sum_{i}\hat{n}_{i\uparrow}\hat{n}_{i\downarrow} - \mu\sum_{i}(\hat{n}_{i\uparrow}+\hat{n}_{i\downarrow}) \\ &= \hat{\mathcal{H}}_0 + U\hat{\mathcal{H}}_{exp}\end{aligned} \tag{II.1}$$

Where we noted $\hat{\mathcal{H}}_0$ the non-interacting Hamiltonian and $\hat{\mathcal{H}}_{exp}$ the interacting expansion Hamiltonian. We choose here to consider U the on-site Coulomb interaction as the perturbation parameter.

$$\hat{\mathcal{H}}_0 = -t\sum_{\langle i,j\rangle}\sum_{\sigma}\hat{c}^{\dagger}_{i\sigma}\hat{c}_{j\sigma} - \mu\sum_{i}(\hat{n}_{i\uparrow}+\hat{n}_{i\downarrow}) \qquad \hat{\mathcal{H}}_{exp} = \sum_{i}\hat{n}_{i\uparrow}\hat{n}_{i\downarrow} \tag{II.2}$$

The goal of perturbation theory is to express a quantity of interest as a function of perturbation orders in U. For an observable $\mathcal{A}$ we write :

$$\mathcal{A} = a_0 + a_1U + a_2U^2 + a_3U^3 + \mathbf{...} \tag{II.3}$$

where a_i is the expansion coefficient of order i. The perturbative approach consists in computing the first coefficients of this development for small i and truncate this series. This would yield meaningful insights on the effect of small interaction in the perturbative regime valid at small values of the perturbation parameter U. However it is not enough to get a controlled and quantitative result in the intermediate coupling for $U \sim t$. What if we were able to compute many of the expansion coefficients up to some large enough order n such that we could extrapolate the remaining coefficients towards infinite order ? We would then describe the observable $\mathcal{A}$ as a power series in U :

$$\mathcal{A} = \sum_{n=0}^{\infty} a_n U^n \tag{II.4}$$

This will be our approach in the Chapters III-IV, using perturbation theory to obtain quantitative results in the strong-to-intermediate coupling regime ($U \gg t$), a regime which is by essence, as stated in the title of this thesis, non-perturbative.

In this chapter we will show how to express the expansion coefficients a_n and interpret them as diagrams, and how several algorithms are taking advantage of perturbation theory to solve impurity or lattice problems.

II.1 Interaction and hybridization expansions

II.1.1 Perturbative expansions of Z and $\mathcal{G}$

We can employ two different perturbative approaches to the many-body problem :

- The interaction expansion for which we treat the Coulomb interaction U as the perturbation parameter, starting the expansion from the non-interacting Hamiltonian,
- The hybridization expansion for which we treat the hybridization function Δ as the perturbation parameter, starting the expansion from the well-defined atomic limit ($U \to \infty$). On the lattice we could expand in the hopping term t and start the expansion at the same limit.

We aim in this section at deriving the perturbative expansions of correlators both in interaction and hybridization. For simplicity we consider a single site impurity embedded in a non-interacting bath :

$$\begin{aligned}\mathcal{H} &= \sum_{\sigma} \epsilon \hat{d}^{\dagger}_{\sigma}\hat{d}_{\sigma} + U\hat{n}_{d,\downarrow}\hat{n}_{d,\uparrow} + \sum_{\mathbf{k},\sigma}(\gamma_{\mathbf{k}}\hat{c}^{\dagger}_{\mathbf{k},\sigma}\hat{d}_{\sigma} + \text{h.c.}) + \sum_{\mathbf{k},\sigma}\epsilon_{\mathbf{k}}\hat{c}^{\dagger}_{\mathbf{k},\sigma}\hat{c}_{\mathbf{k},\sigma} \\ &= \mathcal{H}_0 + \mathcal{H}_{int} + \mathcal{H}_{hyb} + \mathcal{H}_{bath}\end{aligned} \tag{II.5}$$

With ϵ the energy level of the impurity, $\epsilon_{\mathbf{k}}$ the energy levels of the non-interacting bath, $\hat{d}^{\dagger}_{\sigma}$ and $\hat{d}_{\sigma}$ (respectively $\hat{c}^{\dagger}_{\mathbf{k},\sigma}$ and $\hat{c}_{\mathbf{k},\sigma}$) are creation and annihilation operators on the impurity (resp. in the bath for electrons with wave vector $\mathbf{k}$), σ is the spin degree of freedom, and $\gamma_{\mathbf{k}}$ the coupling constant between the bath and impurity.

After integrating over the degrees of freedom of the bath we can describe the impurity by the action expressed in imaginary time τ at equilibrium with $\beta = 1/T$:

$$\begin{aligned}\mathcal{S} = &\sum_{\sigma}\int_0^{\beta} \mathrm{d}\tau d^{\dagger}_{\sigma}(\tau)(\partial_{\tau} + \epsilon)d_{\sigma}(\tau) + U\int_0^{\beta}\mathrm{d}\tau n_{\downarrow}(\tau)n_{\uparrow}(\tau) \\ &+ \sum_{\sigma}\int_0^{\beta}\mathrm{d}\tau\mathrm{d}\tau' d^{\dagger}_{\sigma}(\tau)\Delta_{\sigma}(\tau-\tau')d_{\sigma}(\tau')\end{aligned} \tag{II.6}$$

Which is written in terms of the hybridization function in imaginary time :

$$\Delta_{\sigma}(\tau) = \sum_{\mathbf{k}} \frac{|\gamma_{\mathbf{k}}|^2}{i\omega_n - \epsilon_{\mathbf{k}}} \tag{II.7}$$

We recall that we can express in terms of Grassmann variables the partition function, the average value of an observable $\mathcal{A}$, and the imaginary-time Green's function in the following form :

$$\begin{aligned} Z &= \int \mathcal{D}[d_\sigma^\dagger, d_\sigma] e^{-\mathcal{S}} \\ \langle A \rangle &= \frac{1}{Z} \int \mathcal{D}[d_\sigma^\dagger, d_\sigma] e^{-\mathcal{S}} A \\ \mathcal{G}_\sigma(\tau) &= \frac{1}{Z} \int \mathcal{D}[d_\sigma^\dagger, d_\sigma] e^{-\mathcal{S}} d_\sigma(\tau) d_\sigma^\dagger(0) = -\frac{\delta \ln Z}{\beta \delta \Delta_\sigma(-\tau)} \end{aligned} \tag{II.8}$$

Expansion in interaction :

We start by describing the expansion in the Coulomb interaction U. The non-interacting system is defined by the action :

$$\begin{aligned} \mathcal{S}_0 &= \sum_\sigma \int_0^\beta \mathrm{d}\tau d_\sigma^\dagger(\tau)(\partial_\tau + \epsilon) d_\sigma(\tau) + \sum_\sigma \int_0^\beta \mathrm{d}\tau \mathrm{d}\tau' d_\sigma^\dagger(\tau) \Delta_\sigma(\tau - \tau') d_\sigma(\tau') \\ &= -\sum_\sigma \int_0^\beta \mathrm{d}\tau \mathrm{d}\tau' d_\sigma^\dagger(\tau) \mathcal{G}_{0\sigma}(\tau - \tau')^{-1} d_\sigma(\tau') \end{aligned} \tag{II.9}$$

Where we recognized the non-interacting Green's function $\mathcal{G}_{0\sigma}(i\omega_n)^{-1} = i\omega_n - \epsilon - \Delta_\sigma(i\omega_n)$. And with $\langle\rangle_0$ designing the average over the non-interacting system we have :

$$\begin{aligned} Z_0 &= \int \mathcal{D}[d_\sigma^\dagger, d_\sigma] e^{-\mathcal{S}_0} \\ \langle A \rangle_0 &= \frac{1}{Z_0} \int \mathcal{D}[d_\sigma^\dagger, d_\sigma] e^{-\mathcal{S}_0} A \end{aligned} \tag{II.10}$$

We can now expand the interaction part in the expression of the partition function with noting T_τ the imaginary time-ordering operator :

$$\begin{aligned} Z &= \int \mathcal{D}[d_\sigma^\dagger, d_\sigma] e^{-\mathcal{S}} \\ &= \int \mathcal{D}[d_\sigma^\dagger, d_\sigma] e^{-\mathcal{S}_0} e^{-U \int_0^\beta \mathrm{d}\tau n_\downarrow(\tau) n_\uparrow(\tau)} \\ &= Z_0 \langle T_\tau e^{-U \int_0^\beta \mathrm{d}\tau n_\downarrow(\tau) n_\uparrow(\tau)} \rangle_0 \\ &= Z_0 \sum_n \int_0^\beta \mathrm{d}\tau_1 ... \mathrm{d}\tau_n \frac{(-U)^n}{n!} \langle T_\tau n_{d\downarrow}(\tau_1) n_{d\uparrow}(\tau_1) ... n_{d\downarrow}(\tau_n) n_{d\uparrow}(\tau_n) \rangle_0 \end{aligned} \tag{II.11}$$

Where we recognize a perturbative expansion in powers of the interaction U. The correlator over the non-interacting system can be computed as a determinant using Wick's theorem. We note $D_{n,\sigma}$ the $n \times n$ matrix of elements $[D_{n,\sigma}]_{i,j} = \mathcal{G}_0(\tau_i - \tau_j)$:

$$Z = Z_0 \sum_n \int_0^\beta \mathrm{d}\tau_1 ... \mathrm{d}\tau_n \frac{(-U)^n}{n!} \mathrm{Det} D_{n,\uparrow} \mathrm{Det} D_{n,\downarrow} \tag{II.12}$$

And the Green's function is obtained through the functional derivation :

$$\begin{aligned}\mathcal{G}_\sigma(\tau-\tau') &= -\frac{\delta \ln Z}{\beta\delta\Delta_\sigma(-\tau+\tau')} \\ &= -\frac{Z_0}{Z}\sum_n \int_0^\beta \mathrm{d}\tau_1 ... \mathrm{d}\tau_n \frac{(-U)^n}{n!}\langle T_\tau n_{d\downarrow}(\tau_1)n_{d\uparrow}(\tau_1)...n_{d\downarrow}(\tau_n)n_{d\uparrow}(\tau_n)d_\sigma(\tau)d_\sigma^\dagger(\tau')\rangle_0\end{aligned} \tag{II.13}$$

Which can also be written in terms of determinants with $D'_{n,\sigma}$ the $(n+1)\times(n+1)$ matrix defined by :

$$D'_{n,\sigma} = \begin{bmatrix} \mathcal{G}_{0\sigma}(0^-) & \dots & \mathcal{G}_{0\sigma}(\tau_1-\tau_n) & \mathcal{G}_{0\sigma}(\tau_1-\tau') \\ \mathcal{G}_{0\sigma}(\tau_2-\tau_1) & \dots & \mathcal{G}_{0\sigma}(\tau_2-\tau_n) & \mathcal{G}_{0\sigma}(\tau_2-\tau') \\ \vdots & \ddots & \vdots & \vdots \\ \mathcal{G}_{0\sigma}(\tau-\tau_1) & \dots & \mathcal{G}_{0\sigma}(\tau-\tau_n) & \mathcal{G}_{0\sigma}(\tau-\tau') \end{bmatrix} \tag{II.14}$$

And the Green's function writes :

$$\mathcal{G}_\sigma(\tau-\tau') = -\frac{Z_0}{Z}\sum_n \int_0^\beta \mathrm{d}\tau_1 ... \mathrm{d}\tau_n \frac{(-U)^n}{n!}\mathrm{Det}D'_{n,\sigma}\mathrm{Det}D_{n,\sigma} \tag{II.15}$$

Hybridization expansion :

An other perturbative approach starts from the atomic limit of the problem ($U\to\infty$) and expands physical quantities in the hybridization function $\Delta_\sigma(\tau)$. The atomic limit is described by the action :

$$S_{\mathrm{loc}} = \sum_\sigma \int_0^\beta \mathrm{d}\tau d_\sigma^\dagger(\tau)(\partial_\tau+\epsilon)d_\sigma(\tau) + U\int_0^\beta \mathrm{d}\tau n_\downarrow(\tau)n_\uparrow(\tau) \tag{II.16}$$

In the local system we have :

$$\begin{aligned} Z_{\mathrm{loc}} &= \int \mathcal{D}[d_\sigma^\dagger, d_\sigma] e^{-\mathcal{S}_{\mathrm{loc}}} \\ \langle A\rangle_{\mathrm{loc}} &= \frac{1}{Z_{\mathrm{loc}}}\int \mathcal{D}[d_\sigma^\dagger, d_\sigma] e^{-\mathcal{S}_{\mathrm{loc}}} A = \frac{\mathrm{Tr}(e^{-\beta\mathcal{H}_{\mathrm{loc}}}A)}{Z_{\mathrm{loc}}} \end{aligned} \tag{II.17}$$

With the local Hamiltonian $\mathcal{H}_{\mathrm{loc}} = \sum_\sigma \epsilon\hat{d}_\sigma^\dagger\hat{d}_\sigma + U\hat{n}_{d,\downarrow}\hat{n}_{d,\uparrow}$. In the same way as we proceeded for the interaction expansion, we can now expand the partition function in the hybridization function :

$$\begin{aligned} Z &= \int \mathcal{D}[d_\sigma^\dagger, d_\sigma] e^{-\mathcal{S}} \\ &= \int \mathcal{D}[d_\sigma^\dagger, d_\sigma] e^{-\mathcal{S}_{\text{loc}}} e^{-\sum_\sigma \int_0^\beta \mathrm{d}\tau \mathrm{d}\tau' d_\sigma^\dagger(\tau)\Delta_\sigma(\tau-\tau')d_\sigma(\tau')} \\ &= Z_{\text{loc}} \langle T_\tau e^{-\sum_\sigma \int_0^\beta \mathrm{d}\tau \mathrm{d}\tau' d_\sigma^\dagger(\tau)\Delta_\sigma(\tau-\tau')d_\sigma(\tau')} \rangle_{\text{loc}} \\ &= \mathrm{Tr}(\sum_n \int_0^\beta \mathrm{d}\tau_1 ... \mathrm{d}\tau_n' \frac{(-1)^n}{n!} T_\tau \exp(-\beta \mathcal{H}_{\text{loc}} \prod_{i,\sigma} d_\sigma^\dagger(\tau_i)\Delta_\sigma(\tau_i - \tau_i')d_\sigma(\tau_i'))) \end{aligned} \tag{II.18}$$

Which can be rewritten in terms of a determinant of the $n \times n$ matrix $\Delta_{n,\sigma}$ of elements $[\Delta_{n,\sigma}]_{i,j} = \Delta_\sigma(\tau_i^\sigma - \tau_j^{'\sigma})$:

$$\begin{aligned} Z = \sum_{n_\uparrow, n_\downarrow} \int_0^\beta \mathrm{d}\tau_1^\uparrow ... \mathrm{d}\tau_{n_\uparrow}^{'\uparrow} \int_0^\beta \mathrm{d}\tau_1^\downarrow ... \mathrm{d}\tau_{n_\downarrow}^{'\uparrow} \prod_\sigma \frac{\mathrm{Det}(\Delta_{n,\sigma})}{n_\sigma!^2} \\ \times \mathrm{Tr}(T_\tau e^{-\beta \mathcal{H}_{\text{loc}}} \prod_{\sigma,i} d_\sigma^\dagger(\tau_i^\sigma) d_\sigma(\tau_i^{'\sigma})) \end{aligned} \tag{II.19}$$

The hybridization expansion of the partition function. Contrary to the interaction expansion, here the average value is over the local Hamiltonian which is not quadratic since it contains the local Coulomb interaction quartic term. Therefore we can not apply Wick's theorem and have to perform a trace over the local degrees of freedom to evaluate the partition function. We obtain the Green's function :

$$\begin{aligned} \mathcal{G}_\sigma(\tau - \tau') = \frac{1}{Z} \sum_{n_\uparrow, n_\downarrow} \int_0^\beta \mathrm{d}\tau_1^\uparrow ... \mathrm{d}\tau_{n_\uparrow}^{'\uparrow} \int_0^\beta \mathrm{d}\tau_1^\downarrow ... \mathrm{d}\tau_{n_\downarrow}^{'\uparrow} \prod_{\sigma'} \frac{\mathrm{Det}(\Delta_{n,\sigma'})}{n_{\sigma'}!^2} \\ \times \mathrm{Tr}(T_\tau e^{-\beta \mathcal{H}_{\text{loc}}} \prod_{\sigma',i} d_{\sigma'}^\dagger(\tau_i^{\sigma'}) d_{\sigma'}(\tau_i^{'\sigma'}) d_\sigma(\tau) d_\sigma^\dagger(\tau')) \end{aligned} \tag{II.20}$$

These equations are easily generalized to any correlator. The equations for the partition function expansions in this form are at the basis of two Continuous-Time Quantum Monte Carlo (CT-QMC) algorithms. We describe them in the next section.

II.1.2 Stochastic sampling and impurity solver

We have shown how to express perturbatively the partition function as a power series :

$$Z = \sum_n Z_n \xi^n \tag{II.21}$$

With ξ the perturbation parameter being either the Coulomb repulsion U or the hybridization function Δ. In both cases the expansion coefficients Z_n are expressed as multidimensional integrals. One of the most efficient tool to evaluate integrals over a high dimensional space is the Monte Carlo method. In this section we describe the continuous

time Monte Carlo algorithms in interaction (CT-INT) and hybridization (CT-HYB) which sample stochastically the partition function. They are part of a class of algorithms called Continuous Time Quantum Monte Carlo (CTQMC). We give general explanations on the Monte Carlo procedure and show how it is applied to these two impurity solvers. These two algorithms consist in a first example of Diagrammatic Monte Carlo algorithms.

Monte Carlo :

The Monte Carlo method aims at computing integrals using a stochastic process to generate configurations over the multidimensional integration space. Here, in the general case of both expansions, we have expressed the partition function as an integration (or sum) over many inner variables x_i :

$$Z = \int \mathrm{d}x_1 ... \mathrm{d}x_m z(x_1, ..., x_m) = \int_\Omega \mathrm{d}x z(x) \tag{II.22}$$

With $\Omega = \{x_1, ..., x_m\}$ the multidimensional integration space. The Monte Carlo method computes this integral through generating configurations in the ensemble $X \in \Omega$ and evaluating $z(X)$ at these configurations. For configurations X_i generated uniformly we obtain :

$$Z = \int_\Omega \mathrm{d}x z(x) \approx \frac{\Omega}{N} \sum_{i=1}^{N} z(X_i) \tag{II.23}$$

Where the sum runs over the randomly generated configurations X_i. This equation becomes exact in the limit of infinite configurations $N \to \infty$.

However sampling uniformly the configuration space will lead to poor convergence properties by generating configurations where the function z is small. We need to sample efficiently the configuration space by defining a Monte Carlo weight $\mathcal{W}(X)$ which is a distribution probability for generating the configurations X_i. This procedure is called importance sampling :

$$Z \approx \frac{1}{N} \sum_{i=1}^{N} \frac{z(X_i)}{\mathcal{W}(X_i)} \tag{II.24}$$

The best strategy would be to sample the configuration space according to a probability density proportional to z so that we only need to accumulate the sign of the non-positive z function :

$$\mathcal{W}(X) = \frac{|z(X)|}{\int_\Omega \mathrm{d}X' |z(X')|} \qquad Z = \sum_{\mathcal{C}}^{MC} \mathrm{sgn}(z(\mathcal{C})) \tag{II.25}$$

Where the sum on 'MC' means that we do the summation according to the Monte Carlo procedure in the limit of a large number of configurations $\mathcal{C}$ which are generated according to the defined Monte Carlo weight $\mathcal{W}(\mathcal{C})$.

In practice we do not know a priori the normalization of the function z and we do not know how to generate configurations directly according to this probability distribution. This means that we can not use this optimal Monte Carlo weight while sampling directly the configuration space. This problem is solved by constructing a Markov chain to explore the configuration space with a probability density which doesn't require normalization. A Markov chain is a stochastic process that generates new configurations iteratively from the existing one. Starting from a configuration X we get to a new configuration Y with a probability W_{XY}. A sufficient condition for the configurations to be generated according to a given density probability $\mathcal{W}$ is the detailed balance condition :

$$W_{XY}\mathcal{W}(X) = W_{YX}\mathcal{W}(Y) \tag{II.26}$$

There are many ways to choose a transition amplitude W_{XY} which satisfies this condition. The most famous approach lies in the Metropolis-Hastings algorithm. It consists in splitting the transition probability W into two parts with $W_{XY} = T_{XY}A_{XY}$:

- We first propose a change from a configuration X to Y with probability T_{XY}.
- The transition is then accepted with probability A_{XY}. If rejected we stay in configuration X.

The detailed balance condition is satisfied by setting the acceptance probability as :

$$A_{XY} = \min(1, \frac{\mathcal{W}(Y)T_{YX}}{\mathcal{W}(X)T_{XY}}) \tag{II.27}$$

More details and concrete examples on Monte Carlo simulations are given in Subsection III.1.2. We make several remarks before applying this procedure to the two impurity solvers detailed in this section :

- The amplitude probability T_{XY} for proposing changes in configuration can be chosen arbitrarily and adapted to the configuration space. It is only required to ensure ergodicity which means that a configuration Y can be reached from a given configuration X in a finite number of steps.
- Only the ratio of Monte Carlo weights appears in the detailed balance Eq. II.26. This shows that the probability density does not require to be normalized when constructing the Markov chain and we can use the optimal distribution of Eq. II.25.
- The convergence property of the Monte Carlo sum is ensured by the Central Limit theorem. For a finite, but large, number N of uncorrelated configurations explored by the Monte Carlo procedure, the standard deviation of the distribution varies like $1/\sqrt{N}$. Therefore it converges to the exact value of the integral in the limit of long computational time and the Monte Carlo belongs to the class of methods called numerically exact.

- Since the statistical error on the Monte Carlo result does not depend on the dimension of the configuration space, it proves to be much more efficient for high dimensional integration than standard discretization scheme such as Simpson integration. For these techniques applied to an integration over a D-dimensional space discretized into N points the convergence scales as $1/\sqrt[D]{N}$ which becomes very slow at large D. Other numerical methods such as Quasi-Monte Carlo [90] or Tensor Trained Cross approximation [97] have proven effective for multidimensional integration.

In the following we apply the Monte Carlo method to the perturbative expansions developed in the previous subsection. We apply it to measure the Green's function as an example which can be generalized to the measurement of the self-energy or any other correlator. Since they are expressed as a ratio of an integral of a determinant-like quantity over the partition function, we use the partition function expansion for importance sampling. We accumulate both the numerator and denominator at every Monte Carlo step and need to reach the convergence for both procedures to obtain the quantity of interest.

CT-INT :

The CT-INT algorithm computes the interacting Green's function through its expansion in the Coulomb interaction U. It is evaluated as a fraction over the partition function as shown in Eq.II.15. To evaluate the multi-dimensional integrals we define a Monte-Carlo configuration as $\mathcal{C} = \{n, \tau_1, ...\tau_n\}$:

$$\sum_{\mathcal{C}}^{MC} \frac{1}{\mathcal{W}(\mathcal{C})} = \sum_n \int_0^\beta \mathrm{d}\tau_1 ... \int_0^\beta \mathrm{d}\tau_n \tag{II.28}$$

We aim at sampling the partition function which expansion is shown in Eq. II.12, hence the weight of a Monte Carlo configuration :

$$\mathcal{W}(\mathcal{C}) = |\frac{(-U)^n}{n!} \mathrm{Det} D_{n,\uparrow} \mathrm{Det} D_{n,\downarrow}| \tag{II.29}$$

So that the partition function is obtained by accumulating its sign :

$$Z = Z_0 \sum_{\mathcal{C}}^{MC} ((-1)^n \mathrm{sgn}(\mathrm{Det} D_{\mathcal{C},\uparrow} \mathrm{Det} D_{\mathcal{C},\downarrow}) \tag{II.30}$$

In order to measure the Green's function it is useful to have the Monte Carlo weight appear in the numerator of its expression. We expand the determinant of $\tilde{D}_{n,\sigma}$ with respect to the last line and last column :

$$\mathcal{G}_\sigma(\tau) = \mathcal{G}_{0\sigma}(\tau) - \frac{1}{\beta Z}\mathcal{G}_{0\sigma}(-\tau)^2 \sum_n \int_0^\beta \mathrm{d}\tau_1 ... \int_0^\beta \mathrm{d}\tau_n \frac{(-U)^n}{n!} \mathrm{Det}D_{n,\uparrow}\mathrm{Det}D_{n,\downarrow} \times \sum_{i,j=1}^{n} \delta(\tau_i - \tau_j + \tau)[D_{n,\sigma}]^{-1}_{ij} \tag{II.31}$$

At the expense of a matrix inversion we obtain a new form for the Green's function to be computed stochastically :

$$\mathcal{G}_\sigma(\tau) = \mathcal{G}_{0\sigma}(\tau) - \frac{1}{\beta Z}\mathcal{G}_{0\sigma}(-\tau)^2 \sum_{\mathcal{C}}^{MC} (-1)^n \mathrm{sgn}(\mathrm{Det}D_{\mathcal{C},\uparrow}\mathrm{Det}D_{\mathcal{C},\downarrow}) \times \sum_{i,j=1}^{n} \delta(\tau_i - \tau_j + \tau)[D_{\mathcal{C},\sigma}]^{-1}_{ij} \tag{II.32}$$

CT-HYB :

The CT-HYB algorithm computes the interacting Green's function through its expansion in the hybridization function Δ. Given the multi-dimensional integral Eq. II.20 we define a Monte Carlo configuration by $\mathcal{C} = \{n_\sigma, \{\tau_i^\sigma, \tau_j^{'\sigma}\}_{1\leq i,j\leq n_\sigma}\}_{\sigma=\uparrow,\downarrow}$:

$$\sum_{\mathcal{C}}^{MC} \frac{1}{\mathcal{W}(\mathcal{C})} = \sum_{n_\uparrow, n_\downarrow} \int_0^\beta \mathrm{d}\tau_1^\uparrow ... \mathrm{d}\tau_{n_\uparrow}^{'\uparrow} \int_0^\beta \mathrm{d}\tau_1^\downarrow ... \mathrm{d}\tau_{n_\downarrow}^{'\uparrow} \tag{II.33}$$

We aim at sampling the partition function which expansion is shown in Eq. II.19, hence the weight of a Monte Carlo configuration :

$$\mathcal{W}(\mathcal{C}) = |\prod_\sigma \frac{\mathrm{Det}(\Delta_{n,\sigma})}{n_\sigma!^2} \times \mathrm{Tr}(T_\tau e^{-\beta\mathcal{H}_{\mathrm{loc}}} \prod_\sigma d_\sigma^\dagger(\tau_i^\sigma) d_\sigma(\tau_i^{'\sigma}))| \tag{II.34}$$

So that the partition function is obtained by accumulating its sign :

$$Z = \sum_{\mathcal{C}}^{MC} \mathrm{sgn}(\prod_\sigma \frac{\mathrm{Det}(\Delta_{\mathcal{C},\sigma})}{n_{\sigma!}^2} \times \mathrm{Tr}(T_\tau e^{-\beta\mathcal{H}_{\mathrm{loc}}} \prod_\sigma d_\sigma^\dagger(\tau_i^\sigma) d_\sigma(\tau_i^{'\sigma}))) \tag{II.35}$$

We perform the functional derivative from the expression of Z Eq. II.19 in order to express the Green's function in terms of the Monte Carlo weight :

$$\mathcal{G}_\sigma(\tau) = -\frac{1}{\beta Z} \sum_{n_\uparrow, n_\downarrow} \int_0^\beta \mathrm{d}\tau_1^\uparrow ... \mathrm{d}\tau_{n_\uparrow}^{'\uparrow} \int_0^\beta \mathrm{d}\tau_1^\downarrow ... \mathrm{d}\tau_{n_\downarrow}^{'\uparrow} \prod_{\sigma'} \frac{\mathrm{Det}(\Delta_{n,\sigma'})}{n_{\sigma'}!^2} \times \mathrm{Tr}(T_\tau e^{-\beta\mathcal{H}_{\mathrm{loc}}} \prod_{\sigma',i} d_{\sigma'}^\dagger(\tau_i^{\sigma'}) d_{\sigma'}(\tau_i^{'\sigma'})) \times \sum_{i,j=1}^{n} \delta(\tau_i^\sigma - \tau_j^\sigma + \tau)[\Delta_{n,\sigma}]^{-1}_{ij} \tag{II.36}$$

And the Green's function is computed stochastically through :

$$\begin{aligned}\mathcal{G}_\sigma(\tau) = -\frac{1}{\beta Z}\sum_{\mathcal{C}}^{MC} \mathrm{sgn}(\prod_{\sigma'} \mathrm{Det}(\Delta_{\mathcal{C},\sigma'}) \times \mathrm{Tr}(T_\tau e^{-\beta\mathcal{H}_{\mathrm{loc}}} \prod_{\sigma',i} d^\dagger_{\sigma'}(\tau_i^{\sigma'}) d_{\sigma'}(\tau_i^{'\sigma'})))\\ \times \sum_{i,j=1}^{n} \delta(\tau_i^\sigma - \tau_j^\sigma + \tau)[\Delta_{\mathcal{C},\sigma}]^{-1}_{ij}\end{aligned} \tag{II.37}$$

Comparison and limitations of the CTQMC algorithms :

Both these algorithms rely on the same approach : expressing a correlator as a ratio of a perturbative series over the partition function, and using the partition function for importance sampling of the stochastic computation. They perform directly the summation over the perturbative orders to obtain a ratio of two Monte Carlo sums. This means that they need to allow updates between configurations with a different number of imaginary times called insertions or removals, as well as simple modifications of times on the imaginary time axis.

At each Monte Carlo step theses methods require the computation of determinant and of inverse matrices of size $n \times n$ which leads to a complexity per Monte Carlo step scaling like n^3 with n the average perturbation order in the stochastic process. This average order can be related to the physical parameters of the problem with $n \sim NU\beta$ for the interaction expansion case (CT-INT) and $n \sim NE_{kin}\beta$ for the hybridization expansion case (CT-HYB) with N the size of the impurity ($N = 1$ here for a single-orbital single-site impurity) and E_{kin} the kinetic energy of the system. Additionally, for the CT-HYB algorithm one needs to compute a trace over the local states, which leads to an exponential complexity with the size of the impurity. This explains the main difference between these two approaches : the interaction expansion works better for weakly interacting systems, while the hybridization expansion is limited by the kinetic energy and works better in the large interaction limit. They are complementary in the sense that their perturbative approach starts form different limits and tries to reach the intermediate coupling regime where the kinetic and potential energies are of the same order.

This could have us think that we found methods that solve strongly correlated systems in a polynomial complexity, for any temperature or system size. Nonetheless, these approaches suffer from an other main issue which we discuss in the next section : the sign problem.

II.1.3 Sign problem and chemical potential shift

The main limitation to the CTQMC algorithms at low temperature and for large system sizes is caused by the sign problem. In the expansion of the partition function or of the Green's function, we see that the Monte Carlo contributions have a changing sign

depending on the imaginary time distribution and on the order. When sampling the partition function we therefore need to accumulate its sign as shown in Eq. II.30 and Eq. II.35. Depending on the Monte Carlo configuration this sign alternates leading to cancellations between different measurements. In the end these cancellations can cause a huge raise of the statistical error and become overwhelming at small temperature. The sign problem is even worsen in the context of CTQMC algorithms by the fact that the quantity of interest is expressed as a ratio over the partition function. This makes the statistical error of the ratio explode after error propagation. This alternating sign ultimately comes from the fermionic anticommutation relations and is believed to make the solving of strongly correlated fermionic systems a nondeterministic polynomial hard problem (NP hard) [137].

The sign problem can be estimated during the Monte Carlo computation as :

$$\langle \mathrm{sgn}(Z) \rangle = \frac{\int \mathrm{d}x_1 ... \mathrm{d}x_m z(x_1, ..., x_m)}{\int \mathrm{d}x_1 ... \mathrm{d}x_m |z(x_1, ..., x_m)|} \tag{II.38}$$

This sign is known to decrease exponentially towards 0 when increasing the system size or decreasing the temperature. It remains the main limitation to Monte Carlo methods for strongly correlated fermions.

The α-shift :

One way to soften the sign problem is to redefine the starting point of the perturbation expansion. In the CT-INT algorithm one can redefine the non-interacting Hamiltonian (or action) and propagator. This technique is called the α-shift and it takes the form of a chemical potential shift. We detail this in a more general and detailed way in Subsection III.1.3. The idea here is to redefine the interaction term as :

$$U n_{d,\downarrow} n_{d,\uparrow} \rightarrow U(n_{d,\downarrow} - \alpha_\uparrow)(n_{d,\uparrow} - \alpha_\downarrow) + U \sum_\sigma n_{d,\sigma} \alpha_\sigma + \mathrm{const} \tag{II.39}$$

This will have no consequence on the final result since we are, up to a non essential constant, describing the same Hamiltonian. We incorporate the quadratic term of this interaction in the non-interacting propagator which is now written :

$$\tilde{\mathcal{G}}_{0,\sigma}(i\omega_n) = \frac{1}{i\omega_n - \epsilon - U\alpha_\sigma - \Delta_\sigma(i\omega_n)} \tag{II.40}$$

This means that the perturbative expansion is performed around a different starting point defined by this new propagator. The perturbative expansion of the partition function (similarly to the one of the Green's function) changes to incorporate the α terms :

$$\begin{aligned}\tilde{Z} &= \tilde{Z}_0 \sum_n \int_0^\beta \mathrm{d}\tau_1 ... \mathrm{d}\tau_n \frac{(-U)^n}{n!} \langle T_\tau (n_{d\downarrow}(\tau_1 - \alpha_\uparrow) ... (n_{d\uparrow}(\tau_n) - \alpha_\downarrow) \rangle_0 \\ &= \tilde{Z}_0 \sum_n \int_0^\beta \mathrm{d}\tau_1 ... \mathrm{d}\tau_n \frac{(-U)^n}{n!} \mathrm{Det}\tilde{D}_{n,\uparrow} \mathrm{Det}\tilde{D}_{n,\downarrow}\end{aligned} \tag{II.41}$$

Where after applying Wick's theorem we obtain the same expression involving determinants of the shifted matrices :

$$\tilde{D}_{n,\sigma} = \begin{bmatrix} \mathcal{G}_{0\sigma}(0^-) - \alpha_{\bar{\sigma}} & \mathcal{G}_{0\sigma}(\tau_1 - \tau_2) & \dots & \mathcal{G}_{0\sigma}(\tau_1 - \tau_n) \\ \mathcal{G}_{0\sigma}(\tau_2 - \tau_1) & \mathcal{G}_{0\sigma}(0^-) - \alpha_{\bar{\sigma}} & \dots & \mathcal{G}_{0\sigma}(\tau_2 - \tau_n) \\ \vdots & \vdots & \ddots & \vdots \\ \mathcal{G}_{0\sigma}(\tau_n - \tau_1) & \mathcal{G}_{0\sigma}(\tau_n - \tau_2) & \dots & \mathcal{G}_{0\sigma}(0^-) - \alpha_{\bar{\sigma}} \end{bmatrix} \tag{II.42}$$

In general, for a system close to half-filling $\langle n_\sigma \rangle \approx 1/2$ we choose to set the α coefficients as :

$$\alpha = \frac{1}{2} + (-1)^\sigma \delta \tag{II.43}$$

With δ a small parameter. With this choice we expect the operators $n_\uparrow - \alpha_\downarrow$ and $n_\downarrow - \alpha_\uparrow$ to have opposite signs on average, creating a new alternating sign depending on the order n. This sign is expected to cancel with the $(-U)^n$ term and has proven to limit the cancellations between different the contributions at different orders [147].

II.2 Diagrammatic Monte Carlo

Although Continuous Time Quantum Monte Carlo algorithms have been a breakthrough for solving impurity problems in the context of the DMFT framework, we have seen that they face strong limits when increasing the system size. In this thesis we aim at going further and addressing the many-body fermionic problem in the thermodynamic limit, and without approximation.

The idea developed in this section is based on the diagrammatic formalism developed initially by Feynman for tackling perturbative expansions in high energy physics. After briefly introducing Feynman diagrams and their application to perturbative expansions, we show how the DiagMC (Diagrammatic Monte Carlo) algorithm computes sums of diagrams to construct perturbative series, and we detail the main limitations to perturbative approaches.

In this section we consider a perturbative approach of the Hubbard Hamiltonian in the Coulomb interaction U, directly on the full lattice of N sites, and we write :

$$\begin{aligned}\mathcal{H} &= -t\sum_{\langle i,j\rangle}\sum_{\sigma}\hat{c}^{\dagger}_{i\sigma}\hat{c}_{j\sigma} + U\sum_{i}\hat{n}_{i\uparrow}\hat{n}_{i\downarrow} - \mu\sum_{i}(\hat{n}_{i\uparrow}+\hat{n}_{i\downarrow}) \\ &= \mathcal{H}_0 + U\mathcal{H}_{exp}\end{aligned} \tag{II.44}$$

$$\mathcal{H}_0 = -t\sum_{\langle i,j\rangle}\sum_{\sigma}\hat{c}^{\dagger}_{i\sigma}\hat{c}_{j\sigma} - \mu\sum_{i}(\hat{n}_{i\uparrow}+\hat{n}_{i\downarrow}) \qquad \mathcal{H}_{exp} = \sum_{i}\hat{n}_{i\uparrow}\hat{n}_{i\downarrow}$$

With $\mathcal{H}_0$ the non-interacting Hamiltonian, and $\mathcal{H}_{exp}$ the interacting expansion Hamiltonian. Similarly to the hybridization expansion developed on the CT-HYB algorithm, we could also start the perturbative treatment from the atomic limit $U \to \infty$ and perform a perturbation in the hopping parameter t. For simplicity we will focus on the interaction expansion which is at the basis of the algorithmic developments presented in this thesis in the chapters III and IV.

II.2.1 Diagrammatic interpretation of perturbative expansions

In the CTQMC approach, we expressed a correlator (or observable) as a ratio of a perturbative expansion over the partition function. Typically for an observable $\mathcal{A}$ we have :

$$\mathcal{A} = \frac{\sum_{n=0}^{\infty} a_n U^n}{Z} \tag{II.45}$$

Even if the expansion coefficients turns out to be relatively easy to compute in a polynomial time, this has a major drawback : the presence of a sign problem at the denominator in the computation of the partition function leads to overwhelming statistical errors. We aim here at getting rid of the fraction and expressing an observable as a simple expansion series :

$$\mathcal{A} = \sum_{n=0}^{\infty} a_n U^n \tag{II.46}$$

In this expansion the coefficients a_n can be interpreted as sums of diagrams. More details on the use of diagrams in quantum physics can be found in [21, 95].

Expansion of the partition function :

To introduce Feynman diagrams we come back to the interaction expansion of the partition function :

$$Z = Z_0\sum_{n}\sum_{i_1,\ldots,i_n=1}^{N}\int_0^{\beta}\mathrm{d}\tau_1\ldots\mathrm{d}\tau_n\frac{(-U)^n}{n!}\langle T_\tau n_{i_1\downarrow}(\tau_1)n_{i_1\uparrow}(\tau_1)\ldots n_{i_n\downarrow}(\tau_n)n_{i_n\uparrow}(\tau_n)\rangle_0 \tag{II.47}$$

Where we added the sum over the sites of the lattice, with $n_{i\sigma}$ the density operator on site i with spin σ. In the context of CTQMC we have used Wick's theorem to express the average value over the non-interacting system $\langle \ldots \rangle_0$ as a determinant. Our idea now is to express each of these terms as diagrams which are a pictorial representation of these expectation values. They are a powerful tool to deal with perturbation theory as they enable one to understand each mathematical term in the expansion expression as a graphic representation and to better understand the combinatory arguments to compute these terms.

In the case of the interaction expansion of the Hubbard model we construct the diagrammatic representation with two main features : bare lines and vertices. The bare fermionic lines are non-interacting propagators between two points with different position and imaginary time and same spin coordinates :

$$(\tau_1, i_1, \sigma) \bullet\!\!\longrightarrow\!\!\bullet\ (\tau_2, i_2, \sigma) \quad = \mathcal{G}_{0,\sigma,i_1 i_2}(\tau_2 - \tau_1) \tag{II.48}$$

And the wiggly lines connect four propagators. They stand for the interaction perturbative term U and are called vertices :

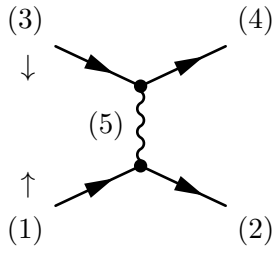

$$= -U \sum_{i_5} \int \mathrm{d}\tau_5 [\mathcal{G}_{0,\uparrow,i_1 i_5}(\tau_5 - \tau_1)\mathcal{G}_{0,\uparrow,i_5 i_2}(\tau_2 - \tau_5) \mathcal{G}_{0,\downarrow,i_3 i_5}(\tau_5 - \tau_3)\mathcal{G}_{0,\downarrow,i_5 i_4}(\tau_4 - \tau_5)] \tag{II.49}$$

Where we used the compact notation for the tips of the propagator lines $(1) = (\tau_1, i_1)$. In the following we will, without loss of generality, omit to write the indices at each vertex. Because of the form of the interacting term $U \sum_i \hat{n}_{i\uparrow}\hat{n}_{i\downarrow}$ the interaction vertices connect propagators with the same imaginary-time and position coordinates, but with opposite spins. For each closed loop one has to multiply by -1 when evaluating a diagram. In the end we notice that the order to which a diagram contributes is equal to the number of vertices it contains.

Returning to the perturbative expansion of the partition function Eq. II.47 and applying Wick's theorem we can rewrite the average value of the product of second quantization operators as a sum and product of contracted terms that we can interpret as diagrams. The partition function is expressed as a sum :

$$Z = Z_0 \sum_n \sum_{i_1,\ldots,i_n=1}^{N} \int_0^\beta \mathrm{d}\tau_1 \ldots \mathrm{d}\tau_n \mathcal{F}_n(\tau_1, i_1, \ldots, \tau_n, i_n) \tag{II.50}$$

With $\mathcal{F}_n(\tau_1, i_1, \ldots, \tau_n, i_n)$ the sum of all the possible diagram topologies with n vertices with coordinates $(\tau_1, i_1), \ldots, (\tau_n, i_n)$ which are connected or not, with no external

vertices (all vertices are linked to four propagators). For instance at the second order in perturbation in U :

$\mathcal{F}_2((1),(2)) =$ 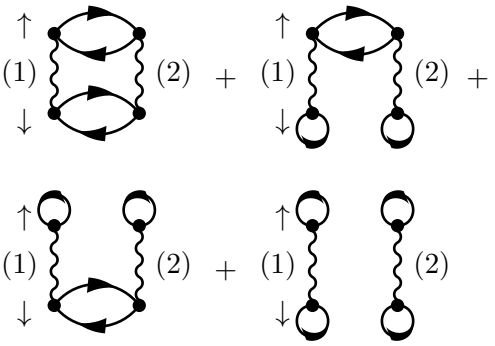 (II.51)

At a perturbation order n the number of different diagrammatic topologies that contribute to $\mathcal{F}_n$ is equal to $(n!)^2$.

Expansion of the Green's function :

Now that we have introduced the diagrammatic expansion of the partition function, we focus on applying the diagrammatic formalism to the perturbation expansion of correlators or physical observables. As in the previous Section, we take the example of the Green's function between sites l and k :

$$\mathcal{G}_{\sigma,lk}(\tau-\tau') = -\frac{Z_0}{Z}\sum_n \sum_{i_1,\dots,i_n=1}^{N} \int_0^\beta \mathrm{d}\tau_1 ... \mathrm{d}\tau_n \frac{(-U)^n}{n!} \langle T_\tau n_{i_1\downarrow}(\tau_1) n_{i_1\uparrow}(\tau_1) \dots \\ \dots n_{i_n\downarrow}(\tau_n) n_{i_n\uparrow}(\tau_n) c_{\sigma,l}(\tau) c^\dagger_{\sigma,k}(\tau') \rangle_0 \tag{II.52}$$

This expression of the numerator is very similar to the one for the partition function with two additional operators with definite sites, spin and imaginary-time. Therefore its diagrammatic expansion follows similar rules and we note :

$$\mathcal{G}_{\sigma,lk}(\tau-\tau') = -\frac{\sum_n \sum_{i_1,\dots,i_n=1}^{N} \int_0^\beta \mathrm{d}\tau_1 ... \mathrm{d}\tau_n \mathcal{B}_n((\tau_1,i_1,\dots,\tau_n,i_n),(\tau,l,\sigma),(\tau',k,\sigma))}{\sum_n \sum_{i_1,\dots,i_n=1}^{N} \int_0^\beta \mathrm{d}\tau_1 ... \mathrm{d}\tau_n \mathcal{F}_n(\tau_1,i_1,\dots,\tau_n,i_n)} \tag{II.53}$$

With $\mathcal{B}_n((\tau_1,i_1,\dots,\tau_n,i_n),(\tau,l,\sigma),(\tau',k,\sigma))$ the sum of all the possible diagram topologies connected or not, and having $n+2$ vertices with :

- n internal vertices of coordinates $(\tau_1,i_1),\dots,(\tau_n,i_n)$ each having two entering and two leaving propagators,
- one external vertex of coordinates τ,k which only has one leaving propagator with spin σ,

- one external vertex of coordinates τ', l which only has one entering propagator with spin σ.

For instance the following diagram is contributing to $\mathcal{B}_2$:

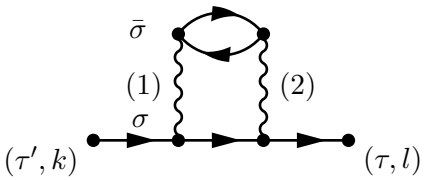

(II.54)

The Green's function is now expressed as a ratio of sums over diagrams' topologies which number grows factorially with the perturbation order n. In this form this expression is not usable for any practical purpose, but it leads to a major combinatory simplification. Indeed, from the linked-cluster theorem, we are able to factorize the numerator by the partition function. We eliminate the ratio by removing the contribution of disconnected diagrams and obtain :

$$\mathcal{G}_{\sigma,lk}(\tau-\tau') = -\sum_{n}\sum_{i_1,\ldots,i_n=1}^{N}\int_0^\beta \mathrm{d}\tau_1 ... \mathrm{d}\tau_n \mathcal{C}_n((\tau_1,i_1,\ldots,\tau_n,i_n),(\tau,l,\sigma),(\tau',k,\sigma)) \quad \text{(II.55)}$$

With $\mathcal{C}_n((\tau_1,i_1,\ldots,\tau_n,i_n),(\tau,l,\sigma),(\tau',k,\sigma))$ the sum of diagrams that follow the same rules as for $\mathcal{B}_n$ but have to be connected. Writing the interacting Green's function as a double arrow and omitting the vertices coordinates we give the Green's function perturbative expansion up to order two :

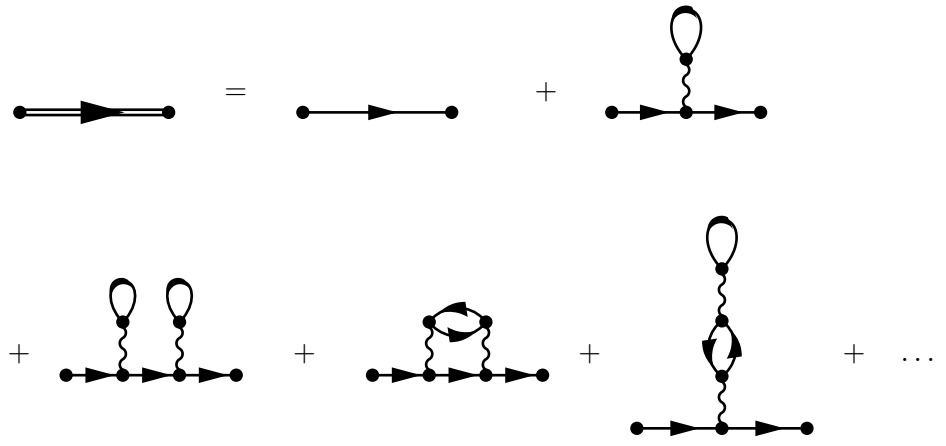

(II.56)

Self-energy :

From this diagrammatic expansion we notice that the interacting Green's function can be expressed as a series of diagrams which are called one-particle irreducible and can not be separated into two diagrams by cutting a single fermionic line. We note the sum over such diagrams as a circle and write the Green's function :

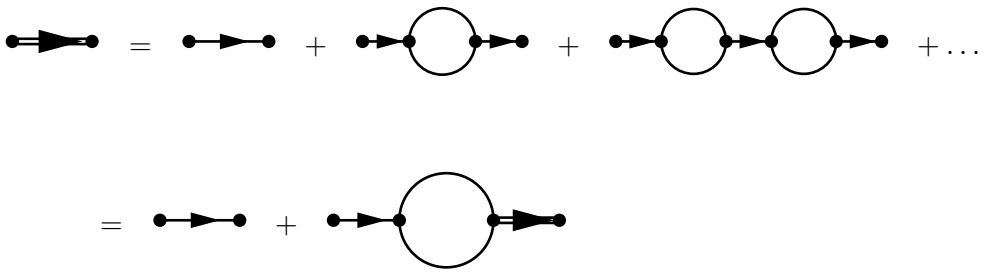

(II.57)

Where we recognize a self-consistent relation on the Green's function which is the diagrammatic expression of the Dyson's equation :

$$\mathcal{G}_{\sigma,ij}(\tau) = \mathcal{G}_{0\sigma,ij}(\tau) + \sum_{kl} \int d\tau_1 d\tau_2 \mathcal{G}_{0\sigma,ik}(\tau_1)\Sigma_{\sigma,kl}(\tau_2 - \tau_1)\mathcal{G}_{\sigma,lj}(\tau - \tau_2) \tag{II.58}$$

It corresponds to the definition of the self-energy in Matsubara frequencies and in $\mathbf{k}$ space :

$$\mathcal{G}_{\mathbf{k}\sigma}(i\omega_n) = \mathcal{G}_{0\mathbf{k}\sigma}(i\omega_n) + \mathcal{G}_{0\mathbf{k}\sigma}(i\omega_n)\Sigma_{\mathbf{k}\sigma}(i\omega_n)\mathcal{G}_{\mathbf{k}\sigma}(i\omega_n) \tag{II.59}$$

With this we identify the diagrammatic expansion of the self-energy which is the sum over all topologies of the connected one-particle irreducible diagrams.

Diagrammatic interpretation of many-body approximations :

Returning to our problem at hand, the Green's function expansion that we have derived above can be generalized to any correlator or observable. In the end, we have found a way to express, as expected without a ratio, an observable $\mathcal{A}$ in the form of a perturbative expansion in the interaction :

$$\mathcal{A} = \sum_{n=0}^{\infty} a_n U^n \tag{II.60}$$

Where the expansion coefficients a_n are a sum of a class (depending on the correlator or observable) of connected diagrams with n internal vertices. This diagrammatic formalism comes out to be very useful and manageable for analytic and algorithmic treatments. Before addressing computational and algorithmic aspects we discuss several many-body approximations which either rely directly on, or can be interpreted with diagrammatic expansions.

Some approximations rely on considering only a certain class of diagrams in the diagrammatic expansion, enabling an analytic treatment of the sum over diagrams topologies

and orders. That is the case of the Non-Crossing Approximation (NCA) which will be detailed in Chapter V. The famous mean-field (or Hatree-Fock) approximation can be interpreted in that sense. It consists in decoupling the quartic interaction term by approximating it by an effective single body interaction in an effective bath of electrons. In practice we write :

$$\hat{n}_{i\uparrow}\hat{n}_{i\downarrow} \to \hat{n}_{i\uparrow}\langle\hat{n}_{i\downarrow}\rangle + \hat{n}_{i\downarrow}\langle\hat{n}_{i\uparrow}\rangle + \langle\hat{n}_{i\uparrow}\rangle\langle\hat{n}_{i\downarrow}\rangle \tag{II.61}$$

And the Hubbard Hamiltonian becomes :

$$\begin{aligned}\hat{\mathcal{H}}_{MF} = &-t\sum_{\langle i,j\rangle}\sum_{\sigma}\hat{c}^{\dagger}_{i\sigma}\hat{c}_{j\sigma} - U\sum_{i}\langle\hat{n}_{i\uparrow}\rangle\langle\hat{n}_{i\downarrow}\rangle + U\sum_{i}\hat{n}_{i\uparrow}\langle\hat{n}_{i\downarrow}\rangle \\ &+ U\sum_{i}\hat{n}_{i\downarrow}\langle\hat{n}_{i\uparrow}\rangle - \mu\sum_{i}(\hat{n}_{i\uparrow}+\hat{n}_{i\downarrow})\end{aligned} \tag{II.62}$$

This is a quadratic Hamiltonian depending on the average values of the number operators which is easily diagonalized in $\mathbf{k}$ space. It leads to a self-consistent analytic solution and the mean-field Green's function is :

$$\begin{aligned}\mathcal{G}_{MF\mathbf{k}\sigma}(i\omega_n) &= \frac{1}{i\omega_n - \epsilon_{\mathbf{k}} - U\langle\hat{n}_{\sigma}\rangle + \mu} \\ &= \mathcal{G}_{0\mathbf{k}\sigma}(i\omega_n) + \sum_{l=0}^{\infty}(U\langle\hat{n}_{\sigma}\rangle)^{l}\mathcal{G}_{0\mathbf{k}\sigma}(i\omega_n)^{l+1}\end{aligned} \tag{II.63}$$

Where we recognize a self-consistent Dyson-like equation :

$$\mathcal{G}_{MF\mathbf{k}\sigma}(i\omega_n) = \mathcal{G}_{0\mathbf{k}\sigma}(i\omega_n) + \mathcal{G}_{0\mathbf{k}\sigma}(i\omega_n)(U\langle\hat{n}_{\sigma}\rangle)\mathcal{G}_{MF\mathbf{k}\sigma}(i\omega_n) \tag{II.64}$$

To link this expression to a diagrammatic interpretation of the mean-field approximation, let us evaluate the single loop diagram, called Hartree insertion. The double fermionic line now stands for the mean-field propagator :

$$\begin{aligned}&= U\mathcal{G}_{MFi_1i_1\sigma}(0^{-}) \\ &= U\langle\hat{c}^{\dagger}_{i_1\sigma}(0^{+})\hat{c}_{i_1\sigma}(0)\rangle_{MF} \\ &= U\langle\hat{n}_{\sigma}\rangle\end{aligned} \tag{II.65}$$

Therefore we can rewrite Eq. II.64 diagrammatically dropping the vertices' coordinates :

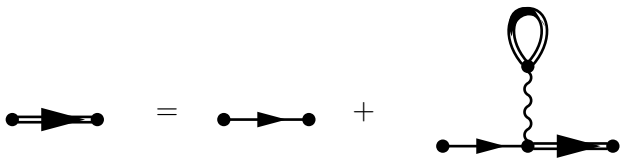

(II.66)

We notice that the mean-field approximation is equivalent to setting the self-energy to a self-consistent Hartree self-loop term. In other words, we approximate the self-energy

by keeping only the first order term (a self-loop) among all the one-particle irreducible diagrams and making it self-consistent.

Other more advanced approximations such as DMFT and its extensions have a diagrammatic interpretation. The DMFT approximation Eq. I.10 corresponds to considering only local diagram insertions in the expansion of the self-energy. This remains valid in the case of the DΓA and Trilex approximations for which only local insertions are considered in the expansion of the two-particle and three-particle irreducible vertices.

II.2.2 The DiagMC algorithm

The first direct consequence of the diagrammatic expansion Eq.II.60 is that it gives a new pertubative numerical approach to the strongly interacting problem. In the CTQMC algorithms, the partition function at the denominator of the expression was significantly worsening the sign problem and by getting rid of it we can expect to reach bigger system sizes and lower temperatures. The stochastic treatment that we detail in this section is called DiagMC (Diagrammatic Monte Carlo) [74, 105, 138].

The idea of this algorithm is to compute for each order n, the expansion coefficient a_n of the perturbation expansion of an observable $\mathcal{A}$. It is expressed as a multidimensional integration over all the topologies of connected diagrams with n internal vertices (and with external legs depending on the observable) noted $\mathbb{T}$, that imply integration over n imaginary-times and n positional indices. We define a Monte Carlo configuration as :

$$\mathcal{C} = \{(\tau_1, i_1), \ldots, (\tau_n, i_n), \mathbb{T}\} \tag{II.67}$$

And the Monte Carlo weight is defined as the absolute value of a diagram defined by the configuration $\mathcal{C}$. We note :

$$\mathcal{W}(\mathcal{C}) = |\mathbb{T}((\tau_1, i_1), \ldots, (\tau_n, i_n))| \tag{II.68}$$

Since diagrams don't have a definite sign, it needs to be accumulated as we perform the Markovian process :

$$a_n = \sum_{\mathcal{C}}^{MC} \mathrm{sgn}|\mathbb{T}((\tau_1, i_1), \ldots, (\tau_n, i_n))| \tag{II.69}$$

It is to be noted that generally, contrary to the CTQMC approach, the computation focuses on a specific perturbation order and the summation over perturbative orders has to be performed afterhand. In practice since the Markov chain does not lead to a normalized results, the stochastic process samples several orders at the same time, allowing for normalization.

A significant difficulty of this algorithm lies in the definition of the Markov chain through the Metropolis-Hasting algorithm. The standard updates for exploring the diagrams' topologies are insertions or removals of vertices. Ensuring ergodicity between all diagrams' topologies and checking their connectivity is in itself an algorithmic challenge.

This algorithm is able to tackle the low-to-intermediate coupling regime of the Hubbard model but is limited by a significant sign problem due to cancellations between diagrams. In practice it is able to reach up to order $n \sim 6-7$. In order to overcome this sign problem one could try to sample individually each diagram at a specific order and perform the sum over all topologies explicitly. However the number of diagrams increases rapidly with the perturbation order, leading to an overwhelming factorial complexity $\mathcal{O}(n!)$. Other approaches aim at generating and regrouping together many diagrams in order to reduce the effect of cancellations [27, 132].

This DiagMC algorithm can be used for computing the fully dressed self-energy in the context of skeleton series [106]. The proper self-energy is expressed self-consistently expressed in terms of renormalized propagators, making the Dyson's equation a self-consistent scheme. Although promising, this self-consistent approach has been shown to lead to misleading results by converging to non-physical propagators [75].

The main advantage of this method lies in the fact that the diagrammatic expansion is formulated directly in the thermodynamic limit. The only algorithmic step that scales with the system size is the computation of the non-interacting propagator which is done by a Fourier transform in polynomial time. Contrary to the CT-INT algorithm, the DiagMC technique is able to tackle large system sizes which is essential for the study of phase transitions. Nevertheless, one problem still remains, after obtaining the expansion coefficients up to some maximal order, how do we perform the summation of the series and what are the limitations involved ?

II.2.3 Resummation and Complex plane structure

The DiagMC technique is limited at high perturbation orders by the factorial increase in the number of diagrams it needs to sample. With this methods we are in general able to obtain a finite number of expansion coefficients with good statistical error, up to a maximal order $n_{max} \sim 6-7$. One of the advantages of the diagrammatic Monte Carlo approach is that an observable $\mathcal{A}$ is directly computed as a function of the perturbative parameter U. But a fair part of the information on this function can be hidden at higher orders.

Extrapolation to infinite perturbation order :

After performing the DiagMC algorithm we obtain the observable $\mathcal{A}$ expressed as :

$$\mathcal{A}(U) = \sum_{n=0}^{n_{max}} a_n U^n \tag{II.70}$$

In order to obtain a controlled result one needs to extrapolate this truncated perturbation series to infinite perturbation order $n_{max} \to \infty$ to retrieve the expression Eq. II.60. Several numerical tools have been developed to handle this procedure called resummation. The partial sum can be extrapolated to an infinite power series using simple polynomial

or exponential fitting of its coefficients. In this thesis we rely on Padé and D-log Padé approximants [10, 20] that express the finite series as a Padé approximant (or the derivative of the log of the finite series). More details on our complete resummation procedure will be given in IV.2.3. Other methods such as Borel summation or conformal mapping have also proven efficient on this matter.

All things considered, the information that is available to us is mostly relevant at small values of the interaction. At high values of U we expect higher orders to carry more weight in the description of the power series. This means that the more orders we are able to compute with good accuracy, the higher the values of the interaction we can describe with good confidence and control.

Limitations to perturbation theory :

The finite number of orders obtained with diagrammatic Monte Carlo is a fair obstacle to reaching strong coupling regimes from perturbation theory. But even if we could obtain an infinite number of expansion coefficients with perfect accuracy we would still face the main limitation to our perturbative approach. This limitation finds its origin in the very first assumption that we have made : that an observable $\mathcal{A}$ can be described as a power series in the interaction U.

Indeed the convergence of such a power series is not ensured, and many analytic functions can not be fully described as a power series. Such a series is characterized by a radius of convergence R which is equal to the limit for $n \to \infty$, when it exists, of the ratio $|a_n/a_{n+1}|$. It is useful here to extend the power series to complex values of U, the real values of the interaction yielding the physical results. In the complex plane the power series can diverge at some values of U called poles, or have branch cuts where the summation is not well defined, see Fig. II.1. The closest pole to the origin defines the value of the radius of convergence. Inside the radius of convergence of the series for $|U| < R$, the series is absolutely convergent and the convergence of the series with the maximal perturbation order is exponentially fast. This is the region where the diagrammatic approach is especially well suited to obtain a controlled result. Outside of the radius of convergence $|U| > R$ the series is diverging, while the power series can either converge or diverge at $|U| = R$. However exiting the radius of convergence does not necessarily mean that the perturbative approach is failing and the resummation techniques evoked above are tools for resumming diverging series [14]. A region close to a pole is however almost impossible to reach since it implies contributions from high perturbation orders.

This is probably the most challenging limitation to the use of perturbation theory directly on the lattice for tackling strongly correlated problems. It is to be noted that this limitation does not matter in the context of the CT-INT algorithm since an observable is expressed as a ratio of two functions which are entire functions of U. This means that they are holomorphic on the whole complex plane and have an infinite radius of convergence. The finite radius of convergence is a drawback of removing the ratio and the contribution of disconnected diagrams to the perturbative expansion. Thus, the poles in the expansion of an observable correspond to the zeroes of the partition function.

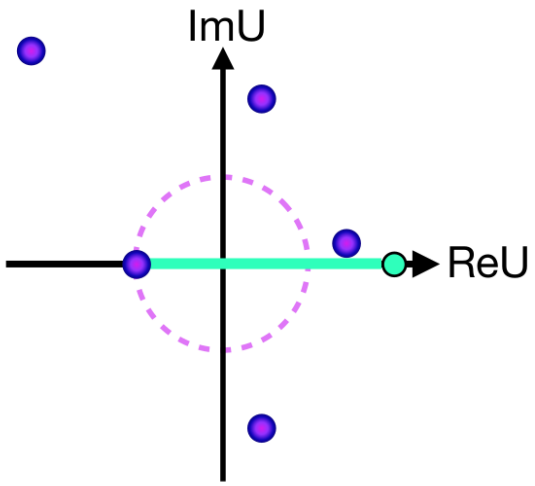

Figure II.1: Example of pole structure in the complex plane of a power series of the complex parameter U. The violet dots are poles. The closest to the origin is the one on the negative real axis, it defines the radius of convergence of the series (violet circle). The physical values we are interested in are the ones on the real axis (for a physical real interaction U). The green line represents the values where one can hope to get a resummable series for the physical value. The pole on the real axis make the region past its value a priori unreachable.

Even if poles in the complex plane are considered an artifact of our perturbative approach which can sometimes be overcome with resummation tools, some poles can be interpreted having a physical meaning. Indeed, a pole may exist because of a phase transition happening at some values of U in the Hubbard model phase diagram. A phase transition causes a divergence or a discontinuity in one of the derivatives of the quantity we are interested in. Such a behaviour is not compatible with expressing it as a power series. This is consistent with a general feature of perturbation theory : one can not describe with perturbation series a crossing of a phase transition line as the behaviours in the different phases can be considered to be analytically disconnected. This has two major consequences:

- studying the pole structure of perturbation series can give insights on the phase diagram of the model at hand,
- we need to find solutions to change the complex plane structure of perturbation series to facilitate the resummation, and ultimately to enter perturbatively ordered phases.

Chapter III

New developments in Determinantal Monte Carlo techniques

Contents

In Chapter II we have understood the essential features of perturbation theory and its diagrammatic formulation. The DiagMC approach is a powerful tool for studying strongly correlated systems directly in the thermodynamic limit, how can we go further and overcome its main limitations ?

In this chapter we show how recent developments in terms of both new algorithms and formulation of perturbation theory are pushing further the limits to Diagrammatic Monte Carlo methods. These advances rely on two main axis of progress :

- Computing more perturbation orders with better accuracy,
- Changing the starting point of the perturbation expansion to modify the complex plane structure of the perturbation series.

III.1 The Connected Determinant algorithm

In this section we present the recent advances that lead to the new Connected Determinant algorithm (CDet) [114]. This numerical technique, and its efficient implementation to study the Hubbard model are at the basis of the work presented in this thesis. All the numerical results presented in the Chapters III and IV rely on the Fast Feynman Diagrams library (FFD) which is a toolkit for implementing efficiently diagrammatic Monte Carlo algorithms.

III.1.1 Algorithm and complexity

The main advantage of the DiagMC approach comes from the cancellation of the disconnected diagrams (see Eq. II.55) in the perturbative expansion of an observable. By simplifying the partition function expansion at the denominator we obtain a numerical scheme that can cope with large system sizes. But this comes at the expense of a severe sign problem from cancellations between diagram's topologies. And trying to perform the summation between different diagram's topologies explicitly gives rise to a huge computational cost as it requires a factorial number of operations. In the CT-INT algorithm, taking advantage of Wick's theorem, the factorial number of contributions of connected or disconnected diagrams is computed as a determinant in polynomial time. The idea of the CDet algorithm is, starting from these determinant-like contributions, to remove recursively the contribution of disconnected diagrams at each order.

Recursion for connected diagrams :

To illustrate this recursive procedure we consider the interacting Green's function $\mathcal{G}_{\sigma i_{in} i_{out}}(\tau_{out} - \tau_{in})$. Its order n expansion coefficient is the sum of connected diagrams with n internal vertices which coordinates are given by the set $V = \{(i_1, \tau_1), \dots, (i_n, \tau_n)\}$ and two external ones $\{x_{in} = (i_{in}, \tau_{in}), x_{out} = (i_{out}, \tau_{ou})\}$. We aim at computing the sum over all possible connected topologies of the diagrams that live on these vertices. We note the sum of the connected diagrams on this ensemble of $n+2$ vertices $\mathbf{C}(V)(x_{in}, x_{out})$. We can compute as a determinant the sum of connected and disconnected diagrams on this set

of vertices which we note $\mathbf{D}(V)(x_{in}, x_{out})$. We recall that in the case of the perturbative expansion in interaction of the Hubbard Hamiltonian it is expressed as :

$$\mathbf{D}(V)(x_{in}, x_{out}) = \mathrm{Det} D'_{n,\sigma} \mathrm{Det} D_{n,\bar{\sigma}} \tag{III.1}$$

Where the $n+1 \times n+1$ matrix $D'_{n,\sigma}$ is expressed in terms of the non-interaction propagator :

$$D'_{n,\sigma} = \begin{bmatrix} \mathcal{G}_{0\sigma i_1 i_1}(0^-) & \dots & \mathcal{G}_{0\sigma i_n i_1}(\tau_1 - \tau_n) & \mathcal{G}_{0\sigma i_{in} i_1}(\tau_1 - \tau_{in}) \\ \mathcal{G}_{0\sigma i_1 i_2}(\tau_2 - \tau_1) & \dots & \mathcal{G}_{0\sigma i_n i_2}(\tau_2 - \tau_n) & \mathcal{G}_{0\sigma i_{in} i_2}(\tau_2 - \tau_{in}) \\ \vdots & \ddots & \vdots & \vdots \\ \mathcal{G}_{0\sigma i_1 i_{out}}(\tau_{out} - \tau_1) & \dots & \mathcal{G}_{0\sigma i_n i_{out}}(\tau_{out} - \tau_n) & \mathcal{G}_{0\sigma i_{in} i_{out}}(\tau_{out} - \tau_{in}) \end{bmatrix} \tag{III.2}$$

And $D_{n,\bar{\sigma}}$ is the same matrix without the last line and column, involving propagators with opposite spin. In order to remove the disconnected contributions to $\mathbf{D}(V)(x_{in}, x_{out})$ we notice that a disconnected diagram is composed of a disconnected part and a connected part that contains the two external vertices, both made of strictly less than $n+2$ vertices. Therefore computing the contribution of the disconnected part to $\mathbf{D}(V)(x_{in}, x_{out})$ reduces to computing the connected and disconnected contributions at lower orders, for subsets of the vertices in V. Hence a recursive scheme on the perturbative order.

In the end, to get the sum of strictly disconnected diagrams we need to sum over all the subsets $S \subsetneq V$ with vertices in S considered connected to the external vertices, and the vertices in its complementary subset V/S being disconnected :

$$\mathbf{C}(V)(x_{in}, x_{out}) = \mathbf{D}(V)(x_{in}, x_{out}) - \sum_{S \subsetneq V} \mathbf{C}(S)(x_{in}, x_{out}) \mathbf{D}(V \backslash S)(\emptyset) \tag{III.3}$$

Where $\mathbf{D}(V \backslash S)(\emptyset)$ designates the disconnected contributions of the subset $V \backslash S$ defined with no external legs. This procedure is easily generalized in the case of observables or correlators with different conditions on the external vertices involved in their diagrammatic expansion.

Complexity :

We obtain a recursive approach for computing explicitly the sum of connected diagrams. What is the computational complexity of this recursive algorithm, and how does it scale with the perturbative order in comparison to the factorial number of diagrams ?

In the recursion, to obtain the sum of connected diagrams at order n, one needs to compute all the diagrams connected or disconnected at every lower order, for every subset $S \subsetneq V$. First one needs to compute at every order k lower than n, all the possible determinants which number is $\binom{n}{k}$. This computation is done for each subset in a

polynomial time k^3. Then, performing the recursive computation, one needs to remove from every set of k vertices all of its connected subsets multiplied by one of the previously computed determinant for its complement. There are 2^k subsets for an initial set of k vertices. The complexity of the algorithm C_n is the sum of the complexities of these two steps :

$$C_n = \sum_{k=0}^{n} \binom{n}{k} k^3 + \sum_{k=0}^{n} \binom{n}{k} 2^k \propto 2^n n^3 + 3^n \tag{III.4}$$

The complexity is no longer factorial but exponential and scales like 3^n. In reality some algorithmic improvements enable one to reach a better asymptotic complexity. Using a fast principal minor computation algorithms [45, 63] one can perform the first step in a smaller 2^n asymptotic complexity. The second step, and overall complexity, can be reduced thanks to a fast subset convolution algorithm [17] leading to an asymptotic complexity increasing like $n^2 2^n$. In practice this last trick only gives a sensible speed up at large perturbation orders for $n > 10$.

In the end the CDet algorithm provides an algorithm for computing the sum of connected diagrams in exponential time. This is much faster than the naive summation over the factorial number of connected topologies. Thanks to the explicit summation of the connected diagrams this algorithm contributes to a significant reduction of the sign problem and higher perturbative orders can be reached comparatively to the DiagMC approach (see Section III.1.4). Even if the computational time for obtaining the expansion coefficient of an observable is exponential, we have seen in Section II.2.3 that the convergence of the resulting power series is exponentially fast inside the radius of convergence. With this we can show that the CDet algorithm provides a method with an overall polynomial complexity for obtaining a controlled result in the Hubbard model, at values of the interaction that sit well into the radius of convergence of the series [113].

It is to be noted that this approach can be adapted to the computation of the self-energy by summing all one-particle irreducible diagrams. The associated algorithm is called Σ-Det [58, 92].

A similar approach expressing expansion coefficients as determinants can be used int the real-time formalism and adapted to the Keldysh contour for studying out-of-equilibrium physics [13–15, 84, 104]. It does not require such a recursion for removing disconnected contributions, but it requires the sum of an exponential number of determinants at each order.

III.1.2 Many-Configuration Markov-Chain Monte Carlo

Now that we have presented an algorithm for efficiently computing explicitly the sum over connected diagrams, we rely on a Monte Carlo algorithm for performing the integration over the imaginary-time and lattice coordinates of vertices. In this approach we fix the external vertices $\{x_{in} = (i_{in}, \tau_{in}), x_{out} = (i_{out}, \tau_{ou})\}$ and define the Monte Carlo

configuration $\mathcal{C} = \{n, (\tau_1, i_1), \ldots, (\tau_n, i_n)\}$. We do not use a simple Metropolis algorithm at a fixed order n for two reasons :

- We want to take advantage of the many connected contributions computed in the CDet recursion at lower orders
- The Markovian process needs to be normalized afterwards since the Monte Carlo weight is not normalized.

Many Configurations in the Monte Carlo :

The CDet algorithm is particularly well adapted to the use of a Many-Configuration Markov Chain Monte Carlo which details are presented in [60]. In the CDet recursive scheme we compute many sums of connected diagrams (2^n subsets at an order n), which we would like to accumulate to get statistics over expansion coefficients at lower orders. This algorithm enables this by exploring many sub-configurations at each Monte Carlo step. It has the advantage of being rejection free.

Let us define n the order at which the computation is performed, and we consider a Markov chain between an infinity of configurations of sets of n vertices $\mathcal{C}_1 \to \ldots \to \mathcal{C}_j \to \mathcal{C}_{j+1} \to \ldots$. At a step j, we call V this set of n vertices. At each Monte Carlo step we perform the CDet recursive computation so that we obtain the Monte Carlo weight for all the subsets $S \subsetneq V$ which is defined as the sum of all connected diagrams :

$$\mathcal{W}(S) = |\mathbf{C}(S)(x_{in}, x_{out})| \tag{III.5}$$

The idea is to accumulate these contributions to the expansion coefficients at lower orders in between the steps j and $j+1$ of the Markov chain. We consider a continuous-time Monte Carlo procedure in this interval where, in a faster than the clock-like feature, we spend a time in each subset configuration proportional to the non normalized probability :

$$P(S) = \mathcal{W}(S)\lambda_l \tag{III.6}$$

Where l is the cardinality of the set S which corresponds to the order at which the sum of diagrams contributes. The λ_l are positive coefficients which enable renormalization between the weight given at different orders. After accumulating for the expansion coefficients at every order $l \leq n$, we select one of these subsets of V in order to update the Markov chain to the next configuration at step $j + 1$. We keep the l vertices present in S and generate the missing $n - l$ vertices. We choose to generate these new vertices with the following procedure :

- We choose randomly one of the vertices of S,
- We generate a new vertex with coordinates around this existing vertex according to a quasi-Gaussian distribution,

- We do the same procedure for generating each new vertex.

The selection of the subset of vertices which we keep to generate this new configuration is done according to a probability which enables the detailed balance condition [60]. This probability can be computed in an exponential time which is negligible at high orders comparing to the CDet recursion complexity. This procedure enables one to compute all expansion orders up to some maximal order n in a single numerical simulation. The many-configuration scheme has been shown to lead to a major speed up for the CDet Monte Carlo computation, of a factor 10^2 for a computation at order 12. It is to be noted that at the maximal order of the computation n, we only sample one configuration at each Monte Carlo step, while we accumulate many configurations at lower orders, and therefore the statistical error on the expansion coefficient at this order is huge in general. In practice if we want to compute the perturbation series up to an order n, we perform the CDet recursion with $n+1$ internal vertices.

The accumulation is done at every step of the Markov chain and we rely on a binning analysis to obtain reliable error estimates from correlated samples and get rid of the auto-correlation time. The thermalisation time is negligible in front of the Monte Carlo simulation time.

Normalizing the result :

Because of the Markovian process which relies on a distribution of probability which is not normalized, the result at each order of this Monte Carlo scheme is defined up to a constant factor. In order to normalize the obtained expansion coefficients we rely on computing the zeroth order perturbation coefficient which is a know constant. In practice we set this constant to 1 and give it the weight λ_0. It is crucial that this normalization term is computed with very good accuracy since its statistical error is propagated to all other expansion orders when normalizing.

In order to understand the complexity that this need for normalization brings, it is useful to better apprehend the effect of the reweighting coefficients λ_l. By affecting the weight given to a set of vertices depending only on its carnality, the coefficients λ_l rescale the weight given to different expansion orders. The weight associated with a specific order is directly correlated to the Monte Carlo time spent and the proportion of updates at this order. Therefore increasing the weight leads to a better Monte Carlo statistic on the corresponding expansion coefficient, at the expense of a bigger statistical error at different orders. In practice we set the coefficients $\lambda_l = 2^l$ for $l \geq 1$ which turns out to give a reliable re-weighting between orders for spending most of the time at high orders where we need a lots of statistics, but also enough statistics for obtaining accurate low expansion orders. This power law is motivated by the fact that the expansion coefficient are the prefactor of U^n in the expansion series. On the other hand, the weight λ_0 requires more work for enabling enough updates at zeroth order and an accurate normalization. It is set by the condition that the stochastic process spends approximately 10% of the Monte Carlo time accumulating at order zero. We follow the procedure :

i. We start from a guess for $\lambda_0 \sim 2^{n/3}$ where n is the maximum order of the CDet computation

ii. We run the Many-Configuration Markov-Chain Monte Carlo procedure and store the time spent accumulating at zeroth order. We need to run the Monte Carlo for enough steps to overcome the thermalization time and obtain good statistics.

iii. We compare the proportion of Monte Carlo time spent at order zero t_0 to 50% and update the coefficient $\lambda_0 \to c\lambda_0 \times 0.5/t_0$

iv. Go back to (ii) until the convergence $t_0 \to 0.5$

v. Finally update $\lambda_0 \to 0.1\lambda_0/0.5$ to rescale the time at order zero $t_0 = 0.1$

The convergence is made towards $t_0 \to 0.5$ to ensure better statistics for the time spent at order zero, before rescaling it to $t_0 = 0.1$. The coefficient c ensures that there is no oscillations in the self-consistent converging scheme $c \sim 0.8$. The convergence of this scheme is essential to the overall computation to avoid ill cases in which we spend no Monte Carlo time on normalization and we are unable to normalize the expansion coefficients, or we spend all the time on normalization and obtain huge statistical errors on the other expansion coefficients. We set limits at the step (ii) to deal with the ill situation where $t_0 = 0$.

Overall, a good value of the λ_0 coefficient is hard to predict since it is dependent on the observable at hand, on the maximal order of the simulation, on temperature, and on the spread of the probability distribution for creating new vertices which we set as a quasi-Gaussian.

III.1.3 Chemical potential shift

With the recursive CDet algorithm associated with a Many-Configuration Markov Chain Monte Carlo we can compute with good statistical accuracy many expansion coefficients up to a maximum order which depends on the observable or correlator at hand $n_{max} \sim 9 - 13$. But one main limitation still remains : how can we model the complex plane structure of the perturbation series to increase its radius of convergence and ensure better convergence properties ?

α-shift :

This can be achieved using a chemical potential shift similar to the one we have introduced in the context of CTQMC algorithms in Section II.1.3. It has been extensively used in the context of diagrammatic Monte Carlo [59, 104, 112, 147] and it can be formulated both as a chemical potential shift (the approach we take in this thesis) and as a shift to the action [71, 115].

To change the pole structure in the complex plane of the perturbation series and increase the radius of convergence we can change the starting point and the path of the perturbation expansion. The chemical potential term is quadratic and it is part of the non-interacting Hamiltonian, therefore a shift in the chemical potential changes the

starting point of the perturbation expansion. Let's formalize this by introducing the shift which expresses the chemical potential as a function of the interaction :

$$\mu \to \mu' = \mu + \alpha(U) \tag{III.7}$$

We now describe the Hubbard Hamiltonian in terms of the non-interacting and interacting expansion Hamiltonian :

$$\begin{aligned}
\mathcal{H}[\mu' = \mu + \alpha(U), U] &= -t \sum_{\langle i,j \rangle} \sum_{\sigma} \hat{c}^{\dagger}_{i\sigma} \hat{c}_{j\sigma} + U \sum_{i} \hat{n}_{i\uparrow} \hat{n}_{i\downarrow} - (\mu + \alpha(U)) \sum_{i} (\hat{n}_{i\uparrow} + \hat{n}_{i\downarrow}) \\
&= \tilde{\mathcal{H}}_0 + U \mathcal{H}_{exp} \\
\\
\tilde{\mathcal{H}}_0 &= -t \sum_{\langle i,j \rangle} \sum_{\sigma} \hat{c}^{\dagger}_{i\sigma} \hat{c}_{j\sigma} - (\mu + \alpha(U=0)) \sum_{i} (\hat{n}_{i\uparrow} + \hat{n}_{i\downarrow}) \\
\mathcal{H}_{exp} &= \sum_{i} \hat{n}_{i\uparrow} \hat{n}_{i\downarrow} - \frac{\alpha(U) - \alpha(U=0)}{U} \sum_{i} (\hat{n}_{i\uparrow} + \hat{n}_{i\downarrow})
\end{aligned} \tag{III.8}$$

We call **path of the perturbation expansion** all the physical systems described by the Hamiltonian $\mathcal{H}[\mu' = \mu + \alpha(U), U]$ as the expansion parameter evolves from $U = 0$ up to a physical value U_ϕ. The parameter U_ϕ is the value of the interaction at which we want to resum the perturbative series and obtain a controlled result for the observable at hand. We see that for the same physical system $\mathcal{H}[\mu + \alpha(U_\phi), U_\phi]$ that we want to solve perturbatively, there are many different perturbation paths possible. They depend on the choices for the free parameters μ and $\alpha(U)$ that change the starting point of the pertubative scheme described by the non-interacting propagator :

$$\tilde{\mathcal{G}}_{0\mathbf{k}\sigma}(i\omega_n) = \frac{1}{i\omega_n - \epsilon_{\mathbf{k}\sigma} + \mu + \alpha(U=0)} \tag{III.9}$$

We can imagine many possibilities for the choice of the shifting function $\alpha(U)$. In this thesis, for the sake of simplicity, we will restrict ourselves to the use of a linear shift which gives a full range of options for the starting point of the perturbative development :

$$\alpha(U) = -\alpha + \alpha \frac{U}{U_\phi} \tag{III.10}$$

This leaves us with two free parameters μ and α which define the perturbative expansion. Other similar choices on the context of different systems have been explored for defining the shift function [59, 139]. Generalizations of the CDet algorithm have shown how powerful the chemical potential shift approach is in the context of Diagrammatic Monte Carlo. The Renormalized Determinant algorithm enables one to consider momentum and frequency dependent chemical potential shifts, as well as higher order polynomial functions of the interaction [61, 116]. The Double-expansion determinant algorithm performs a double expansion in the interaction and chemical potential, enabling one to choose during the resummation procedure the polynomial shape of the chemical potential shift, and to consider a perturbation path at fixed density [64].

Linear chemical potential shift :

Considering a linear function of the interaction for the chemical potential shift, we see that the added term to the expansion Hamiltonian $-\alpha/U_\phi \sum_i (\hat{n}_{i\uparrow} + \hat{n}_{i\downarrow})$ does not depend on the expansion parameter. It is a quadratic one-body term which acts as an external potential on the system. Diagrammatically it corresponds to a local vertex which connects two propagators on the same site at identical imaginary-time and with the same spin, noted as a wiggly line with a dashed circle. For instance the diagrammatic expansion of the Green's function up to the second order Eq. II.56 becomes :

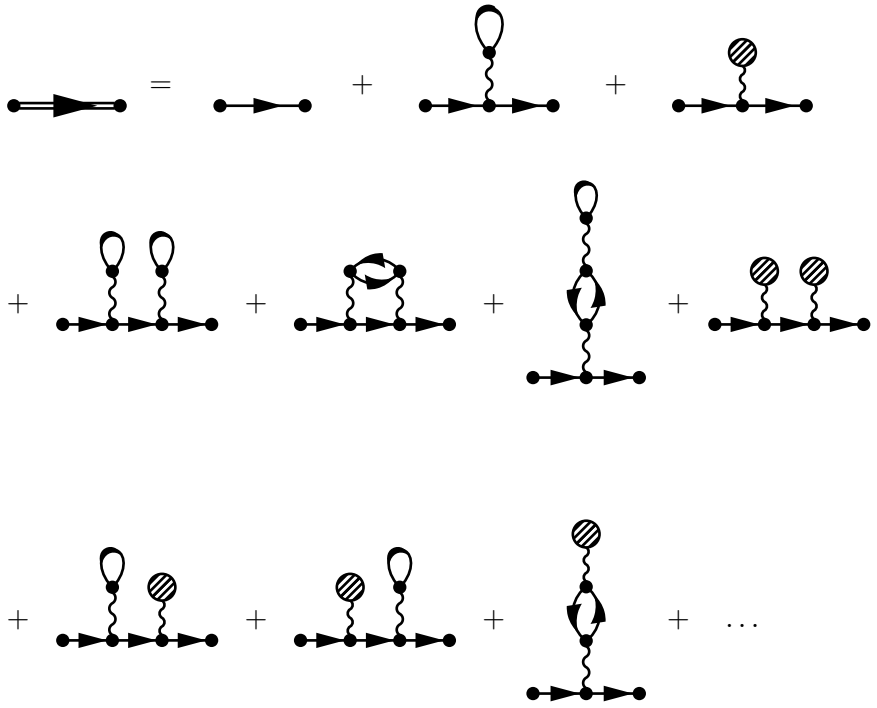

(III.11)

We note that this additional external potential term induces many new diagrams in which a self-loop is replaced by this new vertex. In fact it implies a renormalization of the self-loop Hartree diagram which becomes :

$$
\begin{aligned}
&= U\mathcal{G}_{0i_1i_1\sigma}(0^-) + \alpha\frac{U}{U_\phi} \\
&= U\langle \hat{c}^\dagger_{i_1\sigma}(0^+)\hat{c}_{i_1\sigma}(0)\rangle_0 + \alpha\frac{U}{U_\phi} \\
&= U(\langle \hat{n}_\sigma\rangle_0 + \frac{\alpha}{U_\phi})
\end{aligned}
\qquad \text{(III.12)}
$$

Therefore we can define a specific choice for the free parameter α which corresponds to canceling the Hartree insertions in the diagrammatic expansion. We call this shift the mean-field chemical potential shift since this means that the bare propagator is renormalized to incorporate all the Hartree insertions and thus corresponds to the mean-field Green's function :

$$\alpha_{MF} = -U_\phi \langle \hat{n}_\sigma \rangle_0 \tag{III.13}$$

Indeed for this self-consistent choice of the chemical potential, the non-interacting system writes :

$$\tilde{\mathcal{H}}_0 = -t \sum_{\langle i,j \rangle} \sum_\sigma \hat{c}^\dagger_{i\sigma} \hat{c}_{j\sigma} - \sum_{i\sigma} (\mu - U_\phi \langle \hat{n}_\sigma \rangle_0) \hat{n}_{i\sigma} \tag{III.14}$$

Which corresponds to the mean-field version of the Hubbard Hamiltonian Eq. C.1. This specific value for the chemical potential shift often turns out to be a good choice for improving the convergence properties of the perturbation series.

One of the main advances presented in this thesis is the development of a new type of chemical-potential shift that enables one to enter perturbatively ordered phases. It is detailed in Section III.2.

CDet implementation :

The chemical potential shift linear in the interaction turns out to be easily implemented in CDet. The added quadratic term to the expansion Hamiltonian gives an additional term in the perturbative expansion Eq. II.11 :

$$\begin{aligned} \hat{c}^\dagger_{i_1\uparrow}(\tau_1)\hat{c}^\dagger_{i_1\downarrow}(\tau_1)\hat{c}_{i_1\uparrow}(\tau_1)\hat{c}_{i_1\downarrow}(\tau_1) \rightarrow & \hat{c}^\dagger_{i_1\uparrow}(\tau_1)\hat{c}^\dagger_{i_1\downarrow}(\tau_1)\hat{c}_{i_1\uparrow}(\tau_1)\hat{c}_{i_1\downarrow}(\tau_1) \\ & - \frac{\alpha}{U_\phi}(\hat{c}^\dagger_{i_1\uparrow}(\tau_1)\hat{c}_{i_1\uparrow}(\tau_1) + \hat{c}^\dagger_{i_1\downarrow}(\tau_1)\hat{c}_{i_1\downarrow}(\tau_1)) \end{aligned} \tag{III.15}$$

After applying Wick's theorem to contract these operators into a determinant of non-interacting Green's function this simply adds $-\alpha/U_\phi$ terms on the diagonal of the matrices (except on the lines and columns dedicated to the external vertices) involved in the CDet recursion Eq. III.2 which become:

$$D'_{n,\sigma} = \begin{bmatrix} \mathcal{G}_{0\sigma i_1 i_1}(0^-) - \alpha/U_\phi & \dots & \mathcal{G}_{0\sigma i_n i_1}(\tau_1 - \tau_n) & \mathcal{G}_{0\sigma i_{in} i_1}(\tau_1 - \tau_{in}) \\ \mathcal{G}_{0\sigma i_1 i_2}(\tau_2 - \tau_1) & \dots & \mathcal{G}_{0\sigma i_n i_2}(\tau_2 - \tau_n) & \mathcal{G}_{0\sigma i_{in} i_2}(\tau_2 - \tau_{in}) \\ \vdots & \ddots & \vdots & \vdots \\ \mathcal{G}_{0\sigma i_1 i_n}(\tau_n - \tau_1) & \dots & \mathcal{G}_{0\sigma i_n i_n}(0^-) - \alpha/U_\phi & \mathcal{G}_{0\sigma i_{in} i_2}(\tau_2 - \tau_{in}) \\ \mathcal{G}_{0\sigma i_1 i_{out}}(\tau_{out} - \tau_1) & \dots & \mathcal{G}_{0\sigma i_n i_{out}}(\tau_{out} - \tau_n) & \mathcal{G}_{0\sigma i_{in} i_{out}}(\tau_{out} - \tau_{in}) \end{bmatrix} \tag{III.16}$$

The CDet recursion is not changed and we simply perform it on these shifted matrices. In addition to changing the complex plane pole structure of the perturbation series, the chemical potential shift also has an effect on the accuracy of the Monte Carlo process : since it decreases the values on the diagonal of the sampled matrices, it reduces the biggest contributions to the final results which are now taken into account exactly in

the non-interacting system. The weight of smaller contributions in the determinants is enhanced so that the final variance of the stochastic process become smaller. This effect is maximized for the mean-field chemical potential shift which cancels the Hartree insertions and therefore puts zeros on the diagonal of the matrix. We show in Chapter IV how the number of expansion coefficients that we are able to compute stochastically varies with the value of the chemical potential shift.

III.1.4 Illustration in the normal phase of the Hubbard model

In this Section we illustrate the CDet algorithm on the Hubbard model at half-filling in two and three dimensions, respectively on a square and cubic lattice. By taking the example of the double occupancy in these specific models we aim at discerning the strength and limitations of CDet. We observe that the antiferromagnetic phase transition in three dimensions and the increase in correlation length in two dimensions limit the series resummation and our perturbative method.

Particle-hole symmetry :

One of the main advantages of studying the Hubbard model on the square or cubic lattice with only nearest-neighbour hopping is that it shows a particle-hole symmetry. It is an additional symmetry to the Hubbard model at half-filling on bipartite lattices. They are lattices which can be separated into two sublattices such that there is no hopping term within one sublattice and only hopping terms between different sublattices. At half-filling ($\langle \hat{n} \rangle = (\langle \hat{n}_\uparrow + \hat{n}_\downarrow \rangle / 2 = 1/2)$ this symmetry fixes the value of the chemical potential to $\mu = U/2$ as shown in Appendix B. Therefore we aim at describing the half-filled Hubbard Hamiltonian :

$$\mathcal{H} = -t \sum_{\langle i,j \rangle} \sum_{\sigma} \hat{c}^\dagger_{i\sigma} \hat{c}_{j\sigma} + U \sum_i \hat{n}_{i\uparrow} \hat{n}_{i\downarrow} - \frac{U}{2} \sum_i (\hat{n}_{i\uparrow} + \hat{n}_{i\downarrow}) \tag{III.17}$$

In general the CDet algorithm works in the grand canonical ensemble at fixed chemical potential. Therefore the density of the system is not fixed and it is varying with the interaction parameter U. When computing an observable, we would in principle need to perform a separate computation along with resummation to control the filling of the system at different values of U. The physics of the Hubbard model is in general presented as a function of the density which is much more practical than the chemical potential for physics considerations. But choosing a chemical potential for the non-interacting system in order to aim at a specific density at some value of U at the end of the perturbative treatment turns out to be a very difficult task. Here, thanks to the predetermined value of the chemical potential, linear in the interaction, we can directly describe the system at half-filling relying on the linear chemical potential shift technique presented in Section III.1.3. We notice that the half-filled Hubbard Hamiltonian corresponds to the Hamiltonian Eq. III.8 described by the perturbation expansion with the linear chemical potential shift :

$$\alpha(U) = -\mu + \frac{U}{2} \tag{III.18}$$

This means that with this chemical potential shift, the density is fixed on the path of the perturbation expansion. We can therefore directly describe an observable $\mathcal{A}(U)$ at half-filling at every value of U with one simulation of the CDet algorithm. It is to be noted that this chemical potential shift corresponds to the mean-field shift which leads to the cancellation of Hartree loops and puts zeros on the diagonal of the matrix in the CDet algorithm.

Three-dimensional Cubic lattice :

In the following, we focus on computing the double-occupancy $\langle \hat{n}_\downarrow \hat{n}_\uparrow \rangle$ which is related to the potential energy of the system through $E_{pot} = UD$. At $U = 0$, since electrons move freely on the lattice with no Coulomb repulsion, $D = \langle n_\downarrow \rangle \langle n_\uparrow \rangle = 0.25$. As the Coulomb repulsion increases, electrons tend to occupy different sites, and D decreases. Diagrammatically the double-occupancy is represented by diagrams with four external vertices, and a corresponding line and column have to added for each spin to the matrices used in the CDet recursion. It is to be noted that the expansion coefficients of even order of D are equal to zero, see Appendix E. We compute the double-occupancy at four different value of the interaction. Depending on the temperature we get accurate expansion orders up to order $n \sim 10 - 12$. We show in Appendix D the results for the truncated partial sums and Pade extrapolation as a function of U, along with the complex pole structure of the series. All energies are expressed in units of the hopping amplitude $t = 1$.

The resummed double-occupancy is displayed in Fig. III.1. The double-occupancy decreases almost linearly with the interaction. The perturbative expansion yields very accurate results at small interaction, but the error increases drastically when increasing the interaction. Close to the estimated position of a pole on the real axis of the complex plane structure of the series, the resummation finally breaks and we can not reach higher values of the interaction. This is consistent with what we know of the half-filled Hubbard model on a cubic lattice. At a given low enough temperature the system undergoes a phase transition towards a Néel order at some critical value of the interaction U_c (see Chapter IV for more details on the cubic half-filled Hubbard model). Therefore this result provides a first method for estimating the phase diagram of this model. The position of the poles as a function of temperature and interaction is shown in Fig. III.2. The result is imprecise and can only be interpreted as a first sketch of the Néel dome which can be explained by the difficulty in estimating the position of poles. Indeed the estimation relies on extrapolation of high perturbation orders and the double-occupancy, having half its expansion coefficient exactly equal to zero, does not yield many coefficients for performing this extrapolation. Recently, the critical value of the interaction has this has been determined precisely by taking advantage of the known critical behaviour in the vicinity of the phase transition and extrapolating the expansion coefficients of the spin structure factor to high order [81].

Two-dimensional square lattice :

Similarly in two dimensions on the square lattice, as shown in Fig. III.3, the double occupancy as a function of the interaction is almost linear at small values of U. We

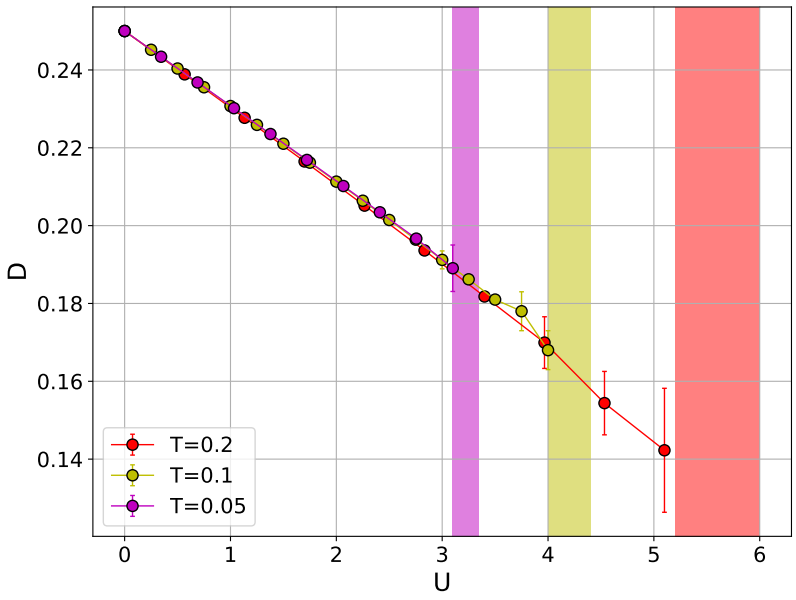

Figure III.1: Double-occupancy as a function of the Coulomb repulsion in the half-filled Hubbard model on a cubic lattice. The system-size is fixed to $L^3 = 20^3$ sites. The double-occupancy value with errorbar is determined after resummation using Padé and D-log Padé approximants. The colored areas correspond to the estimated position of a pole on the positive real axis for each temperature

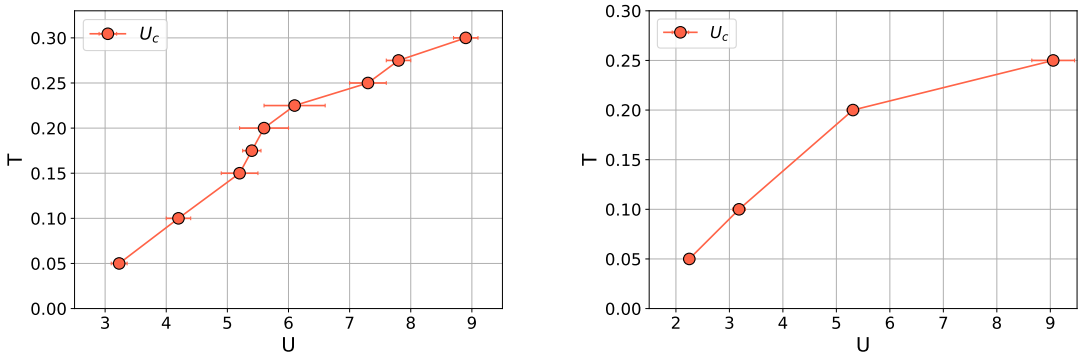

(a) (b)

Figure III.2: Position of the pole on the real positive axis as a function of temperature and interaction, in three (a) and two dimensions (b). In three dimensions these poles can be interpreted as the critical value of the interaction at which the system undergoes the Néel phase transition.

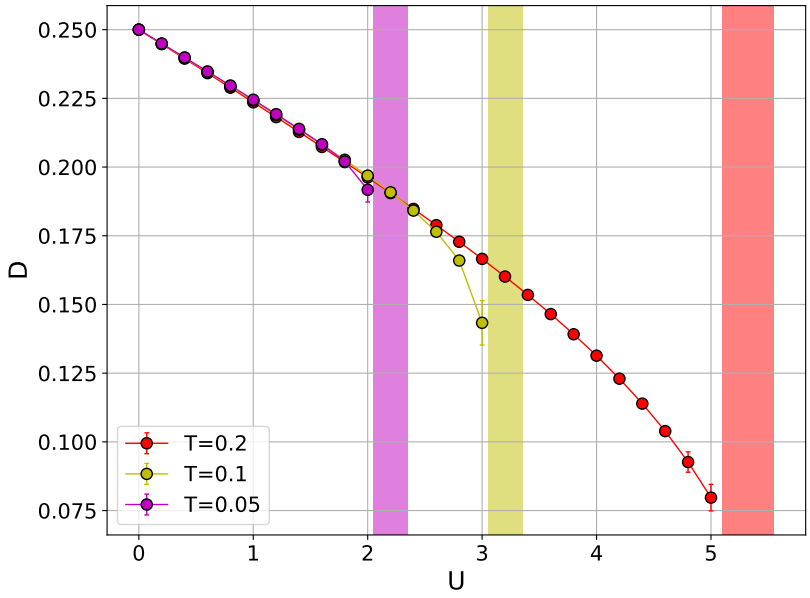

Figure III.3: Double-occupancy as a function of the Coulomb repulsion in the half-filled Hubbard model on a square lattice. The system-size is fixed to $L^2 = 64^2$ sites. The double-occupancy value with errorbar is determined after resummation using Padé and D-log Padé approximants. The colored areas correspond to the estimated position of a pole on the positive real axis for each temperature

observe the bending of the curve towards zero and a huge increase in the error when approaching interactions close to the regions where a pole seats on the positive real axis. In two dimensions, the Mermin–Wagner theorem impedes the breaking of a continuous symmetry at finite temperature. Therefore this pole can not happen as a consequence of a phase transition. We interpret this as a limitation due to an overwhelming increase in the correlation length at these values of the interaction. Indeed, even if a proper magnetic phase transition can not happen because of fluctuations, the antiferromagnetic correlation length can become very large. Even though the system size considered is large ($L^2 = 64^2$ sites), it is not enough to distinguish between a long or an infinite correlation length. This can lead to poles very close to the positive real axis which we can not discriminate from a pole on the real axis, and can not overcome with our finite number of expansion coefficients. The position of the poles as a function of temperature and interaction is shown in Fig. III.2.

III.2 Symmetry-broken CDet

In the previous section we have detailed how to apply the CDet algorithm in the context of a chemical-potential shift. The main restriction to obtaining results in the strong

coupling regime turns out to be the appearance of a phase transition (or the sudden increase in correlation length). We introduce in this section the new symmetry-broken CDet algorithm which overcomes this limitation and enables one to enter perturbatively an ordered phase.

III.2.1 Symmetry-broken chemical potential shift

The idea of the symmetry-broken version of the CDet algorithm is to take advantage of the chemical potential shift for breaking a symmetry of the model in the non-interacting system. We want to remove the pole on the positive real axis of the series and therefore we need to find a perturbation path which does not undergo a phase transition at some value of the expansion parameter. This is achieved by choosing a different transformation for the chemical potential.

Breaking the spin inversion symmetry :

We take the example of the antiferromagnetic phase of the three dimensional half-filled Hubbard model which will be developed in more details in Chapter IV, but this approach can be generalized to any system with a different spontaneous symmetry breaking. The case of s-wave superconductivity will be tackled in Section IV.5. We introduce the chemical potential shift with a dependency on the spin and on the sublattice :

$$\mu \to \mu'_{\sigma i} = \frac{U}{2} + h \sum_{i\sigma} \sigma(-1)^i - \frac{U}{U_\phi} h \sum_{i\sigma} \sigma(-1)^i \tag{III.19}$$

Where h is an external Zeeman magnetic field which sign alternates on the different sublattices characterized by the site index i being odd or even, and acts on the spin $\sigma = \pm 1$. With this shift we describe the following Hamiltonian at every value of the expansion parameter U :

$$\begin{aligned}
\hat{\mathcal{H}} =& -t \sum_{\langle i,j \rangle} \sum_{\sigma} \hat{c}^\dagger_{i\sigma} \hat{c}_{j\sigma} - \frac{U}{2} \sum_{i\sigma} \hat{n}_{i\sigma} + h \sum_i (-1)^i \hat{S}^z_i + U \sum_i \hat{n}_{i\uparrow} \hat{n}_{i\downarrow} - \frac{U}{U_\phi} h \sum_i (-1)^i \hat{S}^z_i \\
=& \mathcal{H}_0 + U \mathcal{H}_{exp} \\
\\
\hat{\mathcal{H}}_0 =& -t \sum_{\langle i,j \rangle} \sum_{\sigma} \hat{c}^\dagger_{i\sigma} \hat{c}_{j\sigma} + h \sum_i (-1)^i \hat{S}^z_i \\
\hat{\mathcal{H}}_{exp} =& \sum_i \hat{n}_{i\uparrow} \hat{n}_{i\downarrow} - \frac{1}{2} \sum_{i\sigma} \hat{n}_{i\sigma} - \frac{h}{U_\phi} \sum_i (-1)^i \hat{S}^z_i
\end{aligned} \tag{III.20}$$

Where $\hat{S}^z_i = (\hat{n}_{i\uparrow} - \hat{n}_{i\downarrow})$. The system described by this Hamiltonian corresponds to the Hubbard model at half-filling to which we add an external staggered Zeeman field $h(1 - U/U_\phi)$. This additional term breaks the spin inversion SU(2) symmetry. On a

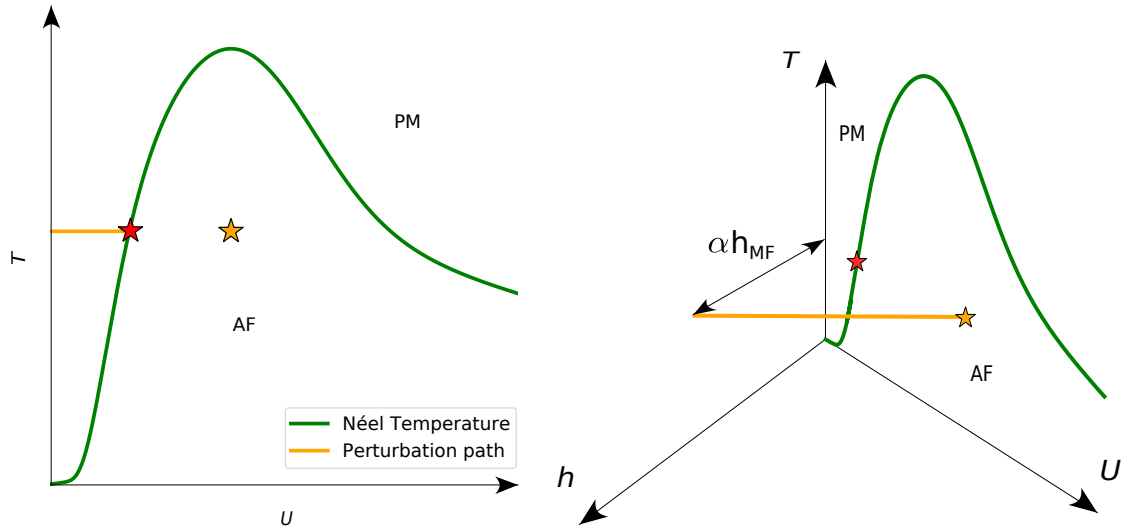

Figure III.4: Sketch of the perturbation path for a perturbative expansion in (a) the normal phase with $\alpha = 0$, (b) a symmetry-broken expansion $\alpha \neq 0$. The yellow star of coordinates $\{T, U_\phi, h = 0\}$ is the point inside the antiferromagnetic phase (AF) at which we want to evaluate the perturbative series. The perturbation path is the ensemble of points described by the perturbative series for all the values of the expansion parameter $U \in [U, U_\phi]$. For the normal state expansion (a), the starting point of the perturbative expansion is in the paramagnetic phase (PM) and at a certain value of U, the perturbation path crosses the Néel temperature curve (red star) which prohibits the perturbation to reach higher values of the interaction. For the symmetry-broken case (b), the starting point of the perturbative expansion is at a non-zero field αh_{MF} in a magnetic state ($m \neq 0$). The perturbation path reaches the yellow star without crossing the Néel phase transition and avoids the associated singularity.

specific site, the density for each spin flavor is no longer the same and the system has a non-zero magnetization $m = (-1)^i \langle \hat{n}_{i\uparrow} - \hat{n}_{i\downarrow} \rangle$. The symmetry is restored for $U = U_\phi$ at which the Hamiltonian corresponds to the Hubbard Hamiltonian. Therefore the Hubbard Hamiltonian can be described by the expansion detailed in Eq. III.20, after resumming the obtained perturbation series at $U = U_\phi$. Since the SU(2) spin inversion symmetry is broken along the expansion path, we expect the system not go through a phase transition at a value of the interaction $U < U_\phi$, and we may enter the ordered phase perturbatively. For a more visual explanation on this, see the sketch on Fig. III.4.

α shift :

Similarly to how we defined the chemical potential shift in the paramagnetic regime (with no symmetry breaking), it is useful to define the external field in terms of the mean-field solution of the Hubbard model. We rewrite the external staggered field as

$h = \alpha h_{MF}$ where $h_{MF} = U_\phi m_{MF}/2$ and m_{MF} is the magnetization of the mean-field Hubbard model in the antiferromagnetic state. We show in Appendix C how we solve the mean-field antiferromagnetic system.

Aiming at computing an observable at some value of the temperature and interaction U_ϕ, we see that we are left with one free parameter for defining the perturbative series : α. It is helpful to consider two limit cases for the choice of α :

- For $\alpha = 1$, the non-interacting system is equal to the mean-field antiferromagnetic solution of the Hubbard model. The bare propagators are the mean-field ones.
- For $\alpha = 0$, the staggered external field vanishes and the non-interacting system does not break the spin inversion symmetry. We go back to the usual expansion limited to the paramagnetic regime.

In general we will choose values of the shift between these two cases $0 < \alpha \leq 1$, even if there is a priori no limitation to taking $\alpha > 1$.

CDet implementation :

The additional term to the expansion Hamiltonian is quadratic and acts as an external potential. Just as we have shown in Section III.1.3, the diagrammatic expansion of an observable is modified by adding a new vertex connected to two propagators, which leads to a renormalization of the self-loop Hartree insertions. Because of the staggered field, this vertex now depends on the sublattice and spin indices. The Hartree self-insertions are renormalized as (for the spin $\uparrow$ with no loss of generality) :

$$\begin{aligned} U\mathcal{G}_{0ii\uparrow}(0^-) &\to U\mathcal{G}_{0ii\uparrow}(0^-) - (-1)^i U\frac{m_{MF}}{2} - \frac{U}{2} \\ &\to U(\langle \hat{n}_{i\sigma}\rangle_0 - (-1)^i\frac{m_{MF}}{2} - \frac{1}{2}) \end{aligned} \tag{III.21}$$

By definition of the magnetization $\langle \hat{n}_{i\sigma}\rangle = n + (-1)^i m/2$ with n the density per site and spin. Therefore, with $\alpha = 1$, since the system is at half-filling $n = 1/2$ and as the non-interacting system corresponds to the antiferromagnetic mean-field Hubbard Hamiltonian, the self-loops are canceled in the diagrammatic expansion.

Similarly to the paramagnetic case, the CDet algorithm applies in the same usual way, with changing the diagonal terms of the matrices for the lines and columns of internal vertices. They take the value computed in Eq. III.21 and we notice that the diagonal terms are nullified for both $\alpha = 0$ and $\alpha = 1$.

III.2.2 Illustration in the normal and antiferromagnetic phases of the Hubbard model

We give an example in this section of the application of the newly developed symmetry-broken CDet algorithm to the half-filled Hubbard model on a cubic and square lattice.

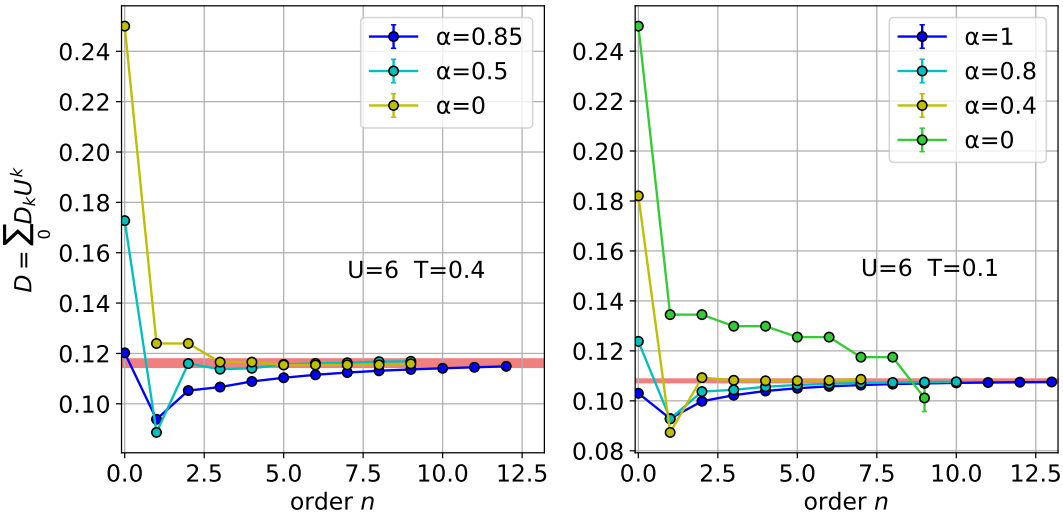

Figure III.5: Partial sums of the double occupancy D for two different values of the interaction U and temperature T as a function of the maximum order n. The colored area corresponds to the estimated resummed value with errorbar.

We show that it enables us to outperform the maximal values of the interaction reached by the perturbative expansion in the paramagnetic regime. As the symmetry is restored at the physical value of the interaction parameter, we are able to resum perturbative series outside and inside the ordered phase in three dimensions.

Double occupancy on the cubic lattice :

We first focus on applying the symmetry-broken chemical potential shift to the Hubbard model on a cubic lattice. We show the obtained partial sums for two sets of parameters (T, U_ϕ), and for different values of the shift α, in Fig. III.4.

On the left panel the computation is done at relatively high temperature and we can expect the system to be in the paramagnetic phase. Indeed, we see that the paramagnetic perturbative expansion for $\alpha = 0$ leads to a converging partial sum. This means that it is not limited by a pole on the positive real axis at a value of the interaction $U < 6$. On the contrary the right panel corresponds to a relatively low temperature at which we expect the system to be in the ordered antiferromagnetic phase. Indeed, according to Fig. III.2, the parameters correspond to a resummation past a pole in the complex plane, which explains why the paramagnetic series for $\alpha = 0$ does not converge with increasing the perturbation order. For $\alpha \neq 0$ the perturbative series converge towards the same result after resummation. This shows that we are able to overcome the limitation of the paramagnetic perturbative series which are due to the phase transition.

Even if the zeroth order value is extremely dependent on the value of the shift, as expected all series for $\alpha \neq 0$ converge towards the same result after resummation. We notice that the maximum number of expansion orders that we are able to compute with

good accuracy and in a reasonable time with the CDet algorithm highly depends on the value of the shift. We reach up to thirteen expansion orders for $\alpha = 1$ and up to eight orders for $\alpha \sim 0.5$. Indeed, a shift closer to 0 or 1 leads to cancellation of the Hartree insertions and zeros on the diagonal of the matrices in the CDet recursion. For $\alpha \sim 0.5$, these diagonal contributions have a large weight which takes over different diagrammatic contributions in the Monte Carlo procedure. This deteriorates the overall accuracy of the Monte Carlo integration and less orders can be computed accurately.

Double occupancy on the square lattice :

On the square lattice, the perturbative expansion in the paramagnetic phase is also limited by its pole structure in the complex plane. Even if a spontaneous breaking of a continuous symmetry is not possible because of the Mermin-Wagner theorem, the antiferromagnetic correlations are large and limit our perturbative method. We show in Fig. III.6 that the symmetry-broken shift enables us to modify the pole structure of the series and obtain converging series up to high interaction.

On the left panel we are able to obtain a resummed result using a symmetry broken expansion at $T = 0.1$ and at a relatively small value of the interaction $U_\phi = 2$. This set of parameters is accessible through a perturbative expansion in the paramagnetic regime and the resummed value $D = 0.1985(5)$ coincides with the one showed in Fig. III.3. At a larger value of the interaction $U = 6$ which is not accessible by the standard paramagnetic expansion, we obtain a converging partial sum and can estimate the resummed result. This shows that the symmetry-broken CDet algorithm can be applied to obtain results in the normal state of a model even if no phase transition occurs.

Entering the antiferromagnetic state :

Going back to the cubic lattice, we aim now at proving that the perturbative expansion enters the ordered phase and that the pole limiting the paramagnetic expansion is indeed due to the appearance of the antiferromagnetic order. For this purpose we compute the staggered magnetization which is the order parameter of the antiferromagnetic phase. We recall its expression $m = (-1)^i \langle \hat{n}_{i\uparrow} - \hat{n}_{i\downarrow} \rangle$. Within the CDet algorithm it is computed as the subtraction of the average value of both density operators. The density operators diagrammatic expansions correspond to the one of the Green's function with $\langle \hat{n}_{i\sigma} \rangle = \mathcal{G}_{ii\sigma}(0^-)$. The CDet recursion applies with the matrices as defined for the Green's function expansion. The subtraction between the weights at each order of both densities is done within the Monte Carlo procedure. Thus we sample the weights corresponding to the magnetization expansion coefficients and obtain a better Monte Carlo accuracy in comparison to sampling both densities and applying the subtraction afterwards.

The partial sums for two sets of parameters (T, U_ϕ), and for different values of the shift α, are presented in Fig. III.7. As α goes from one to zero, the value of the magnetization changes from its high mean-field value, towards zero in the paramagnetic non-interacting system. Independently on the value of the shift all partial sums seem to converge towards

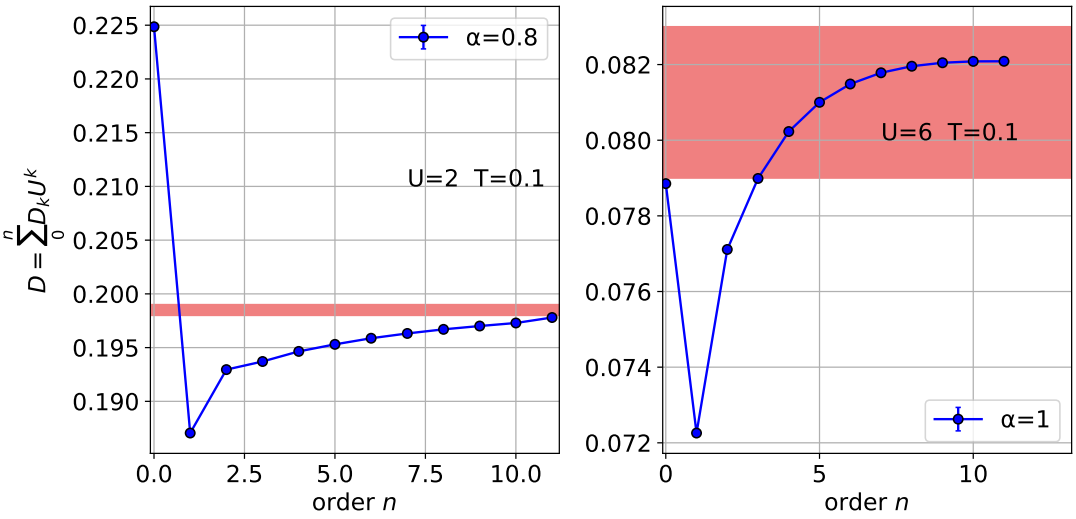

Figure III.6: Partial sums of the perturbative series for the double occupancy D for two different values of the interaction U and temperature T as a function of the maximum order n. The colored area corresponds to the estimated resummed value with errorbar.

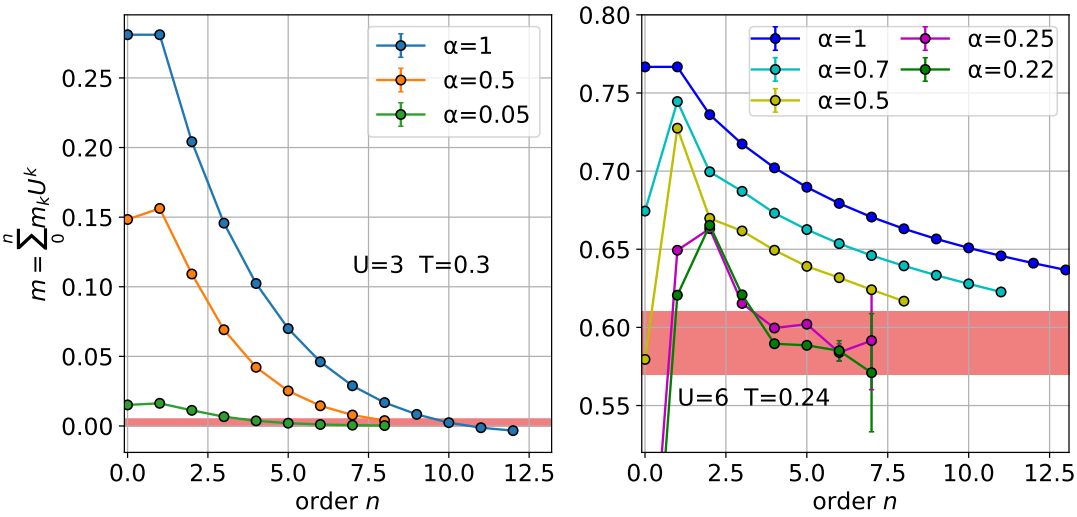

Figure III.7: Partial sums of the perturbative series for the magnetization m for two different values of the interaction U and temperature T as a function of the maximum order n. The colored area corresponds to the estimated resummed value with errorbar.

the same value when increasing the maximum order n. At $U = 3$ and $T = 0.3$ the magnetization is resummed to zero which shows that we restore the spin inversion symmetry inside the paramagnetic regime. At $U = 6$ and $T = 0.24$, the magnetization is resummed to a non-zero value indicating that we have entered the antiferromagnetic phase.

In the end the implementation of a symmetry-broken chemical potential shift within the CDet algorithm enables us to remodel the complex plane structure of perturbative series and reach regimes which are not accessible to the usual normal state perturbation expansion. In the context of spontaneous symmetry breaking it even proves to be able to enter the ordered phase and obtain controlled results at relatively high values of the interaction.

Chapter IV

Néel order and superconductivity in the 3D half-filled Hubbard model

Contents

In this Chapter we devote ourselves to studying the three-dimensional Hubbard model at half-filling on a cubic lattice. At half-filling the particle-hole symmetry fixes the value of the chemical potential which facilitates our perturbative approach. This model shows an antiferromagnetic phase at low temperature which we aim at describing by applying the symmetry-broken CDet algorithm. Even if this phase transition is well understood qualitatively and has been studied extensively by many numerical methods, it still misses a quantitative unbiased description. We present state of the art controlled results in the thermodynamic limit, close to the phase transition and inside the ordered phase, a regime which is inaccessible to most of the available numerical numerical methods for strongly correlated systems.

First, we present the half-filled cubic Hubbard model and provide an outline of its physical characteristics and previous numerical studies. We then describe our methodology for obtaining controlled results from applying the CDet algorithm and resumming the resulting series. In a third and fourth section we detail our results in two dissimilar physical regimes : close to the Néel phase transition and deep inside the ordered phase at low temperature. We finish by giving few insights and results for the negative U attractive counterpart of this model, applying the symmetry-broken CDet algorithm to a superconducting phase.

The results presented in this chapter are the object of published (as of preprints at the moment) articles studying respectively the repulsive and attractive models [36, 128]. They are reproduced in Appendix J. All energies are expressed in units of $t = 1$.

IV.1 Physics of the half-filled repulsive cubic Hubbard model

As explained in Chapter I, despite its apparent simplicity, the Hubbard model on the cubic lattice exhibits a rich phase diagram and a variety of distinct physical regimes, making it an excellent starting point for investigating the possibility of novel algorithms. In this Section we present what is known of the physics of this testing ground model from prior scientific works, and what still remains to be understood or misses a precise description.

We recall the Hubbard Hamiltonian at half-filling :

$$\mathcal{H} = -t \sum_{\langle i,j \rangle} \sum_{\sigma} \hat{c}^{\dagger}_{i\sigma} \hat{c}_{j\sigma} + U \sum_{i} \hat{n}_{i\uparrow} \hat{n}_{i\downarrow} - \frac{U}{2} \sum_{i} (\hat{n}_{i\uparrow} + \hat{n}_{i\downarrow}) \tag{IV.1}$$

Where the chemical potential is determined by $\mu = U/2$ at half-filling because of the particle-hole symmetry on the cubic bipartite lattice (see Appendix B).

IV.1.1 Mott physics

The Hubbard Hamiltonian embodies a competition between the kinetic and potential Coulomb repulsion energies. The kinetic term tends to delocalize electrons on the lattice and at $U = 0$ the system is diagonalized in $\mathbf{k}$ space. For this single-orbital model, the eigenenergies form one conduction band of dispersion $\epsilon_{\mathbf{k}} = -2t(\cos k_x + \cos k_y + \cos k_z)$

which is half-filled. The system is metallic since empty energy levels are accessible at any arbitrary small energy above the Fermi sea. At small values of the interaction and small temperatures the conducting system can be described in terms of a metallic Fermi liquid.

On the contrary at $U \to \infty$ in the atomic limit, electrons are localized on each site to avoid paying the large energetic cost of on-site Coulomb repulsion : the system is a Mott insulator. In the high interaction limit the system becomes equivalent to the three dimensional Heisenberg model. Indeed for almost localized electrons, at half-filling, each site is occupied by one electron. On a specific site, at first order in $1/U$, the electron can gain negative kinetic energy by hopping on a neighbouring site and hopping back. This process is only possible if neighbouring sites are occupied by electrons with opposite spins because of the Pauli exclusion principle, hence a difference in energy depending on the spins of neighbouring sites. Exchanging two electrons gives a gain in kinetic energy of $2t$, hence the superexchange coupling constant $J = 4t^2/U$ and the Heisenberg model :

$$\mathcal{H} = -J \sum_{\langle i,j \rangle} \hat{\vec{S}}_i \cdot \hat{\vec{S}}_j \tag{IV.2}$$

In between these two regimes with opposite transport properties, making the assumption that the system remains in a paramagnetic phase, a metallic to insulator transition happens as U is increased from small to large values. This transition has been extensively studied in the DMFT framework [39]. In this approximation, it has been shown to take the form of a first order phase transition at small temperatures with a coexisting region which vanishes as the temperature increases. At higher temperatures the metallic to insulating transition happens as a succession of two continuous crossovers. As the interaction rises, the system is successively in metallic state, goes to an incoherent bad metal behaviour, and for $U > T$ becomes a gaped insulator. These crossovers can be linked to properties of the underlying Mott transition which extends to higher temperatures [123].

IV.1.2 Néel ordering

At half-filling, and for any non-zero interaction, the ground state of the Hubbard Hamiltonian is ordered in an antiferromagnetic state. Starting from the normal phase, as the temperature is decreased the system will eventually go through a second order phase transition. The SU(2) spin-inversion symmetry is broken and the system shows an antiferromagnetic long-range spin order. This phase transition belongs to the $O(3)$ Heisenberg universality class which gives information about the universal critical behaviour of the system in the vicinity of the phase transition [24]. The resulting antiferromagnetic phase is called Néel order, and we will write T_N the Néel temperature which corresponds to the critical temperature of the Néel ordering. We distinguish two dissimilar mechanisms for this spontaneous symmetry-breaking :

- At weak coupling, the system is metallic, fermions are essentially delocalized over the lattice, and the double-occupancy is relatively high. Therefore the phase transition towards an antiferromagnetic state essentially leads to a gain (negative) in

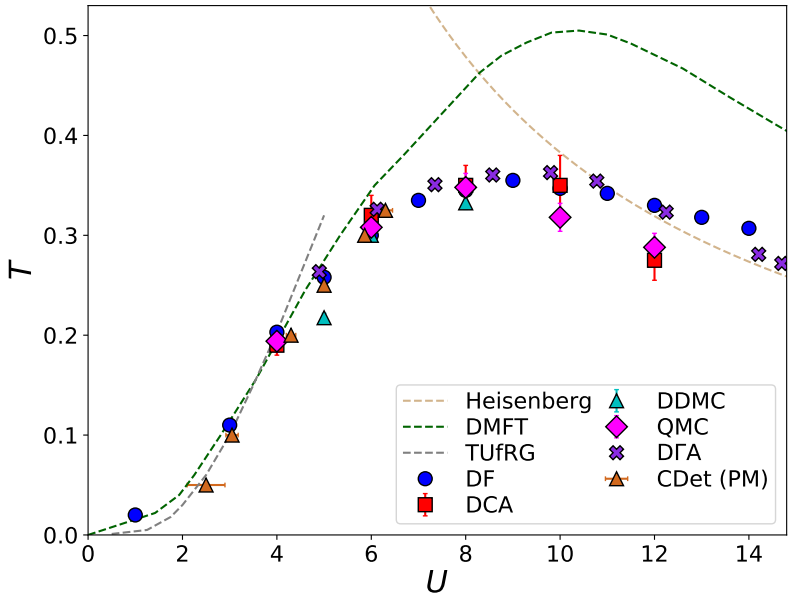

Figure IV.1: Phase diagram and Néel temperature of the half-filled Hubbard model on a cubic lattice according to different numerical techniques. At high temperature the system is paramagnetic and goes to an antiferromagnetic phase at low T. See the main text for a full description of the methods and the corresponding references.

potential energy which compensates a small loss in kinetic energy. This effect becomes stronger as the interaction increases, hence a rising of the Néel temperature. This is called the Slater mechanism [127].

- At strong coupling, the phase transition happens from cooling a Mott insulating regime. The system is factually localized, and the phase transition towards an antiferromagnetic state is driven by a gain in kinetic energy enabled by the superexchange phenomenon. As the interaction increases, the superexchange coupling constant decreases as $1/U$ and this effect is less substantial, leading to a decrease of the Néel temperature. This is the Heisenberg mechanism.

These two regimes are by essence very dissimilar. In the intermediate coupling regime we therefore expect the Néel temperature to change from a rising to a decreasing function of the interaction, forming a Néel antiferromagnetic dome. This change from a potential energy to a kinetic-energy driven transition has been documented with DMFT like methods and in cold atoms simulations [34, 41, 133].

The phase diagram of the half-filled Hubbard model on a cubic lattice has been studied by many different numerical methods and we show in Fig. IV.1 their numerical results for the Néel temperature. These methods are described in more details in Section I.3.

The dual fermion (DF) and DMFT [54] are embedding methods mapping an impurity problem to a lattice system. The Determinant Diagrammatic Monte Carlo [73] (DDMC) is a generalization of the CT-INT impurity solver to the lattice. The Dynamical Cluster Approximation (DCA) [62, 70] is an extension of DMFT which creates clusters in the reciprocal space for describing the self-energy. The study is extrapolated to infinite cluster size. The recently improved dynamical vertex approximation DΓA [131] is a particular mapping of an impurity into the lattice system. The Truncated-unity Functional Renormalization Group [32] applies deep-learning methods to the renormalization group concept, it is limited to low values of the interaction. The Quantum Monte Carlo (QMC) [129] approach performs a discretization of the imaginary-time axis and evaluates path integrals stochastically. The CDet PM technique [81] relies on precise CDet computations in the paramagnetic phase. The phase transition is determined accurately by extrapolating the expansion series of the spin structure factor to infinite order and finding the interaction at which a singularity stands. This computation is performed at fixed temperature, hence the horizontal errorbar. Finally the Heisenberg line matches the Néel temperature curve in the large interaction limit. It is proportional to the superexchange coupling constant and is determined to vary as $T_N \simeq 0.946J$ [121]. At very small interaction the Néel temperature is known from the mean-field analysis to decay as $T_N \propto \exp -1/|U|$.

At the exception of the CDet approach, all of these methods either perform an approximation by relying on an embedding scheme, or have a complexity which scales poorly with the size of the lattice and are limited to small system sizes from which they try to extrapolate to the thermodynamic limit. Except for the single-site DMFT which highly overestimates the Néel temperature, they give a reasonably accurate description of the Néel dome, but are not always agreeing within errorbar with each other. They provide a good set of data for comparing with our numerical results.

It is to be noted that none of these numerical approaches have the ability to enter the ordered phase and obtain controlled results in the antiferromagnetic state. Only biased methods based on the DMFT approximation such as CDMFT or DCA could impose the breaking of a symmetry but, studying small clusters, they tend to excessively overestimate the magnetization and the Néel temperature. Recently, antiferromagnetic states were realized in cold-atomic experiments on optical lattices. Unbiased controlled results inside the antiferromagnetic phase could provide a useful benchmark for guiding these state-of-the-art experiments [43, 50, 87, 134].

IV.1.3 Signatures of the Mott transition

In practice DMFT and its extensions suggest that the Mott transition would happen at small temperatures where the physics is in fact governed by the Néel ordering. The transition from a metallic to Mott insulator happens above the antiferromagnetic phase as a continuous crossover. The Néel dome hides the first order phase transition which is observed with DMFT techniques and its extensions.

Indeed, the DMFT method, by relying on a self-consistent mean-field-like scheme, can observe for the same set of parameters several solutions corresponding to different

prechosen symmetries. One then has to compare the free energies of the different solutions to determine the actual phase of the system. Although the inhomogeneous DMFT scheme [101] lets the system organize by itself and is a proper method for determining the phase at hand.

In the end the DMFT, as an artifact of the mean-field scheme, has access to underlying phases. By comparing the potential and kinetic energies of the paramagnetic and antiferromagnetic solutions, the study [34] was able to map the Néel dome into Slater and Heisenberg regions, and linked their separation to the underlying Mott phase transition. This would imply a significant effect of the underlying normal state in defining the ordered state's characteristics.

In the following we apply the unbiased symmetry-broken CDet algorithm to the half-filled Cubic Hubbard model and try to answer the following questions : Can we obtain controlled results inside the antiferromagnetic phase ? Can we determine accurately the Néel temperature and critical region close to the phase transition ? Can we reach the strong coupling limit and observe the Slater to Heisenberg change of mechanism ? And finally, without having access to the hidden paramagnetic phase, is there at low temperature an effect of Mott physics inside the antiferromagnetic dome ?

IV.2 Methodology and resummation procedure

We start by describing our methodology for acquiring accurate data from the symmetry-broken CDet algorithm. We detail our procedure for obtaining and resumming perturbative series into precise results with estimating their error, and controlling sources for biases.

IV.2.1 Impact of the chemical potential shift

The choice of the $\alpha \in [0, 1]$ parameter in the symmetry-broken CDet algorithm has a major influence on the perturbative series and on our ability to resum it efficiently. We rely on multiple choices of this free parameter in order to optimize our perturbative approach.

We recall that $\alpha = 0$ corresponds to a perturbative expansion in the normal phase with no external field breaking the spin-inversion symmetry, while $\alpha = 1$ is a symmetry-broken expansion starting from the antiferromagnetic mean-field solution of the Hubbard model. Reducing α from 1 to 0.5 leads to a raise of the diagonal coefficient in the CDet matrices, and hence a reduction of the maximal order available with good accuracy in a reasonable computational time. This maximal order increases again but gains only around two expansion coefficients when going from 0.5 to 0. However, having more expansion orders available is not the only key to a more controlled and accurate resummation. Indeed the α parameter choice has an other important effect as it modifies the starting point of the perturbative expansion and changes the perturbation path towards the Hubbard Hamiltonian at interaction U_ϕ. For an observable $\mathcal{A}$, this changes the function $\mathcal{A}(U)$

for $U \in [0, U_\phi]$ (see Eq. III.20), and hence modifies its perturbative expansion. Therefore the choice of the α parameter influences strongly the convergence properties of the perturbative series, and hence our ability to resum it accurately.

We illustrate the impact of α on the convergence properties of the expansion series for different sets of parameters and observables in Fig. IV.2. The left panels correspond to parameters close to the Néel phase transition, while the panels on the right side are deep inside the antiferromagnetic phase. We show computations for the three quantities which we compute with the CDet algorithm in this chapter, the grand potential will be introduced in the Subsection IV.3.3. As a general remark, we see that for shifts α close to 1 we obtain many orders, up to 15 expansion orders for the grand potential, but the resulting series is converging very slowly towards the result. In some cases other values of the shift lead to a much faster convergence of the series with respect to the expansion order and enable a much more accurate resummation. This is especially true in the regime close to the phase transition where the magnetization shows large variations when changing the temperature. From this we establish a strategy for obtaining converging expansion series. When deep inside the dome, we rely on shifts close to the mean-field value $\alpha \sim 0 - 0.3$ which yield many orders and converging partial sums. At higher temperatures the same plan is not as efficient as it can be seen from the much bigger errorbar on the grand potential resummed value on the left panel. In the vicinity of the phase transition we rely on shifts in the range $\alpha \sim 0.5 - 0$ which lead to converging partial sums and thus precise resummations. This is especially true for computing the magnetization. A precise choice for the α parameter gives a converging partial sum $\alpha = 0.162$. Finding this value is not an easy task and it requires many computations with varying parameters. In order to determine accurately the magnetization in the critical region of the phase diagram we will rely on scanning values of the shift parameter in search for the 'magic' α-shift. In the end our resummation procedure always rely on at least two different expansion series with different values of the shift and their discrepancy enters the estimated error of the resummed result.

IV.2.2 High order behaviour

The resummation procedure for estimating a perturbative series essentially relies on an extrapolation to infinite orders, which is equivalent to finding the behaviour of the expansion coefficients a_n as the order becomes large $n \to \infty$. This asymptotic behaviour encodes the convergence properties of the perturbative series of an observable $\mathcal{A} = \sum_n a_n U^n$. We give here several arguments to understand the limitations and the high order behaviour of perturbative series for the symmetry-broken expansion. We discuss here the Grand potential density $-\Omega/L^3$ which is introduced in details in the Subsection IV.3.3.

Goldstone singularity :

Even if the symmetry-broken expansion enables one to enter perturbatively the Néel order, it comes with a singularity at the physical value of the interaction $U = U_\phi$. It is due to long-wavelength thermal fluctuations, called Goldstone modes, as we enter the antiferromagnetic phase with canceling an external staggered field. This singularity is

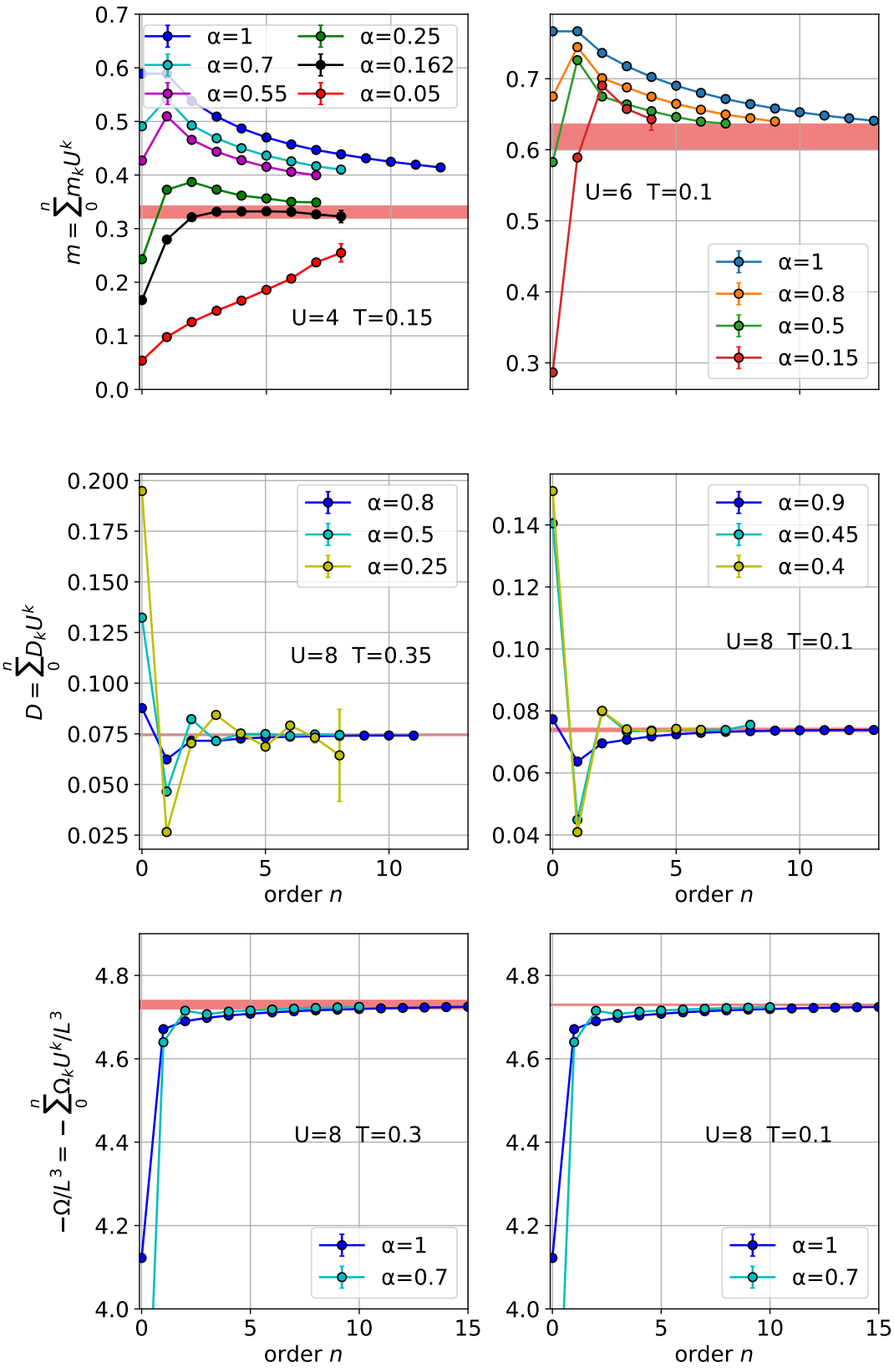

Figure IV.2: Partial sums of the double occupancy D, magnetization m and Grand potential density $-\Omega/L^3$ for two different values of the interaction U and temperature T as a function of the maximum order n. The colored area corresponds to the estimated resummed value with errorbar.

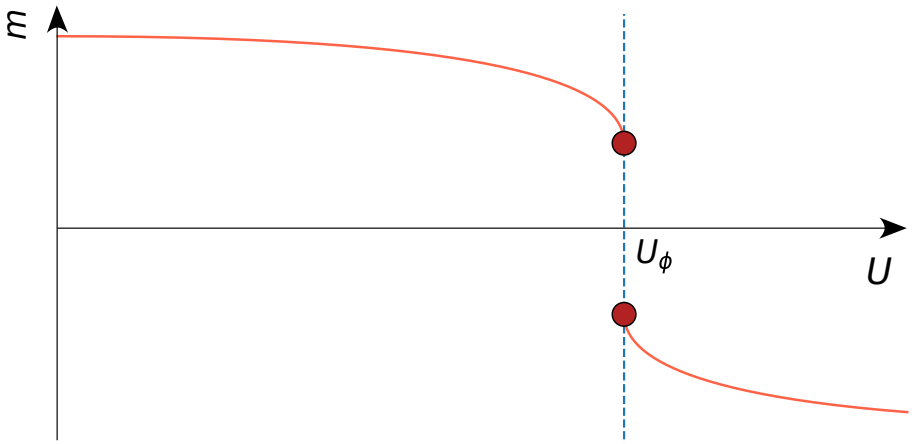

Figure IV.3: Sketch of the expected variation of the magnetization as a function of the expansion parameter U for a symmetry-broken perturbative series performed at $T < T_N$(U_ϕ inside the ordered phase. At $U \to U_\phi$ the magnetization gets an infinite derivative and shows a vertical asymptotic line (blue dashed line). At $U = U_\phi$ the magnetization changes sign and is discontinuous.

different from the critical behaviour at the phase transition $T = T_N$ and due to the divergence of the magnetic susceptibility as we restore the spin inversion symmetry by canceling the external field. Indeed we see in Eq. III.20 that the external field along the perturbation path varies as $h(1 - \frac{U}{U_\phi})$. Considering a perturbative expansion at $T < T_N$, the Goldstone fluctuations lead to a singularity as the external field vanishes for $U \to U_\phi$ [19, 99] :

$$\chi(U \to U_\phi) \propto \frac{1}{\sqrt{h(1 - \frac{U}{U_\phi})}} \tag{IV.3}$$

With χ the antiferromagnetic susceptibility which is the derivative of the magnetization with respect to an external staggered Zeeman magnetic field. This gives the behaviour of the magnetization and grand potential as the expansion parameter goes to its physical value $U \to U_\phi$:

$$\begin{aligned} m &\propto \sqrt{h(1 - \frac{U}{U_\phi})} \\ -\frac{\Omega}{L^3} &\propto [h(1 - \frac{U}{U_\phi})]^{\frac{3}{2}} \end{aligned} \tag{IV.4}$$

Supposing that there is no singularity closer to to the origin in the perturbative series of the grand potential and magnetization (which is observed by the possible resummation and convergence of the computed series at $U = U_\phi$ in Fg. IV.2), this singularity determines the behaviour of high perturbative orders. By expanding these expressions we obtain for $n \to \infty$ the behaviour of the expansion coefficients :

$$\begin{aligned} m_n &\propto \frac{1}{U_\phi^n n^{3/2}} \\ -\frac{\Omega_n}{L^3} &\propto \frac{1}{U_\phi^n n^{5/2}} \end{aligned} \tag{IV.5}$$

Hence the series are converging and can be resummed at $U \to U_\phi$. Given Eq. IV.21, the double occupancy expansion coefficients behave in the same way as for the magnetization at high expansion orders.

This predicted behaviour can be modified in two cases :

- Considering a symmetry-broken perturbative expansion right at the Néel phase transition with a temperature and an interaction verifying $T = T_N(U_\phi)$, the universal critical behaviour has to be taken into account. It gives the asymptotic form $m(U \to U_\phi) \propto [h(1 - U/U_\phi)]^{\frac{1}{\delta}}$ with $\delta = 4.783(3)$ [24]. This leads to slowly converging series at $U = U_\phi$ with a high order behaviour :

$$\begin{aligned} m_n &\propto \frac{1}{U_\phi^n n^{1+1/\delta}} \\ -\frac{\Omega_n}{L^3} &\propto \frac{1}{U_\phi^n n^{2+1/\delta}} \end{aligned} \tag{IV.6}$$

- At low temperatures $T \to 0$, the long-wavelength fluctuations become dominated by quantum fluctuations [30]. This changes the expected high order behaviour as :

$$\begin{aligned} m_n &\propto \frac{1}{U_\phi^n n^2} \\ -\frac{\Omega_n}{L^3} &\propto \frac{1}{U_\phi^n n^3} \end{aligned} \tag{IV.7}$$

Discontinuous magnetization at U_ϕ :

At $U = U_\phi$, as the external magnetic field vanishes and the symmetry of the Hubbard Hamiltonian is restored, an other singularity arises. It finds its origin in the discontinuity of the order parameter as the external field changes sign as shown in Fig. IV.3. Indeed as we approach U_ϕ, the magnetization is aligned with the staggered magnetic field $h(1 - U/U_\phi)$ which changes sign at $U = U_\phi$. This leads to a change of sign at the physical value of the interaction and $m(U = U_\phi^-) = -m(U = U_\phi^+)$. For $T > T_N$ the value of magnetization is zero in the paramagnetic regime and there is no singularity, we can expect an exponential convergence of the perturbative series at $U = U_\phi$. But for $T < T_N$ the magnetization has a non-zero value and the order parameter is discontinuous at $U = U_\phi$, the system goes through a first order phase transition as the external field changes sign. This yields a new singularity with an associated high order behaviour of the perturbative series.

The first order phase transition can be associated with a branch cut in the complex plane of the perturbative series. We expect a singularity in the grand potential perturbative series which goes like $e^{-\beta B(U)}$ where $B(U) \propto 1/\sqrt{1-U/U_\phi}$ is the grand potential barrier between the metastable and stable phases [33, 48, 77]. Such a behaviour for the grand potential can be estimated to lead to a stretched exponential decay for the expansion coefficients at high orders :

$$-\frac{\Omega_n}{L^3} \propto e^{-cn^a} \tag{IV.8}$$

With c a constant coefficient and $0 < a < 1$. In the end this singularity is weaker than the Goldstone singularity and the associated polynomial decay dominates at high order.

All things considered, the presence of a singularity at the physical value defines the radius of convergence of the series which is equal to the physical value of the interaction U_ϕ. Even if we aim at resumming series right at the singularity, the series prove to be converging at $U \to U_\phi$ which makes our approach viable.

IV.2.3 Resummation tools

At the end of the symmetry-broken CDet algorithm, we are left with a finite number of expansion coefficients obtained with a stochastic error due to the Monte Carlo computation. In order to obtain a controlled result at $U = U_\phi$ one needs to extrapolate this truncated perturbation series to infinite perturbation order. This procedure is called resummation and we use several tools to perform the extrapolation. The final result and its estimated error are given after comparing the different techniques.

For simplicity we do not consider the correlation between expansion coefficients at different orders obtained within the CDet procedure. In fact determining accurately the covariance matrix of the expansion coefficients at different perturbation orders is not an easy task and has been tested to have a minor impact on the estimated result after resummation. The resummation techniques are implemented with error propagation of the stochastic error on the coefficients. For better convergence with respect to the number of sampling of the resummation procedure, we consider as the error the median absolute deviation. The standard deviation of a supposed Gaussian distribution is obtained by multiplying this estimation by a constant factor 1.4826 .

Padé and D-log Padé :

We rely on Padé and D-log Padé extrapolation [10, 20] of the truncated expansion series. These methods are well known state-of-the-art resummation techniques which consist in approximating the truncated power series by a rational function such that :

$$\sum_{n=0}^{n_{max}} a_n U^n \simeq \frac{\sum_{i=0}^{k} b_i U^i}{1 + \sum_{i=1}^{l} d_i U^i} \tag{IV.9}$$

The right hand side of this equation is called Padé approximant of order $[k, l]$. It contains $k + l + 1$ free parameters which are determined to be the best approximation to the truncated power series and we must impose $n_{max} = k+l$. For obtaining the resummed result at $U = U_\phi$ we rely on the Padé approximants of three different orders (for n_{max} even for instance) $[n_{max}/2, n_{max}/2]$, $[n_{max}/2-1, n_{max}/2+1]$ and $[n_{max}/2+1, n_{max}/2-1]$, and compare there result.

The D-log Padé extrapolation approximates the logarithmic derivative of the partial sum by a Padé approximant. It is known for giving a better description of singularities of the perturbative series. As for the Padé approach, we use three different orders for the approximants and compare their result with each other.

Exponential and power-law fits :

As the Goldstone instability and first-order phase transition imply at $U \to U_\phi$, we can search for the corresponding high-order behaviour of the expansion coefficients as described in Subsection IV.2.2. We therefore look for such a high order behaviour and, when verified, obtain a resummed result.

We rely on this only for symmetry-broken series obtained with a coefficient $\alpha \sim 1-0.7$ for which we have many expansion coefficients $n_{max} \simeq 10-13$ with the same definite sign within errorbar, and enough orders to look for an asymptotic behaviour for expansion orders $n \to n_{max}$.

We give in Fig. IV.4 an example for the magnetization expansion obtained with the symmetry-broken CDet algorithm. The Bottom panels show the search for an exponential and a power law decreasing as the series is resummed at $U = U_\phi$. We see on the bottom right panel that the power-law behaviour predicted by the Goldstone singularity does not appear within the 13 orders available. However, the exponentially decreasing high order behaviour is well verified on the bottom left panel. The linear regression gives a coefficient leading to a radius of convergence bigger than U_ϕ, hence an exponential convergence of the series at $U = U_\phi$. Considering this exponential high order behaviour we can resum the perturbative series and obtain $m = 0.618$ for this set of parameters. This value is in good agreement with the resummed result obtained with Padé and D-log Padé resummation as shown on the top panel.

This observation for this specific example is actually general and the same approach with other sets of parameters and observables leads to the same conclusion. The large order behaviour predicted by the Goldstone singularity is in fact never observed within the number of expansion coefficients that we are able to compute and we can conclude that its contribution to the final result must be negligible in front of the estimated error on the resummed result.

IV.2.4 System size study

The Diagrammatic Monte Carlo methods offer the main advantage of being formulated in the thermodynamic limit, on the contrary to most numerical techniques for strongly

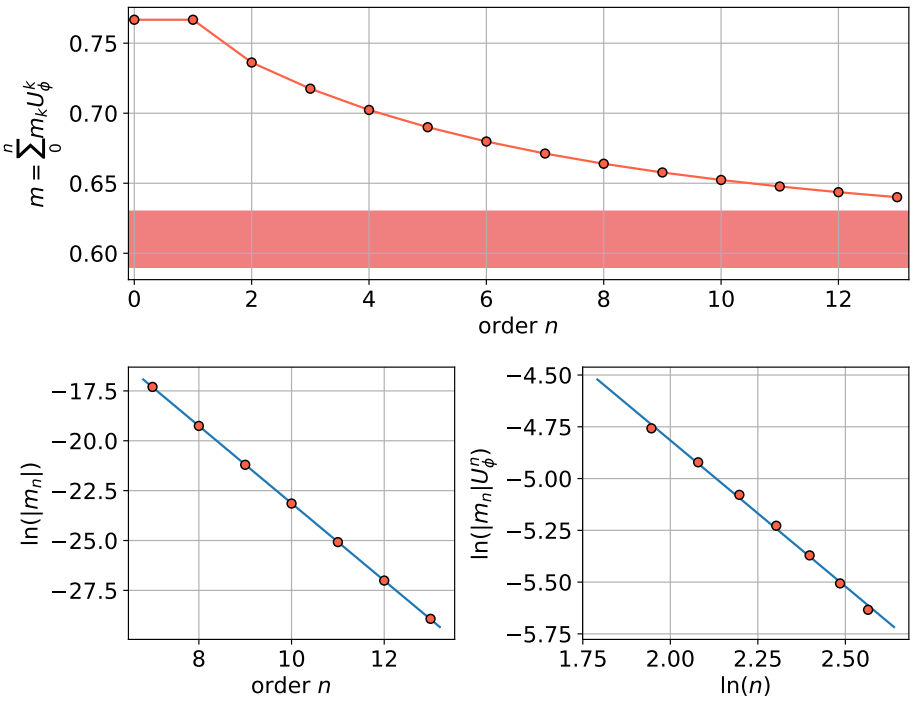

Figure IV.4: Expansion series of the magnetization for $U_\phi = 6$, $T = 0.2$ and $\alpha = 1$. Top panel : Truncated series as a function of he maximum expansion order up to order 13. The colored area is the estimated value of the magnetization after the complete resumation procedure. Bottom left panel : Logarithm of the expansion coefficients of the magnetization as a function of the expansion order. The blue line corresponds to the best linear fit. Bottom right panel : Contribution at each order of the magnetization expansion coefficients in a log-log scale. The blue line corresponds to the best linear fit.

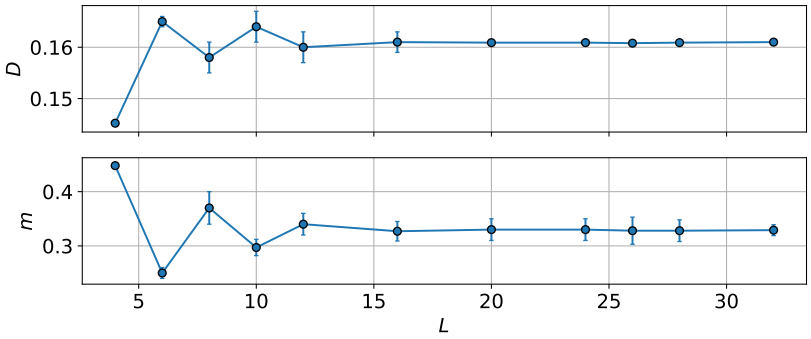

Figure IV.5: Double occupancy and magnetization at $U = 4$, $T = 0.15$ as a function of the linear system size L.

correlated systems which are limited to small system sizes. Indeed the system size enters at two different steps of the CDet algorithm : for solving the non-interacting system and obtaining the bare propagators on which the perturbative expansion is built, and during the markovian process since the sites' indices are a part of the Monte Carlo configuration. For our study we fix the system size to $L^3 = 20^3 = 8000$ sites and we show that this is large enough to neglect finite size effects, even in the vicinity of the phase transition.

Finite-size effects :

We conduct a system size study of our method. We show in Fig. IV.5 the evolution of the double occupancy and magnetization after resummation. The CDet computation is performed on a lattice of size L^3 and we vary L from 4 up to 32. Starting at $L = 16$, the results are fixed within error and we can consider that, within our precision, the thermodynamic limit is reached. In more details, we display the expansion coefficients of the perturbative treatment of the magnetization, as a function of the linear system size, in Fig. IV.6. The CDet calculation is completed at $U = 4$, $T = 0.18$ which is located very close to the phase transition ($T_N \simeq 0.19$ at an interaction $U = 4$). The biggest finite-size effects are expected to be observed in the critical region for temperatures near the Néel temperature. However we conclude that for a linear system size $L \geq 20$, up to high order and negligible contribution to the resummed result ($m_n U^n \leq 10^{-3}$), the contribution from each order is converged within statistical error. Therefore our results are obtained directly in the thermodynamic limit and, thus, do not involve any finite size scaling. In the end the final error is dominated by statistical and resummation errors.

Phase transition on a finite lattice :

It is counter intuitive that we can describe the antiferromagnetic phase by performing computations on a finite lattice. Indeed, the spontaneous breaking of a symmetry can not occur on finite system, but is a characteristic of macroscopic systems in which an infinite number of particles develop long range correlations. Therefore one could expect any magnetization computation to be resummed to zero and the physical system to remain

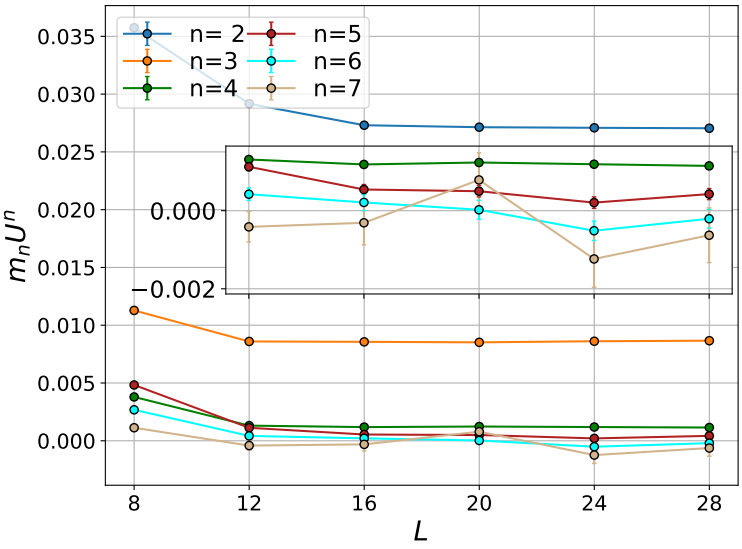

Figure IV.6: Contribution to the magnetization of its expansion coefficients m_n at different orders n, as a function of the linear system size L. The perturbation expansion is done at $T = 0.18$, $U = 4$, $\alpha = 0.1$. The inset is the same plot for smaller contributions.

paramagnetic at any temperature. This is not what we observe, how can we explain that we are able to describe a phase transition with a finite number of sites ?

In fact in the CDet recursion, as any Diagrammatic Monte Carlo algorithm, computes stochastically diagrams which vertices take a position on the finite lattice in real space. All of these vertices belong to connected diagrams which weight decreases fast with increasing the spacing between vertices. This is explained by the fact that the bare propagator decreases fast with increasing the distance between two vertices.

Numerically we estimate for $T = 0.2$ and independently on the imaginary-time τ, the average value of the spreading of the Green's function from the origin i_0. It is given by $\delta r = \sum_i |\mathcal{G}_{0,i_0 i,\sigma}(\tau)| \times d_{i i_0} / \sum_i |\mathcal{G}_{0,i_0 i,\sigma}(\tau)| \simeq 0.5$ with $d_{i i_0}$ the distance between the sites i and i_0. We want to evaluate the average spreading of diagrams at a certain order in real space with a simplified approach. We consider a connected diagram formed with n vertices and two external vertices fixed at the origin. Given the fast decreasing weight of the non-interacting Green's function, we consider an average distance between two vertices given by the average value of the bare propagator spreading $\delta r \simeq 0.5$. We can build the diagram by performing a random walk of step δr in the three dimensional cubic lattice and imposing it to form a closed loop with the external vertices at the origin. This situation is close to the worst case by giving the diagram a linear form, maximizing its spread. The expected translation distance from the origin of this random walk made of n steps is given by :

$$D \simeq \frac{\sqrt{n}}{2} \delta r \tag{IV.10}$$

Hence the critical expansion order at which the diagrams start to have significant contributions outside of the cubic lattice of linear size $L = 20$ is :

$$n_c \simeq 4\frac{L^2}{\delta r^2} \simeq 6400 \tag{IV.11}$$

Although extremely simplified, this approach shows that within the number of orders available we are far from the order of magnitude where diagrams have important contributions outside of the box defined by the finite cubic lattice of $L^3 = 20^3$ sites. At expansion orders of the order of magnitude of n_c, one would expect the contributions to be significantly influenced by the finite cubic box of the system and to lead to a cancellation of the magnetization which is equal to zero in a finite system. The spreading of the bare propagator is increasing as the temperature is decreasing which leads to a larger spreading in real space of diagrams.

This estimate is extremely rough and it could be checked numerically during the Monte Carlo simulation. By storing the spreading of diagrams through the Markovian process one could verify that they mostly remain inside the finite-size cubic lattice. This would provide an additional argument that the expansion orders are obtained directly within the thermodynamic limit.

IV.2.5 Numerical instabilities

At high orders and for large system sizes, the perturbative expansion sometimes turns out to show inconsistent results due to round-off errors in the CDet recursion.

In order to understand this issue let us consider a configuration of n vertices with at least one vertex which is far away from the rest of the vertices. As the bare propagator decreases fast with increasing the distance between two vertices, the sum of connected diagrams that leave on these vertices is going to be small. However the sum of disconnected diagrams does not have to be small given that it includes diagrams where the far away vertices are not connected to the rest of the vertices. Naming V the set of considered diagrams we therefore have, using the notations of Eq. III.3 :

$$|\mathbf{C}(V)(x_{in}, x_{out})| \ll |\mathbf{D}(V)(x_{in}, x_{out})| \tag{IV.12}$$

This means that many cancellations have to happen in the CDet recursion which implies 2^n operations between determinant like quantities. It leads to round-off errors that give a wrong and uncontrolled weight to the sum of connected diagrams.

This problem vanishes at $\alpha = 1$ and is extremely enhanced for $\alpha \to 0.5$ since it gives a more important weight to Hartree self-loops. Indeed they contribute highly to disconnected configurations in the case of far away vertices that do not need to be connected to any other vertex. Increasing the system size also worsen this effect by increasing the volume available for far away vertices.

To solve this issue we define a numerical threshold ϵ to cut-off small contributions in the CDet recursion and avoid errors. We implement the condition :

$$|\mathbf{C}(V)(x_{in}, x_{out})| < \epsilon |\mathbf{D}(V)(x_{in}, x_{out})| + |\sum_{S \subsetneq V} \mathbf{C}(S)(x_{in}, x_{out}) \mathbf{D}(V \backslash S)(\emptyset)| \qquad \text{(IV.13)}$$

At every step of the CDet recursion. If this condition is fulfilled, we set the connected contribution $\mathbf{C}(V)(x_{in}, x_{out})$ to zero and continue the recursion. To be certain not to miss important contributions to the final result we perform the full computation with two significantly different values of the ϵ parameter and check that the expansion coefficients obtained are consistent within statistical errors. In practice this cut-off is chosen to be a few orders of magnitude above machine precision ϵ_0. In general we use $\epsilon/\epsilon_0 = 10^3$ and 10^5 and utilize the long double accuracy of the C++ standard library.

In the end the resummation procedure enables us to obtain a controlled result. The finale estimated error on our results are due to the propagation from the stochastic error on the expansion coefficients, after comparing the resummation with Padé, D-log Padé, the truncated partial sum, and the exponential fitting of the expansion coefficients, for at least two different values of the shift α, and with two different coefficients for handling round-off errors for each computed perturbative series. This procedure gives a controlled estimation of the result within its determined errorbar, which we have shown is dominating the error due to the finite size of the lattice.

IV.3 Critical behaviour and Néel ordering

We start our study of the physics of the Néel order by focusing on the critical properties of the system in the vicinity of the phase transition. We focus in this section on describing how the magnetization, double occupancy, and entropy behave both within the ordered phase and across the phase transition.

IV.3.1 Criticality of the Néel phase transition

Applying the symmetry-broken CDet algorithm and our resummation procedure we are able to compute the order parameter of the antiferromagnetic phase with very good accuracy. The magnetization is determined at low temperatures where it saturates to its zero temperature value, up to the Néel temperature at which it vanishes to zero. Results are shown in Fig. IV.7 for three different values of the interaction up to intermediate coupling $U = 6$. A non-zero magnetization indicates that we enter the Néel phase and we determine from our grid in temperature the critical Néel temperatures : $T_N(U = 2) = 0.0425(25)$, $T_N(U = 4) = 0.191(1)$ and $T_N(U = 6) = 0.315(5)$. More precisely, taking advantage of our precise data, we manage to find the critical behaviour of the magnetization close to the phase transition $m(T) \simeq a(T_N - T)^\beta$. We show in Fig. IV.8 (left panel) the acquired values for the β critical exponent which compare remarkably well with literature for the O(3) Heisenberg universality class [24, 111, 122]. Relying on this critical behaviour we also get the very precise estimates of the Néel temperature : $T_N(U = 2) = 0.0411(8)$,

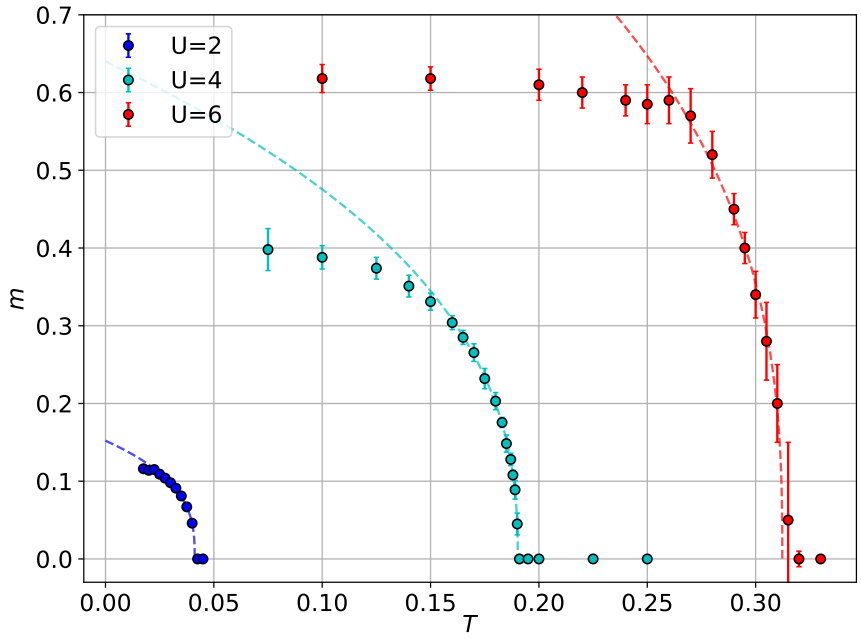

Figure IV.7: Magnetization as a function of temperature at interaction $U = 2$, 4 and 6. A non zero magnetization indicates that the system is ordered in the antiferromagnetic phase. The dashed curve corresponds to the best critical behaviour in the vicinity of the Néel temperature, as fitted with our data.

$T_N(U=4)=0.1902(3)$ and $T_N(U=6)=0.312(2)$. At $U = 4$ we see that the linear relation in the log-log scale is verified on a large scale of temperature. The critical region, defined as the temperature range $T \in [T_N - \delta T, T_N]$ where $m(T) = a(T_N - T)^\beta$ is a good fit to our data, is of the order of $\delta T \simeq 0.025$ for $U \geq 4$.

These computations are the first direct computation of the β critical exponent on a fermionic lattice and in the thermodynamic limit as other methods are either not able to enter the ordered phase, or show approximate critical exponents since they rely on the DMFT approximation. The estimated values of the Néel temperature compare well with the paramagnetic CDet approach [81], the improved dynamical vertex approximation $D\Gamma A$ [131], and the DCA extrapolated to infinite cluster size [62, 70].

The magnetization computations are limited to the weak-to-intermediate coupling $U \leq 6$ with our approach. At stronger interaction, the expansion series convergence becomes slower with respect to the expansion order, and the search for the 'magic shift' requires more effort. This leads to series which turn out to be hard to resum in a controlled way. However, even if the critical region will remain inaccessible to our method, we show in Section IV.4.1 that the magnetization can be determined at low temperature up to very high interaction.

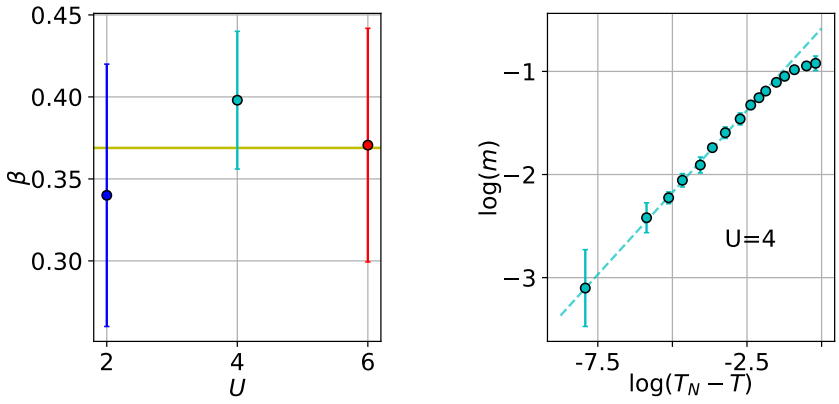

Figure IV.8: Left panel : β critical exponent as it is obtained from the critical behaviour of the magnetization close to the phase transition. The three values obtained from the three magnetization curves in Fig. IV.7 are consistent with each other within errorbars. They agree with the theoretically predicted value of β for the O(3) Heisenberg universality class [24] which is displayed as a gold horizontal band. Right panel : magnetization as a function of $T_N - T$ at $U = 4$ on a log-log scale. The Néel temperature T_N and the dashed line correspond to the fitted critical behaviour from Fig. IV.7.

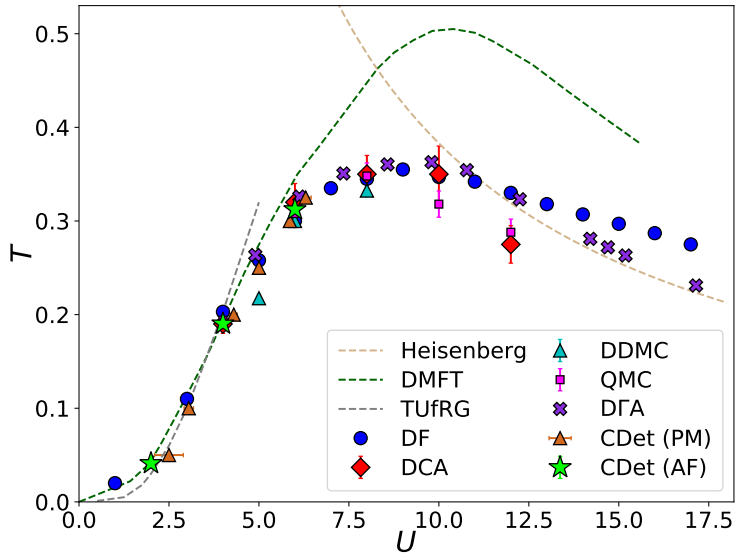

Figure IV.9: Phase diagram of the half-filled Hubbard model on a cubic lattice according to several numerical methods. We add our data from the symmetry-broken CDet technique (CDet (AF)) as lime stars.

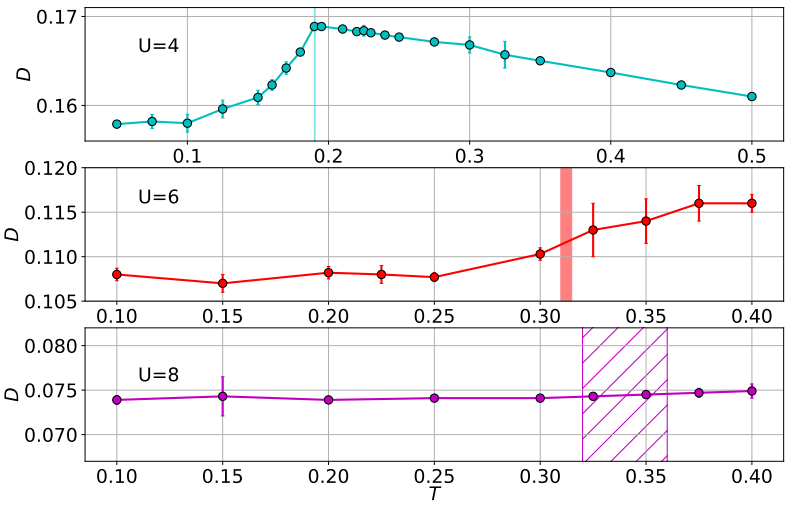

Figure IV.10: Double occupancy D as a function of temperature for three different values of the interaction U. The vertical bands at $U = 4$ and $U = 6$ correspond to the estimate of the Néel temperature from our study, while the hashed area at $U = 8$ is an estimate of the Néel transition from other numerical methods displayed in Fig. IV.9

IV.3.2 The Slater mechanism

We present the variations of the double occupancy with respect to temperature, in the paramagnetic and antiferromagnetic phases, in Fig. IV.10. At $U = 4$ we observe a singularity in the double occupancy which corresponds to the Néel phase transition. As expected at this relatively small value of the interaction, the double occupancy bends towards zero when entering the antiferromagnetic phase with decreasing the temperature. Therefore the phase transition provokes a gain in potential energy $E_{pot} = UD$ which is consistent with the Slater mechanism. Interestingly in the paramagnetic phase at $T \geq 0.19$, D decreases with increasing temperature. This is the Pomeranchuk effect [29, 39, 41, 141] which happens in this part of the phase diagram. It is driven by the spin entropy which is larger in a localized state than in the Fermi liquid. Therefore an increase in temperature leads to less localization and an increase of the double occupancy for the half-filled system.

At higher values of the interaction we loose in accuracy because of harder resummations and the curve flattens. We can not observe a singularity at the phase transition. We do not report any change in the double occupancy at the Néel temperature or inside the antiferromagnetic phase within our 10^{-2} relative accuracy on the displayed results. For this coupling we are close to the maximum of the Néel temperature, at the top of the antiferromagnetic dome. We therefore expect to be seated at an intermediate interaction between the Slater and Heisenberg domains which is consistent with a quite still potential energy as we enter the ordered phase, on a range of temperature much larger than the

critical region.

At higher values of the coupling, the double occupancy computations does not show the same limitations as for the magnetization and we show further results as a function of the interaction in Section IV.4.1. However, as seen at $U = 8$, a much better sensitivity on the double occupancy would be needed to witness the change from a Slater to Heisenberg mechanism.

IV.3.3 Entropy through the phase transition

Grand potential :

To derive the entropy we compute the grand potential per lattice site of the system $-\Omega/L^3 = P$ where L is the linear system size of the cubic lattice, and P the thermodynamic pressure. The entropy density can be obtained from the grand potential density through :

$$S = -\frac{\partial \Omega}{L^3 \partial T} \tag{IV.14}$$

The grand potential density, or pressure, is defined on a lattice with L^3 sites by the logarithm of the partition function :

$$-\frac{\Omega}{L^3} = \frac{1}{\beta L^3} \log(\mathrm{Tr}[e^{-\beta \hat{\mathcal{H}}}]) \tag{IV.15}$$

From the linked-cluster theorem, one can show that its diagrammatic expansion is made of the sum of fully connected diagrams with no external vertices. To implement this computation within the CDet framework we need external vertices see Eq. III.3. We take advantage of the position and imaginary-time translation invariance of the system and fix one of the vertices, taken as a reference, on a specific site and time. The other vertices coordinates stay part of the Monte Carlo configuration. This definition of a vertex of reference is required in order to distinguish the connected from the disconnected part in the CDet recursion. In the end the quantity that we compute is defined diagrammatically by the sum of fully connected diagrams with four external vertices that have the same coordinate of reference in the time and space-translational invariant system and are connected to one propagator. We call this quantity Λ and note Λ_n its expansion coefficient of order n.

Because of this scheme the pertubative expansion of Λ is not exactly the one of P, and we need to make a few adjustments. Indeed the reference vertex being defined as an external vertex, for a computation with k internal vertices we compute the expansion coefficient Λ_k. It corresponds to an expansion coefficient at order $k+1$ of the pressure once the reference vertex is considered as internal. At an order k, the prefactor of the sum of the factorial number of diagrams goes as $1/k!$ and therefore one has to add a coefficient $k!/(k+1)! = 1/(k+1)$ in the process of going from Λ to P. In the end we get the expansion coefficients for the pressure :

$$P_{k+1} = -\frac{\Lambda_k}{k+1} \tag{IV.16}$$

This means that, after normalization of the coefficients Λ_k up to a maximal order n we obtain the expansion coefficients of the pressure from order 2 to $n+1$. We now have to determine analytically two expansion coefficients to complete the perturbative series. At $U = 0$ the pressure for free fermions with eigenenergies E_i is given by :

$$P_0 = \frac{1}{\beta L^3} \sum_i \log(1 + e^{-\beta E_i}) \tag{IV.17}$$

From the expression of the Hamiltonian on the expansion path Eq. III.20 for $U \in [0, U_\phi]$ we get the first derivative for the pressure :

$$\frac{dP}{dU} = -\frac{1}{L^3} \frac{\mathrm{Tr}[(\sum_i \hat{n}_{i\uparrow}\hat{n}_{i\downarrow} - \frac{1}{2}\sum_i(\hat{n}_{i\uparrow} + \hat{n}_{i\downarrow}) - \frac{\alpha h_{MF}}{U_\phi}\sum_i(-1)^i \hat{S}_i^z) e^{-\beta\hat{\mathcal{H}}}]}{\mathrm{Tr}[e^{-\beta\hat{\mathcal{H}}}]} \tag{IV.18}$$

With recalling $D = \langle \hat{n}_{i\uparrow}\hat{n}_{i\downarrow} \rangle$, and $m = \langle (-1)^i \hat{S}_i^z \rangle$ and at half-filling $\langle \hat{n}_{i\uparrow} + \hat{n}_{i\downarrow} \rangle = 1$ we get :

$$\frac{dP}{dU} = -D(U) + \frac{1}{2} + \frac{\alpha h_{MF}}{U_\phi} m(U) \tag{IV.19}$$

Which gives :

$$P_1 = \frac{dP}{dU}(U = 0) = -D(0) + \frac{1}{2} + \frac{\alpha h_{MF}}{U_\phi} m(U = 0) \tag{IV.20}$$

This links the perturbative expansions of the grand potential with the double occupancy and magnetization, and at any expansion order $n \geq 2$ we have :

$$P_{n+1} = \frac{1}{n+1}(-D_n + \frac{\alpha h_{MF}}{U_\phi} m_n) \tag{IV.21}$$

We notice that the quantity Λ can be expressed in terms of the magnetization and double occupancy. Indeed the diagrammatic expansion of Λ is similar to the double occupancy one but with a possible external interaction due to the shift on the reference vertex. For a CDet expansion in the paramagnetic regime ($\alpha = 0$), the grand potential is obtained directly from computing the double occupancy.

Deriving the entropy :

We determine the grand potential at $U = 4$ from low to high temperatures in Fig. IV.11. Within our numerical data we can not observe a singularity of the grand potential at the Néel temperature. Indeed its critical behavior at the phase transition is determined by the α critical exponent which defines the specific heat variations in the vicinity of the Néel temperature $C \propto (T_N - T)^{-\alpha}$, with $\alpha \simeq -0.1336$ for the O(3) Heisenberg universality class. Hence the specific heat is continuous at the critical temperature with a diverging derivative. The specific heat is related to the grand potential through $C = -T\partial^2\Omega/L^3\partial T^2$. Therefore the grand potential is continuous up to its third derivative and the function appears smooth at our scale and numerical accuracy.

In order to evaluate its derivative with respect to the temperature and get the entropy density of the system, we suppose a polynomial behaviour of the grand potential. At low temperatures $T \to 0$ in the antiferromagnetic phase, the low energy excitations of the ground state take the form of spin wave excitations which analysis leads to a low temperature behaviour $\Omega(T) - \Omega(T = 0) \propto T^4$ [140]. This motivates the polynomial expression $-\Omega(T)/L^3 = -\Omega(T{=}0/L^3) + aT^4 + bT^5 + cT^6$ which fits well our data inside the antiferromagnetic phase (cyan curve). At $T > T_N$ we expect a quadratic dependency on the temperature in the degenerate Fermi liquid regime. The data is well fitted by the expression $-\Omega/L^3(T) = d + eT^2$ (yellow curve). The two relations are linked at the Néel temperature by imposing continuity of the grand potential and of its derivative. At higher temperatures $T \geq 0.4$ the grand potential becomes almost linear in temperature $-\Omega(T) \simeq \log(4)T$. The entropy density is then extracted with a finite difference scheme. These different behaviors of the grand potential lead to different physical regimes for the evolution of the entropy density with temperature. In the Néel phase and at small temperatures the entropy density varies as $S \propto T^3$. For temperatures just above the transition $T \in [T_N, 0.35]$ the entropy density increases linearly with the temperature which is a signature of the expected metallic behaviour of the system in this part of the phase diagram. At higher temperatures $T \sim U = 4$ the entropy density saturates to $S(T \to +\infty) = \log(4)$. It corresponds to its expected value in the disordered system for $T \to \infty$ as the system has four possible configurations on each site.

This study enables us to recover the expected different physical regimes present at intermediate coupling $U = 4$ of the half-filled Hubbard model. We lack accuracy and results close to the Néel temperature to be able to describe the critical behaviour of the grand potential and entropy. In this context the obtained entropy at the phase transition can only be given as a general estimate and we document $S \simeq 0.22$ at $T_N \simeq 0.19$ which is consistent with the estimated value of the DDMC study at $S(T = 0.2) = 0.215(11)$ [73].

IV.4 Low temperature physics

Our attention is now focused on the system's low temperature characteristics where the magnetization has reached saturation. The region with saturated magnetization makes up a considerable portion of the antiferromagnetic dome since we have shown that the magnetization only noticeably changes in a shell of size $\delta T \sim 0.1$ below the Néel temperature.

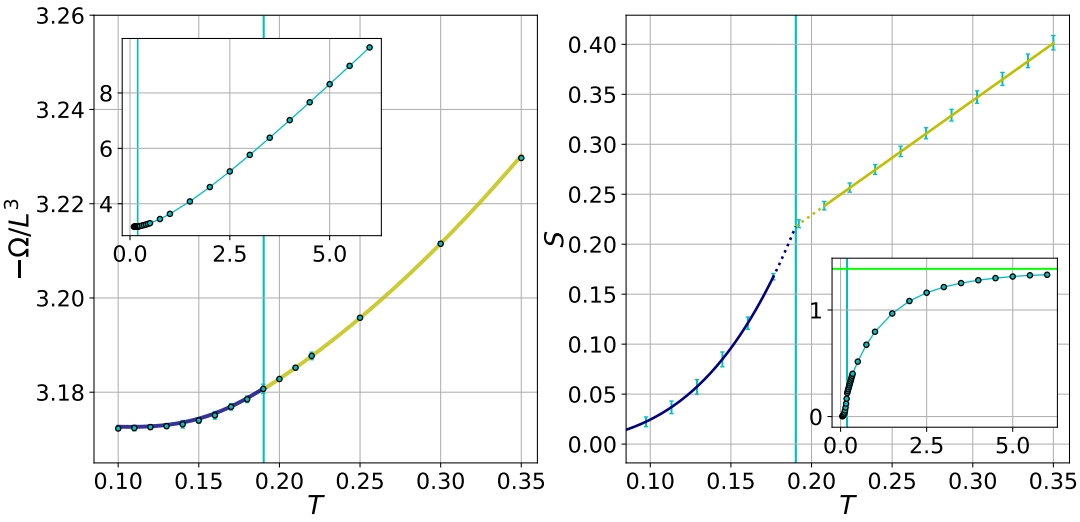

Figure IV.11: Left panel: At interaction $U = 4$, grand potential density $-\Omega/L^3$ as a function of temperature T. When not visible the error bar is smaller than the markers. Right panel: Entropy density S as a function of temperature and computed as derivative of the grand potential fitting curves (see text). The cyan error bars give the error on the entropy curve. The entropy curve is dashed in the temperature range where we lack sufficient data to fully resolve the critical behavior of entropy. The insets are the same plots on a larger temperature range. The lime horizontal line indicates the high temperature limit $S = \log(4)$. On both panels the vertical lines correspond to the value of the Néel temperature.

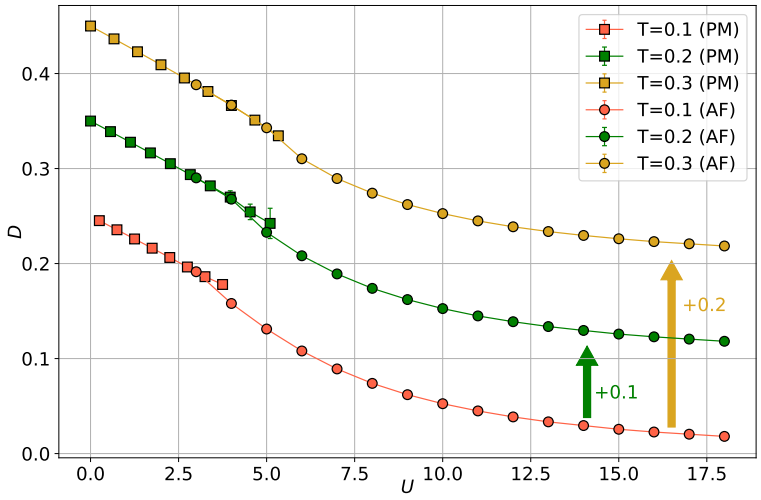

Figure IV.12: Double occupancy D as a function of the interaction U for three different values of the temperature. For better visibility the data at $T = 0.2$ ($T = 0.3$) is shifted by $+0.1$ ($+0.2$). The square markers are are obtained with the paramagnetic CDet algorithm (PM) in the normal phase with $\alpha = 0$. The round markers are obtained with the antiferromagnetic symmetry-broken CDet with $\alpha \neq 0$ (AF).

In this regime the perturbative series turn out to be easier to resum and we systematically rely on series with a chemical potential shift $\alpha \sim 1 - 0.7$ for double occupancy and grand potential computations.

IV.4.1 Double occupancy at low T

As a measure of localization, the double occupancy is highly sensible on the interaction U. We display its variations with the coupling at three different values of the temperature in Fig. IV.12.

At small values of the interaction the double occupancy obtained with CDet algorithm with no symmetry breaking matches the symmetry-broken CDet results, up to the critical value of the interaction at which the paramagnetic phase computation breaks and the series can not be resummed. As anticipated, a singularity in the double occupancy is observed during the transition at U_c, and this observation may be utilized to determine the value of the critical interaction at fixed temperature. The double occupancy decreases faster with increasing interaction when entering the Néel phase which is consistent with the Slater mechanism at the transition on this part of the Néel dome. Inside the phase and at higher interaction, the double occupancy decreases slowly towards zero at $U \to \infty$. We are able to accurately determine the double occupancy up to very strong coupling $U = 18$. Our error on the resummed result which is too small to be visible here, remains approximately constant over the different temperatures and values of U. But since the overall result decreases with increasing the interaction, it goes from a 1% error at $U = 7$ up to a 5% error at $U = 18$. For $U \geq 8$ and within our errorbar, we do not see any change

in the double occupancy as the temperature varies from $T = 0.3$ to $T = 0.1$. Even if we could expect the to have reached the paramagnetic phase on the other side of the Néel dome at high interaction and $T = 0.3$, we do not observe any signature of this in the temperature.

In the end our results are not precise enough for documenting a change to a Heisenberg mechanism of the Néel ordering or a change in behaviour indicating an underlying insulating paramagnetic system, since the variations of the double occupancy with respect to the temperature are inaccessible. Still, our approach shows powerful for reaching the strong coupling regime in which it is able to provide controlled and accurate resummed results.

IV.4.2 Grand potential as a path to magnetization

As the interaction is increased, it becomes increasingly difficult to resum the perturbative series of the magnetization and the direct computations fail for $U \geq 7$. However the perturbative series for the grand potential behaves in a much better way and we can, as for the double occupancy, resum them accurately up to high interaction. Our approach relies on determining the magnetization from the grand potential computations. In this purpose we describe the Hubbard Hamiltonian with an additional term $H_{\text{ext}} \sum_i (-1)^i \hat{S}_i^z$ which acts as an external staggered Zeeman field. This term does not depend on the interaction and enters the definition of the non-interacting Hamiltonian. The magnetization is obtained as :

$$m = -\left.\frac{\partial \Omega}{L^3 \partial H_{\text{ext}}}\right|_{H_{\text{ext}}=0} \tag{IV.22}$$

By determining the grand potential for different values of the external field we are able to determine its derivative and obtain the magnetization at low temperatures and up to strong interactions. Depending on the data we use a first or second order polynomial fit at relatively small values of the field $H_{ext} \leq 0.2$. This method enables one to reach very high values of the interaction up to $U = 18$ as shown in Fig. IV.13.

However this approach is limited to the region where the magnetization is saturated and has almost reached its zero temperature value. As the temperature is increased, the significant changes in the grand potential happen at small fields. Moreover the series at small external fields become harder to resum and the error on the grand potential becomes larger. These two elements are consistent with the fact that the values at smaller fields are more dependent on the magnetic fluctuations when approaching the Néel transition. Therefore this approach is unable to access the regime where the magnetization changes significantly with the temperature.

We display the magnetization at low temperature $T = 0.1$ and $T = 0.2$ as a function of the interaction. When available the direct computations of the magnetization at $U \leq 7$ coincide with the value derived from differentiating the grand potential. As for the double occupancy, for $U \geq 7$ we see no difference between the values of the magnetization at the

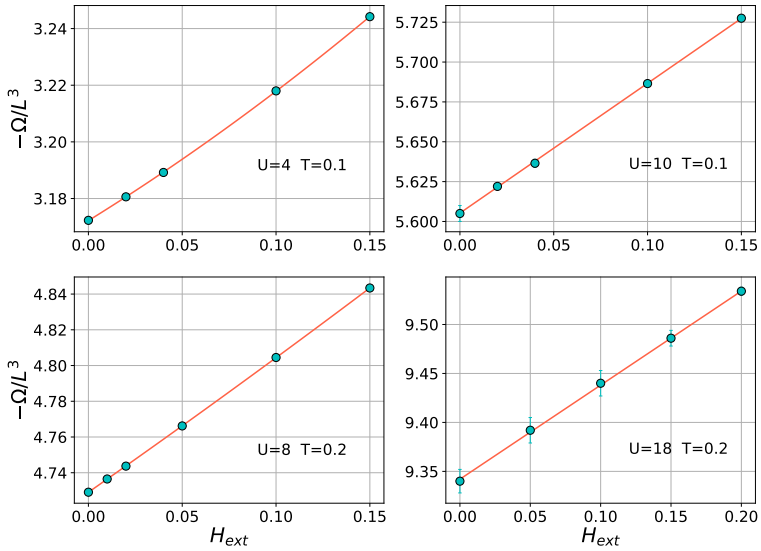

Figure IV.13: Grand potential density $-\Omega/L^3$ as a function of the external staggered field H_{ext} for different values of the temperature and interaction parameters. The orange line corresponds to the best fit by a second (first) order polynomial on the top and bottom left (right) panels

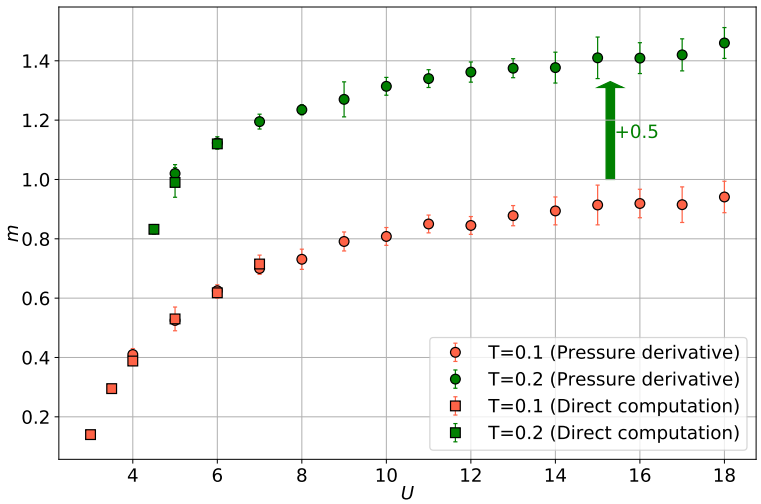

Figure IV.14: Magnetization as a function of the interaction U for two different values of the temperature. For better visibility the magnetization at $T = 0.2$ is shifted by $+0.5$. The square markers are obtained through direct computation of the order parameter. The round markers are obtained by numerically differentiating the grand potential density at an external field $H_{\text{ext}} \to 0$.

two temperatures. This means that we have reached the regime where the magnetization is saturated to its zero temperature value. The magnetization becomes very close to its maximum value which is close to 1 for $U \geq 14$. As these computations are done at finite temperature we would expect the magnetization to show a maximum with the interaction before decreasing towards zero as we exit the antiferromagnetic phase on the high interaction part of the Néel dome. This must therefore happen at $U > 18$.

IV.5 The attractive Hubbard model

The study of antiferromagnetism with the symmetry-broken CDet algorithm is an example of its reliable application to a specific ordered system. This technique is general for any symmetry-broken system, provided that we know the symmetries and the order parameter involved. In this section we study an other application of our method to the Hubbard model on a cubic lattice, but with negative interaction $U < 0$. The attractive interaction gives rise to forming pair of electrons with opposite spins, and at low temperature leads to a superconducting state with long-range order in the s-wave pairing channel.

The study presented in this Section is detailed in the article (preprint) [128] which is reproduced in Appendix J.

IV.5.1 Superconductivity and correspondence to the repulsive model

The repulsive Hubbard model :

The half-filled Hubbard model on a bipartite cubic lattice shows a correspondence between the attractive and repulsive models which is detailed in Appendix E. As the interaction U changes sign the Néel order is transformed in an s-wave superconducting phase described by the order parameter $\langle \hat{\mathcal{O}} \rangle = \langle \hat{c}_{i\uparrow} \hat{c}_{i\downarrow} \rangle$. Moreover shifting the chemical potential in the model at $U < 0$ and doping the system away from half-filling keeps the equivalence to the repulsive model at half-filling with an additional external Zeeman field. And vice versa : adding a Zeeman field to the attractive Hubbard Hamiltonian corresponds to doping the repulsive model.

Replacing the superconducting order by an antiferromagnetic one, both models at half-filling are equivalent and have the same physical properties. In the attractive system, as for the repulsive model, the superconducting phase can be described by two different regimes which are the analogous of the Slater and Heisenberg mechanisms. At small interaction the phase transition happens because of a gain in potential energy and gives a BCS-like superconductor where the critical temperature is linked to the value of the gap and rises as the interaction is increased. At high values of the interaction the transition goes to a Bose-Einstein Condensate regime, the transition is caused by a gain in kinetic energy and the critical temperature is essentially determined by the superconducting stiffness which decreases as the interaction is increased. In the middle of these two regimes the crossover from the BCS to BEC regime has been extensively documented with DMFT like approaches at different temperatures and fillings [11, 28, 35, 135].

Entering the superconducting phase :

In order to describe the superconducting phase of the attractive Hubbard model, the symmetry-broken CDet approach needs to be adapted to this new ordering. We define the perturbative expansion with the Hamiltonian, away from half-filling ($\mu \neq U/2$) and in the presence of an external and uniform Zeeman field h :

$$\begin{aligned}\mathcal{H}[U] = &-t \sum_{\langle i,j \rangle} \sum_{\sigma} \hat{c}^{\dagger}_{i\sigma} \hat{c}_{j\sigma} \sum_{i} + U \sum_{i} \hat{n}_{i\uparrow} \hat{n}_{i\downarrow} - \sum_{i\sigma} (\mu - U \langle n_{\bar{\sigma}} \rangle_{H_0})(\hat{n}_{i\sigma}) \\ &+ h \sum_{i} \hat{S}^{z}_{i} + \Delta_0 \sum_{i} (\hat{c}^{\dagger}_{i\uparrow} \hat{c}^{\dagger}_{i\downarrow} + \ h.c.) \ - \Delta_0 \frac{U}{U_{\phi}} \sum_{i} (\hat{c}^{\dagger}_{i\uparrow} \hat{c}^{\dagger}_{i\downarrow} + \ h.c.) \ ) \\ &= \mathcal{H}_0 + U \mathcal{H}_{exp}\end{aligned} \tag{IV.23}$$

Where *h.c.* stands for hermitian conjugate, $\mathcal{H}_0 = \mathcal{H}(U = 0)$ is the non-interacting Hamiltonian, and $\mathcal{H}_{exp}$ the expansion one which comes with a linear term in interaction U in the definition of $\mathcal{H}$. The linear shift to the chemical potential $\mu - U\langle n_{\bar{\sigma}} \rangle_{H_0}$ corresponds to the one which cancels the Hartree self-insertions in the diagrammatic expansion, and cancels the diagonal coefficients of the matrix used in the CDet recursion. The pairing field Δ_0 is breaking the symmetry associated with the superconducting phase and enables one to enter the phase perturbatively. By analogy to the repulsive study, we can choose : $\Delta_0 = \alpha \Delta_{MF} = -\alpha U_{\phi} \langle \hat{\mathcal{O}} \rangle_{\mathcal{H}_0}$. For $\alpha = 1$ the non-interacting system therefore corresponds to the mean-field BCS solution of the model. We perform an expansion in U going from 0 to U_{ϕ} at which the pairing term vanishes in $\mathcal{H}$ and we get back to the Hubbard Hamiltonian. U_{ϕ} is the targeted value of U which is negative in the attractive case.

The pairing term is part of the expansion Hamiltonian and it therefore impacts the diagrammatic expansion. It is quadratic and acts as an external field which links two propagators. On the contrary to the antiferromagnetic case, the pairing term does not conserve the number of particles and one needs to include anomalous propagators in the construction of the perturbative expansion. In the diagrammatic expansion these propagators correspond to lines which create or destroy a particle at both ends. The bare propagator is now expressed in terms of the four components :

$$\begin{aligned}\mathcal{G}^{00}_{0,ij}(\tau_j - \tau_i) &= -\langle \mathcal{T} \hat{c}^{\dagger}_{j\uparrow}(\tau_j) \hat{c}_{i\uparrow}(\tau_i) \rangle \\ \mathcal{G}^{11}_{0,ij}(\tau_j - \tau_i) &= -\langle \mathcal{T} \hat{c}_{j\downarrow}(\tau_j) \hat{c}^{\dagger}_{i\downarrow}(\tau_i) \rangle \\ \mathcal{G}^{10}_{0,ij}(\tau_j - \tau_i) &= -\langle \mathcal{T} \hat{c}_{j\downarrow}(\tau_j) \hat{c}_{i\uparrow}(\tau_i) \rangle \\ \mathcal{G}^{01}_{0,ij}(\tau_j - \tau_i) &= -\langle \mathcal{T} \hat{c}^{\dagger}_{j\uparrow}(\tau_j) \hat{c}^{\dagger}_{i\uparrow}(\tau_i) \rangle\end{aligned} \tag{IV.24}$$

This leads to a matrix for the CDet recursion of size $(2n+1) \times (2n+1)$ at order n for the computation of Green's function $\mathcal{G}^{a_{out} a_{in}}_{i_{in} i_{out}}(\tau_{out} - \tau_{in})$, which is expressed as follow :

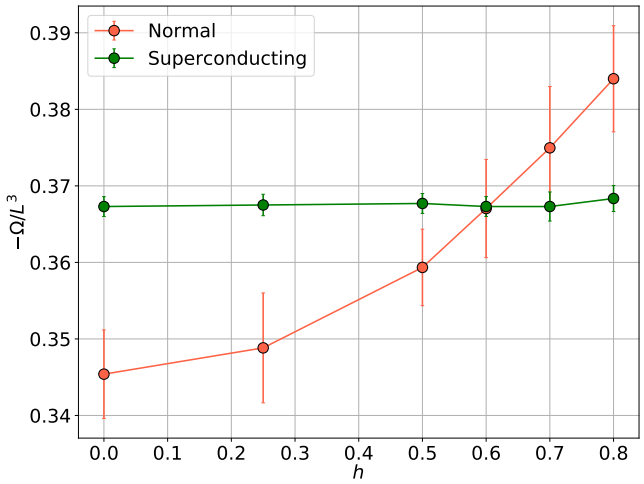

Figure IV.15: Grand potential density as a function of the uniform Zeeman field at $T = 0.0625$. The orange Normal data is obtained from expanding the grand potential in the normal phase with $\alpha = 0$. The green data is obtained with symmetry-broken mean-field expansion series $\alpha = 1$. We acknowledge G. Spada and F. Werner for producing and treating for resummation the data presented here.

$$D'_{n,\sigma} = \begin{bmatrix} 0 & \delta & \dots & \mathcal{G}^{00}_{0,i_1 i_n}(\tau_1 - \tau_n) & \mathcal{G}^{01}_{0,i_1 i_n}(\tau_1 - \tau_n) & \mathcal{G}^{0a_{in}}_{0 i_{in} i_1}(\tau_1 - \tau_{in}) \\ \delta & 0 & \dots & \mathcal{G}^{10}_{0,i_1 i_n}(\tau_1 - \tau_n) & \mathcal{G}^{11}_{0,i_1 i_n}(\tau_1 - \tau_n) & \mathcal{G}^{1a_{in}}_{0 i_{in} i_1}(\tau_1 - \tau_{in}) \\ \vdots & \vdots & \ddots & \vdots & \vdots & \vdots \\ \mathcal{G}^{00}_{0,i_n i_1}(\tau_n - \tau_1) & \mathcal{G}^{01}_{0,i_n i_1}(\tau_n - \tau_1) & \dots & 0 & \delta & \mathcal{G}^{0a_{in}}_{0,i_{in} i_n}(\tau_n - \tau_{in}) \\ \mathcal{G}^{10}_{0,i_n i_1}(\tau_n - \tau_1) & \mathcal{G}^{11}_{0,i_n i_1}(\tau_n - \tau_1) & \dots & \delta & 0 & \mathcal{G}^{1a_{in}}_{0,i_{in} i_n}(\tau_n - \tau_{in}) \\ \mathcal{G}^{a_{out}0}_{0,i_{out} i_1}(\tau_{out} - \tau_1) & \mathcal{G}^{a_{out}1}_{0,i_{out} i_1}(\tau_{out} - \tau_1) & \dots & \mathcal{G}^{a_{out}0}_{0,i_{out} i_n}(\tau_{out} - \tau_n) & \mathcal{G}^{a_{out}1}_{0,i_{out} i_n}(\tau_{out} - \tau_n) & \mathcal{G}^{a_{out}a_{in}}_{0,i_{out} i_{in}}(\tau_{out} - \tau_{in}) \end{bmatrix} \tag{IV.25}$$

Where the chemical potential shift leads to the cancellation of diagonal terms. $\delta = \langle \hat{\mathcal{O}} \rangle_{\mathcal{H}_0}(1 - \alpha)$ and vanishes for $\alpha = 1$. This bigger matrix does not change the overall complexity of the algorithm since the complexity due to the calculation of determinants is dominated by the recursion.

In the end, the obtained perturbative series have the same behaviour that we displayed for computations in the repulsive model and we can apply a similar resummation procedure to get controlled results inside and out of the superconducting phase. The order parameter can be resummed accurately at low temperatures to non-zero values, showing that we enter perturbatively the superconducting phase of the attractive Hubbard Hamiltonian on a cubic lattice.

IV.5.2 Superconductivity and depairing magnetic field

The perturbative expansion Eq. IV.23 enables us to study the superconducting phase in the presence of a Zeeman field. By favoring one spin flavor over the other one, the Zeeman field enters in competitions with the Cooper s-wave pairing of electrons which forms pairs of opposite spins fermions. For a big enough field, the gain in energy of the polarized state compensates the gain due to the pairing gap of the superconducting phase. We therefore expect a critical field h_c such that for $h \geq h_c$ the superconductivity is suppressed. The magnetization $m = \langle \hat{S}_i^z \rangle$ and superconducting gap are discontinuous at the critical field, hence a first order phase transition between the normal polarized state and the superconducting phase.

We show in Fig. IV.15 the grand potential obtained from the normal and symmetry-broken CDet algorithms as a function of the external Zeeman field. The results are obtained at a value of the interaction $U_\phi = -5$ and fixing the chemical potential in Eq. IV.23 to $\mu = -3.38$. The temperature is fixed to 0.0625 which is in the superconducting phase at $h = 0$ and around $T_c/4$. Since the system is not at half-filling any more, the density is not fixed but varies along the perturbation path, and depends on the parameters of the Hamiltonian. For this starting chemical potential at $U = 0$ and this value of the physical interaction, the density turns out to be close to $\langle \hat{n}_{i\uparrow} + \hat{n}_{i\downarrow} \rangle \simeq 0.5$, and is almost independent on the value of the magnetic field at small temperatures. Since Ω is the thermodynamic potential of the system in the grand canonical ensemble, the thermodynamic solution of the model has to maximize the value of $-\Omega/L^3$. We see that we obtain different resummed solutions depending on the used perturbative expansion with or without a symmetry-breaking field. For $h < h_c \simeq 0.6$ the thermodynamic solution is given by the symmetry-broken expansion and we are in the superconducting phase. In this phase the value of the grand potential is almost independent on the field which means that the magnetization is close to zero. For $h > h_c$ the thermodynamic solution is obtained via the normal state expansion. The variations of this curve with the field indicate a non-zero magnetization. The crossing of the two solutions indicates a discontinuity at $h = h_c$ of the first derivative of the grand potential, hence a first order phase transition. The fact that we are able to resum normal expansions in a regime where the system is ordered in a superconducting state, and that we obtain a different solution from the symmetry-broken expansion at $h > h_c$ could be due to the existence of metastable solutions in a first order phase transition. This still remains to be fully understood to state if our method can describe metastable states or if we are missing important contributions at high perturbative orders.

IV.6 Conclusion and perspectives on the symmetry-broken CDet algorithm

We have shown in this chapter that the symmetry-broken CDet algorithm is a powerful tool for studying in a controlled and accurate way ordered systems, directly in the thermodynamic limit. Our approach to the antiferromagnetic and s-wave superconductivity can be generalized to any symmetry-broken phase provided that its symmetry and order parameter are known before hand. When adding a Zeeman field, the superconducting state

shows a first order phase transition around which the properties of the symmetry-broken and normal expansion series still remain to be understood in details.

In the half-filled repulsive Hubbard model we have documented the critical regime in the weak to intermediate coupling regimes and have documented the Slater mechanism at the phase transition. Due to increasingly hard resummation, our approach remains limited in the critical region at strong coupling. At low temperature though we have been able to reach very strong couplings ($U = 18$). However this is not enough to document a crossover to a Heisenberg regime. Deep inside the dome the double occupancy does not show any feature of a crossover happening and the transition seems to be smooth from the Slater to Heisenberg regions. The implementation of the recent new Renormalized CDet algorithm [61, 116] could yield expansion series with a faster convergence with respect to the expansion order, and easier resummations, by enabling a symmetry-broken chemical potential shift with a staggered magnetic field varying as a polynomial in the expansion parameter U. Considering the cubic model, a rich physics happens at finite doping away from half-filling and the antiferromagnetic order is gradually suppressed as the doping increases. At low temperatures it even transforms to incommensurate spin density wave ordering as it was studied e.g. in $D\Gamma A$ [122]. The Néel temperature goes to zero at fixed interaction when increasing the doping, and the magnetic order finishes as a phase transition at $T = 0$ in a quantum critical point whose physics still remains to be determined numerically. In the doped regime the chemical potential has no predetermined value and the density varies on the expansion path. This issue could be overcome by making use of the newly developed double-expansion CDet algorithm [64] which enables one to fix the density along the perturbative path, at the expense of a slightly worse computational complexity.

One of the next objectives would be to tackle the two dimensional model on a square lattice whose properties in the doped regimes at low temperatures are still debated and which has been extensively studied by many different methods in the past years [79, 123]. Even if the Mermin-Wagner theorem prevents any spontaneous breaking of a continuous symmetry in two dimensions, the low temperature regime is characterized by very long correlation lengths and many different competing orders such as charge density orders, and d-wave superconductivity. The symmetry-broken expansion could prove useful for studying these regimes with long-distance correlations as done in [80]. However the perturbative series obtained with symmetry-broken diagrammatic expansions have been observed to show slow convergence and obtaining controlled results in these regimes remains very challenging.

Chapter V

NCA solver for out-of-equilibrium systems

Contents

In the previous chapters, we have focused on developing a new method for understanding strongly-correlated systems at equilibrium. In this chapter we rely on a different approach to study interacting systems in the presence of a time-dependent perturbation driving the system out of equilibrium.

The richness of the physics of strongly correlated materials gives rise to many interesting phenomena when submitting them to external perturbations. One example is the the recently observed metal-to-insulator transition in $Ca2RuO4$ induced by an electric field [94, 96, 120]. Even if recently the impact of local heating has been pointed out in these experiments [86], it has been suspected that small electrical fields can provoke a structural transition of the crystal, leading to a radical change in the resistance of the material [1, 42].

Describing theoretically these phenomena is challenging and the associated numerical methods can become extremely heavy when considering the many different orbitals at play, and the different components of correlators in the out-of-equilibrium formalism. In this chapter we rely on the DMFT approximation which can be generalized to out-of-equilibrium systems [5,6,82,85,102]. We therefore focus on developing an impurity solver in the real-time Keldysh formalism. We introduce a strong coupling expansion called the NCA (Non-Crossing-Approximation) which sums analytically an infinite number of terms in the hybridization diagrammatic expansion. It provides a simple and light numerical impurity solver for out-of-equilibrium systems.

In this chapter we introduce the out-of-equilibrium formalism for strongly-correlated systems and the NCA approximation. We implement an impurity solver in the steady-state limit and apply it to the Kondo resonance of the Anderson impurity model. In general this approximation is formulated directly on the Green's function of the impurity [16, 31]. This chapter enables us to introduce a different approach for the out-of-equilibrium many-body problem and the NCA approximation in terms of the local propagator R [91, 100, 119].

The NCA approximation is well known and has been extensively used to tackle impurity problems in the past three decades. This approach is not new, but in its general formulation it struggles for providing relying results for out-of-equilibrium systems and in multi-orbital models for strongly correlated materials. We provide in this chapter a novel algorithm for solving efficiently the NCA equations, by alternating between the time and frequency domain.

V.1 NCA equations

To introduces the NCA impurity solver, we consider an impurity described by a local Hamiltonian $\hat{\mathcal{H}}_{loc}$ which exchanges electrons with a bath at equilibrium temperature $\beta = 1/T$ and Hamiltonian $\hat{\mathcal{H}}_{bath}$ through a hybridization function Δ.

We recall the expressions of the hybridization functions Δ which characterize the bath. In the general case with $\hat{d}_i$ operators acting on the impurity (the i index stands for local sites or spin degrees of freedom) and $\hat{c}_k$ operators on the bath :

$$\begin{aligned}\hat{\mathcal{H}} = &\ \hat{\mathcal{H}}_{loc} + \hat{\mathcal{H}}_{hyb} + \hat{\mathcal{H}}_{bath} \\ = &\ \hat{\mathcal{H}}_{loc} + \sum_{\mathbf{k},i} \gamma_{\mathbf{k},i}(\hat{c}^\dagger_{\mathbf{k}}\hat{d}_i + h.c) + \sum_{\mathbf{k}} \epsilon_{\mathbf{k}}\hat{c}^\dagger_{\mathbf{k}}\hat{c}_{\mathbf{k}}\end{aligned} \tag{V.1}$$

Since the bath is considered to be at equilibrium we can write the hybridization function in Matsubara frequencies as follow :

$$\Delta_{ij}(i\omega_n) = \sum_{\mathbf{k}} \frac{\gamma_{i\mathbf{k}}\gamma_{\mathbf{k}j}}{i\omega_n - \epsilon_{\mathbf{k}}} \tag{V.2}$$

Δ has the standard properties of Green's functions and has a spectral representation :

$$\Delta_{ij}(i\omega_n) = \int \frac{A_{\Delta_{ij}}(\epsilon)}{i\omega_n - \epsilon} \mathrm{d}\epsilon \tag{V.3}$$

V.1.1 NCA at equilibrium

The local states propagator :

We introduce the local propagator and NCA equations in imaginary-time for an impurity at equilibrium, before generalizing it to out-of-equilibrium systems. After tracing over the bath degrees of freedom with $Z_{\mathrm{bath}} = \mathrm{Tr}_{\mathrm{bath}}[e^{-\beta\hat{\mathcal{H}}_{\mathrm{bath}}}]$, the impurity local state propagator reads :

$$R(\tau) = -\frac{1}{Z_{\mathrm{bath}}}\mathrm{Tr}_{\mathrm{bath}}[e^{-(\beta-\tau)\hat{\mathcal{H}}_{\mathrm{bath}}}e^{-\tau(\hat{\mathcal{H}}_{\mathrm{loc}}+\hat{\mathcal{H}}_{\mathrm{hyb}}+\hat{\mathcal{H}}_{\mathrm{bath}})}] \tag{V.4}$$

R is an operator that acts on the local impurity Hilbert space and it has a $2^N \times 2^N$ matrix representation with N the number of states in the impurity. From the definition we see that R is linked to the local density matrix ρ_{loc} and has the following properties for describing the system :

$$\begin{aligned}R(\beta) &= -\frac{1}{Z_{\mathrm{bath}}}\mathrm{Tr}_{\mathrm{bath}}[e^{-\beta\hat{\mathcal{H}}}] \\ \rho_{\mathrm{loc}} &= -\frac{Z_{\mathrm{bath}}}{Z}R(\beta) \\ Z &= -Z_{\mathrm{bath}}\mathrm{Tr}_{\mathrm{loc}}(R(\beta))\end{aligned} \tag{V.5}$$

And for any observable O, it expectation value is given by :

$$O(\beta) = -\frac{Z_{\mathrm{bath}}}{Z}\mathrm{Tr}_{\mathrm{loc}}[R(\beta)\hat{O}] \tag{V.6}$$

In the absence of hybridization we find the propagator for an isolated system :

$$R_0(\tau) = -e^{-\tau\mathcal{H}_{\mathrm{loc}}} \tag{V.7}$$

Hybridization expansion :

We want to expand the local state propagator in the hybridization function as we did in Chapter II. R can be written in terms of an imaginary time path-integral representation :

$$R(\tau) = -T_\tau \exp(-\tau \mathcal{H}_{\rm loc} - \int_0^\tau \mathrm{d}\tau_1 \sum_{ij} \mathrm{d}_i\tau_2 \Delta_{ij}(\tau_1 - \tau_2) d_j^\dagger(\tau_1) d(\tau_2)) \tag{V.8}$$

Expanding the time-ordered exponential we obtain the hybridization perturbative expansion of the local propagator :

$$\begin{aligned} R(\tau) = \sum_{n\geq 0} \frac{(-1)^n}{n!} \int_0^\tau \mathrm{d}\tau_1 \mathrm{d}\tau_1' ... \mathrm{d}\tau_n \mathrm{d}\tau_n' \sum_{a_i b_i} (\prod_{i=1}^n \Delta_{a_i b_i}(\tau_i - \tau_i')) \\ \times T_\tau (R_0(\tau) \prod_{j=1}^n (d_{a_j}^\dagger(\tau_j) d_{b_j}(\tau_j'))) \end{aligned} \tag{V.9}$$

From this equation we can deduce the diagrammatic rules for expanding R in the hybridization function. The diagrammatic expansion of R is made of vertices with local coordinates (a, τ), bare lines linking two vertices at different imaginary-time and contributing as $R_0(\tau - \tau')$, and hybridization dashed lines between vertices of coordinates (a, τ) and (b, τ') which contribute as $\Delta_{ab}(\tau - \tau') d_a^\dagger(\tau) d_b(\tau')$. The expansion coefficient of order n is the diagram with n hybridization lines summed over all internal vertices coordinates, with time-ordering the d operators according to their imaginary-time arguments multiplied by $(-1)^{s+f}$ with s the number of crossings of hybridization lines, and f the number of back lines going backward in time.

For instance the first order expansion term is written with two vertices and one hybridization line (omitting the internal vertices coordinates) :

(0) 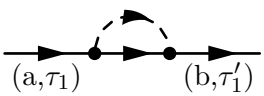

$(\tau) = \sum_{a,b} \int_0^\tau \mathrm{d}\tau_1 \mathrm{d}\tau_1' \Delta_{ab}(\tau_1' - \tau_1) R_0(\tau_1) d_a^\dagger(\tau_1) R_0(\tau_1' - \tau_1) d_b(\tau_1') R_0(\tau - \tau_1')$ (V.10)

From this diagrammatic expansion we see that R obeys a Dyson-like equation with S the associated self-energy which is the sum of all one-particle irreducible diagrams. It writes :

$$R(\tau) = R_0(\tau) + \int_0^\tau \mathrm{d}\tau' \mathrm{d}\bar{\tau} R_0(\tau - \tau') S(\tau - \bar{\tau}) R(\tau') \tag{V.11}$$

After differentiating with respect to τ we obtain an integro-differential Volterra equation :

$$-\partial_\tau R(\tau) = \mathcal{H}_{loc} R(\tau) + \int_0^\tau \mathrm{d}\tau' S(\tau - \tau') R(\tau') \tag{V.12}$$

With initial condition $R(\tau = 0) = R_0(\tau = 0) = -\mathbb{1}$

Fourier representation :

Since we define these functions for $\tau \in [0, \beta]$ it can be extended to $\tau \in \mathbb{R}$ to use the usual transformations on functions. For example it could be periodicized to be represented by a Fourier series in Matsubara frequencies. R and S can also be defined by the Volterra equation for $\tau > 0$ and taken equal to 0 for $\tau \leq 0$. The Volterra equation then becomes :

$$-\partial_\tau R(\tau) = \delta(\tau) + \mathcal{H}_{loc} R(\tau) + \int_\infty^{+\infty} d\tau' S(\tau - \tau') R(\tau') \tag{V.13}$$

And assuming that we can perform the Fourier transform of R and S through :

$$R(i\omega) = \int_0^\infty \mathrm{d}\tau R(\tau) e^{i\omega\tau} \tag{V.14}$$

The Volterra equation becomes :

$$R(i\omega) = [i\omega - \mathcal{H}_{loc} - S(i\omega)]^{-1} \tag{V.15}$$

We supposed here that is is possible to perform a Fourier transform on the $R(\tau)$ function, which according to Eq.V.4 is only possible if the spectrum of the Hamiltonian $\hat{\mathcal{H}}_{\mathrm{loc}} + \hat{\mathcal{H}}_{\mathrm{hyb}}$ is positive. Supposing that it is bounded at low energies, this condition can be fulfilled by switching the overall Hamiltonian by an energy constant.

NCA approximation :

In the Non-Crossing Approximation we consider the sum of diagrams without any crossing of hybridization lines and omit the other diagrams. In this approximation the self-energy S is the sum of two diagrams with a single hybridization line : the one of Eq. V.10 and the same one with inverting the orientation of the hybridization line. The self-energy can be written as :

$$S(\tau) = -\sum_{ab} [d_a^\dagger R(\tau) d_b \Delta_{ab}(\tau) - d_a R(\tau) d_b^\dagger \Delta_{ba}(-\tau)] \tag{V.16}$$

By summing explicitly a class of diagrams, the NCA approximation leads to a closed system of two equations which can be solved self-consistently and provides an easy solver

for impurity problems. However the approximation is uncontrolled and will yield better results in the high interaction limit where the weight of high-order hybridization diagrams can be neglected.

In this approximation, the Green's functions can then be expressed through :

$$\begin{aligned} G_{ab}(\tau) &= -\frac{1}{Z}\mathrm{Tr}[e^{-(\beta-\tau)\mathcal{H}}d_a e^{-\tau\mathcal{H}}d_b^\dagger] \\ &= -\frac{Z_{\mathrm{bath}}}{Z}\mathrm{Tr}_{\mathrm{loc}}[R(\beta-\tau)d_a R(\tau)d_b^\dagger] \\ &= \frac{\mathrm{Tr}_{\mathrm{loc}}[R(\beta-\tau)d_a R(\tau)d_b^\dagger]}{\mathrm{Tr}_{\mathrm{loc}}[R(\beta)]} \end{aligned} \tag{V.17}$$

Which is only valid in the NCA approximation since we ignored the crossing with external bath lines to perform the trace over the bath degrees of freedom.

V.1.2 Out-of-equilibrium formalism

In the following, we aim at studying a system out-of-equilibrium. The local Hamiltonian can evolve either as a quench at $t = 0$ and be time-independent for $t > 0$, or evolve with time $\hat{\mathcal{H}}_{\mathrm{loc}} = \hat{\mathcal{H}}_{\mathrm{loc}}(t)$. The initial state is defined by the density matrix :

$$\rho(t=0) = \frac{e^{-\beta\mathcal{H}_{\mathrm{bath}}}}{Z_{\mathrm{bath}}}\rho_{\mathrm{loc}}(t=0) \tag{V.18}$$

Where $\rho_{\mathrm{loc}}(t=0) = \mathbb{1}/Z_{\mathrm{loc}}$ is the local density matrix.

The triple contour :

We start by introducing the formalism that we use for the many-body problem out-of-equilibrium. For a complete introduction to non-equilibrium physics in quantum systems see [130].

In the condition of a time-dependent Hamiltonian, the expected value of an operator $\hat{O}$ is expressed as :

$$O(z) = \frac{\mathrm{Tr}[\bar{\mathcal{T}}e^{-i\int_{\bar{\mathcal{C}}}\mathrm{d}\bar{z}\hat{\mathcal{H}}(\bar{z})}\hat{O}(z)]}{\mathrm{Tr}[\bar{\mathcal{T}}e^{-i\int_{\bar{\mathcal{C}}}\mathrm{d}\bar{z}\hat{\mathcal{H}}(\bar{z})}]} \tag{V.19}$$

With $\bar{\mathcal{C}}$ the Baym-Kadanoff contour shown in Fig. V.1, z a point of this contour and $\bar{\mathcal{T}}$ the time-ordering operator along this contour. The contour is oriented such that $\bar{\mathcal{T}}$ is the time-ordering operator on the $\mathcal{C}_+$ and $\mathcal{C}_T$, the anti-time ordering operator on the $\mathcal{C}_-$ axis. The time axis carry the properties of out-of-equilibrium time-evolution, while the imaginary-time axis enables one to start at $t = 0$ from a correlated many-body state at

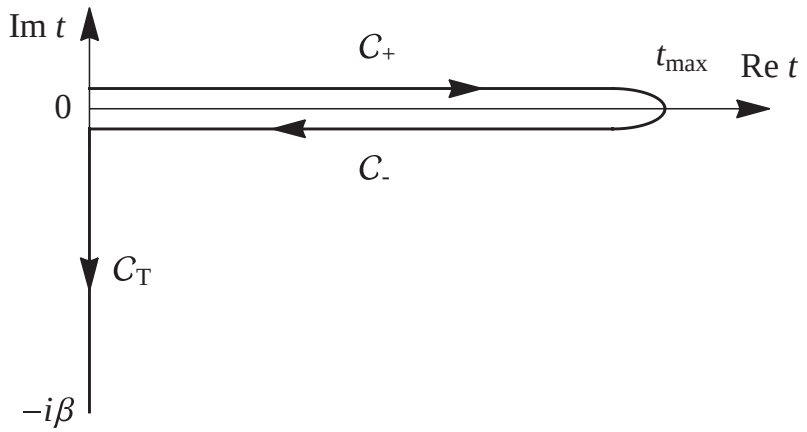

Figure V.1: Oriented Baym-Kadanoff contour used for out-of-equilibrium time-evolution. The time-coordinate evolves from 0 to t_{max} on the $\mathcal{C}_+$ axis, from t_{max} to 0 on the $\mathcal{C}_-$ axis, and on $\mathcal{C}_T$ as an imaginary-time which final point $-i\beta$ coincides with the origin of $\mathcal{C}_+$.

temperature β. A point z of this contour is therefore expressed as $z = (t, +)$ or $z = (t, -)$ depending on the real-time axis, and $z = -i\tau$ on the imaginary-time axis.

The local state propagator R function is now defined on the full Baym-Kadanoff contour by the expression :

$$R(z, z') = -i\mathrm{Tr}_{\mathrm{bath}}[\frac{e^{-\beta\mathcal{H}_{\mathrm{bath}}}}{Z_{\mathrm{bath}}}\bar{\mathcal{T}}\exp(-i\int_{\bar{\mathcal{C}}}\mathcal{H}_{\mathrm{bath}} - i\int_{z'}^{z}\mathcal{H}_{\mathrm{loc}} + \mathcal{H}_{\mathrm{hyb}})] \tag{V.20}$$

Which leads after tracing the bath out in the path integral formulation :

$$R(z, z') = -i\bar{\mathcal{T}}\exp(-i\int_{z'}^{z}\mathcal{H}_{\mathrm{loc}}(z_1)\mathrm{d}z_1 - i\int_{z'}^{z}\mathrm{d}z_1\mathrm{d}z_2\Delta(z_1, z_2)d^\dagger(z_1)d(z_2)) \tag{V.21}$$

The local propagator, as well as the impurity Green's function are function of two time variables and are now expressed in terms of nine components depending on the axis these variables belong to. We note R as a 3×3 matrix :

$$R(z, z') = \begin{pmatrix} R^{++}(t, t') & R^{<}(t, t') & R^{\rceil}(t, \tau') \\ R^{>}(t, t') & R^{--}(t, t') & R^{\rceil}(t, \tau') \\ R^{\lceil}(\tau, t') & R^{\lceil}(\tau, t') & iR^{M}(\tau, -\tau') \end{pmatrix} \tag{V.22}$$

Where the last component corresponds to the equilibrium propagator defined in Eq.V.4 : $R(-i\tau, -i\tau') = iR^M(\tau - \tau')$. These nine components are not independent and they obey the following relations :

$$\begin{aligned} R^{++}(t,t') &= \theta(t-t')R^{>}(t,t') + \theta(t'-t)R^{<}(t,t') \\ R^{--}(t,t') &= \theta(t-t')R^{<}(t,t') + \theta(t'-t)R^{>}(t,t') \\ R^{\rceil}(t,\tau) &= -R^{\lceil}(\beta-\tau,t) \end{aligned} \tag{V.23}$$

With θ the Heaviside function. In the end only four components of the local propagator are independent. Additionally the following symmetry relation holds :

$$R^{>(<)}(t,t')^{\dagger} = -R^{>(<)}(t',t) \tag{V.24}$$

For an isolated impurity in the absence of hybridization the bare propagator writes :

$$R_0(z,z') = -i\bar{\mathcal{T}}e^{-i\int_{z'}^{z}\hat{\mathcal{H}}_{\mathrm{loc}}(z_1)\mathrm{d}z_1} \tag{V.25}$$

And the partition function is given by :

$$Z_{\mathrm{loc}} = i\mathrm{Tr}_{\mathrm{loc}}[R^{<}(t,t)] = -\mathrm{Tr}_{\mathrm{loc}}[R^{M}(\beta)] \tag{V.26}$$

NCA approximation :

By analogy with the equilibrium case, the same diagrammatic can be defined with hybridization lines ending on points of the triple contour. It leads to a Dyson-like equation which can be written as a Volterra integro-differential equation :

$$i\partial_z R(z,z') = \mathcal{H}_{loc}R(z,z') + \int_{z'}^{z}\mathrm{d}z_1 S(z,z_1)R(z_1,z') \tag{V.27}$$

Performing the NCA approximation we obtain an analytic expression for the self-energy :

$$S(z,z') = iT(z,z')\sum_{ab}[d_a^{\dagger}R(z,z')d_b\Delta_{ab}(z,z') - d_aR(z,z')d_b^{\dagger}\Delta_{ba}(z',z)] \tag{V.28}$$

With $T(z,z') = 1$ if $z > z'$ and -1 otherwise. The Volterra and NCA equations can be solved together using a time discretization scheme for each components of R and S and relying on their symmetries [91].

In the NCA approximation, each component of the the Green's functions on the triple contour can be obtained through :

$$G_{ab}(z,z') = \frac{i}{Z_{\mathrm{loc}}}T(z,z')\mathrm{Tr}_{\mathrm{loc}}[R(z',z)d_aR(z,z')d_b^{\dagger}] \tag{V.29}$$

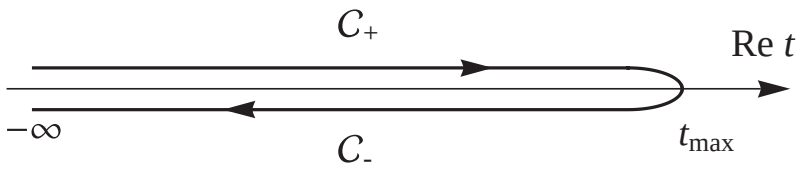

Figure V.2: Oriented Keldysh contour $\mathcal{C}$ used for steady-state NCA solving. The time-coordinate evolves from $-\infty$ to t_{max} on the $\mathcal{C}_+$ axis, from t_{max} to $-\infty$ on the $\mathcal{C}_-$ axis.

V.1.3 Steady-state NCA equations

Keldysh contour :

The out-of-equilibrium equations enable us to compute the time-evolution of the system and describe its transient behaviour before it reaches long-time limit. In this part we suppose that the system reaches a steady-state after a long time evolution and we aim at describing this limit. We first simplify the out-of-equilibrium formalism described before by restricting ourselves to the double contour $\mathcal{C}$ of the Keldysh formalism by dropping the imaginary-time axis (Fig. V.2). Without the third branch of the contour we can't describe a correlated state at $t = 0$, but we suppose that the information on the initial state is lost in the long-time regimes.

Recalling that the evolution operator writes $U(t,t') = e^{-i\int_t^{t'} \mathcal{H}(t_1)\mathrm{d}t_1}$ we can remove the time-ordering and write the local propagator as :

$$\begin{aligned} R(z,z') &= -i\mathrm{Tr}_{\mathrm{bath}}[\frac{e^{-\beta\mathcal{H}_{\mathrm{bath}}}}{Z_{\mathrm{bath}}} T_{\mathcal{C}} \exp(-i\int_{\mathcal{C}} \mathcal{H}_{\mathrm{bath}} - i\int_{z'}^{z} \mathcal{H}_{\mathrm{loc}} + \mathcal{H}_{\mathrm{hyb}})] \\ &= -i\mathrm{Tr}_{\mathrm{bath}}[\frac{e^{-\beta\mathcal{H}_{\mathrm{bath}}}}{Z_{\mathrm{bath}}} U_{\mathrm{bath}}(0^-,z)U(z,z')U_{\mathrm{bath}}(z',0^+)] \text{ if } z > z' \\ &= -i\mathrm{Tr}_{\mathrm{bath}}[U_{\mathrm{bath}}(z',z)U(z,0^+)\frac{e^{-\beta\mathcal{H}_{\mathrm{bath}}}}{Z_{\mathrm{bath}}} U_{\mathrm{bath}}(0^-,z')] \text{ if } z < z' \end{aligned} \tag{V.30}$$

Which depends on the relative position on the double-contour of the coordinates z and z'. The local propagator is now completely defined by its two independent components $R^>$ and $R^<$ which obey the symmetry relation $R^{>(<)}(t,t')^\dagger = -R^{>(<)}(t',t)$ (See Appendix F). It is to be noted that the hybridization function, Green's function, and self-energy S obey the same relation. We have for any observable on the local system :

$$O(t) = \mathrm{Tr}[\frac{e^{-\beta\hat{\mathcal{H}}_{\mathrm{bath}}}}{Z} U(0,t)\hat{O}U(t,0)] \tag{V.31}$$

Rearranging the order of the trace we get :

$$O(t) = i\mathrm{Tr}[\frac{Z_{\mathrm{bath}}}{Z} R^<(t,t)\hat{O}] \tag{V.32}$$

And we deduce :

$$\begin{aligned} Z_{\rm loc} &= i{\rm Tr}_{\rm loc}[R^<(t,t)] \\ \rho_{\rm loc}(t) &= i\frac{R^<(t,t)}{Z_{\rm loc}} \end{aligned} \tag{V.33}$$

Restricting the system to the double contour we get the Dyson like Volterra equation obtained from the diagrammatic expansion of R :

$$i\partial_z R(z,z') = \mathcal{H}_{\rm loc}R(z,z') + \int_{z'}^{z} {\rm d}z_1 S(z,z_1)R(z_1,z') \tag{V.34}$$

NCA equations :

Performing the NCA approximation as we did before but this time on the double-contour :

$$S(z,z') = iT(z,z')\sum_{ab}[d_a^\dagger R(z,z')d_b\Delta_{ab}(z,z') - d_aR(z,z')d_b^\dagger\Delta_{ba}(z',z)] \tag{V.35}$$

This leads to two systems of self-consistent equations for the greater and lesser components which have to be solved one after the other independently. On the double-contour the NCA equations become :

$$\begin{aligned} i\partial_t R^>(t,t') &= \mathcal{H}_{\rm loc}R^>(t,t') + \int_{t'}^{t} {\rm d}u S^>(t,u)R^>(u,t') \\ S^>(t,t') &= i\sum_{ab}[d_a^\dagger R^>(t,t')d_b\Delta_{ab}^>(t,t') - d_aR^>(t,t')d_b^\dagger\Delta_{ba}^<(t',t)] \end{aligned} \tag{V.36}$$

Where we have the initial condition $R^>(t,t) = -i\mathbb{1}$. This system of equations is independent of the lesser component functions and can be solved first. The solutions are then used to compute the lesser components which obey the equations :

$$\begin{aligned} i\partial_t R^<(t,t') &= \mathcal{H}_{\rm loc}R^<(t,t') - \int_0^{t'} {\rm d}u S^<(t,u)R^>(u,t') + \int_0^{t} {\rm d}u S^>(t,u)R^<(u,t') \\ S^<(t,t') &= -i\sum_{ab}[d_a^\dagger R^<(t,t')d_b\Delta_{ab}^<(t,t') - d_aR^<(t,t')d_b^\dagger\Delta_{ba}^>(t',t)] \end{aligned} \tag{V.37}$$

The equations for $R^>$ are non-linear given the multiplication between $R^>$ and $S^>$ in the self-energy equation, whereas the equation for $R^<$ is linear in $S^<$ and it is therefore defined up to a constant. It is fixed here by noticing that $R^<(0,0) = -i\rho_{loc}(t=0)Z_{loc} = -i\mathbb{1}$.

In this approximation the green's functions are obtained through :

$$\begin{aligned} G_{ab}(z,z') &= -i\mathrm{Tr}[\frac{e^{-\beta\mathcal{H}}}{Z}T_C e^{-i\int_C H(z)\mathrm{d}z} d_a(z) d_b^\dagger(z')] \\ &= \mathrm{Tr}_{\mathrm{loc}}[\frac{1}{Z_{\mathrm{loc}}}T_C R((0,-),(0,+)) d_a(z) d_b^\dagger(z')] \end{aligned} \tag{V.38}$$

It gives for the greater and lesser components :

$$\begin{aligned} G_{ab}^{>}(t,t') &= i\mathrm{Tr}_{\mathrm{loc}}[\frac{1}{Z_{\mathrm{loc}}}R^{<}(t',t) d_a R^{>}(t,t') d_b^\dagger] \\ G_{ab}^{<}(t,t') &= -i\mathrm{Tr}_{\mathrm{loc}}[\frac{1}{Z_{\mathrm{loc}}}R^{<}(t,t') d_a^\dagger R^{>}(t',t) d_b] \end{aligned} \tag{V.39}$$

Steady-state limit :

Supposing that the local Hamiltonian is time-independent, it is possible in the long-time limit to reach a steady-state regime. We make the assumption that we are in this limit. The R and S functions only depend on the time-difference : $R^{>}(t,t') = R^{>}(t-t')$, and the initial time of the double-contour is pushed to $t_{in} \to -\infty$.

The NCA system of equations for the greater and lesser components can be simplified to :

$$\begin{aligned} i\partial_t R^{>}(t) &= \mathcal{H}_{\mathrm{loc}} R^{>}(t) + \int_0^t \mathrm{d}u S^{>}(t-u) R^{>}(u) \\ S^{>}(t) &= i\sum_{ab}[d_a^\dagger R^{>}(t) d_b \Delta_{ab}^{>}(t) - d_a R^{>}(t) d_b^\dagger \Delta_{ba}^{<}(-t)] \end{aligned} \tag{V.40}$$

The initial condition is valid in this limit $R^{>}(0) = R^{>}(t-t) = -i\mathbb{1}$.

$$\begin{aligned} i\partial_t R^{<}(t) &= \mathcal{H}_{\mathrm{loc}} R^{<}(t) - \int_{-\infty}^{t'} \mathrm{d}u S^{>}(t-u) R^{<}(u) + \int_{-\infty}^{0} \mathrm{d}u S^{<}(t-u) R^{>}(u) \\ S^{<}(t) &= -i\sum_{ab}[d_a^\dagger R^{<}(t) d_b \Delta_{ab}^{<}(t) - d_a R^{<}(t) d_b^\dagger \Delta_{ba}^{>}(-t)] \end{aligned} \tag{V.41}$$

In the steady-state limit we have lost the initial condition for $R^{<}$ and it is now defined up to a constant. It is chosen by setting the partition function to 1 as it is usually done in the Keldysh formalism : $Z_{\mathrm{loc}} = i\mathrm{Tr}_{\mathrm{loc}}[R^{<}(0)] = 1$. The Green's functions are obtained through :

$$\begin{aligned} G_{ab}^{>}(t) &= i\mathrm{Tr}_{\mathrm{loc}}[\frac{1}{Z_{\mathrm{loc}}}R^{<}(-t) d_a R^{>}(t) d_b^\dagger] \\ G_{ab}^{<}(t) &= -i\mathrm{Tr}_{\mathrm{loc}}[\frac{1}{Z_{\mathrm{loc}}}R^{<}(t) d_a^\dagger R^{>}(-t) d_b] \end{aligned} \tag{V.42}$$

The NCA approximation, associated with the Dyson equation for the self-energy can be solved for the greater and lesser components by a time-discretization and finite difference scheme. It can be done self-consistently by starting from a guess for the self-energy,

or directly by noticing that the Volterra integro-differential equation only implies anterior times to the computed one. However solving of the NCA equations using a finite difference method shows some limitations. Because of the Volterra integro-differential equation, the finite difference scheme has a complexity varying with the square of the number of points in the time-grid $O(N^2)$. The functions are oscillating which fixes the step of the time-discretization, and are decaying slowly at large times. In practice a new algorithm has been found recently for reducing this complexity to $O(N \log N)$ [68, 69].

In this section we have expressed the Non-Crossing Approximation equations for out-of-equilibrium systems and in the steady-state limit. Even if uncontrolled, this approximation has the benefit to provide an analytic expression for the self-energy and therefore an impurity solver computationally light and easy to implement.

V.2 NCA impurity solver in the steady-state limit

In this section we introduce a new efficient solver for the steady-state NCA equations by alternating between the time and frequency domain. Relying on a fast Fourier Transform algorithm it gives an overall complexity in $O(N \log N)$ with N the size of the time-discretization grid. It aims at overcoming the limitations that faces the usual NCA solvers in the time domain, and improving the efficiency of the NCA approach for out-of-equilibrium materials.

V.2.1 NCA solver

Volterra equation in the frequency domain :

While the relation for the self-energy in the NCA approximation is linear and easy to implement in the time-domain, the Volterra equation, because of its integro-differential form, leads to a complex finite difference scheme In fact the integrated part of the equation is similar to a convolution which guides us towards expressing it simply in the frequency domain.

R and S are infinitely differentiable functions and therefore they have Fourier transforms which decay exponentially fast at large $|\omega|$. We define :

$$\begin{aligned} R^{<(>)}(\omega) &= \int_{-\infty}^{+\infty} R^{<(>)}(t) e^{-i\omega t} \mathrm{d}t \\ S^{<(>)}(\omega) &= \int_{-\infty}^{+\infty} S^{<(>)}(t) e^{-i\omega t} \mathrm{d}t \end{aligned} \tag{V.43}$$

Given that R and S obey the symmetry relations Eq.V.24 , the Fourier transform functions have purely imaginary diagonal coefficients and we have :

$$\begin{aligned} R^{>(<)}(\omega)^\dagger &= -R^{>(<)}(\omega) \\ S^{>(<)}(\omega)^\dagger &= -S^{>(<)}(\omega) \end{aligned} \tag{V.44}$$

In order to transform the Volterra integration into a convolution we introduce retarded functions of the local propagator and self-energy (for the greater and lesser components) :

$$\begin{aligned} \tilde{R}(t) &= \theta(t)R(t) \\ \tilde{S}(t) &= \theta(t)S(t) \end{aligned} \tag{V.45}$$

We notice that the symmetry relations Eq. V.44 imply that $R^>(\omega) = 2i\mathrm{Im}\tilde{R}^>(\omega)$. The Volterra equations rewrite in terms of these functions (with the $\delta(t)\mathbb{1}$ accounting for the discontinuity in $t = 0$) :

$$\begin{aligned} i\partial_t \tilde{R}^>(t) &= \delta(t)\mathbb{1} + \mathcal{H}_{\mathrm{loc}}\tilde{R}^>(t) + \int_{-\infty}^{+\infty} \mathrm{d}u \tilde{S}^>(t-u)\tilde{R}^>(u) \\ i\partial_t R^<(t) &= \mathcal{H}_{\mathrm{loc}}R^<(t) - \int_{-\infty}^{+\infty} \mathrm{d}u \tilde{S}^>(t-u)R^<(u) + \int_{-\infty}^{+\infty} \mathrm{d}u S^<(t-u)\bar{R}^>(u) \end{aligned} \tag{V.46}$$

Where $\bar{R} = \theta(-t)R(t)$. Because of their non-linearity at $t = 0$, the $\tilde{R}$,$\tilde{S}$ and $\bar{R}$ functions have Fourier transforms which decay slowly in frequency. The integrating parts are now convolutions and they become algebraic equations in Fourier space. We are left with the system of equations for the greater component :

$$\begin{aligned} \tilde{R}^>(\omega) &= [\omega - \mathcal{H}_{\mathrm{loc}} - \tilde{S}^>(\omega)]^{-1} \\ S^>(t) &= i\sum_{ab}[d_a^\dagger R^>(t)d_b\Delta_{ab}^>(t) - d_a R^>(t)d_b^\dagger\Delta_{ba}^<(-t)] \end{aligned} \tag{V.47}$$

Which has to be solved with its initial condition $R^>(0) = -i\mathbb{1}$. For the lesser condition :

$$\begin{aligned} R^<(\omega) &= -[\omega - \mathcal{H}_{\mathrm{loc}} - \tilde{S}^>(\omega)]^{-1}S^<(\omega)\bar{R}^>(\omega) \\ S^<(t) &= -i\sum_{ab}[d_a^\dagger R^<(t)d_b\Delta_{ab}^<(t) - d_a R^<(t)d_b^\dagger\Delta_{ba}^>(-t)] \end{aligned} \tag{V.48}$$

For which we impose $Z_{\mathrm{loc}} = i\mathrm{Tr}_{\mathrm{loc}}[R^<(0)] = 1$. We notice that the equation on $\tilde{R}^>(\omega)$ is similar to what was obtained at equilibrium in the imaginary-time formalism in Eq. V.15. We explain this in Appendix G by showing that R has a spectral representation which links its imaginary-time and real-time expressions at equilibrium.

Implementation :

We tackle this system of equations self-consistently by alternating between real-time and frequency domains. We can first solve the system of equations for the greater component and then use the solutions for $R^>$ and $S^>$ to solve the lesser component system.The Fourier transforms are performed using an FFT (fast Fourier Transform) algorithm on a discretized time-grid. For the greater component system we use the algorithm :

- Start from a guess for $R^>(\omega)$
- Compute $\tilde{R}^>(t)$ with the FFT algorithm
- Use the self-energy equations to get $\tilde{S}^>(t)$
- Compute $\tilde{S}^>(\omega)$ by reverse FFT algorithm
- Use the Volterra equation in frequency domain to get $\tilde{R}(\omega)$
- We loop until convergence of the function $R^>(\omega) = 2i\mathrm{Im}\tilde{R}^>(\omega)$.

The Fourier transform of the discontinuous functions $\tilde{R}(\omega)$ and $\tilde{S}(\omega)$ have a real part which decays slowly at high frequencies. We could think that this would lead to a major drawback by requiring very large frequency grids in order to resolve their slowly decaying behaviour. However the main advantage of this solver is that this slowly decaying tail does not need to be handled. Indeed using the symmetries on R we have $R^>(\omega) = 2i\mathrm{Im}\tilde{R}^>(\omega)$. This means that we never need to perform the Fourier transform of a tilde function in frequency and we can restrict the frequency domain to the support of $R^>(\omega)$. This point is essential to reduce the size of the considered grid and obtain a fast NCA solver.

The algorithm for the lesser component is the same one without the need to compute the tilde functions. The normalization condition on $R^<(0)$ must be fixed at each step of the algorithm to avoid a drifting of the numerical solution.

We make a few remarks on this scheme :

- We need to perform the Fourier transform of discontinuous functions. In order to avoid numerical errors due to the discontinuity at $t = 0$, one can substract auxiliary functions of known Fourier transform which discontinuity compensates the one of $\tilde{S}$.
- It is useful to take advantage of the symmetries of Δ and $\hat{\mathcal{H}}_{\mathrm{loc}}$ to block diagonalise R and S and simplify the matrix computations.

The overall complexity is dominated by the FFT which scales as $O(N \log N)$ with N the number of points in the time-discretized grid.

V.2.2 Application to the Anderson Impurity model

In order to test and show the limitation of the NCA solver, we apply it to the Anderson impurity model [2, 3, 125] at equilibrium, and out-of-equilibrium in the presence of an external electric field. This model constitutes a simple testing ground for our impurity solver and we show that the NCA approximation enables one to describe the Kondo resonance [37, 53, 72] at small temperatures and close to half-filling. This model is made of a single site and single orbital impurity in a bath of free electrons :

$$\begin{aligned}\hat{\mathcal{H}} &= \hat{\mathcal{H}}_{loc} + \hat{\mathcal{H}}_{hyb} + \hat{\mathcal{H}}_{bath} \\ &= U\hat{n}_{d\uparrow}\hat{n}_{d\downarrow} - \mu\sum_{\sigma}\hat{d}^{\dagger}_{\sigma}\hat{d}_{\sigma} + \sum_{\mathbf{k},\sigma}\gamma_{\mathbf{k}}(\hat{c}^{\dagger}_{\mathbf{k},\sigma}\hat{d}_{\sigma} + h.c) + \sum_{\mathbf{k},\sigma}\epsilon_{\mathbf{k}}\hat{c}^{\dagger}_{\mathbf{k},\sigma}\hat{c}_{\mathbf{k},\sigma}\end{aligned} \tag{V.49}$$

The system has a spin inversion symmetry. Because of the particle-hole symmetry, the condition for half-filling is $\mu = U/2$. The bath is characterized by its hybridization function :

$$\Delta(i\omega_n) = \sum_{\mathbf{k}}\frac{|\gamma_{\mathbf{k}}|^2}{i\omega_n - \epsilon_{\mathbf{k}}} \tag{V.50}$$

Here we only consider non-interacting baths made of free electrons. Δ has the standard properties of Green's functions and has a spectral representation :

$$\Delta(i\omega_n) = \int\frac{A_{\Delta}(\epsilon)}{i\omega_n - \epsilon}\mathrm{d}\epsilon \tag{V.51}$$

We set a flat bath of width w :

$$A_{\Delta}(\epsilon) = \Gamma/\pi \text{ if} - w < \epsilon < w;\ 0 \text{ else} \tag{V.52}$$

With $\Gamma = 1$ the unit energy.

NCA at equilibrium :

In the absence of an external electric field, the system is at equilibrium at temperature $\beta = 1/T$, and we apply the steady-state NCA solver to retrieve the properties of the Anderson impurity. The NCA equations are diagonal in the local basis and because of the spin-inversion symmetry, we have three different diagonal functions which are labeled by the indices 0,1 and 2 for the different local sates $|0\rangle$, $|\uparrow>$ or $|\downarrow\rangle$ and $|\uparrow\downarrow\rangle$. We note $E = (0, -\mu, -\mu, U - 2\mu)$ the eigenvalues of the local Hamiltonian.

The equations on the local propagator write :

- for the greater component :

$$\begin{aligned}
&\tilde{R}_j^>(\omega) = [\omega - E_j - \tilde{S}_j^>(\omega)]^{-1} \\
&S_0^>(t) = -2iR_1^>(t)\Delta^<(-t) \\
&S_1^>(t) = i(R_0^>(t)\Delta^>(t) - R_2^>(t)\Delta^<(-t)) \\
&S_2^>(t) = 2iR_1^>(t)\Delta^>(t)
\end{aligned} \tag{V.53}$$

- for the lesser component :

$$\begin{aligned}
&R_j^<(\omega) = -[\omega - Ej - \tilde{S}_j^>(\omega)]^{-1} S_j^<(\omega)\bar{R}_j^>(\omega) \\
&S_0^<(t) = 2iR_1^<(t)\Delta^>(-t) \\
&S_1^<(t) = -i(R_0^<(t)\Delta^<(t) - R_2^<(t)\Delta^>(-t)) \\
&S_2^<(t) = -2iR_1^<(t)\Delta^<(t)
\end{aligned} \tag{V.54}$$

We get the Green's functions through (we drop the spin indices) :

$$\begin{aligned}
G^>(t) &= \frac{i}{Z}(R_0^<(-t)R_1^>(t) + R_1^<(-t)R_2^>(t) \\
G^<(t) &= \frac{-i}{Z}(R_0^>(-t)R_1^<(t) + R_1^>(-t)R_2^<(t)
\end{aligned} \tag{V.55}$$

With $Z = i\mathrm{Tr}[R^<(0)] = i(R_0^<(0) + 2R_1^<(0) + R_2^<(0))$. The spectral function is obtained with $G^R(t) = \theta(t)(G^>(t) + G^<(t))$ and $A(\omega) = (-1/\pi)\mathrm{Im}G^R(\omega)$. Its integration over frequency space is normalized to 1.

The density per spin at a given temperature is given by :

$$n = \int \mathrm{d}\omega \mathcal{A}(\omega) f(\beta, \omega) = -iG^<(t = 0) \tag{V.56}$$

We study the system at half-filling for different temperatures β. We set $U = 6$ and $\mu = U/2 = 3$. The eigen-energies for the local system are : $E = [0, -3, -3, 0]$. We show the evolution of the spectral function with temperature in Fig. V.3. At half-filling the spectral function is symmetric around $\omega = 0$. For $\beta \geq 2$ we see the appearance of the Kondo peak at $\omega = 0$ in the spectral function. The small peaks at $\omega = \pm 10$ correspond to the effect of the discontinuous flat bath at $w = 10$.

Away from half-filling, at $U = 6$ and $\mu = 3U/4$, we show the evolution of the R and S functions when decreasing the temperature in Appendix H. The eigen-energies for the local system are : $E = [0, -\mu, -\mu, U - 2\mu]$. For this set of parameters we are in the regime of the Anderson impurity model with a density around $n >\sim 0.5$. The evolution with temperature of the spectral function is shown if Fig. V.4. The spectral function presents peaks corresponding to the different local eigen energies which are broaden by the bath, and to the limits of the bath of width $w = 10$. As the temperature decreases the spectral weight is concentrated into the Kondo resonance peak at $\omega = 0$.

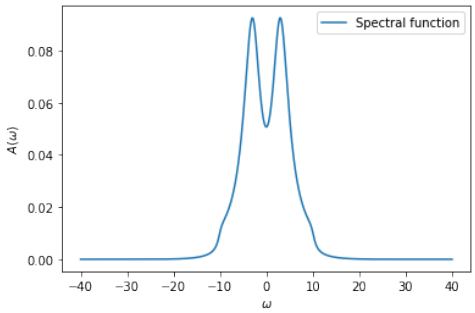

(a) $\mathcal{A}(\omega), \beta = 0.5$

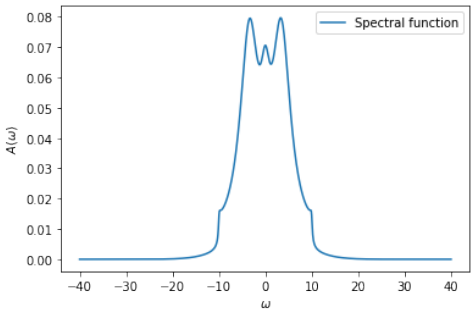

(b) $\mathcal{A}(\omega), \beta = 2$

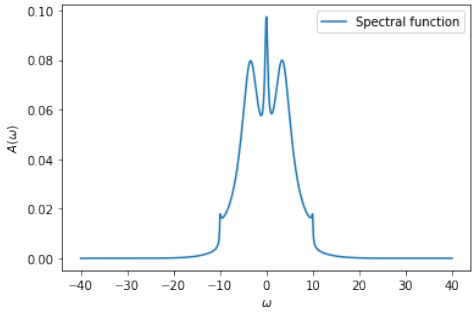

(c) $\mathcal{A}(\omega), \beta = 6$

Figure V.3: Spectral function as a function of frequency for different temperatures, at half-filling and $U = 6$.

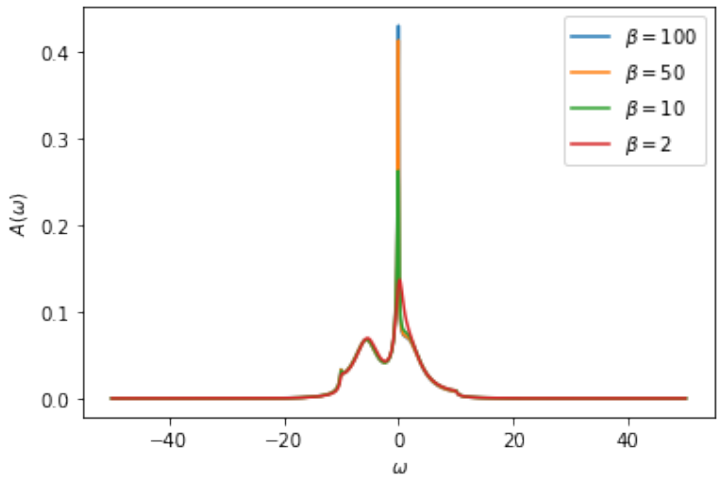

Figure V.4: Spectral function as a function of frequency for different temperatures, at $U = 6$ and $\mu = 3U/4$.

Current out-of-equilibrium :

As an example of a simple out-of-equilibrium model we study the current through a single orbital impurity. We use a model similar to the previous Anderson impurity model but this time with two baths R and L at equilibrium, which have different chemical potential to account for a potential difference driving an electric current through the impurity. The Hamiltonian reads :

$$\begin{aligned}\hat{\mathcal{H}} &= \hat{\mathcal{H}}_{\text{loc}} + \hat{\mathcal{H}}_{\text{hyb}} + \hat{\mathcal{H}}_{\text{bath}} \\ &= U\hat{n}_{d\uparrow}\hat{n}_{d\downarrow} - \mu\sum_{\sigma}\hat{d}^{\dagger}_{\sigma}\hat{d}_{\sigma} + \sum_{\mathbf{k},\sigma,\alpha=(R,L)}\gamma_{\mathbf{k}}(\hat{c}^{\dagger}_{\mathbf{k},\alpha,\sigma}\hat{d}_{\sigma} + h.c) + \sum_{\mathbf{k},\sigma,\alpha=(R,L)}\epsilon_{\mathbf{k},\alpha}\hat{c}^{\dagger}_{\mathbf{k},\alpha,\sigma}\hat{c}_{\mathbf{k},\alpha,\sigma}\end{aligned} \tag{V.57}$$

The two baths are described by two chemical potentials μ_R and μ_L which differ to account for a potential difference $V = \mu_R - \mu_L$ ($e = 1$). We consider a symmetric potential difference between the left and right baths with $\mu_L = -\mu_R$. This difference is taken into account for defining their characteristic hybridization functions ($a = L, R$) :

$$\begin{aligned}\Delta^{>}_{a}(t) &= -i\int \mathrm{d}\epsilon A_{\Delta}(\epsilon)(1 - f(\epsilon - \mu_a))e^{-i\epsilon t} \\ \Delta^{<}_{a}(t) &= i\int \mathrm{d}\epsilon A_{\Delta}(\epsilon) f(\epsilon - \mu_a)e^{-i\epsilon t}\end{aligned} \tag{V.58}$$

The system is now out-of-equilibrium and we can use the real-time framework developed before to tackle it in the steady-state limit. We aim at computing the current which is expressed per spin as [89] :

$$I_{\sigma} = \frac{i}{2}\sum_{\mathbf{k}}[\langle\hat{c}^{\dagger}_{\mathbf{k},L,\sigma}\hat{d}_{\sigma}\rangle - \langle\hat{d}^{\dagger}_{\sigma}\hat{c}_{\mathbf{k},L,\sigma}\rangle + \langle\hat{d}^{\dagger}_{\sigma}\hat{c}_{\mathbf{k},R,\sigma}\rangle - \langle\hat{c}^{\dagger}_{\mathbf{k},R,\sigma}\hat{d}_{\sigma}\rangle] \tag{V.59}$$

We introduce the Green's functions (with d the index referring to the impurity and $a = R, L$ the bath index) :

$$\begin{aligned}G^{<}_{d\to a,\sigma\mathbf{k}}(t - t') &= i\langle\hat{c}^{\dagger}_{\mathbf{k},a,\sigma}(t)\hat{d}_{\sigma}(t')\rangle \\ G^{<}_{a\to d,\sigma\mathbf{k}}(t - t') &= i\langle\hat{d}^{\dagger}_{\sigma}(t)\hat{c}_{\mathbf{k},a,\sigma}(t')\rangle\end{aligned} \tag{V.60}$$

Which gives after Fourier transform and noting g the non-interacting Green's functions describing the bath :

$$\begin{aligned}G^{<}_{d\to a,\sigma\mathbf{k}}(\omega) &= \gamma_{\mathbf{k}}[g^{<}_{\mathbf{k},a,\sigma}(\omega)G^{++}_{\sigma}(\omega) - g^{--}_{\mathbf{k},a,\sigma}(\omega)G^{<}_{\sigma}(\omega)] \\ G^{<}_{a\to d,\sigma\mathbf{k}}(\omega) &= \gamma_{\mathbf{k}}[g^{++}_{\mathbf{k},a,\sigma}(\omega)G^{<}_{\sigma}(\omega) - g^{<}_{\mathbf{k},a,\sigma}(\omega)G^{--}_{\sigma}(\omega)]\end{aligned} \tag{V.61}$$

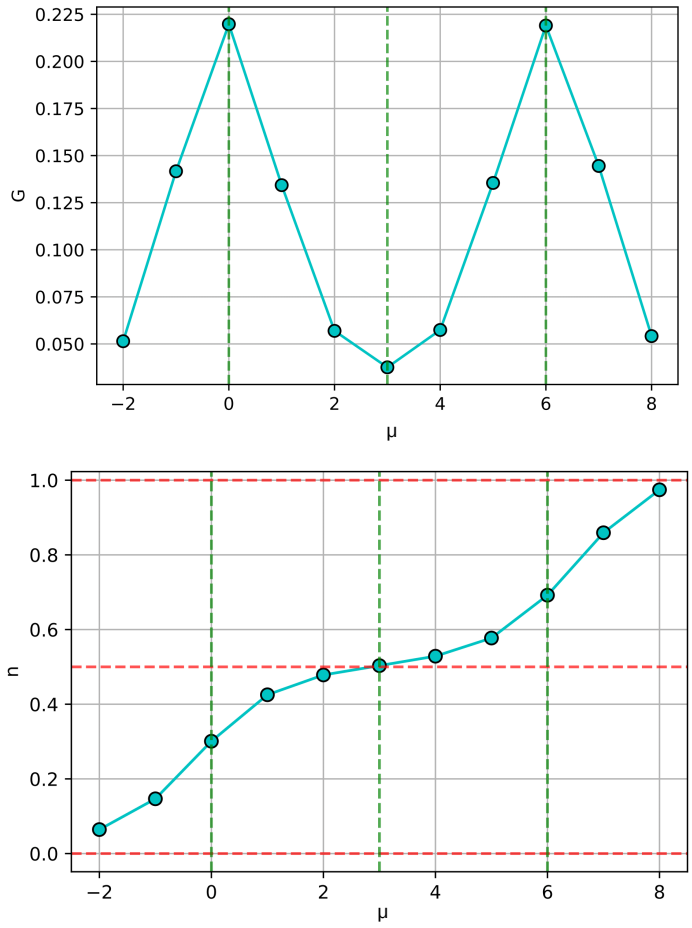

Figure V.5: Conductivity G and density per spin n as a function of the chemical potential μ, at $U = 6$, $T = 0.5$. The green dashed lines correspond to the specific values of the chemical potential $\mu = U/2$ at half-filling, and $\mu - U/2 = \pm U/2$ in the mixed-valence states for which the total density is around half an integer. The red dashed vertical lines correspond to the expected value of the density at half-filling and at $\mu \to \pm\infty$.

And noting that the hybridization functions write $\Delta_{a,\sigma} = \sum_{\mathbf{k}} \gamma_{\mathbf{k}}^2 g_{\mathbf{k},a,\sigma}$ we get the expression of the current as a function of the local Green's functions and of the hybridization functions :

$$I_\sigma = \frac{1}{2}\int \frac{\mathrm{d}\omega}{2\pi}[(\Delta^<_{\sigma,L}(\omega) - \Delta^<_{\sigma,R}(\omega))G^>_\sigma(\omega) - (\Delta^>_{\sigma,L}(\omega) - \Delta^>_{\sigma,R}(\omega))G^<_\sigma(\omega)] \tag{V.62}$$

The model is solved identically to the Anderson impurity model as described in the previous section. The NCA equations apply with a total hybridization which is the sum of the hybridization functions for both baths $\Delta_\sigma(\omega) = \Delta_{L,\sigma}(\omega) + \Delta_{R,\sigma}(\omega)$ for the lesser and greater components.

We show the conductance $G = I/V$ as a function of the chemical potential at $U = 6$ and $T = 0.5$ in Fig. V.5. The conductance of the system is maximum at $\mu - U/2 = \pm U/2$ when the system is in a mixed-valence state with a density which is nit an entire number. To see this we also show the evolution of the density with the chemical potential. At $\mu \to \pm\infty$ or $\mu = U/2$, the density is fixed to an entire number and the conductivity is minimal because of the Coulomb blockade, preventing transport through the impurity. At $\mu \simeq U/2$, the conductivity does not go to zero because of the rise of the Kondo peak in the spectral function as seen in Fig. V.4.

V.2.3 Conclusion and discussion

The NCA approximation provides an impurity solver which does not require heavy numerical resources and is easy to implement. By treating the Volterra equation in the frequency domain and reducing the considered frequency interval to the support of R and S, we obtain an efficient solving of the NCA equations by alternating between the frequency and real-time domains.

The main limitation to our approach stands in the divergence of the R functions at small temperatures as observed in Appendix H. As the temperature is decreased, these functions show a peak which diverges exponentially towards a vertical asymptote. This divergence can be seen in the frequency Volterra equation and happens in the vicinity of the local Hamiltonian eigenvalues for $|\omega - \mathcal{H}_{\mathrm{loc}} - \tilde{S}^>(\omega)| \simeq 0$. In the frequency domain, the discretized grid must have a small enough step in order to be able to resolve these peaks. The width of the considered grid is fixed by the spread of the self-energy S function which is determined by the width of the bath. At small temperatures the observed peaks becomes extremely narrow and leads to an overwhelming number of points on the considered frequency grid. In order to overcome this difficulty we consider using adaptive logarithmic grids to resolve the peaks with a fixed number of points sampling the frequency axis. These threshold singularities appearing at zero temperature have been documented before [93, 98] and would require further work for better understanding their frequency position and asymptotic behaviour at small temperatures.

The purpose of the NCA solver is to be able to solve efficiently out-of-equilibrium problems for actual materials with several orbitals and large unit cells. The NCA solver

provides a fast solution for the impurity problem that arises in the DMFT approximation. Even if the NCA approximation is quite rough, it shows to be able to describe qualitatively phenomena of strongly interacting quantum problems, such as the Kondo effect in the Anderson impurity model. One way to improve the NCA approximation is to add successively other class of diagrams on top of the non-crossing ones [47, 51, 119, 136]. The novel inchworm algorithm performs a Monte Carlo computation on the Keldysh contour of classes of diagrams differentiated according to the allowed number of crossings between hybridization line [4, 25, 26]. When converging, it provides an unbiased result, but it remains computationally heavy and is limited for multi-orbital systems.

Chapter VI

Conclusion

In this thesis we have described new algorithmic developments for studying strongly correlated systems both in and out of equilibrium. At equilibrium, we have focused on developing an unbiased perturbative method that yields precise results. Out-of-equilibrium, finding the exact solution to the problem is extremely complicated, and we have endeavoured to develop an efficient and lightweight perturbation solver that nevertheless suffers from approximations.

First, we have shown that the symmetry-broken CDet algorithm is a powerful method to study the Hubbard model at equilibrium. Our approach implies no approximation and is formulated in the thermodynamic limit. For the half-filled cubic model, we have controlled all sources of bias to obtain accurate and controlled results. It turns out to be able to perturbatively reach the very strong coupling regime at small temperatures. These computations are the first unbiased perturbative computations inside an ordered phase and open the way to the numerical study of symmetry-broken phases, and of the physics of phase transitions. However, some parts of the phase diagram are still difficult to reach with our method, and require further study and algorithmic development. Our approach is an example of the power of chemical potential shifts for perturbation expansion. The linear symmetry-breaking shift can be generalized to almost any function in the expansion parameter and could lead to significant improvements in the convergence properties of the perturbation series. This could lead to new methods capable of handling the doped regimes or the challenging two-dimensional Hubbard model.

In a second step, we developed and implemented an efficient solver for the NCA equations. By switching between the time and frequency domains and reducing the frequency window for the resolution of the involved functions, we have developed an efficient impurity solver in the steady-state limit. The main limitation of our solver lies in the threshold singularities that occur at small temperatures. The use of adaptive logarithmic frequency grids could allow us to reach lower temperatures. This solver still needs to be implemented in a DMFT loop to handle multi-orbital systems that model more specifically the behaviour of a particular material.

Appendix A

Non-interacting Green's functions

We introduce in this part the Green's function formalism used for the perturbation theory development. We specifically want to show how to compute the non-interacting Green's function with $U = 0$ in the Hubbard model (and in general for every quadratic Hamiltonian).

We describe our system in term of the imaginary-time ($\tau = it$) fermionic Green's function correlator :

$$\mathcal{G}_{ij\sigma\sigma'}(\tau, \tau') = - < \mathcal{T}_\tau \hat{c}_{i\sigma}(\tau) \hat{c}^\dagger_{j\sigma'}(\tau') > \tag{A.1}$$

With $\mathcal{T}_\tau$ being the time ordering operator. The time dependence of the second quantization operators makes reference to their time evolution in the Heisenberg picture. We recall that (for imaginary-time evolution) :

$$\hat{c}_{i\sigma}(\tau) = e^{\tau H} \hat{c}_{i\sigma} e^{-\tau H} \tag{A.2}$$

$$\hat{c}^\dagger_{i\sigma}(\tau) = e^{\tau H} \hat{c}^\dagger_{i\sigma} e^{-\tau H} \tag{A.3}$$

In the non-interacting picture $U = 0$, the Hubbard Hamiltonian is diagonal in $\mathbf{k}$ space and we get after performing the Fourier transform of the lattice :

$$\hat{\mathcal{H}} = \sum_{\mathbf{k}} \xi_{\mathbf{k}\sigma} \hat{c}^\dagger_{\mathbf{k}\sigma} \hat{c}_{\mathbf{k}\sigma} \tag{A.4}$$

Where $\xi_{\mathbf{k}\sigma} = \epsilon_{\mathbf{k}} - \mu$ and $\epsilon_{\mathbf{k}}$ the energy dispersion depending on the lattice geometry and easily computed in the tight-binding approximation. This leads to :

$$\hat{c}_{\mathbf{k}\sigma}(\tau) = e^{-\xi_{\mathbf{k}\sigma}\tau} \hat{c}_{\mathbf{k}\sigma} \tag{A.5}$$

$$\hat{c}^\dagger_{\mathbf{k}\sigma}(\tau) = e^{\xi_{\mathbf{k}\sigma}\tau} \hat{c}^\dagger_{\mathbf{k}\sigma} \tag{A.6}$$

And we get, with $\theta(\tau)$ the Heaviside function : $\theta(\tau) = 1$ for $\tau > 0$ and 0 otherwise, the non-interacting Green's function :

$$\begin{aligned}\mathcal{G}_{0\mathbf{k}\sigma}(\tau-\tau') &= -<\mathcal{T}_\tau \hat{c}_{\mathbf{k}\sigma}(\tau)\hat{c}^\dagger_{\mathbf{k}\sigma}(\tau')> \\ &= -\theta(\tau-\tau')<\hat{c}_{\mathbf{k}\sigma}(\tau)\hat{c}^\dagger_{\mathbf{k}\sigma}(\tau')> +\theta(\tau'-\tau)<\hat{c}^\dagger_{\mathbf{k}\sigma}(\tau')\hat{c}_{\mathbf{k}\sigma}(\tau)> \\ &= -[\theta(\tau-\tau')(1-n_F(\xi_{\mathbf{k}\sigma}))-\theta(\tau'-\tau)n_F(\xi_{\mathbf{k}\sigma})]e^{-\xi_{\mathbf{k}\sigma}(\tau-\tau')}\end{aligned} \tag{A.7}$$

With $n_F(\epsilon)=\frac{1}{1+e^{\beta\epsilon}}$ being the Fermi-Dirac distribution function. One can show that this Green's function is antiperiodic with a period $\beta = 1/k_BT$ so that one can develop it as a Fourier series to get the well known formula of a non-interacting single-particle Green's function for the Matsubara frequencies $\omega_n = (2n+1)\frac{\pi}{\beta}$:

$$\begin{aligned}\mathcal{G}_{0\mathbf{k}\sigma}(i\omega_n) &= \int_0^\beta d\tau e^{i\omega_n\tau}\mathcal{G}_{0\mathbf{k}\sigma}(\tau) \\ &= -(1-n_F(\xi_{\mathbf{k}\sigma}))\int_0^\beta d\tau e^{i\omega_n\tau}e^{-\xi_{\mathbf{k}\sigma}\tau} \\ &= -(1-n_F(\xi_{\mathbf{k}\sigma}))\frac{1}{i\omega_n-\xi_{\mathbf{k}\sigma}}(e^{i\omega_n\beta}e^{-\xi_{\mathbf{k}\sigma}\beta}-1)\end{aligned} \tag{A.8}$$

And after noticing that $e^{i\omega_n\beta}=-1$ and $1-n_F(\xi_{\mathbf{k}\sigma})=(e^{-\beta\xi_{\mathbf{k}\sigma}}+1)^{-1}$ we get:

$$\mathcal{G}_{0\mathbf{k}\sigma}(i\omega_n)=\frac{1}{i\omega_n-\epsilon_{\mathbf{k}\sigma}+\mu} \tag{A.9}$$

Appendix B

Particle-hole symmetry

In some cases the Hubbard Hamiltonian possesses a particle-hole symmetry that we aim at introducing in this appendix and which enables us to derive an important result : in the grand canonical ensemble, the system is at half-filling for a specific value of the chemical potential $\mu_{HF} = U/2$. It requires a geometric condition on the considered model : having a bipartite lattice. A lattice is said to be bipartite if it can be separated into two sublattices such that there is no hopping term within one sublattice, and thus only hopping terms between different sublattices. For instance the square or cubic lattices are bipartite when considering only nearest neighbour site hopping, whereas the triangular lattice, because of its high connectivity, is not.

For a bipartite lattice with two sublattices, one can introduce the particle-hole symmetry transformation exchanging the role of creation and annihilation operators. The second quantization operators transform as follow :

$$\hat{c}^{\dagger}_{i\sigma} \rightarrow \pm \hat{c}_{i\sigma} \tag{B.1}$$

With the sign depending on the sublattice the site i belongs to. This unitary transformation conserves the fermionic anti-commutation relations. The number operators then transform as $\hat{n}_{i\sigma} \rightarrow 1 - \hat{n}_{i\sigma}$. The Hubbard Hamiltonian gives after performing the transformation :

$$\begin{aligned} \hat{\mathcal{H}}' = & -t \sum_{\langle i,j \rangle} \sum_{\sigma} \hat{c}^{\dagger}_{i\sigma} \hat{c}_{j\sigma} + U \sum_{i} \hat{n}_{i\uparrow} \hat{n}_{i\downarrow} - (U - \mu) \sum_{i} (\hat{n}_{i\uparrow} + \hat{n}_{i\downarrow}) \\ & + (U - 2\mu) N \end{aligned} \tag{B.2}$$

where we notice that for i and j neighbouring sites $\hat{c}^{\dagger}_{i\sigma} \hat{c}_{j\sigma} \rightarrow -\hat{c}_{i\sigma} \hat{c}^{\dagger}_{j\sigma} = \hat{c}^{\dagger}_{j\sigma} \hat{c}_{i\sigma}$ and the kinetic part of the Hamiltonian remains unchanged after reorganizing the sum. N is the number of sites of the lattice. This Hamiltonian is equivalent to the Hubbard Hamiltonian with a shifted chemical potential and an inessential energy constant.

One can then compute the density per site and spin for these two equivalent Hamiltonians :

$$\begin{aligned} n &= \frac{1}{2N}\sum_i \langle \hat{n}_{i\uparrow} + \hat{n}_{i\downarrow}\rangle_{\hat{\mathcal{H}}_{Hubbard}} \rightarrow \\ &\frac{1}{2N}\sum_i \langle (1-\hat{n}_{i\uparrow}) + (1-\hat{n}_{i\downarrow})\rangle_{\hat{\mathcal{H}}'} = 1 - \frac{1}{2N}\sum_i \langle \hat{n}_{i\uparrow} + \hat{n}_{i\downarrow}\rangle_{\hat{\mathcal{H}}'} \end{aligned} \tag{B.3}$$

But the density is a physical quantity which has to remain invariant with the transformation, and since both Hamiltonians are equivalent with just a change in the chemical potential, this leads to (for every T, U, t and μ) :

$$n(U-\mu) = 1 - n(\mu) \tag{B.4}$$

At half-filling (one electron per site on average), the density per site and spin is $n = 0.5$. From the previous equation, we notice that a sufficient condition is that :

$$n(\mu_{HF}) = n(U-\mu_{HF}) \tag{B.5}$$

Which is satisfied for $\mu_{HF} = U - \mu_{HF}$. In the end we get a value for the chemical potential which sets the system at half-filling for the Hubbard model on a bipartite lattice :

$$\mu_{HF} = \frac{U}{2} \tag{B.6}$$

We notice that for $\mu = U/2$ we get $\hat{\mathcal{H}}' = \hat{\mathcal{H}}_{Hubbard}$ and therefore the Hubbard model has a particle-hole symmetry at half-filling. In fact the particle-hole transformation in Eq. E.3 implies that the Hubbard Hamiltonian phase diagram is symmetric about half-filling. When modeling cuprates, one would have to add a next-nearest-neighbour hopping t' which breaks the particle-hole symmetry since the square lattice is no longer bipartite.

Appendix C

Mean-field solution of the Hubbard model

We derive the mean-field solution of the Hubbard model which is used as a starting point for perturbative series in the context of the chemical potential shift. We solve the mean-field equations in order to solve the non-interacting starting point of the perturbation expansion and obtain the zeroth order coefficient.

Performing the mean-field approximation, we neglect the last non-quadratic term supposing that the number operator does not deviate a lot from its average value. This leads to the mean-field Hubbard Hamiltonian :

$$\begin{aligned}\hat{\mathcal{H}}_{MF} = &-t\sum_{\langle i,j\rangle}\sum_{\sigma}\hat{c}^{\dagger}_{i\sigma}\hat{c}_{j\sigma} - U\sum_{i}\langle\hat{n}_{i\uparrow}\rangle\langle\hat{n}_{i\downarrow}\rangle + U\sum_{i}\hat{n}_{i\uparrow}\langle\hat{n}_{i\downarrow}\rangle \\ &+ U\sum_{i}\hat{n}_{i\downarrow}\langle\hat{n}_{i\uparrow}\rangle - \mu\sum_{i}(\hat{n}_{i\uparrow}+\hat{n}_{i\downarrow})\end{aligned} \tag{C.1}$$

This is a quadratic Hamiltonian depending on the average values of the number operators which thus leads to a self-consistent analytic solution. It can be used to study magnetic orders in the Hubbard model. It leads, for instance, to competing ferromagnetic, paramagnetic and anti-ferromagnetic phases among others. In our study we need the solutions for the paramagnetic and antiferromagnetic phases.

Paramagnetic solution :

If we make the assumption that the spin inversion symmetry is not broken, then on-site density does not depend on the spin degree of freedom and the mean-field Hamiltonian can be written :

$$\hat{\mathcal{H}}_{MF} = -t\sum_{\langle i,j\rangle}\sum_{\sigma}(\hat{c}^{\dagger}_{i\sigma}\hat{c}_{j\sigma} + \hat{c}^{\dagger}_{j\sigma}\hat{c}_{i\sigma}) + (Un-\mu)\sum_{i}(\hat{n}_{i\uparrow}+\hat{n}_{i\downarrow}) \tag{C.2}$$

With n the density per spin and site. It is diagonalised in $\mathbf{k}$ space :

$$\hat{\mathcal{H}}_{MF} = \sum_{\mathbf{k}} \sum_{\sigma} (\epsilon_{\mathbf{k}} + Un - \mu) \hat{c}^{\dagger}_{\mathbf{k}\sigma} \hat{c}_{\mathbf{k}\sigma} \tag{C.3}$$

Where $\epsilon_{\mathbf{k}}$ is the energy dispersion depending on the lattice geometry and easily computed in the tight-binding approximation :

- $\epsilon_{\mathbf{k}} = -2t(\cos k_x + \cos k_y)$ for the square lattice.
- $\epsilon_{\mathbf{k}} = -2t(\cos k_x + \cos k_y + \cos k_z)$ for the cubic lattice.

Hence the mean-field paramagnetic Green's function in Matsubara frequencies :

$$\mathcal{G}_{MF\mathbf{k}}(i\omega_n) = \frac{1}{i\omega_n - \epsilon_{\mathbf{k}} - Un + \mu} \tag{C.4}$$

For a given filling n, temperature T, interaction U, and hopping t of the model, the chemical potential can be determined through the self-consistent equation :

$$\begin{aligned} n &= \frac{1}{2N} \sum_{i} \langle \hat{n}_{i\uparrow} + \hat{n}_{i\downarrow} \rangle_{\hat{\mathcal{H}}_{MF}} \\ &= \frac{1}{N} \sum_{\mathbf{k}} n_F(\epsilon_{\mathbf{k}} + Un - \mu) \\ &= \int_{-\infty}^{\infty} n_F(\epsilon + Un - \mu) \rho(\epsilon) \mathrm{d}\epsilon \end{aligned} \tag{C.5}$$

Where n_F is the Fermi-Dirac distribution function and $\rho(\epsilon)$ the density of states. As expected, since the density of states is symmetric around 0, and the the couple $\mu = \frac{U}{2}$ and $n = \frac{1}{2}$ is a solution of this equation for half-filling.

Antiferromagnetic phase :

We now assume a breaking of the spin inversion symmetry towards an antiferromagnetic phase. To restore the translation symmetry one needs to consider a new unit cell composed of one site from each sublattice of the bipartite lattice. As the unit cell becomes bigger, this leads to a reduced Brillouin zone in $\mathbf{k}$ space. We introduce the magnetization per site and spin $m = \langle \hat{n}_{i\uparrow} - \hat{n}_{i\downarrow} \rangle$. It is the order parameter which is zero in the paramagnetic phase while it has a non-zero value inside the antiferromagnetic order. We therefore have $\langle \hat{n}_{i\sigma} \rangle = n + \sigma(-1)^i \frac{m}{2}$ with the sign depending on the spin $\sigma = \pm 1$, and on the sublattice of the site i. The mean-field Hamiltonian then becomes :

$$\begin{aligned} \hat{\mathcal{H}}_{MF} = &-t \sum_{\langle i,j \rangle} \sum_{\sigma} \hat{c}^{\dagger}_{i\sigma} \hat{c}_{j\sigma} + U \sum_{i\sigma} (n + \sigma(-1)^i \frac{m}{2}) \hat{c}^{\dagger}_{i\sigma} \hat{c}_{i\sigma} \\ &- \mu \sum_{i} (\hat{n}_{i\uparrow} + \hat{n}_{i\downarrow}) \end{aligned} \tag{C.6}$$

Performing a Fourier transform and going to $\mathbf{k}$ space the Hamiltonian is no longer diagonal and we add an index $1, 2$ depending on the sublattice :

$$\hat{\mathcal{H}}_{MF} = \sum_{\mathbf{k}\sigma} \begin{bmatrix} \hat{c}^\dagger_{\mathbf{k}1\sigma} & \hat{c}^\dagger_{\mathbf{k}2\sigma} \end{bmatrix} \begin{bmatrix} -\sigma\frac{Um}{2} - \mu + Un & \Xi \\ \Xi^* & \sigma\frac{Um}{2} - \mu + Un \end{bmatrix} \begin{bmatrix} \hat{c}_{\mathbf{k}1\sigma} \\ \hat{c}_{\mathbf{k}2\sigma} \end{bmatrix} \tag{C.7}$$

Where Ξ is the geometric factor depending on the lattice, such that $\epsilon_k = |\Xi|$. One needs to diagonalise the two by two matrix to get a quadratic diagonal Hamiltonian. Its eigenvalues are :

$$E_\pm = -\mu + Un \pm \sqrt{\epsilon^2_{\mathbf{k}} + \Delta^2} \tag{C.8}$$

Where the antiferromagnetic symmetry breaking leads to the opening of a gap $\Delta = \frac{Um}{2}$ in the energy spectrum. In the case of $m = 0$ with no antiferromagnetic order we find back the results of the paramagnetic mean-field solution.

Similarly as in the paramagnetic case we get the two self-consistent equations relating the density per site and spin, the chemical potential, and the magnetization :

$$\begin{aligned} n &= \int_{-\infty}^{\infty} \frac{\Delta}{2\sqrt{\Delta^2+\epsilon^2}} [n_F(Un - \mu + \sqrt{\Delta^2+\epsilon^2}) + n_F(Un - \mu - \sqrt{\Delta^2+\epsilon^2})]\rho(\epsilon)d\epsilon \\ m &= \int_{-\infty}^{\infty} \frac{\Delta}{\sqrt{\Delta^2+\epsilon^2}} [n_F(Un - \mu + \sqrt{\Delta^2+\epsilon^2}) - n_F(Un - \mu - \sqrt{\Delta^2+\epsilon^2})]\rho(\epsilon)d\epsilon \end{aligned} \tag{C.9}$$

Supposing that we work at half-filling with $n = \frac{1}{2}$ and $\mu = \frac{U}{2}$ we compute the magnetization thanks to the second self-consistent equation which becomes :

$$m = \int_{-\infty}^{\infty} \frac{\Delta}{\sqrt{\Delta^2+\epsilon^2}} [n_F(\sqrt{\Delta^2+\epsilon^2}) - n_F(-\sqrt{\Delta^2+\epsilon^2})]\rho(\epsilon)d\epsilon \tag{C.10}$$

Since $\Delta = \frac{Um}{2}$ this equation has a paramagnetic solution $m = 0$ which restores the translation symmetry, and possibly a second non-zero solution. When the equation has two solutions, one needs to compare the value of the grand canonical potential for each solution to see which phase actually minimizes it.

Appendix D

Partial sum and resummation in the paramagnetic phase

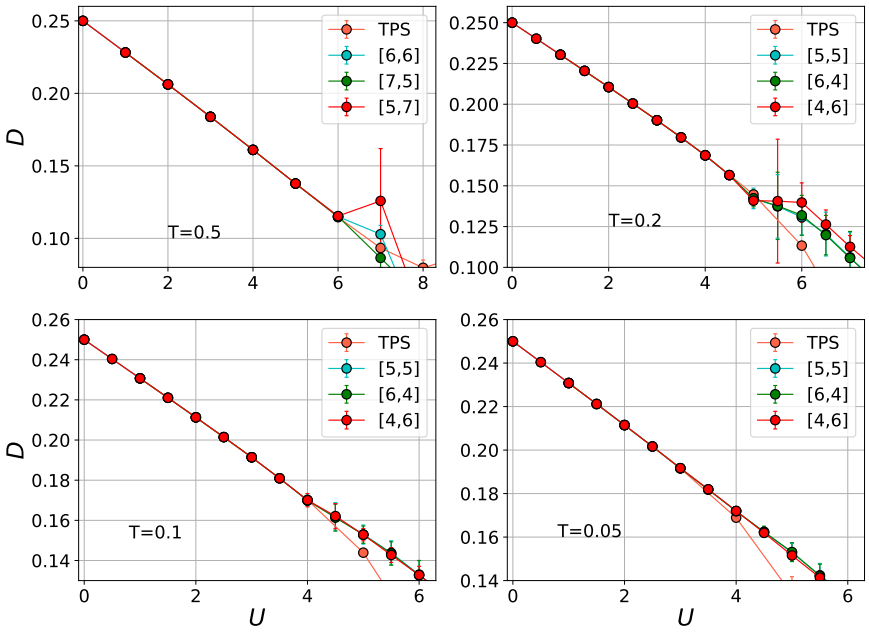

Figure D.1: Double occupancy as a function of the interaction for four different values of the temperature. We display results obtained after resummation of the perturbation series using Padé approximant at different orders $[j, l]$ with j being the order of the polynomial at the numerator of the approximant, and l the one of the denominator. We set $j + l = n$ with n the maximal expansion order obtained in the pertubative expansion of D. TPS stands for Truncated Perturbative Series and simply is the power series summed up to the order n.

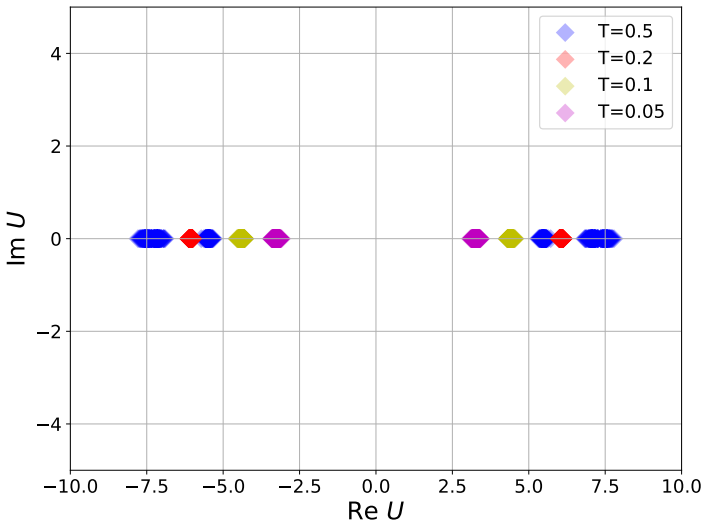

Figure D.2: Position of the poles in the complex plane structure of the perturbative series of the double occupancy at different temperatures. The singularities positions are estimated using a specific Padé approximant scheme [40]. On each side of the real axis, the spread of the colored diamond marks represents the spread of the position of the pole after error propagation of the statistical error on the expansion coefficients.

We give some insights on the resummation of the series in the normal phase of the half-filled Hubbard model on a cubic lattice. Using Padé approximants we are able to perform the resummation of the pertubative series of the double occupancy. We estimate the error to derive a controlled result with propagating the error from the expansion coefficients and by comparing several Padé approximants as shown in Fig. D.1. We also use Padé approximants to draw the complex plane structure of the series and estimate the positions of poles which limit the resummation. The position of the pole concurs with a huge increase in the resummation error. Even if the Padé resummation gives an estimate of the series past the pole on the real axis, it can not be considered reliable past this value of the interaction.

Appendix E

Equivalence of the repulsive and attractive half-filled Hubbard model

The half-filled Hubbard model on a bipartite lattice possesses a correspondence between the attractive ($U < 0$) and repulsive ($U > 0$) cases which we introduce in this appendix. The transformation studied here is explained in more details in [55].

For a bipartite lattice with two sublattices, one can introduce the following transformation in terms of second quantization operators :

$$\begin{aligned} \hat{c}^{\dagger}_{i\uparrow} &\rightarrow (-1)^{i}\hat{c}_{i\uparrow} \\ \hat{c}^{\dagger}_{i\downarrow} &\rightarrow \hat{c}^{\dagger}_{i\downarrow} \end{aligned} \tag{E.1}$$

With the sign depending on the sublattice the site i belongs to. This unitary transformation conserves the fermionic anti-commutation relations. The operators for the spin $\downarrow$ are left unchanged while the number operator for the spin $\uparrow$ transforms as $\hat{n}_{i\uparrow} \rightarrow 1 - \hat{n}_{i\uparrow}$. The Hubbard Hamiltonian gives after performing the transformation :

$$\begin{aligned} \hat{\mathcal{H}}' = &- t \sum_{\langle i,j \rangle} \sum_{\sigma} \hat{c}^{\dagger}_{i\sigma}\hat{c}_{j\sigma} - U \sum_{i} \hat{n}_{i\uparrow}\hat{n}_{i\downarrow} - (\mu - U) \sum_{i} \hat{n}_{i\downarrow} \\ &- (-\mu) \sum_{i} \hat{n}_{i\uparrow} + \mu N \end{aligned} \tag{E.2}$$

Which simplifies at half-filling for $\mu = U/2$:

$$\begin{aligned} \hat{\mathcal{H}}' = &- t \sum_{\langle i,j \rangle} \sum_{\sigma} \hat{c}^{\dagger}_{i\sigma}\hat{c}_{j\sigma} - U \sum_{i} \hat{n}_{i\uparrow}\hat{n}_{i\downarrow} + \frac{U}{2} \sum_{i} (\hat{n}_{i\uparrow} + \hat{n}_{i\downarrow}) \\ &+ \mu N \end{aligned} \tag{E.3}$$

Where N is the number of sites of the lattice. This Hamiltonian is equivalent to the Hubbard Hamiltonian at half-filling with an opposite U and an inessential energy constant. This transformation shows how observables are modified when inverting the

sign of the interaction U, hence the correspondence between the attractive and repulsive half-filled Hubbard models.

Double occupancy :

Under this transformation of the second quantization operators the double occupancy transforms as follow :

$$\begin{aligned} D &= \frac{1}{N}\sum_i \langle \hat{n}_{i\uparrow}\hat{n}_{i\downarrow}\rangle_{\hat{\mathcal{H}}_{Hubbard}} \rightarrow \\ &\frac{1}{N}\sum_i \langle \hat{n}_{i\uparrow}(1-\hat{n}_{i\downarrow})\rangle_{\hat{\mathcal{H}}'} = \langle \hat{n}_{\uparrow}\rangle - D \end{aligned} \tag{E.4}$$

But since both Hamiltonian are equivalent with changing the sign of U and we obtain (for every T, U, and t) at half-filling :

$$D(-U) = 0.5 - D(U) \tag{E.5}$$

Which can be rewritten recalling that $D(U=0) = 0.25$:

$$(D(U) - D(U=0)) = -(D(U) - D(U=0)) \tag{E.6}$$

Therefore the double-occupancy, minus its value at zero interaction, is an odd function of the interaction.

Magnetization :

For the repulsive model we know that the system shows at half-filling a phase transition towards an antiferromagnetic state breaking the SU(2) spin inversion symmetry. How does this order change as we inverse the sign of the interaction U ?

Performing the transformation described in Eq. E.1 we have a look at the transformation of different operators. We write on the left side the operators at $U > 0$ for the repulsive case, and on the left their corresponding operator in the repulsive $U < 0$ case :

$$\begin{aligned} (-1)^i \hat{S}_i^z = (-1)^i(\hat{n}_{i\downarrow} - \hat{n}_{i\uparrow}) &\rightarrow (-1)^i(\hat{n}_{i\uparrow} + \hat{n}_{i\downarrow} - 1) \\ (-1)^i \hat{S}_i^+ = (-1)^i(\hat{c}_{i\downarrow}^\dagger \hat{c}_{i\uparrow}) &\rightarrow \hat{c}_{i\downarrow}^\dagger \hat{c}_{i\uparrow}^\dagger \\ h\hat{S}_i^z &\rightarrow h(\hat{n}_{i\uparrow} + \hat{n}_{i\downarrow} - 1) \end{aligned} \tag{E.7}$$

Therefore we see that the staggered magnetization which is the order parameter of the antiferromagnetic phase in the $U > 0$ model corresponds in the z direction to the order parameter of a charge density wave order (first line), and in the other directions (second line), to the order parameter of s-wave superconductivity. These orders are equivalent through the global spin rotation symmetry of the system. Thus, at half-filling the phase diagram of the Hubbard model is symmetric as $U \rightarrow -U$ with the Néel order becoming

a superconducting order. Moreover, the last line shows that a change in the chemical potential at $U < 0$ from its value at half-filling corresponds to adding a uniform Zeeman field in the $U > 0$ model. Hence doping the attractive model is equivalent to adding a uniform field in the half-filled repulsive model.

Appendix F

Symmetry of the R propagator

Out-of equilibrium the R function is defined on the full Baym-Kadanoff contour by :

$$R(z,z') = -iT_{\bar{\mathcal{C}}} \exp(-i\int_{z'}^{z} \mathcal{H}_{loc}(z_1)\mathrm{d}z_1 - i\int_{z'}^{z} \mathrm{d}z_1\mathrm{d}z_2\Delta(z_1,z_2)d^\dagger(z_1)d(z_2)) \tag{F.1}$$

Where R is expressed in terms of 9 different functions depending on the different branches of the contour.

In the steady-state limit, we can drop the imaginary-time axis. From the Keldysh contour, and supposing R invariant by translation in time (we set $z' = 0$), we get the two components :

$$\begin{aligned}
R^<(t,0) &= -iT_{\mathcal{C}} \exp(-it\mathcal{H}_{\mathrm{loc}} - i\int_0^t \mathrm{d}t_1 \int_{0,t1>t2}^{t} \mathrm{d}t_2\Delta^>(t_1-t_2)d^\dagger(t_1)d(t_2) \\
&\quad - i\int_0^t \mathrm{d}t_1 \int_{0,t2>t1}^{t} \mathrm{d}t_2\Delta^<(t_1-t_2)d^\dagger(t_1)d(t_2)) \\
R^>(t,0) &= -iT_{\mathcal{C}} \exp(-it\mathcal{H}_{\mathrm{loc}} - i\int_0^{+\infty} \mathrm{d}t_1 \int_{0,t1>t2}^{+\infty} \mathrm{d}t_2\Delta^>(t_1-t_2)d^\dagger(t_1)d(t_2) \\
&\quad - i\int_0^{+\infty} \mathrm{d}t_1 \int_{0,t2>t1}^{+\infty} \mathrm{d}t_2\Delta^<(t_1-t_2)d^\dagger(t_1)d(t_2) \\
&\quad - i\int_t^{+\infty} \mathrm{d}t_1 \int_{t,t2>t1}^{+\infty} \mathrm{d}t_2\Delta^>(t_1-t_2)d^\dagger(t_1)d(t_2) \\
&\quad - i\int_t^{+\infty} \mathrm{d}t_1 \int_{t,t1>t2}^{+\infty} \mathrm{d}t_2\Delta^<(t_1-t_2)d^\dagger(t_1)d(t_2) \\
&\quad + i\int_0^{+\infty} \mathrm{d}t_1 \int_{t}^{+\infty} \mathrm{d}t_2\Delta^>(t_1-t_2)d^\dagger(t_1)d(t_2) \\
&\quad + i\int_t^{+\infty} \mathrm{d}t_1 \int_{0}^{+\infty} \mathrm{d}t_2\Delta^<(t_1-t_2)d^\dagger(t_1)d(t_2))
\end{aligned} \tag{F.2}$$

Which are supposed invariant by translation and we note $R(t) = R(t,0)$. With this

we verify the usual properties on R :

$$\begin{aligned} R^<(t,0)^\dagger &= iT_\mathcal{C} \exp(-i(-t)\mathcal{H}_{\text{loc}} - i\int_0^t \mathrm{d}t_1 \int_{0,t1>t2}^t \mathrm{d}t_2 \Delta^>(t_2-t_1) d^\dagger(t_2) d(t_1) \\ &- i\int_0^t \mathrm{d}t_1 \int_{0,t2>t1}^t \mathrm{d}t_2 \Delta^<(t_2-t_1) d^\dagger(t_2) d(t_1)) \\ &= iT_\mathcal{C} \exp(-i(-t)\mathcal{H}_{\text{loc}} - i\int_0^t \mathrm{d}t_2 \int_0^{t_2} \mathrm{d}t_1 \Delta^>(t_1-t_2) d^\dagger(t_1) d(t_2) \\ &- i\int_0^t \mathrm{d}t_2 \int_{t_2}^t \mathrm{d}t_1 \Delta^<(t_1-t_2) d^\dagger(t_1) d(t_2)) \end{aligned} \tag{F.3}$$

And since :

$$\int_0^t \mathrm{d}t_2 \int_0^{t_2} \mathrm{d}t_1 = \int_0^t \mathrm{d}t_1 \int_{t_1}^t \mathrm{d}t_2 = \int_t^0 \mathrm{d}t_1 \int_t^{t_1} \mathrm{d}t_2 \tag{F.4}$$

And similarly :

$$\int_0^t \mathrm{d}t_2 \int_{t_2}^t \mathrm{d}t_1 = \int_t^0 \mathrm{d}t_1 \int_{t_1}^0 \mathrm{d}t_2 \tag{F.5}$$

And we get supposing the time-translation invariance :

$$R^<(t)^\dagger = R^<(t,0)^\dagger = -R^<(0,t) = -R^<(-t) \tag{F.6}$$

We get the same relation for the greater component with a similar calculation.

Appendix G

Spectral representation of the local propagator

We define $\tilde{R}^{>}(t) = \theta(t)R^{>}(t)$ whose spectral function is the real function $iR^{>}(\omega)/2\pi$. We can write by extending $\tilde{R}$ to the complex plane :

$$\tilde{R}^{>}(z) = \frac{1}{2\pi}\int_{-\infty}^{+\infty} \frac{iR^{>}(\omega)}{z-\omega}\mathrm{d}\omega \tag{G.1}$$

On the real frequency axis it gives :

$$\tilde{R}^{>}(\omega) = \frac{1}{2\pi}\int_{-\infty}^{+\infty} \frac{iR^{>}(\omega')}{\omega-\omega'+i\eta}\mathrm{d}\omega' \tag{G.2}$$

Which corresponds to the Fourier transform of $\tilde{R}^{>}(t) = \theta(t)R(t)$. At equilibrium, using the steady-state and noting $U(t,t') = e^{-i(t-t')\mathcal{H}}$ the time-evolution operator :

$$R^{>}(t) = -i\mathrm{Tr}_{\mathrm{bath}}[\frac{e^{-\beta\mathcal{H}_{\mathrm{bath}}}}{Z_{\mathrm{bath}}}U_{\mathrm{bath}}(0,t)U(t,0)] \tag{G.3}$$

And we recall :

$$R(\tau) = -\frac{1}{Z_{\mathrm{bath}}}Tr_{\mathrm{bath}}[e^{-(\beta-\tau)\mathcal{H}_{\mathrm{bath}}}e^{-\tau(\mathcal{H}_{\mathrm{loc}}+\mathcal{H}_{\mathrm{hyb}}+\mathcal{H}_{\mathrm{bath}})}] \tag{G.4}$$

We see that at equilibrium, $R(\tau)$ is the analytic continuation of $R^{>}(t)$ for $t \to -i\tau$. We have a similar relation for $R^{<}$:

$$\begin{aligned} R^{>}(-i\tau) &= iR(\tau) \\ R^{<}(-i\tau) &= i\frac{Z_0}{Z}R(\tau+\beta) \end{aligned} \tag{G.5}$$

where Z_0 is the partition function of the isolated system. And therefore we have :

$$R(\tau) = -i \int \frac{\mathrm{d}\omega}{2\pi} R^{>}(\omega) e^{-\omega\tau} \tag{G.6}$$

Recalling the frequency definition of R in Eq.V.14 we see that the imaginary frequency R function is the analytic continuation of $\tilde{R}^{>}(\omega)$:

$$R(\omega) = -i \int_0^{+\infty} \mathrm{d}\tau \int \frac{\mathrm{d}\omega}{2\pi} R^{>}(\omega') e^{-\omega'\tau} e^{i\omega\tau} = i \int \frac{\mathrm{d}\omega}{2\pi} \frac{R^{>}(\omega')}{i\omega - \omega'} = \tilde{R}^{>}(i\omega) \tag{G.7}$$

Which explains that they obey the same equation. We can deduce the fluctuation-dissipation theorem for the R propagator at equilibrium from Eq. G.5, by noticing that $iR(\tau) = R^{>}(-i\tau) = R^{<}(-i\tau + i\beta)Z/Z_0$. After performing a Fourier transform we get :

$$R^{<}(\omega) = \frac{Z_0}{Z} R^{>}(\omega) e^{-\beta\omega} \tag{G.8}$$

These analytic continuation properties can also be seen in NCA by taking the analytic continuation of the Volterra equations in real and imaginary time as they completely define the local propagator given the associated initial conditions.

Appendix H

R and S functions

We study the system for different temperatures β with $U = 6$ and $\mu = 3U/4$. We show the evolution of the R and S functions when decreasing the temperature. The eigen-energies for the local system are : $E = [0, -\mu, -\mu, U - 2\mu]$. For this set of parameters we are in the regime of the Anderson impurity model with a density around $n >\sim 0.5$ so that we are away from half-filling.

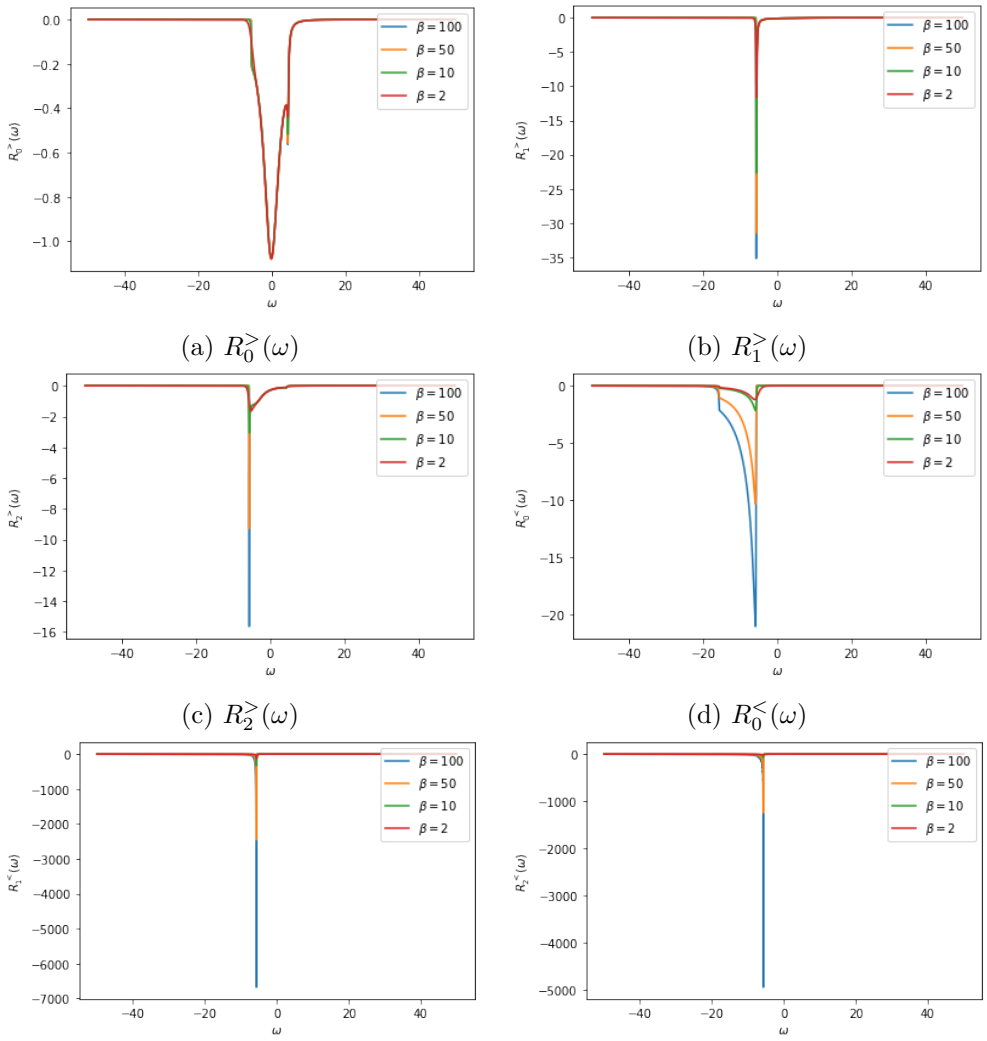

(a) $R_0^>(\omega)$ (b) $R_1^>(\omega)$

(c) $R_2^>(\omega)$ (d) $R_0^<(\omega)$

(e) $R_1^<(\omega)$ (f) $R_2^<(\omega)$

Figure H.1: R functions for different temperatures

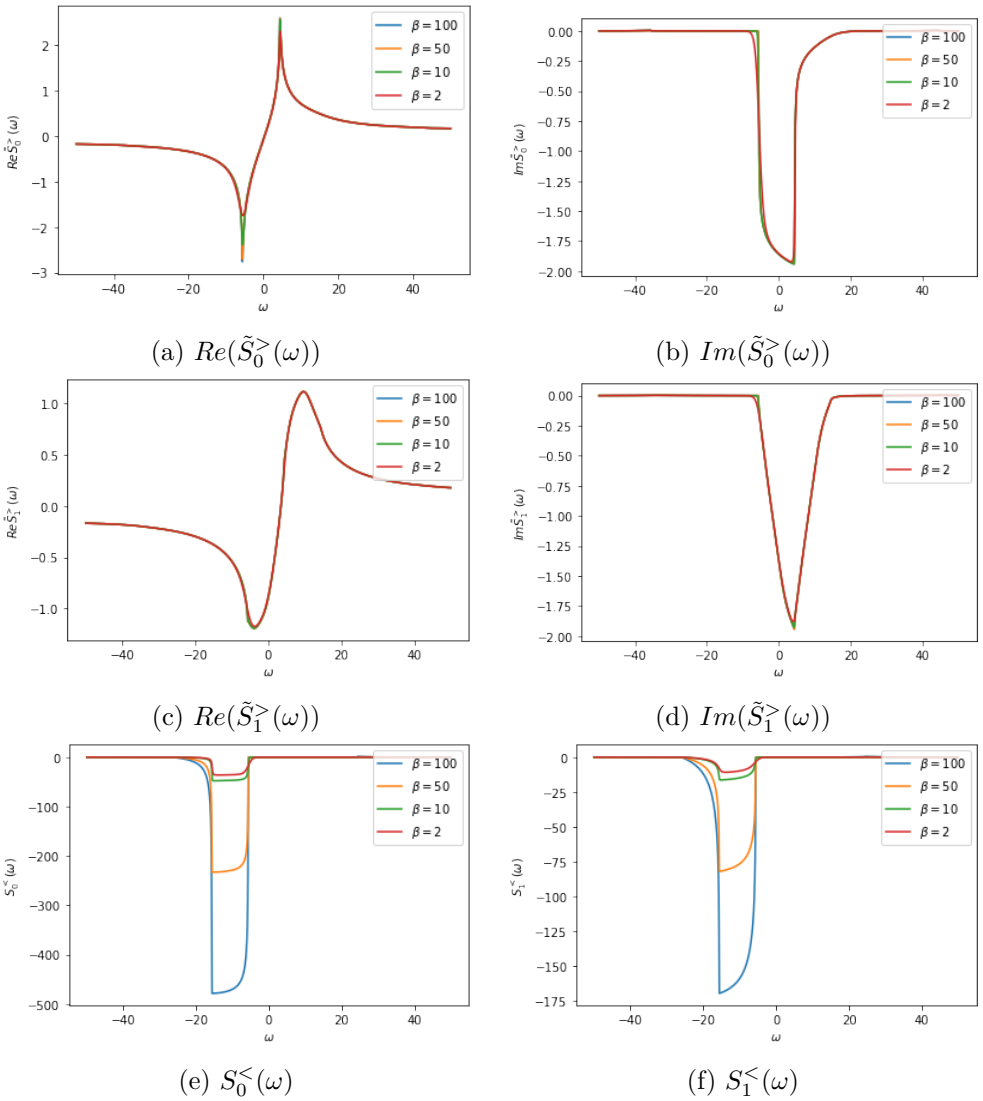

(a) $Re(\tilde{S}_0^{>}(\omega))$ (b) $Im(\tilde{S}_0^{>}(\omega))$

(c) $Re(\tilde{S}_1^{>}(\omega))$ (d) $Im(\tilde{S}_1^{>}(\omega))$

(e) $S_0^{<}(\omega)$ (f) $S_1^{<}(\omega)$

Figure H.2: Example of S and $\tilde{S}$ functions for different temperatures. The $S^{<}(\omega)$ functions are purely imaginary.

Appendix I

Environmental impact of numerical methods

The numerical results presented in Chapter IV are obtained through computations made on computational resources of TGCC (Très Grand Centre de Calcul du CEA) and IDRIS (Institut du développement et des ressources en informatique scientifique) attributed by GENCI (Grand Equipment National de Calcul Intensif). The Monte Carlo computations and CDet recursion can be very greedy in numerical resources and we propose in this appendix to estimate their environmental impact which is essentially linked to the generated emission of green house gases and of CO_2.

Far from being negligible, the contribution of data centers and high performance computing to the global CO_2 emissions can be estimated to a quarter of the emissions of modern country like France (around 100Mt) [78]. However this impact is rarely mentioned or thought of when conducting greedy numerical studies. In a concern of transparency we want to estimate the impact of the three years of computations on high performance cluster machines presented in this thesis.

In the following we use the energetic emission of France to evaluate the impact of electricity consumption which is about $60g/kWh$ of CO_2 emissions. Estimating the emissions provoked by computational centers is not an easy task. The electric energy used for one hour on one CPU core on the super-calculator Jean-Zay (IDRIS) has been estimated by the CNRS [88] to be of $10Wh$. The cluster uses a heat recovery network which in the end reduces this energetically consumption to $5.3Wh$. However the calculation leading to this number is not detailed, and we fear that it only includes the electrical consumption of the cluster and not the emissions due to its overall operating and building. Here we rely on a realistic, complete and detailed estimation which is given in [12]. It gives the value of $3.6g$ of CO_2 emissions for 1 h.core computation. Taking into account the heat recovery network effect would only reduce this amount by $0.3g$ to a final value of $3.3g$.

The CDet computations are very greedy and usually one computation requires 20 hours on a hundred cores. We estimate the number of CPU hours used for all our computations on the Hubbard model to amount to 1.9×10^6 hours. This corresponds to an emission of 6.3 tones of CO_2. This almost compares to the yearly emissions on average of

a someone living in France ($\sim$ 9 tones) and corresponds approximately to the emissions of 6 passengers flying from Paris to New-York.

Appendix J

Preprint papers

Precise many-body simulations of antiferromagnetic phases using broken-symmetry perturbative expansions

Renaud Garioud[1,2],* Fedor Šimkovic IV[1,2], Riccardo Rossi[3,4], Gabriele Spada[5,6], Thomas Schäfer[7], Félix Werner[5], and Michel Ferrero[1,2]

[1] *CPHT, CNRS, Ecole Polytechnique, Institut Polytechnique de Paris, Route de Saclay, 91128 Palaiseau, France*
[2] *Collège de France, 11 place Marcelin Berthelot, 75005 Paris, France*
[3] *Institute of Physics, École Polytechnique Fédérale de Lausanne (EPFL), CH-1015 Lausanne, Switzerland*
[4] *Sorbonne Université, CNRS, Laboratoire de Physique Théorique de la Matière Condensée, LPTMC, F-75005 Paris, France*
[5] *Laboratoire Kastler Brossel, École Normale Supérieure - Université PSL, CNRS, Sorbonne Université, Collège de France, 75005 Paris, France*
[6] *INO-CNR BEC Center and Dipartimento di Fisica, Università di Trento, 38123 Trento, Italy*
[7] *Max-Planck-Institut für Festkörperforschung, Heisenbergstraße 1, 70569 Stuttgart, Germany*

(Dated: November 1, 2022)

We introduce a spin-symmetry-broken extension of the connected determinant algorithm [Phys. Rev. Lett. 119, 045701 (2017)]. The resulting systematic perturbative expansions around an antiferromagnetic state allow for numerically exact calculations directly inside a magnetically ordered phase. We show new precise results for the magnetic phase diagram and thermodynamics of the three-dimensional cubic Hubbard model at half-filling. With detailed computations of the order parameter in the low to intermediate-coupling regime, we establish the Néel phase boundary. The critical behavior in its vicinity is shown to be compatible with the $O(3)$ Heisenberg universality class. By determining the evolution of the entropy with decreasing temperature through the phase transition we identify the different physical regimes at $U/t=4$. We provide quantitative results for several thermodynamic quantities deep inside the antiferromagnetic dome up to large interaction strengths and investigate the crossover between the Slater and Heisenberg regimes.

In strongly correlated materials, such as high temperature superconducting copper oxides or iron-based pnictides, the interactions between electrons yield intricate phase diagrams, exhibiting, e.g., magnetically or charge-ordered phases, superconductivity or Mott insulating behaviors. Understanding the properties of these different phases, their interplay and driving mechanisms is one of the outstanding challenges of modern condensed matter theory.

From the theoretical point of view, one of the simplest models to investigate phase transitions is the three-dimensional cubic Hubbard model [1–6] given by the Hamiltonian

$$\hat{\mathcal{H}} = -t \sum_{\langle i,j \rangle} \sum_{\sigma} \hat{c}^{\dagger}_{i\sigma} \hat{c}_{j\sigma} + U \sum_{i} \hat{n}_{i\uparrow} \hat{n}_{i\downarrow} - \mu \sum_{i\sigma} \hat{n}_{i\sigma}, \quad (1)$$

where t is the hopping amplitude between nearest-neighbor sites $\langle i,j \rangle$ on a cubic lattice, $U \geq 0$ the on-site Coulomb interaction, μ the chemical potential, $\hat{n}_{i\sigma} = \hat{c}^{\dagger}_{i\sigma} \hat{c}_{i\sigma}$ and $\hat{c}^{\dagger}_{i\sigma}$ creates an electron on site i with spin σ. At half-filling ($\mu = U/2$), the ground state has antiferromagnetic long-range spin order. In three dimensions this SU(2) symmetry-broken phase survives up to the Néel temperature $T_N(U)$ above which the system becomes paramagnetic. While there is qualitative understanding of the mechanisms that produce the antiferromagnetic order both at weak and strong coupling, obtaining unbiased quantitative results, especially close to the phase transition and inside the ordered phase, is still very challenging [7–16]. Therefore, despite its apparent simplicity, the Hubbard model on the cubic lattice is an ideal platform to explore the potential of new algorithms before engaging in the study of more realistic systems. The model was realized in cold-atomic experiments on optical lattices where antiferromagnetism is under active investigation [17–25].

The main challenge for theoretical approaches based on finite size lattices is to properly account for the increasing correlation length in the vicinity of a second order phase transition, and, as such, to extrapolate to the thermodynamic limit. In that respect, the diagrammatic Monte Carlo approach [26–28] is very promising as it offers the possibility to investigate a system directly in the thermodynamic limit. The method stochastically computes the coefficients a_k appearing in the perturbative expansion in U of a physical observable, $\mathcal{A}(U) = \sum_k a_k U^k$ in the simplest formulation. The computational cost rapidly increases with increasing perturbation orders and only so many coefficients can be computed before the statistical variance becomes overwhelming. Nevertheless, important improvements [29, 30] make it now possible to reach perturbation orders as large as $10-12$. In the context of the repulsive Hubbard model, diagrammatic Monte Carlo has already been successfully applied to non-perturbative regimes in the two-dimensional square lattice [28, 31–40].

In the usual formulation, the perturbation series is constructed starting from the non-interacting ($U = 0$) SU(2)-symmetric solution of Eq. (1). This allows to obtain results for the interacting system in its paramagnetic regime. As the phase transition to the antiferromagnetic state is approached, however, the resummation of the series becomes increasingly difficult. The reason is that

a second-order phase transition happening at $U = U_c$ is accompanied by a singularity in the complex-U plane for observables $\mathcal{A}(U)$ that show a non-analyticity at U_c. Consequently, investigating the antiferromagnetic transition in the cubic Hubbard model can only be done from temperatures above and not too close to the Néel temperature T_N. Very recently, the spin structure factor perturbation series has been computed this way in the paramagnetic phase of the cubic Hubbard model [39]. Assuming the critical behavior in the vicinity of the phase transition, the authors were able to accurately compute T_N in the weak-to-intermediate coupling regime both at half-filling and at finite doping. This approach is however not able to address the properties of the model inside the ordered phase.

In this Letter, we take a complementary approach and compute the perturbation series for physical observables within the antiferromagnetic phase of the cubic half-filled Hubbard model. We show that our broken-symmetry approach to perturbative expansions is a powerful tool for studying magnetically ordered phases and phase transitions. Our results are obtained directly in the thermodynamic limit and, thus, do not involve any finite size scaling. We document the vanishing of the magnetic order parameter at T_N and the corresponding critical exponent β and report and discuss the behavior of the double occupancy, grand potential and entropy across the phase transition and inside the ordered phase.

Method. The possibility to construct symmetry-broken perturbation series comes from a flexibility in the choice of the starting point around which the perturbation is expanded. This freedom has been extensively applied to diagrammatic Monte Carlo computations in the non-magnetic phase to improve the convergence properties of the series [36–38, 41–49]. Very recently, it has been used to construct a perturbation theory around a BCS state and inside the superconducting phase of the attractive Hubbard model [50]. Here, we follow similar steps and introduce the modified Hamiltonian

$$\begin{aligned}\hat{\mathcal{H}}_\xi = &-t\sum_{\langle i,j\rangle}\sum_\sigma \hat{c}^\dagger_{i\sigma}\hat{c}_{j\sigma} - \xi\frac{U}{2}\sum_{i\sigma}\hat{n}_{i\sigma} \\ &+ (1-\xi)h\sum_i p_i\hat{S}^z_i + \xi U\sum_i \hat{n}_{i\uparrow}\hat{n}_{i\downarrow},\end{aligned} \tag{2}$$

where $\hat{S}^z_i = (\hat{n}_{i\uparrow} - \hat{n}_{i\downarrow})/2$ and $p_i = \pm 1$ depending on whether i belongs to one or the other sub-lattice of the bipartite cubic lattice. Observables are expressed as perturbation series in ξ and physical results are recovered for $\xi = 1$ where both Hamiltonians become equivalent, $\hat{\mathcal{H}}_{\xi=1} = \hat{\mathcal{H}}$. The perturbation series in ξ is built around a state that breaks the SU(2) spin rotation symmetry of the original Hamiltonian. Indeed, $\hat{\mathcal{H}}_{\xi=0}$ describes free electrons in a staggered external magnetic field h. Because this state breaks the symmetry from the start, the perturbation series can describe a magnetically ordered phase without the need of undergoing a phase transition. Accordingly, singularities in the complex-ξ plane associated to the phase transition are avoided.

We compute the coefficients of the perturbation series with the CDet [29] algorithm using a rejection-free many-configuration Monte Carlo [51] as well as a fast principal minor algorithm [52, 53] to improve the speed of the determinant calculations. The series are evaluated with different resummation techniques [54, 55] that serve as a basis to determine the error bars of our results, see Supplementary Material [56]. While the diagrammatic expansion can be formulated directly in the thermodynamic limit, in practice, we use a system with $L^3 = 20^3$ sites for our computations. We have carefully checked that this is large enough to avoid finite-size effects, even in the vicinity of the phase transition, as discussed in the Supplementary Material [56]. In the following, we will denote this spin symmetry-broken algorithm by CDet(AF).

In the Hamiltonian of Eq. (2), the field h can be chosen arbitrarily and different choices for h define different series. In order to obtain the best convergence and to cross-check different results, we have computed several values in the range $0 \leq h \leq h_{\mathrm{MF}}$, where h_{MF} is the effective field found in the mean-field solution of Eq. (1). In the following, we will parameterize $h = \alpha h_{\mathrm{MF}}$ with $0 \leq \alpha \leq 1$. Note that when $\alpha = 0$, the perturbation series is the usual expansion limited to the paramagnetic regime.

For our analysis we compute the double occupancy $D = \langle \hat{n}_{i\uparrow}\hat{n}_{i\downarrow}\rangle = E_{\mathrm{pot}}/U$, the staggered magnetization $m = \langle \hat{n}_{i\uparrow} - \hat{n}_{i\downarrow}\rangle$ (which is the order parameter for the Néel phase transition) and the grand potential per lattice site $-\Omega/L^3 = P$ where L is the linear system size

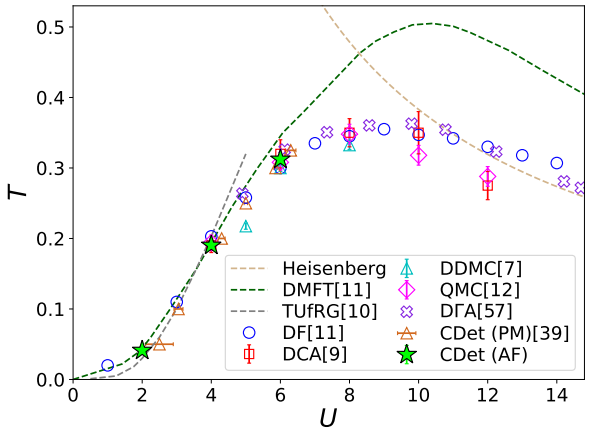

FIG. 1. Comparison of the Néel temperature $T_N(U)$ (lime stars), obtained with the symmetry broken CDet(AF), with other numerical methods. References for the numerical methods data are indicated in the legend.

of the cubic lattice, and P the thermodynamic pressure. The grand potential computations enable us to determine the entropy density and magnetization through

$$s = -\frac{\partial \Omega}{L^3 \partial T} \qquad m = -\left.\frac{\partial \Omega}{L^3 \partial H_{\rm ext}}\right|_{H_{\rm ext}=0}, \qquad (3)$$

where $H_{\rm ext}$ is an external Zeeman staggered field whose sign alternates on neighboring sites in the form of an additional term to the Hubbard Hamiltonian Eq. (1): $H_{\rm ext} \sum_i p_i \hat{S}_i^z$. All energies are expressed in units of the hopping amplitude $t=1$.

Phase diagram and universality class. We start our study by determining the Néel temperature for different values of the interaction in order to establish the magnetic phase diagram of the system.

In Fig. 1 we compare our values for the critical temperature $T_N(U)$ from CDet(AF) against numerous other numerical methods [7, 9–12, 39, 57]. The Néel temperature is expected to increase with increasing interaction at small U since the transition is driven by the Slater mechanism [58] and reaches a maximum in the intermediate coupling around $U \simeq 6-10$, before decreasing like $T_N \simeq 0.946J$ [59] in the high-U Heisenberg limit, where $J = 4t^2/U$ is the super-exchange coupling. We have been able to determine the critical temperature up to an intermediate coupling strength of $U = 6$. For $U > 6$, regarding the magnetization, we experience increased difficulty in resumming our perturbation series and loss of Monte Carlo accuracy in the critical region close to the phase transition.

The values of the Néel temperature displayed in Fig. 1 are obtained from the computation of the magnetization as a function of temperature $m(T)$, which we show in Fig. 2. The order parameter m indicates the phase transition by assuming a non-zero value when decreasing the temperature. Thanks to our high precision data, we manage to compute directly the β critical exponent along with the Néel temperature from the critical behaviour $m(T) \simeq a(T_N - T)^\beta$. The obtained values for the critical exponent Fig. 2 (top right) compare remarkably well to the literature values for the $O(3)$ Heisenberg universality class [8, 11, 60, 61]. They establish the first direct computations of the β critical exponent on a fermionic lattice and in the thermodynamic limit. They also yield the Néel temperature with very good accuracy: $T_N(U=2) = 0.0411(8)$, $T_N(U=4) = 0.1902(3)$ and $T_N(U=6) = 0.312(2)$. As shown in Fig. 1, the values that we obtain for the Néel temperature compare well with paramagnetic DiagMC [39] and DCA extrapolated to infinite cluster size [9], as well as to the recently improved dynamical vertex approximation DΓA [57], but are out of the error bounds obtained by finite-size scaling of $L \leq 10$ DDMC data [7]. The critical region, defined as the temperature range $T \in [T_N - \delta T, T_N]$ where $m(T) = a(T_N - T)^\beta$ is a good fit to our data, is of the order of $\delta T \simeq 0.025$ for $U \geq 4$. The magnetization and

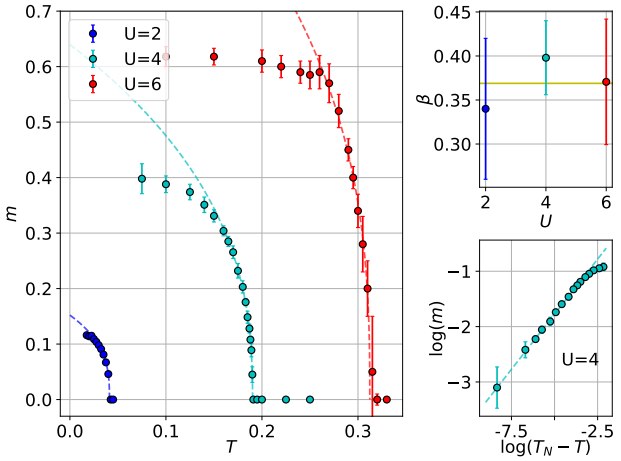

FIG. 2. Magnetization and critical behavior - Left panel: Magnetization m as a function of temperature T for three different values of the interaction U. The dashed curves represent the critical behavior as determined from our data close to the critical temperature fitted with the formula: $m(T) \simeq a(T_N - T)^\beta$. Top right panel: Critical exponent obtained from the three magnetization curves. The gold horizontal band corresponds to the theoretically predicted value of β for the $O(3)$ Heisenberg universality class in [60]. Lower right panel: magnetization as a function of $T_N - T$ at $U = 4$ on a log-log scale. T_N is determined with the critical behavior fit from the left panel. The dashed line corresponds to the fitting curve on the left panel.

the other thermodynamic quantities (see Figs 3 and 4) only have a variation in a temperature interval $\delta T \simeq 0.1$ below T_N before they essentially saturate to their low temperature value. This interval does not seem to expand when increasing the interaction and hence the Néel temperature for $U \geq 4$.

Double occupancy. The signatures of the phase transition can also be read from the double occupancy, shown in Fig. 3. At $U=4$, we observe a singularity in the double occupancy at a temperature in good agreement with the value of the Néel temperature determined in Fig. 2. At this value of the interaction, the double occupancy increases with decreasing temperature in the normal phase because of the Pomeranchuk effect [62–66]. It decreases in the antiferromagnetic phase which is consistent with the Slater mechanism expected at small interaction: The ordered phase is stabilized because of a gain in potential energy $E_{pot} = UD$ and, hence, a lowering of double occupancy at fixed interaction. At higher values of U the double occupancy curve flattens, and within our accuracy, we are not able to document the non-analyticity of the double occupancy at the Néel temperature. We do not observe significant changes of the double occupancy around the Néel temperature at $U = 8$ within the 10^{-2} relative accuracy of our computation. Further work with better sensitivity or studying the kinetic energy would be

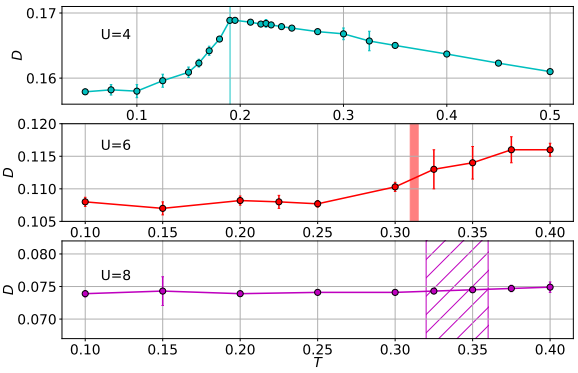

FIG. 3. Double occupancy D as a function of temperature for three different values of the interaction U. The vertical bands at $U = 4$ and $U = 6$ correspond to the estimate of the Néel temperature from our study, while the hashed area at $U = 8$ is an estimate of the Néel transition from other numerical methods displayed in Fig. 1.

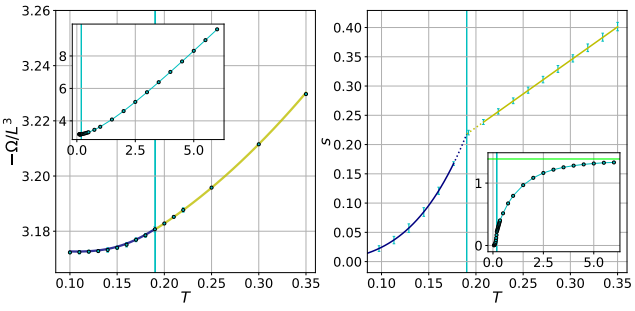

FIG. 4. Left panel: Grand potential density $-\Omega/L^3$ as a function of temperature T at interaction $U = 4$. When not visible the error bar is smaller than the markers. Right panel: Entropy density s as a function of temperature T obtained as derivative of the grand potential fitting curves (see text). The cyan error bars give the error on the entropy curve. We do not have enough data close to the Néel temperature to resolve the critical behaviour of the entropy, and the entropy curve is dashed in this region. The insets are the same plots on a larger temperature range. The lime horizontal line indicates the high temperature limit $s = \log(4)$. On both panels the vertical lines correspond to the value of the Néel temperature obtained in Fig. 2.

needed to clearly document the change from a Slater to a Heisenberg regime with a kinetic-energy driven phase transition, as was done in DMFT and extensions thereof in [67–69].

Grand potential. The grand potential at $U = 4$ is displayed in Fig. 4. In order to evaluate the entropy density from Eq. (3) we suppose a polynomial behavior of the grand potential with temperature. Since $\Omega(T) - \Omega(T = 0) \propto T^4$ for $T \to 0$, we fit the $T < T_N$ data with the expression $-\Omega(T) = -\Omega(T=0) + aT^4 + bT^5 + cT^6$ (cyan curve). At $T > T_N$ we expect a quadratic behavior in the degenerate Fermi liquid regime. The data is well fitted by the expression $-\Omega/L^3(T) = d + eT^2$ (yellow curve). We impose continuity up to first order derivative at $T = T_N$. At higher temperatures $T \geq 0.4$ the grand potential becomes almost linear in temperature $-\Omega(T) \simeq \log(4)T$. The entropy density is then extracted with a finite difference scheme. These different behaviors of the grand potential lead to different physical regimes for the evolution of the entropy density with temperature. In the AF phase the entropy density varies as $s \propto T^3$ at small temperatures. For temperatures just above the transition $T \in [T_N, 0.35]$ the entropy density increases linearly with the temperature which is a signature of a metallic behaviour of the system in this part of the phase diagram. At higher temperatures of the order of the interaction $T \sim U = 4$ the entropy density saturates to $s(T \to +\infty) = \log(4)$.

Magnetically saturated regime at low T. We are now interested in the low temperature properties of the system where the magnetization has reached saturation. We have observed earlier that the magnetization only changes significantly in a shell of size $\delta T \sim 0.1$ below the Néel temperature, so that the region with saturated magnetization represents an important part of the antiferromagnetic dome.

Direct computations of the magnetization become problematic for $U > 6$ because the associated series are difficult to resum. At small temperature it turns out to be more practical to compute the grand potential density and extract the magnetization as its variation with the external field as stated in Eq. (3). More details, and the associated computations are shown in [56].

The directly computed magnetization compares well with differentiating the grand potential as shown in Fig. 5. For $U \geq 6$ we observe no difference between the $T = 0.1$ and $T = 0.2$ curves which shows that the magnetization is already saturated at its zero temperature value. The magnetization will eventually have a maximum with respect to U, but this must happen for values of $U > 18$.

The variations of the double occupancy with the interaction at low temperatures are shown in Fig. 5. In the normal phase the double occupancy is decreasing quasi-linearly with the interaction. In the vicinity of the phase transition we observe good agreement between results for the paramagnetic and symmetry-broken computations. As expected, at the transition U_c we observe a singularity in the double occupancy, and these results can be used to estimate the value of the critical interaction at fixed temperature. The double occupancy decreases faster with increasing interaction when entering the AF phase which is consistent with the Slater mechanism at the transition for values of the critical interaction $U_c < 6$. In the antiferromagnetic phase the double occupancy is a convex

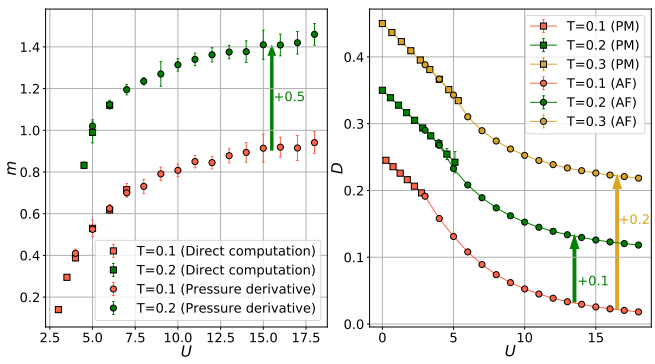

FIG. 5. Left panel: Magnetization as a function of the interaction U for two different values of the temperature. For better visibility the magnetization at $T = 0.2$ is shifted by $+0.5$. The square markers are obtained through direct computation of the order parameter like in Fig. 2. The round markers are obtained by numerically differentiating the grand potential density at an external field $H_{\text{ext}} \to 0$, see Eq. (3). Right panel: Double occupancy D as a function of the interaction U for three different values of the temperature. For better visibility the data at $T = 0.2$ ($T = 0.3$) is shifted by $+0.1$ ($+0.2$). The square markers are in the normal phase and are obtained with the paramagnetic CDet algorithm (no symmetry-breaking at $\alpha = 0$). The round markers are obtained with the antiferromagnetic symmetry-broken CDet with $\alpha \neq 0$ (AF).

function of the interaction which decays slowly to zero at infinite interaction. At $U > 7$ we cannot distinguish between the different temperatures within our accuracy as expected from Fig. 3.

Conclusions. To conclude, we have applied the new algorithmic developments of the symmetry-broken CDet approach to produce the first high order diagrammatic computations inside an antiferromagnetic phase and directly in the thermodynamic limit. We have provided a quantitative description of the antiferromagnetic phase of the cubic half-filled Hubbard model. After determining the critical behavior of the system and its phase diagram we have reported resummed results at small temperatures deep inside the antiferromagnetic dome up to high interactions $U = 18$. We have shown that diagrammatic Monte Carlo is a powerful tool to study the physics of ordered systems with no need for an embedding scheme or system size extrapolation. A more advanced, nonlinear chemical-potential shift combined with other CDet extensions [38] may lead to further improvements for describing the critical behaviour in the strong-coupling Heisenberg part of the antiferromagnetic dome. This symmetry-broken expansion could be applied to incommensurate orders in the doped regime, similarly to what was done in the normal phase [39] or with embedding methods [61]. Another interesting possibility would be to extend our study by including an anisotropic hopping term $t_{\text{perp}} < t$ in the z-direction (similarly to what was done in [70]) in order to investigate how the magnetic properties are modified as the two-dimensional limit is approached. This application would be especially relevant for the physics of cuprate superconductors.

The authors are grateful to A. Georges, A.J. Kim, E. Kozik, C. Lenihan, G. Rohringer, and J. Stobbe for valuable discussions. This work was granted access to the HPC resources of TGCC and IDRIS under the allocations A0110510609 attributed by GENCI (Grand Equipement National de Calcul Intensif). This work has been supported by the Simons Foundation within the Many Electron Collaboration framework. High Performance Computing resources were provided by the IT support team of CPHT laboratory.

* garioudrenaud@gmail.com

[1] J. Hubbard and Brian Hilton Flowers. Electron correlations in narrow energy bands. *Proc. R. Soc. London, Sect. A*, 276(1365):238–257, 1963. URL: https://royalsocietypublishing.org/doi/abs/10.1098/rspa.1963.0204, doi:10.1098/rspa.1963.0204.

[2] J. Hubbard and Brian Hilton Flowers. Electron correlations in narrow energy bands III. An improved solution. *Proc. R. Soc. London, Sect. A*, 281(1386):401–419, 1964. URL: https://royalsocietypublishing.org/doi/abs/10.1098/rspa.1964.0190, doi:10.1098/rspa.1964.0190.

[3] Junjiro Kanamori. Electron Correlation and Ferromagnetism of Transition Metals. *Prog. Theor. Phys.*, 30(3):275–289, 09 1963. doi:10.1143/PTP.30.275.

[4] Martin C. Gutzwiller. Effect of Correlation on the Ferromagnetism of Transition Metals. *Phys. Rev. Lett.*, 10:159–162, Mar 1963. URL: http://link.aps.org/doi/10.1103/PhysRevLett.10.159, doi:10.1103/PhysRevLett.10.159.

[5] Daniel P. Arovas, Erez Berg, Steven A. Kivelson, and Srinivas Raghu. The Hubbard Model. *Annual Review of Condensed Matter Physics*, 13(1):239–274, 2022. arXiv:https://doi.org/10.1146/annurev-conmatphys-031620-102024, doi:10.1146/annurev-conmatphys-031620-102024.

[6] Mingpu Qin, Thomas Schäfer, Sabine Andergassen, Philippe Corboz, and Emanuel Gull. The Hubbard Model: A Computational Perspective. *Annual Review of Condensed Matter Physics*, 13(1):275–302, 2022. arXiv:https://doi.org/10.1146/annurev-conmatphys-090921-033948, doi:10.1146/annurev-conmatphys-090921-033948.

[7] E. Kozik, E. Burovski, V. W. Scarola, and M. Troyer. Néel temperature and thermodynamics of the half-filled three-dimensional Hubbard model by diagrammatic determinant Monte Carlo. *Phys. Rev. B*, 87:205102, May 2013. URL: https://link.aps.org/doi/10.1103/PhysRevB.87.205102, doi:10.1103/PhysRevB.87.205102.

[8] G. Rohringer, A. Toschi, A. Katanin, and K. Held. Critical Properties of the Half-Filled Hubbard Model in Three Dimensions. *Phys. Rev. Lett.*, 107:256402,

Dec 2011. URL: https://link.aps.org/doi/10.1103/PhysRevLett.107.256402, doi:10.1103/PhysRevLett.107.256402.

[9] P. R. C. Kent, M. Jarrell, T. A. Maier, and Th. Pruschke. Efficient calculation of the antiferromagnetic phase diagram of the three-dimensional Hubbard model. *Phys. Rev. B*, 72:060411, Aug 2005. URL: https://link.aps.org/doi/10.1103/PhysRevB.72.060411, doi:10.1103/PhysRevB.72.060411.

[10] J. Ehrlich and C. Honerkamp. Functional renormalization group for fermion lattice models in three dimensions: Application to the Hubbard model on the cubic lattice. *Phys. Rev. B*, 102:195108, Nov 2020. URL: https://link.aps.org/doi/10.1103/PhysRevB.102.195108, doi:10.1103/PhysRevB.102.195108.

[11] Daniel Hirschmeier, Hartmut Hafermann, Emanuel Gull, Alexander I. Lichtenstein, and Andrey E. Antipov. Mechanisms of finite-temperature magnetism in the three-dimensional Hubbard model. *Phys. Rev. B*, 92:144409, Oct 2015. URL: https://link.aps.org/doi/10.1103/PhysRevB.92.144409, doi:10.1103/PhysRevB.92.144409.

[12] R. Staudt, M. Dzierzawa, and A. Muramatsu. Phase diagram of the three-dimensional hubbard model at half filling. *The European Physical Journal B - Condensed Matter and Complex Systems*, 2000. doi:10.1007/s100510070120.

[13] A. N. Tahvildar-Zadeh, J. K. Freericks, and M. Jarrell. Magnetic phase diagram of the Hubbard model in three dimensions:The second-order local approximation. *Phys. Rev. B*, 55:942–946, Jan 1997. URL: https://link.aps.org/doi/10.1103/PhysRevB.55.942, doi:10.1103/PhysRevB.55.942.

[14] G. Rohringer and A. Toschi. Impact of nonlocal correlations over different energy scales: A dynamical vertex approximation study. *Phys. Rev. B*, 94:125144, Sep 2016. URL: https://link.aps.org/doi/10.1103/PhysRevB.94.125144, doi:10.1103/PhysRevB.94.125144.

[15] Sergei Iskakov and Emanuel Gull. Phase transitions in partial summation methods: Results from the three-dimensional Hubbard model. *Phys. Rev. B*, 105(4):045109, January 2022. arXiv:2110.06857, doi:10.1103/PhysRevB.105.045109.

[16] G. Rohringer, H. Hafermann, A. Toschi, A. A. Katanin, A. E. Antipov, M. I. Katsnelson, A. I. Lichtenstein, A. N. Rubtsov, and K. Held. Diagrammatic routes to nonlocal correlations beyond dynamical mean field theory. *Rev. Mod. Phys.*, 90:025003, May 2018. URL: https://link.aps.org/doi/10.1103/RevModPhys.90.025003, doi:10.1103/RevModPhys.90.025003.

[17] Leticia Tarruell and Laurent Sanchez-Palencia. Quantum simulation of the Hubbard model with ultracold fermions in optical lattices. *Comptes Rendus Physique*, 19(6):365–393, 2018. Quantum simulation / Simulation quantique. URL: https://www.sciencedirect.com/science/article/pii/S1631070518300926, doi:https://doi.org/10.1016/j.crhy.2018.10.013.

[18] Russell A. Hart, Pedro M. Duarte, Tsung-Lin Yang, Xinxing Liu, Thereza Paiva, Ehsan Khatami, Richard T. Scalettar, Nandini Trivedi, David A. Huse, and Randall G. Hulet. Observation of antiferromagnetic correlations in the Hubbard model with ultracold atoms. *Nature*, 519(7542):211–214, Mar 2015. doi:10.1038/nature14223.

[19] Anton Mazurenko, Christie S. Chiu, Geoffrey Ji, Maxwell F. Parsons, Márton Kanász-Nagy, Richard Schmidt, Fabian Grusdt, Eugene Demler, Daniel Greif, and Markus Greiner. A cold-atom Fermi–Hubbard antiferromagnet. *Nature*, 545(7655):462–466, May 2017. doi:10.1038/nature22362.

[20] Daniel Greif, Gregor Jotzu, Michael Messer, Rémi Desbuquois, and Tilman Esslinger. Formation and Dynamics of Antiferromagnetic Correlations in Tunable Optical Lattices. *Phys. Rev. Lett.*, 115:260401, Dec 2015. URL: https://link.aps.org/doi/10.1103/PhysRevLett.115.260401, doi:10.1103/PhysRevLett.115.260401.

[21] Lawrence W Cheuk, Matthew A Nichols, Katherine R Lawrence, Melih Okan, Hao Zhang, Ehsan Khatami, Nandini Trivedi, Thereza Paiva, Marcos Rigol, and Martin W Zwierlein. Observation of spatial charge and spin correlations in the 2d fermi-hubbard model. *Science*, 353(6305):1260–1264, 2016.

[22] Peter T Brown, Debayan Mitra, Elmer Guardado-Sanchez, Peter Schauß, Stanimir S Kondov, Ehsan Khatami, Thereza Paiva, Nandini Trivedi, David A Huse, and Waseem S Bakr. Spin-imbalance in a 2d fermi-hubbard system. *Science*, 357(6358):1385–1388, 2017.

[23] Joannis Koepsell, Jayadev Vijayan, Pimonpan Sompet, Fabian Grusdt, Timon A Hilker, Eugene Demler, Guillaume Salomon, Immanuel Bloch, and Christian Gross. Imaging magnetic polarons in the doped fermi–hubbard model. *Nature*, 572(7769):358–362, 2019.

[24] Marcell Gall, Nicola Wurz, Jens Samland, Chun Fai Chan, and Michael Köhl. Competing magnetic orders in a bilayer hubbard model with ultracold atoms. *Nature*, 589(7840):40–43, 2021.

[25] Pimonpan Sompet, Sarah Hirthe, Dominik Bourgund, Thomas Chalopin, Julian Bibo, Joannis Koepsell, Petar Bojović, Ruben Verresen, Frank Pollmann, Guillaume Salomon, et al. Realizing the symmetry-protected haldane phase in fermi–hubbard ladders. *Nature*, pages 1–5, 2022.

[26] Nikolai V. Prokof'ev and Boris V. Svistunov. Polaron Problem by Diagrammatic Quantum Monte Carlo. *Phys. Rev. Lett.*, 81:2514–2517, Sep 1998. URL: https://link.aps.org/doi/10.1103/PhysRevLett.81.2514, doi:10.1103/PhysRevLett.81.2514.

[27] Kris Van Houcke, Evgeny Kozik, Nikolay Prokof'ev, and Boris Svistunov. *Phys. Procedia*, 6:95, 2010. doi:10.1016/j.phpro.2010.09.034.

[28] E. Kozik, K. Van Houcke, E. Gull, L. Pollet, N. Prokof'ev, B. Svistunov, and M. Troyer. Diagrammatic monte carlo for correlated fermions. *Europhys. Lett.*, 90:10004, 2010. doi:10.1209/0295-5075/90/10004.

[29] Riccardo Rossi. Determinant Diagrammatic Monte Carlo Algorithm in the Thermodynamic Limit. *Phys. Rev. Lett.*, 119:045701, Jul 2017. URL: https://link.aps.org/doi/10.1103/PhysRevLett.119.045701, doi:10.1103/PhysRevLett.119.045701.

[30] R. Rossi, N. Prokof'ev, B. Svistunov, K. Van Houcke, and F. Werner. Polynomial complexity despite the fermionic sign. *EPL (Europhysics Letters)*, 118(1):10004, apr 2017. doi:10.1209/0295-5075/118/10004.

[31] Fedor Šimkovic, J. P. F. LeBlanc, Aaram J. Kim, Youjin Deng, N. V. Prokof'ev, B. V. Svistunov, and Evgeny Kozik. Extended Crossover from a Fermi

Liquid to a Quasiantiferromagnet in the Half-Filled 2D Hubbard Model. *Phys. Rev. Lett.*, 124:017003, Jan 2020. URL: https://link.aps.org/doi/10.1103/PhysRevLett.124.017003, doi:10.1103/PhysRevLett.124.017003.

[32] Thomas Schäfer, Nils Wentzell, Fedor Šimkovic, Yuan-Yao He, Cornelia Hille, Marcel Klett, Christian J. Eckhardt, Behnam Arzhang, Viktor Harkov, François-Marie Le Régent, Alfred Kirsch, Yan Wang, Aaram J. Kim, Evgeny Kozik, Evgeny A. Stepanov, Anna Kauch, Sabine Andergassen, Philipp Hansmann, Daniel Rohe, Yuri M. Vilk, James P. F. LeBlanc, Shiwei Zhang, A.-M. S. Tremblay, Michel Ferrero, Olivier Parcollet, and Antoine Georges. Tracking the Footprints of Spin Fluctuations: A MultiMethod, MultiMessenger Study of the Two-Dimensional Hubbard Model. *Phys. Rev. X*, 11:011058, Mar 2021. URL: https://link.aps.org/doi/10.1103/PhysRevX.11.011058, doi:10.1103/PhysRevX.11.011058.

[33] Aaram J. Kim, Fedor Simkovic, and Evgeny Kozik. Spin and Charge Correlations across the Metal-to-Insulator Crossover in the Half-Filled 2D Hubbard Model. *Phys. Rev. Lett.*, 124:117602, Mar 2020. URL: https://link.aps.org/doi/10.1103/PhysRevLett.124.117602, doi:10.1103/PhysRevLett.124.117602.

[34] Connor Lenihan, Aaram J. Kim, Fedor Šimkovic IV., and Evgeny Kozik. Entropy in the Non-Fermi-Liquid Regime of the Doped 2D Hubbard Model. *Phys. Rev. Lett.*, 126:105701, Mar 2021. URL: https://link.aps.org/doi/10.1103/PhysRevLett.126.105701, doi:10.1103/PhysRevLett.126.105701.

[35] J. P. F. LeBlanc, Andrey E. Antipov, Federico Becca, Ireneusz W. Bulik, Garnet Kin-Lic Chan, Chia-Min Chung, Youjin Deng, Michel Ferrero, Thomas M. Henderson, Carlos A. Jiménez-Hoyos, E. Kozik, Xuan-Wen Liu, Andrew J. Millis, N. V. Prokof'ev, Mingpu Qin, Gustavo E. Scuseria, Hao Shi, B. V. Svistunov, Luca F. Tocchio, I. S. Tupitsyn, Steven R. White, Shiwei Zhang, Bo-Xiao Zheng, Zhenyue Zhu, and Emanuel Gull. Solutions of the Two-Dimensional Hubbard Model: Benchmarks and Results from a Wide Range of Numerical Algorithms. *Phys. Rev. X*, 5:041041, Dec 2015. URL: https://link.aps.org/doi/10.1103/PhysRevX.5.041041, doi:10.1103/PhysRevX.5.041041.

[36] Wei Wu, Michel Ferrero, Antoine Georges, and Evgeny Kozik. Controlling Feynman diagrammatic expansions: Physical nature of the pseudogap in the two-dimensional Hubbard model. *Phys. Rev. B*, 96:041105, Jul 2017. URL: https://link.aps.org/doi/10.1103/PhysRevB.96.041105, doi:10.1103/PhysRevB.96.041105.

[37] Riccardo Rossi, Fedor Šimkovic, and Michel Ferrero. Renormalized perturbation theory at large expansion orders. *EPL (Europhysics Letters)*, 132(1):11001, 2020.

[38] Fedor Šimkovic, Riccardo Rossi, and Michel Ferrero. The Weak, the Strong and the Long Correlation Regimes of the Two-Dimensional Hubbard Model at Finite Temperature. *arXiv e-prints*, page arXiv:2110.05863, October 2021. arXiv:2110.05863.

[39] Connor Lenihan, Aaram J. Kim, IV. Šimkovic, Fedor, and Evgeny Kozik. Evaluating second-order phase transitions with Diagrammatic Monte Carlo: Néel Transition in the doped three-dimensional Hubbard model. *arXiv e-prints*, page arXiv:2112.15209, December 2021. arXiv:2112.15209.

[40] Fedor Simkovic, Riccardo Rossi, Antoine Georges, and Michel Ferrero. URL: https://arxiv.org/abs/2209.09237, arXiv:arXiv:2209.09237, doi:10.48550/ARXIV.2209.09237.

[41] Rosario E. V. Profumo, Christoph Groth, Laura Messio, Olivier Parcollet, and Xavier Waintal. Quantum Monte Carlo for correlated out-of-equilibrium nanoelectronic devices. *Phys. Rev. B*, 91:245154, Jun 2015. URL: https://link.aps.org/doi/10.1103/PhysRevB.91.245154, doi:10.1103/PhysRevB.91.245154.

[42] Fedor Šimkovic, Riccardo Rossi, and Michel Ferrero. Efficient one-loop-renormalized vertex expansions with connected determinant diagrammatic Monte Carlo. *Phys. Rev. B*, 102:195122, Nov 2020. URL: https://link.aps.org/doi/10.1103/PhysRevB.102.195122, doi:10.1103/PhysRevB.102.195122.

[43] Aaram J. Kim, Nikolay V. Prokof'ev, Boris V. Svistunov, and Evgeny Kozik. Homotopic Action: A Pathway to Convergent Diagrammatic Theories. *Phys. Rev. Lett.*, 126:257001, Jun 2021. URL: https://link.aps.org/doi/10.1103/PhysRevLett.126.257001, doi:10.1103/PhysRevLett.126.257001.

[44] James P. F. LeBlanc, Kun Chen, Kristjan Haule, Nikolay V. Prokof'ev, and Igor S. Tupitsyn. Dynamic response of the electron gas: Towards the exact exchange-correlation kernel. URL: https://arxiv.org/abs/2205.13595, arXiv:arXiv:2205.13595, doi:10.48550/ARXIV.2205.13595.

[45] R. Rossi, T. Ohgoe, K. Van Houcke, and F. Werner. Resummation of diagrammatic series with zero convergence radius for strongly correlated fermions. *Phys. Rev. Lett*, 121:130405, 2018. URL: https://link.aps.org/doi/10.1103/PhysRevLett.121.130405, doi:10.1103/PhysRevLett.121.130405.

[46] K. Chen and K. Haule. A combined variational and diagrammatic quantum monte carlo approach to the many-electron problem. *Nature Comm.*, 10:3725, 2019. doi:10.1038/s41467-019-11708-6.

[47] R. Rossi, F. Werner, N. Prokof'ev, and B. Svistunov. Shifted-action expansion and applicability of dressed diagrammatic schemes. *Phys. Rev. B*, 93:161102(R), 2016. doi:10.1103/PhysRevB.93.161102.

[48] Igor S. Tupitsyn and Nikolay V. Prokof'ev. Phase diagram topology of the haldane-hubbard-coulomb model. *Phys. Rev. B*, 99:121113(R), 2019. URL: https://link.aps.org/doi/10.1103/PhysRevB.99.121113, doi:10.1103/PhysRevB.99.121113.

[49] Yuan Huang, Kun Chen, Youjin Deng, Nikolay Prokof'ev, and Boris Svistunov. Spin-Ice State of the Quantum Heisenberg Antiferromagnet on the Pyrochlore Lattice. *Phys. Rev. Lett.*, 116:177203, 2016. doi:10.1103/PhysRevLett.116.177203.

[50] G. Spada, R. Rossi, F. Simkovic, R. Garioud, M. Ferrero, K. Van Houcke, and F. Werner. High-order expansion around BCS theory. *arXiv e-prints*, page arXiv:2103.12038, March 2021. arXiv:2103.12038.

[51] Fedor Šimkovic and Riccardo Rossi. Many-Configuration Markov-Chain Monte Carlo. *arXiv e-prints*, page arXiv:2102.05613, February 2021. arXiv:2102.05613.

[52] Kent Griffin and Michael J. Tsatsomeros. Principal minors, Part I: A method for computing all the principal minors of a matrix. *Linear Algebra and its Applications*, 419(1):107–124, 2006. URL: https://www.sciencedirect.

com/science/article/pii/S0024379506002126, doi:https://doi.org/10.1016/j.laa.2006.04.008.

[53] Fedor Šimkovic and Michel Ferrero. Fast principal minor algorithms for diagrammatic Monte Carlo. *Phys. Rev. B*, 105:125104, Mar 2022. URL: https://link.aps.org/doi/10.1103/PhysRevB.105.125104, doi:10.1103/PhysRevB.105.125104.

[54] George A. Baker. Application of the Padé Approximant Method to the Investigation of Some Magnetic Properties of the Ising Model. *Phys. Rev.*, 124:768–774, Nov 1961. URL: https://link.aps.org/doi/10.1103/PhysRev.124.768, doi:10.1103/PhysRev.124.768.

[55] Fedor Šimkovic and Evgeny Kozik. Determinant Monte Carlo for irreducible Feynman diagrams in the strongly correlated regime. *Phys. Rev. B*, 100:121102, Sep 2019. URL: https://link.aps.org/doi/10.1103/PhysRevB.100.121102, doi:10.1103/PhysRevB.100.121102.

[56] *See supplemental material at.*

[57] Julian Stobbe and Georg Rohringer. Consistency of potential energy in the diagrammatic vertex approximation, 2022. URL: https://arxiv.org/abs/2208.05824, doi:10.48550/ARXIV.2208.05824.

[58] J. C. Slater. Magnetic Effects and the Hartree-Fock Equation. *Phys. Rev.*, 82:538–541, May 1951. URL: https://link.aps.org/doi/10.1103/PhysRev.82.538, doi:10.1103/PhysRev.82.538.

[59] Anders W. Sandvik. Critical Temperature and the Transition from Quantum to Classical Order Parameter Fluctuations in the Three-Dimensional Heisenberg Antiferromagnet. *Phys. Rev. Lett.*, 80:5196–5199, Jun 1998. URL: https://link.aps.org/doi/10.1103/PhysRevLett.80.5196, doi:10.1103/PhysRevLett.80.5196.

[60] Massimo Campostrini, Martin Hasenbusch, Andrea Pelissetto, Paolo Rossi, and Ettore Vicari. Critical exponents and equation of state of the three-dimensional Heisenberg universality class. *Phys. Rev. B*, 65:144520, Apr 2002. URL: https://link.aps.org/doi/10.1103/PhysRevB.65.144520, doi:10.1103/PhysRevB.65.144520.

[61] T. Schäfer, A. A. Katanin, K. Held, and A. Toschi. Interplay of Correlations and Kohn Anomalies in Three Dimensions: Quantum Criticality with a Twist. *Phys. Rev. Lett.*, 119:046402, Jul 2017. URL: https://link.aps.org/doi/10.1103/PhysRevLett.119.046402, doi:10.1103/PhysRevLett.119.046402.

[62] Antoine Georges and Werner Krauth. Physical properties of the half-filled Hubbard model in infinite dimensions. *Phys. Rev. B*, 48:7167–7182, Sep 1993. URL: https://link.aps.org/doi/10.1103/PhysRevB.48.7167, doi:10.1103/PhysRevB.48.7167.

[63] F. Werner, O. Parcollet, A. Georges, and S. R. Hassan. Interaction-Induced Adiabatic Cooling and Antiferromagnetism of Cold Fermions in Optical Lattices. *Phys. Rev. Lett.*, 95:056401, Jul 2005. URL: https://link.aps.org/doi/10.1103/PhysRevLett.95.056401, doi:10.1103/PhysRevLett.95.056401.

[64] Lorenzo De Leo, Corinna Kollath, Antoine Georges, Michel Ferrero, and Olivier Parcollet. Trapping and Cooling Fermionic Atoms into Mott and Néel States. *Phys. Rev. Lett.*, 101:210403, Nov 2008. URL: https://link.aps.org/doi/10.1103/PhysRevLett.101.210403, doi:10.1103/PhysRevLett.101.210403.

[65] E. V. Gorelik, I. Titvinidze, W. Hofstetter, M. Snoek, and N. Blümer. Néel Transition of Lattice Fermions in a Harmonic Trap: A Real-Space Dynamic Mean-Field Study. *Phys. Rev. Lett.*, 105:065301, Aug 2010. URL: https://link.aps.org/doi/10.1103/PhysRevLett.105.065301, doi:10.1103/PhysRevLett.105.065301.

[66] Sebastian Fuchs, Emanuel Gull, Lode Pollet, Evgeni Burovski, Evgeny Kozik, Thomas Pruschke, and Matthias Troyer. Thermodynamics of the 3D Hubbard Model on Approaching the Néel Transition. *Phys. Rev. Lett.*, 106:030401, Jan 2011. URL: https://link.aps.org/doi/10.1103/PhysRevLett.106.030401, doi:10.1103/PhysRevLett.106.030401.

[67] C. Taranto, G. Sangiovanni, K. Held, M. Capone, A. Georges, and A. Toschi. Signature of antiferromagnetic long-range order in the optical spectrum of strongly correlated electron systems. *Phys. Rev. B*, 85:085124, Feb 2012. URL: https://link.aps.org/doi/10.1103/PhysRevB.85.085124, doi:10.1103/PhysRevB.85.085124.

[68] L. Fratino, P. Sémon, M. Charlebois, G. Sordi, and A.-M. S. Tremblay. Signatures of the Mott transition in the antiferromagnetic state of the two-dimensional Hubbard model. *Phys. Rev. B*, 95:235109, Jun 2017. URL: https://link.aps.org/doi/10.1103/PhysRevB.95.235109, doi:10.1103/PhysRevB.95.235109.

[69] E. V. Gorelik, I. Titvinidze, W. Hofstetter, M. Snoek, and N. Blümer. Néel Transition of Lattice Fermions in a Harmonic Trap: A Real-Space Dynamic Mean-Field Study. *Phys. Rev. Lett.*, 105:065301, Aug 2010. URL: https://link.aps.org/doi/10.1103/PhysRevLett.105.065301, doi:10.1103/PhysRevLett.105.065301.

[70] Anne-Marie Daré, Y. M. Vilk, and A. M. S. Tremblay. Crossover from two- to three-dimensional critical behavior for nearly antiferromagnetic itinerant electrons. *Phys. Rev. B*, 53:14236–14251, Jun 1996. URL: https://link.aps.org/doi/10.1103/PhysRevB.53.14236, doi:10.1103/PhysRevB.53.14236.

Supplemental material for "Precise many-body simulations of antiferromagnetic phases using broken-symmetry perturbative expansions"

TUNING THE SHIFT α

We detail in this section the effect of the choice of the shift parameter on the series behaviour and discuss our method for selecting the optimal value of the α parameter. The expression of the perturbation Hamiltonian $\hat{\mathcal{H}}_\xi$ is given in Eq. 1 with ξ the expansion parameter. We parameterize $h = \alpha h_{\mathrm{MF}}$ with h_{MF} the effective field which corresponds to the mean-field solution at interaction U and temperature T. The free parameter α modifies the intensity of the staggered field in the non-perturbed system. There is no limitation prohibiting choices of $\alpha > 1$, however, it was not beneficial in our studies and we limit ourselves to values of the shift $\alpha \in [0, 1]$. The value $\alpha = 1$ leads to a non-perturbed Hamiltonian $\hat{\mathcal{H}}_{\xi=0}$ corresponding to the antiferromagnetic mean-field Hamiltonian for which the Hartree insertions are canceled in the diagrammatic expansion of an observable $\mathcal{A}$.

We employ different resummation techniques in order to extrapolate the computed series to infinite orders. We use Padé and D-log Padé approximants [1, 2] cross checked with an exponential fitting of the expansion coefficient with respect to the order to establish a controlled result. In the end the error on an observable is determined through error propagation of the MC error on the expansion orders, after comparing the results from different resummations techniques, for at least two different values of the shift parameter α.

The choice of the value of the α parameter changes the non-interacting Hamiltonian $\hat{\mathcal{H}}_0$ and therefore modifies the series behavior and its convergence properties. We illustrate in Fig. S1 the effect of the value of the shift parameter on the shape of the partial sums for different observables. The value of the α parameter leading to the best convergence of the partial sum depends on the parameters T and U of the computation and on the computed observable. If the best convergence is usually given by shifts in the range $\alpha \in [0.7-1]$, it is helpful (especially for the magnetization close to the Néel temperature) to calibrate its value in order to obtain a quickly converging partial sum. At $U = 4$, $T = 0.15$ we find a 'magical shift' $\alpha = 0.162$ for which the convergence of the series is optimal, leading to an accurate result. The maximum expansion order we are able to reach with good accuracy depends strongly on the value of the shift and is higher for α close to 1, which can be explained by the cancellation of Hartree insertion which reduces the MC variance.

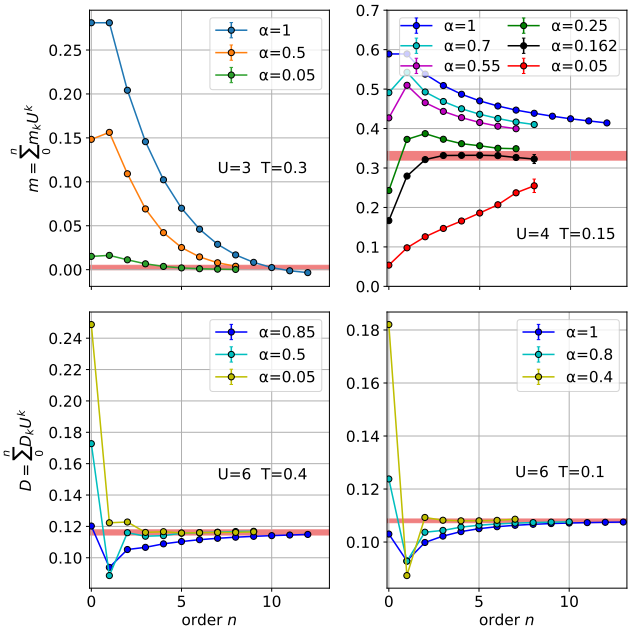

FIG. S1. Partial sums of magnetization m and double-occupancy D for different values of the interaction U and temperature T as a function of the maximum order n. The partial sums are highly dependent on the value of the shift α. The red colored band corresponds to the result with error after resummation.

SYSTEM-SIZE EFFECTS

The diagrammatic expansion is formulated directly in the thermodynamic limit. In practice we solve the unperturbed Hamiltonian and tabulate for finite L the non-interacting Green's functions to build the diagrammatic expansion of the problem. Considering an expansion series of the magnetization at $U = 4$, $T = 0.18$ close to the phase transition ($T_N \simeq 0.19$ at an interaction $U = 4$), we show in Fig. S2 that, up to relatively high order and negligible contribution to the resummed result, the contribution from each order is converged within statistical error for a linear system size $L \geq 20$. This shows that the final error on our results is dominated by statistical and resummation error. Finite size effects would only affect very high perturbation orders which can be neglected to determine the converging value of the series. This property remains valid when getting closer to the Néel temperature (see [3]). In our study, we fix the system-size to $L^3 = 20^3$ sites on a cubic lattice which proves to be large enough to avoid finite-size effects, even in the critical region in the vicinity of the Néel phase transition.

To illustrate this we show the evolution of the value of different observables with linear system size in Fig. S3, with a convergence reached for $L \geq 20$.

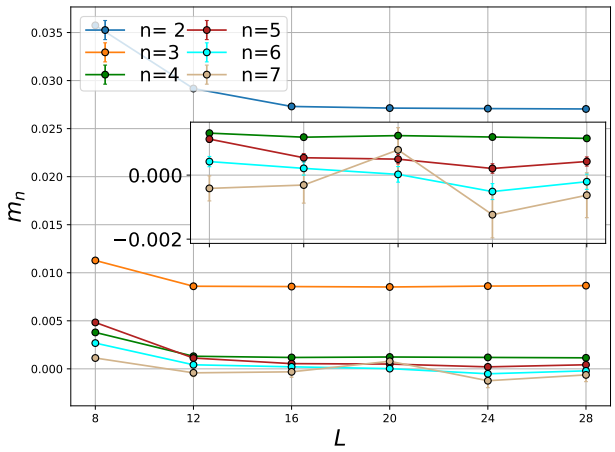

FIG. S2. System-size study : Contribution to the magnetization of its expansion coefficients m_n at different orders n, as a function of the linear system size L. The parameters of the perturbation expansion are $T = 0.18$, $U = 4$, $\alpha = 0.1$. The inset is the same plot for smaller contributions.

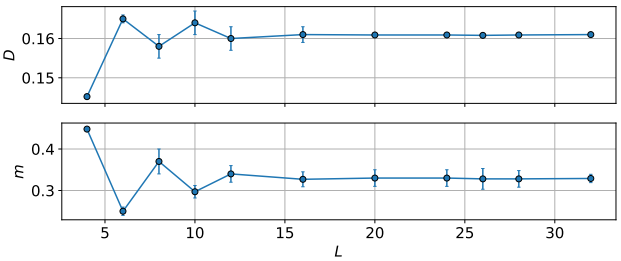

FIG. S3. System-size study : Double-occupancy and magnetization at $U = 4$, $T = 0.15$ as a function of the linear system size L for a cubic lattice of L^3 sites.

GRAND-POTENTIAL COMPUTATIONS

Grand potential computations are shown in Fig. S4. The corresponding magnetization is obtained with a first or second order polynomial fit of the grand potential data as a function of the external field H_{ext}. This method for estimating indirectly the magnetization as a derivative of the grand potential proves to be efficient deep inside the antiferromagnetic dome, in the regime where magnetization is saturated to its zero temperature value. In the vicinity of the phase transition we expect the grand potential curve as a function of the external field $H_{\rm ext}$ to be flattening close to the origin $H_{\rm ext} = 0$ as the temperature gets higher. These changes at very small fields are hard to resolve and we rely on direct computations of the magnetization in this regime.

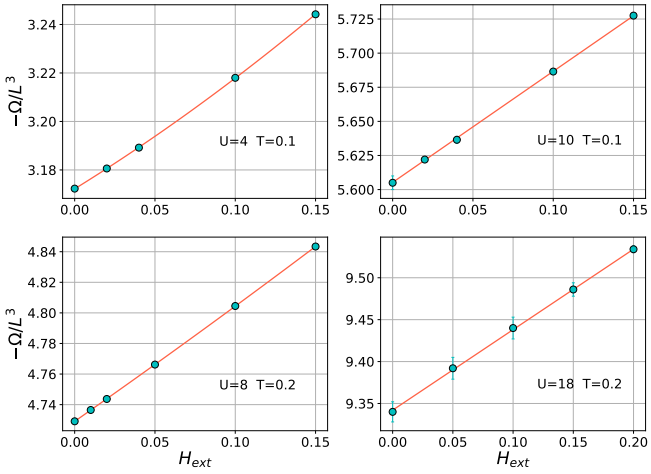

FIG. S4. Grand potential density $-\Omega/L^3$ as a function of the external staggered field $H_{\rm ext}$ for different values of the temperature and interaction parameters. The orange line corresponds to the best fit by a second (first) order polynomial on the top and bottom left (right) panels

[1] F. Šimkovic and E. Kozik, "Determinant monte carlo for irreducible feynman diagrams in the strongly correlated regime," *Phys. Rev. B*, vol. 100, p. 121102, Sep 2019.

[2] G. A. Baker, "Application of the padé approximant method to the investigation of some magnetic properties of the ising model," *Phys. Rev.*, vol. 124, pp. 768–774, Nov 1961.

[3] G. Spada, R. Rossi, F. Simkovic, R. Garioud, M. Ferrero, K. Van Houcke, and F. Werner, "High-order expansion around BCS theory," *arXiv e-prints*, p. arXiv:2103.12038, Mar. 2021.

High-order diagrammatic expansion around BCS theory

G. Spada,[1,2,3,*] R. Rossi,[4,5,†] F. Šimkovic,[6,7] R. Garioud,[6,7] M. Ferrero,[6,7] K. Van Houcke,[2] and F. Werner[1,‡]

[1] *Laboratoire Kastler Brossel, École Normale Supérieure - Université PSL, CNRS, Sorbonne Université, Collège de France, 75005 Paris, France*
[2] *Laboratoire de Physique de l'École Normale Supérieure, ENS - Université PSL, CNRS, Sorbonne Université, Université de Paris, 75005 Paris, France*
[3] *INO-CNR BEC Center and Dipartimento di Fisica, Università di Trento, 38123 Trento, Italy*
[4] *Center for Computational Quantum Physics, The Flatiron Institute, New York, NY 10010, USA*
[5] *Institute of Physics, École Polytechnique Fédérale de Lausanne, 1015 Lausanne, Switzerland*
[6] *CPHT, CNRS, École Polytechnique, Institut Polytechnique de Paris, 91128 Palaiseau, France*
[7] *Collège de France, 11 place Marcelin Berthelot, 75005 Paris, France*

(Dated: April 16, 2021)

We demonstrate that summation of connected diagrams to high order on top of the BCS hamiltonian is a viable generic unbiased approach for strongly correlated fermions in superconducting or superfluid phases. For the 3D attractive Hubbard model in a strongly correlated regime, we observe convergence of the diagrammatic series, evaluated up to 12 loops thanks to the connected determinant diagrammatic Monte Carlo algorithm. Our study includes the polarized regime, where conventional quantum Monte Carlo methods suffer from the fermion sign problem. Upon increasing the Zeeman field, we observe the first-order superconducting-to-normal phase transition at low temperature, and a significant polarization of the superconducting phase at higher temperature.

After the discovery of superconductivity 110 years ago [1], it took nearly half a century before Bardeen, Cooper and Schrieffer provided a microscopic explanation based on an ansatz for the many-body ground-state wavefunction – a coherent state of pairs, breaking the $U(1)$ symmetry corresponding to particle number conservation [2]. Variational minimization over this ansatz leads to the well-known BCS mean-field theory which captures not only the "BCS regime" where the attractive interaction is weak, but also the "BEC regime" where the attractive interaction is strong, suggesting a smooth crossover from a fermionic superfluid with large Cooper pairs to a Bose-Einstein condensate of small composite bosons [3, 4]. This BCS-BEC crossover scenario, confirmed experimentally in ultracold atomic gases [5–7], is relevant to neutron matter [8, 9] and to various solid-state materials [10, 11] where s-wave pairing arises between opposite-spin electrons [12] or between an electron and a hole [13]. The problem becomes even more interesting in presence of a Zeeman field h, *i.e.*, a chemical potential offset between $\uparrow$ and $\downarrow$ fermions, which favors a difference between $\uparrow$ and $\downarrow$ densities, and tends to destabilize the fully paired superconducting state.

A minimal theoretical formulation of the BCS-BEC crossover problem is the attractive Hubbard model on the cubic lattice, which was widely studied at $h = 0$ (and generic filling [14]) by different versions and extensions of BCS mean-field theory [15, 16] and of the T-matrix approximation [11, 17], dynamical mean-field theory (DMFT) in the normal [18, 19] and the superconducting [20, 21] phase, and the dynamical vertex approximation [22]. Unbiased studies, based on the auxiliary field quantum Monte Carlo (AFQMC) [23–25] or determinant diagrammatic Monte Carlo (DDMC) methods [26, 27], are mostly restricted to a Zeeman field $h = 0$: In the $h \neq 0$ regime, where there is no symmetry between $\uparrow$ and $\downarrow$, these methods are plagued by the infamous fermion sign problem [28], and most studies resort to the static [15, 29, 30] or dynamical [31] mean-field approximations. A very different route is to emulate the Hubbard model with cold atoms, although long-range order in 3D was not reached so far [6, 32].

In this Letter, we demonstrate that unbiased accurate results in the polarized superconducting phase can be obtained from a high-order diagrammatic expansion around the BCS hamiltonian. By extending the connected determinant (CDet) algorithm [33] to anomalous propagators, we go up to twelve-loop order and observe convergence of the series. This extends the realm of controlled diagrammatic computations for strongly correlated fermions in the thermodynamic limit [33–36] to superconducting phases. We determine the critical Zeeman field where a first-order superconducting-to-normal phase transition takes place at low temperature, and find a significant polarization of the superconducting phase at higher temperature. Our results deviate very substantially from the BCS mean-field predictions and provide reliable benchmarks for optical-lattice experiments.

The Hubbard model is defined by the hamiltonian

$$H = H_{\rm kin} - \sum_{\sigma=\uparrow,\downarrow} \mu_\sigma N_\sigma + H_{\rm int} \tag{1}$$

with $\mu_{\uparrow/\downarrow} = \mu \pm h$ the chemical potentials, $H_{\rm kin} = -t \sum_{\langle \mathbf{i},\mathbf{j}\rangle\,\sigma} (c^\dagger_{\mathbf{i}\sigma} c_{\mathbf{j}\sigma} + h.c.)$ the nearest-neighbor hopping, and $H_{\rm int} = U \sum_{\mathbf{i}} n_{\mathbf{i}\uparrow} n_{\mathbf{i}\downarrow}$ the on-site interaction ($c_{\mathbf{i}\sigma}$ are the fermion annihilation operators, while $n_{\mathbf{i}\sigma} = c^\dagger_{\mathbf{i}\sigma} c_{\mathbf{i}\sigma}$ and $N_\sigma = \sum_{\mathbf{i}} n_{\mathbf{i}\sigma}$ are the single-site and total particle-number-operators).

To set up a diagrammatic expansion for the infinite-

size system in the superconducting phase, we must expand around an unperturbed hamiltonian H_0 that breaks the $U(1)$ symmetry. We take

$$H_0 = H_{\rm kin} - \sum_\sigma \mu_{0,\sigma}\, N_\sigma + H_{\rm pair}^{(\Delta_0)} \tag{2}$$

with a symmetry-breaking pairing term

$$H_{\rm pair}^{(\Delta_0)} := \Delta_0 \sum_{\mathbf{i}} c_{\mathbf{i}\uparrow}^\dagger c_{\mathbf{i}\downarrow}^\dagger + h.c. \tag{3}$$

The most natural choice for the free parameters Δ_0 and $\mu_{0,\sigma}$ is given by the self-consistency conditions of BCS mean-field theory

$$\mu_{0,\sigma} = \mu_\sigma - U\,\langle n_{\mathbf{0},-\sigma}\rangle_{H_0} \tag{4}$$

$$\Delta_0 = -U\,\langle\hat{\mathcal{O}}\rangle_{H_0} \tag{5}$$

where $\langle\hat{\mathcal{O}}\rangle := \langle c_{\mathbf{0}\uparrow} c_{\mathbf{0}\downarrow}\rangle$ is the order parameter for the superconducting phase with long-range order in the s-wave pairing channel. In what follows we will denote this mean-field choice of Δ_0 by $\Delta_{\rm MF}$. We will also use other values of Δ_0, but always keep the mean-field choice (4) for the unperturbed chemical potential.

As usual we then introduce a hamiltonian that depends on a formal parameter ξ,

$$H_\xi = H_0 + \xi\ (H - H_0), \tag{6}$$

expand intensive observables in powers of ξ, and finally set $\xi = 1$. For the order parameter, this means introducing

$$\mathcal{O}(\xi) := \langle\hat{\mathcal{O}}\rangle_{H_\xi} \equiv {\rm Tr}(\hat{\mathcal{O}}\, e^{-\beta H_\xi}) \,/\, {\rm Tr}\, e^{-\beta H_\xi} \tag{7}$$

and expanding $\mathcal{O}(\xi) = \sum_{N=0}^\infty \mathcal{O}_N\, \xi^N$. We will see numerically that this series converges at $\xi = 1$. We can thus obtain the physical order parameter simply by evaluating the series $\sum_{N=0}^\infty \mathcal{O}_N$.

Thermodynamic limit and spontaneous symmetry breaking. Here it is actually crucial to work directly in the thermodynamic limit [37]. This limit should be taken in the definition (7) of $\mathcal{O}(\xi)$, and hence the thermodynamic limit should be taken before summing the $\mathcal{O}_N$ over N. Indeed, recall that in presence of spontaneous symmetry breaking, the order parameter is defined by introducing an external symmetry-breaking field η that couples to the order parameter, and sending η to zero *after* taking the thermodynamic limit:

$$\mathcal{O} = \lim_{\eta\to 0^+}\ \lim_{L\to\infty}\ \langle\hat{\mathcal{O}}\rangle_{H^{(\eta)},\,L} \tag{8}$$

where $H^{(\eta)} := H + H_{\rm pair}^{(\eta)}$ and L is the linear system size. Let us denote by $\mathcal{O}_L(\xi)$ and $\mathcal{O}_{N,L}$ the finite-system versions of $\mathcal{O}(\xi)$ and $\mathcal{O}_N$. Since there is no spontaneous symmetry breaking for a finite system, $\mathcal{O}_L(\xi = 1) = 0$. What we should do instead, to obtain the order parameter defined in (8), is to first take the thermodynamic limit: $\mathcal{O} = \lim_{\xi\to 1^-} \lim_{L\to\infty} \mathcal{O}_L(\xi)$. This follows simply from the fact that H_ξ contains a symmetry-breaking field which by construction vanishes in the limit $\xi \to 1$ where the symmetry of the physical hamiltonian is restored. Explicitly, $H_\xi = H_{\rm kin} - \sum_\sigma \left[(1-\xi)\,\mu_{0,\sigma} + \xi\,\mu_\sigma\right] N_\sigma + (1-\xi)\, H_{\rm pair}^{(\Delta_0)} + \xi\ H_{\rm int}$, which is equal to $H^{(\eta_{\rm eff} = (1-\xi)\,\Delta_0)}$ plus corrections that have no effect to leading order in the limit $\xi \to 1$.

Diagrams and CDet algorithm. Each coefficient $\mathcal{O}_N$ is a sum of connected Feynman diagrams with N vertices. We compute these coefficients up to a maximal order $N_{\rm max}$ using the CDet algorithm generalized to the broken-symmetry phase. In addition to the normal propagator lines, diagrams contain anomalous propagator lines, where particles are destroyed at both ends, or created at both ends. These anomalous propagators are the off-diagonal elements of the 2 by 2 propagator matrix

$$\mathcal{G}_{\alpha\alpha'}(X - X') = -\langle {\rm T}\ \Psi_\alpha^\dagger(X)\, \Psi_{\alpha'}(X')\rangle_{H_0} \tag{9}$$

with the Nambu spinor notation $(\Psi_0, \Psi_1) := (c_\uparrow, c_\downarrow^\dagger)$. Here $X \equiv (\mathbf{i}, \tau)$ stands for space and imaginary-time, and T is the time-ordering operator.

Following the CDet approach, we express the diagrammatic series for the order parameter, or for the densities, as

$$\langle\Psi_\alpha^\dagger(0)\Psi_{\alpha'}(0)\rangle_{H_\xi} = \\ -\sum_{N=0}^\infty \frac{(\xi\, U)^N}{N!} \int dX_1 \ldots dX_N\ \ {\rm cdet}(X_1, \ldots, X_N) \tag{10}$$

where $\int dX := \sum_{\mathbf{i}} \int_0^\beta d\tau$ with β the inverse temperature, and ${\rm cdet}(X_1, \ldots, X_N)$ is the sum of all connected Feynman diagrams with internal vertex positions $X_1, \ldots, X_N$, which is evaluated by recursively subtracting out all disconnected diagrams from the sum of all connected plus disconnected diagrams, the latter being given by the determinant of the $(2N+1)$ by $(2N+1)$ propagator matrix

$$\begin{pmatrix} 0 & \delta_{\rm sh} & \ldots & \mathcal{G}_{00}(X_{1n}) & \mathcal{G}_{01}(X_{1n}) & \mathcal{G}_{0i_0}(X_1) \\ \delta_{\rm sh} & 0 & \ldots & \mathcal{G}_{10}(X_{1n}) & \mathcal{G}_{11}(X_{1n}) & \mathcal{G}_{1\alpha}(X_1) \\ \vdots & \vdots & \ddots & \vdots & \vdots & \vdots \\ \mathcal{G}_{00}(X_{n1}) & \mathcal{G}_{01}(X_{n1}) & \ldots & 0 & \delta_{\rm sh} & \mathcal{G}_{0\alpha}(X_n) \\ \mathcal{G}_{10}(X_{n1}) & \mathcal{G}_{11}(X_{n1}) & \ldots & \delta_{\rm sh} & 0 & \mathcal{G}_{1\alpha}(X_n) \\ \mathcal{G}_{\alpha'0}(-X_1) & \mathcal{G}_{\alpha'1}(-X_1) & \ldots & \mathcal{G}_{\alpha'0}(-X_n) & \mathcal{G}_{\alpha'1}(-X_n) & \mathcal{G}_{\alpha'\alpha}(0) \end{pmatrix}$$

where $X_{ij} := X_i - X_j$, and $\delta_{\rm sh} := \langle\hat{\mathcal{O}}\rangle_{H_0} + \Delta_0/U$ is the anomalous tadpole minus a counter-term, which vanishes when $\Delta_0 = \Delta_{\rm MF}$. The zeros on the diagonal reflect the cancellation of normal tadpoles by chemical-potential counter-terms, ensured by (4). We will also evaluate the series for the pressure, $P(\xi) = \ln {\rm Tr} \exp(-\beta H_\xi)/(\beta L^3) = \sum_{N=0}^\infty P_N \xi^N$, whose coefficients P_N are given by fully closed diagrams and are obtained with CDet by removing the last row and column from the above propagator matrix.

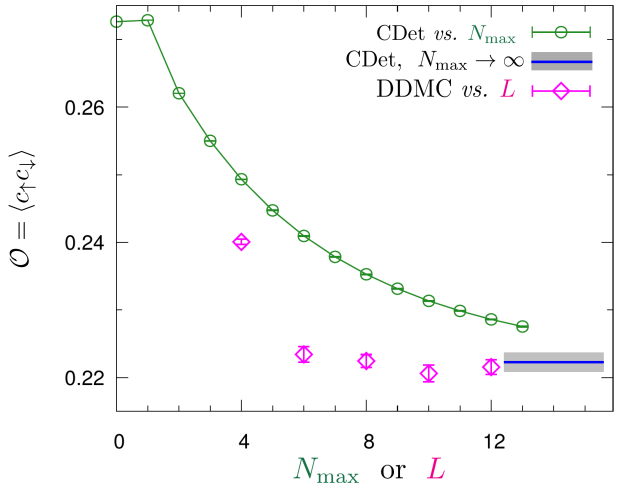

FIG. 1. *Benchmark at zero Zeeman field:* Order parameter at $T = 1/8 \approx T_c/2$. Green circles: CDet results *vs.* truncation order $N_{\max}$ ($N_{\max} = 0$ corresponds to BCS mean field theory). Blue line with grey error-band: $N_{\max} \to \infty$ extrapolated result. Pink diamonds: DDMC benchmark *vs.* system size L (CDet data are in the thermodynamic limit $L \to \infty$).

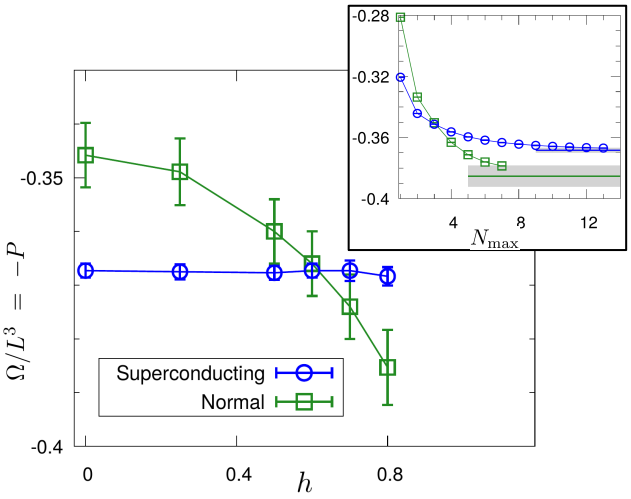

FIG. 2. Grand-potential density *vs.* Zeeman field, at $T = 1/16 \approx T_c/4$. Circles: superconducting phase, obtained by expanding around BCS mean-field theory ($\Delta_0 = \Delta_{\rm MF}$). Squares: normal phase, obtained by expanding around the normal mean-field solution ($\Delta_0 = 0$). The crossing between the curves signals the first-order phase transition. Inset: same quantity *vs.* truncation order $N_{\max}$, at $h = 0.8$; horizontal lines with error bands are the $N_{\max} \to \infty$ extrapolated results also shown in the main panel.

Our computer code is based on a library [38] providing a generic implementation of CDet, the integration over the internal vertex positions being done for all diagram orders $N \leq N_{\max}$ at once thanks to a recently introduced many-configuration Monte Carlo algorithm [39].

Results. Taking the hopping $t = 1$ as unit of energy, we set $U = -5$, and $\mu = -3.38$ so that the density $n = n_\uparrow + n_\downarrow$ is close to 0.5 particles per site, *i.e.* quarter filling – a standard choice of generic filling that differs from the special half-filled case. For $h = 0$, AFQMC is sign free and provides the critical temperature curve $T_c(U)$ [23]: Our choice of U lies in the strongly correlated regime where the curve has a broad maximum – we have $T_c(U = -5) \approx 0.25$, which is not far from the maximal value 0.33, and much larger than in the weak-coupling regime where T_c vanishes exponentially with $1/|U|$.

We start with a benchmark at $h = 0$. We compute the order parameter at $T = 1/8 \approx T_c/2$ and compare with the DDMC method [26, 40] also known as continuous-time interaction expansion in the context of impurity solvers [41]. Our data for the partial sum $\sum_{N=0}^{N_{\max}} \mathcal{O}_N$ converge as a function of the truncation order $N_{\max}$ to a result which agrees with the DDMC benchmark, see Fig. 1. Here and in what follows we use Padé approximants for the $N_{\max} \to \infty$ extrapolation [42]. We used $\Delta_0 = \Delta_{\rm MF}$ and checked that the extrapolated results agree for different choices of Δ_0.

We turn to the polarized regime $h > 0$, where conventional approaches such as AFQMC and DDMC have a sign problem and unbiased results are unavailable. We start by setting the temperature to $T \approx T_c/4$, increase the Zeeman field h, and compute the thermodynamic grand potential per unit volume, $\Omega/L^3 = -P$ with P the (electronic) pressure. We obtain the pressure of the superconducting phase using again the expansion around the broken-symmetry mean-field solution ($\Delta_0 = \Delta_{\rm MF}$). We also evaluate the expansion around the normal mean-field solution ($\Delta_0 = 0$) which yields the normal-phase pressure. As shown in Fig. 2, the two curves cross, which indicates a first order phase transition. The error bars are dominated by the $N_{\max} \to \infty$ extrapolation, and are larger for the normal phase because we could only evaluate the series up to order 7, instead of 12 for the superconducting phase. We attribute this difference to the fact that the superconducting-phase propagators are gapped, and hence decay faster with position, which reduces the Monte Carlo variance. Within error bars, the superconducting pressure is independent of h, which means that the magnetization $m := n_\uparrow - n_\downarrow$ is zero. This indicates that we are in the regime where h is smaller than the pairing gap E_g, *i.e.* the Zeeman field is not large enough to overcome the energy cost of having an unpaired fermion, and the magnetization is exponentially suppressed at low temperature, $m \sim e^{-(E_g - h)/T}$. So the pairing gap essentially prevents the superconducting phase from polarizing, until a first-order phase transition occurs when the polarized normal phase becomes energetically favorable. Ultracold atom experiments [43] and fixed-node Monte Carlo calculations [44] in continuous space are consistent with this scenario. This is also what is predicted by BCS mean-field theory [15, 45] albeit with a

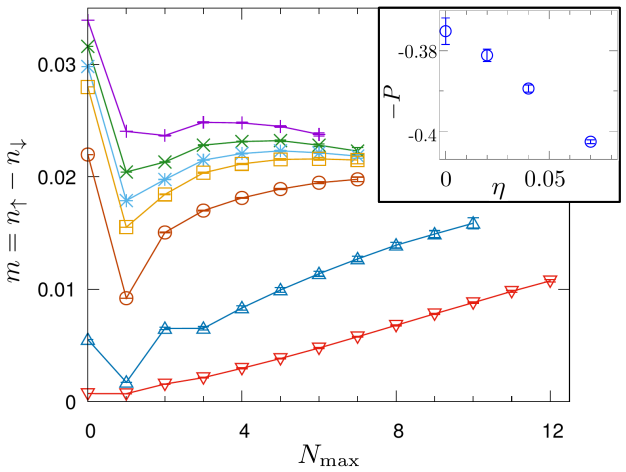

FIG. 3. Magnetization *vs.* maximal expansion order at $T = 0.19 \approx 3\,T_c/4$ and $h = 0.35$, for different choices of the unperturbed pairing field (from bottom to top: $\Delta_0 = 1.357 \approx \Delta_{\rm MF}, \Delta_0 = 0.9, 0.5, 0.4, 0.37, 0.34,$ and 0.3), from which we obtain $m = 0.0206(9)$. The BCS mean-field result (the value of the bottom curve at $N_{\max} = 0$) is 30 times smaller. Inset: Pressure *vs.* external symmetry-breaking field η, whose slope at the origin, and hence the order parameter, is non-zero.

critical field nearly twice larger than our unbiased result $h_c = 0.62(11)$.

For $h > h_c$ the superconducting phase is metastable. We have checked that the order parameter is still non-zero at $h = 0.8$. In this regime the convergence of the series $\sum \mathcal{O}_N$ is slower and the extrapolation becomes less stable. Therefore, instead of computing the order parameter directly, we extracted it from the response to a small symmetry-breaking field: $2\,\mathcal{O} = -dP^{(\eta)}/d\eta|_{\eta=0^+}$, where $P^{(\eta)}$ is the pressure in presence of the field η (*i.e.* for the hamiltonian $H^{(\eta)}$), whose expansion can be extrapolated reliably [46]. As always, the notion of a metastable phase has to be taken with a grain of salt: It is only well defined asymptotically close to the first-order transition point, where the energy barrier for nucleating the stable phase inside the metastable phase diverges. Accordingly, the diagrammatic expansion must actually diverge, but as long as we are not too deep in the metastable regime, this divergence is slow and only visible at very large orders, see below. Similarly, the normal phase is metastable for $h < h_c$, and we are able to follow it all the way to $h = 0$ without encountering the divergence of the series within the 7 orders that are accessible to us.

While we have seen that the pairing gap prevents the superfluid from polarizing at low temperature, the situation changes at higher temperature. At $T \approx 3\,T_c/4$ and $h = 0.35$, we find a magnetization $m = 0.0206(9)$, which corresponds to a polarization $(n_\uparrow - n_\downarrow)/(n_\uparrow + n_\downarrow)$ of 4.1%. This is 30 times larger than the BCS mean-field prediction. Therefore, BCS mean-field is not a good starting point for the expansion in this case, and we had to tune Δ_0 away from $\Delta_{\rm MF}$ in order to obtain convergence of the partial sums within accessible orders, see Fig. 3. Furthermore we can again check that the order parameter is non-zero by computing P *vs.* external field η, see inset of Fig. 3. We thus observe a polarized superconducting phase. This phase is possibly metastable, since its pressure (at $\eta = 0$) does not differ from the one of the normal phase within our error bars.

We end with a discussion of the large-order behavior of the expansion for the superconducting phase, which is determined by the singularities as a function of the formal expansion parameter ξ. In the limit $\xi \to 1^-$, we effectively have an external field $\eta_{\rm eff} = (1-\xi)\,\Delta_0$, hence the long-wavelength thermal fluctuations of the Goldstone mode lead to a singularity $\mathcal{O}(\xi) - \mathcal{O} \sim C\,\sqrt{1-\xi}$, with $C = [\mathcal{O}/(2\,D_s)]^{3/2}\,T\sqrt{\Delta_0}/\pi$, $\mathcal{O} \equiv \mathcal{O}(\xi \to 1^-)$, and D_s the superfluid stiffness [47]. This yields the power-law asymptotics $\mathcal{O}_N \sim -C/(N^{3/2}\,2\sqrt{\pi})$ and $P_N \sim C\,\Delta_0/(N^{5/2}\,\sqrt{\pi})$ for $N \to \infty$. When $T \to 0$ there is a crossover to the quantum-fluctuation regime where the Goldstone singularity is only logarithmic [48], leading to a faster $1/N^3$ decay of P_N. We expect another, weaker singularity at $\xi = 1$, given that the change of sign of $1-\xi$ causes a first-order phase transition associated to a change of sign of the equilibrium order parameter. Such a first-order transition is generally expected to cause an essential singularity, with a branch-cut discontinuity $\sim e^{-\beta B(\xi)}$ for $\xi \to 1$, with $B(\xi)$ the grand-potential barrier for nucleating a critical bubble of the stable phase inside the metastable phase [49], which diverges like a power of $1/|1-\xi|$ [50], This gives a streched-exponential large-order behavior $\sim \exp(-\#N^a)$ with $a < 1$. In the vicinity of the physical first-order transition from Fig. 2, we expect a third singularity at a point ξ_c that moves continuously from the right to the left of the physical point $\xi = 1$ when h changes from below to above h_c, with a branch-cut discontinuity $\sim e^{-\beta \mathcal{B}(\xi)}$ for $\xi \to \xi_c$ with $\mathcal{B}(\xi)$ the barrier for nucleating the stable normal phase inside the metastable superconducting phase, which diverges like a power of $1/|\xi_c - \xi|$ [51], hence a large-order behavior $(1/\xi_c)^N$ times a streched exponential. None of these three singularities lead to a divergence of the series, except for the third one in the metastable regime where $\xi_c < 1$, but this is a slow divergence only visible at very large N as long as ξ_c is close to 1, as anticipated. In the stable regime, the Goldstone singularity dominates asymptotically, but the prefactor C is much smaller than what would correspond to our numerically obtained coefficients, assuming that D_s is not much smaller than the value 0.5 predicted by DMFT at $T = 0$ [21]. Thus at $N = 12$ we are still far from the true large-N behavior; furthermore the smallness of C implies that the contribution of the Goldstone singularity to the final result is negligible. To estimate the effect of the sub-exponential decay of the coefficients, we supplemented the Padé results with Dlog-Padé, as well as with power-law extrap-

olations of the series shifted by N_s orders with $|N_s| \leq 3$, and we increased the final error bars to include all obtained results. As seen in Fig. 2 and in the inset of Fig. 3, the resulting error bars are still remarkably small. In this sense, 12 loops are sufficient for accurate extrapolation.

Outlook. BCS mean-field theory predicts [29] that in a large part of the phase diagram, the true equilibrium state is an exotic FFLO [52] phase. This open question can be tackled with the present approach by making Δ_0 space dependent. Stronger couplings can be accessed using renormalized expansions, following [36, 53]. This would allow to look for the breached-pair gapless superconducting phase [31] and to extend the continuous-space approach of [35] to superfluid phases. For the repulsive Hubbard model, the d-wave superconducting phase is accessible by expanding around a momentum-dependent Δ_0, as was done to second order in [54]. Another natural extension would be to go beyond the third-order expansion for open-shell nuclei [55].

Acknowledgements. We thank G. Biroli, E. Burovski, Y. Castin, N. Dupuis and J. Kurchan for discussions. We acknowledge support from the Paris Île-de-France region in the framework of DIM SIRTEQ (G.S.), H2020/ERC Advanced grant Critisup2 No. 743159 (F.W.), and the Simons Foundation through the Simons Collaboration on the Many Electron Problem (F.S. and M.F.). The Flatiron Institute is a division of the Simons Foundation. This work was granted access to the HPC resources of TGCC and IDRIS under the allocations A0090510609 attributed by GENCI (Grand Equipement National de Calcul Intensif).

* gabriele.spada@lkb.ens.fr
† rrossi@flatironinstitute.org
‡ werner@lkb.ens.fr

[1] H. Kamerlingh Onnes, Leiden Comm. **124c** (1911).
[2] J. Bardeen, L. N. Cooper, and J. R. Schrieffer, Phys. Rev. **106**, 162 (1957); *ibid.* **108**, 1175 (1957).
[3] D. M. Eagles, Phys. Rev. **186**, 456 (1969).
[4] A. J. Leggett, J. Phys. (Paris) **42**, C7 (1980); A. J. Leggett, *Diatomic Molecules and Cooper Pairs*, in: *Modern Trends in the Theory of Condensed Matter*, ed. A. Pekalski and J. A. Przystawa (Springer, 1980).
[5] S. Giorgini, L. P. Pitaevskii, and S. Stringari, Rev. Mod. Phys. **80**, 1215 (2008).
[6] I. Bloch, J. Dalibard, and W. Zwerger, Rev. Mod. Phys. **80**, 885 (2008); I. Bloch, J. Dalibard, and S. Nascimbène, Nature Phys. **8**, 267 (2012).
[7] *The BCS-BEC Crossover and the Unitary Fermi Gas*, Lect. Notes Phys. **836**, ed. W. Zwerger (Springer, Heidelberg, 2012).
[8] S. Gandolfi, A. Gezerlis, and J. Carlson, Annu. Rev. Nucl. Part. Sci. **65**, 303 (2015).
[9] G. C. Strinati, P. Pieri, G. Roepke, P. Schuck, and M. Urban, Phys. Rep. **738**, 1 (2018).
[10] R. Micnas, J. Ranninger, and S. Robaszkiewicz, Rev. Mod. Phys. **62**, 113 (1990).
[11] P. Nozières and S. Schmitt-Rink, J. Low Temp. Phys. **59**, 195 (1985).
[12] M. Capone, M. Fabrizio, C. Castellani, and E. Tosatti, Rev. Mod. Phys. **81**, 943 (2009); S. Kasahara, T. Watashige, T. Hanaguri, Y. Kohsaka, T. Yamashita, Y. Shimoyama, Y. Mizukami, R. Endo, H. Ikeda, K. Aoyama, T. Terashima, S. Uji, T. Wolf, H. von Löhneysen, T. Shibauchi, and Y. Matsuda, PNAS **111**, 16309 (2014); S. Rinott, K. B. Chashka, A. Ribak, E. D. L. Rienks, A. Taleb-Ibrahimi, P. Le Fevre, F. Bertran, M. Randeria, and A. Kanigel, Science Adv. **3**, e1602372 (2017); J. M. Park, Y. Cao, K. Watanabe, T. Taniguchi, and P. Jarillo-Herrero, Nature **590**, 249 (2021); Y. Nakagawa, Y. Kasahara, T. Nomoto, R. Arita, T. Nojima, and Y. Iwasa, Science , eabb9860 (2021).
[13] L. V. Keldysh and A. N. Kozlov, Zh. Eksp. Teor. Fiz. **54**, 978 (1968) [Sov. Phys. JETP **27**, 521 (1968)] ; M. Combescot, R. Combescot, and F. Dubin, Rep. Prog. Phys. **80**, 066501 (2017); J. Wang, P. Nie, X. Li, H. Zuo, B. Fauqué, Z. Zhu, and K. Behnia, PNAS **117**, 30215 (2020).
[14] The attractive and repulsive model are related by a transformation that exchanges doping away from half-filling and polarization. In particular the attractive doped model is equivalent to the repulsive polarized model, which is also relevant to materials [18]. The half-filled attractive model, equivalent to the unpolarized repulsive model, is a special case where the broken symmetry is $SO(3)$, and will be studied elsewhere.
[15] A. Cichy and R. Micnas, Ann. Phys. **347**, 207 (2014).
[16] D.-H. Kim, P. Törmä, and J.-P. Martikainen, Phys. Rev. Lett. **102**, 245301 (2009).
[17] J. R. Engelbrecht, H. Zhao, and A. Nazarenko, J. Chem. Phys. Sol. **63**, 223 (2002); H. Tamaki, Y. Ohashi, and K. Miyake, Phys. Rev. A **77**, 063616 (2008).
[18] L. Laloux, A. Georges, and W. Krauth, Phys. Rev. B **50**, 3092 (1994).
[19] J. K. Freericks and M. Jarrell, Phys. Rev. B **50**, 6939 (1994); M. Keller, W. Metzner, and U. Schollwöck, Phys. Rev. Lett. **86**, 4612 (2001); M. Capone, C. Castellani, and M. Grilli, Phys. Rev. Lett. **88**, 126403 (2002); A. Garg, H. R. Krishnamurthy, and M. Randeria, Phys. Rev. B **72**, 024517 (2005); A. Toschi, P. Barone, M. Capone, and C. Castellani, New J. Phys. **7**, 7 (2005); R. Peters and J. Bauer, Phys. Rev. B **92**, 014511 (2015); S. Sakai, M. Civelli, Y. Nomura, and M. Imada, Phys. Rev. B **92**, 180503 (2015).
[20] A. Garg, H. R. Krishnamurthy, and M. Randeria, Phys. Rev. B **72**, 024517 (2005); A. Toschi, M. Capone, and C. Castellani, Phys. Rev. B **72**, 235118 (2005); J. Bauer and A. C. Hewson, Europhys. Lett. **85**, 27001 (2009).
[21] J. Bauer, A. C. Hewson, and N. Dupuis, Phys. Rev. B **79**, 214518 (2009); A. Koga and P. Werner, Phys. Rev. A **84**, 023638 (2011); Y. Murakami, P. Werner, N. Tsuji, and H. Aoki, Phys. Rev. B **88**, 125126 (2013); N. A. Kuleeva, E. Z. Kuchinskii, and M. V. Sadovskii, JETP **119**, 264 (2014).
[22] L. Del Re, M. Capone, and A. Toschi, Phys. Rev. B **99**, 045137 (2019).
[23] A. Sewer, X. Zotos, and H. Beck, Phys. Rev. B **66**, 140504 (2002).
[24] J. Carlson, S. Gandolfi, K. E. Schmidt, and S. Zhang, Phys. Rev. A **84**, 061602(R) (2011); J. E. Drut, T. A.

Lähde, G. Wlazłowski, and P. Magierski, Phys. Rev. A **85**, 051601(R) (2012); M. G. Endres, D. B. Kaplan, J.-W. Lee, and A. N. Nicholson, Phys. Rev. A **87**, 023615 (2013); S. Jensen, C. N. Gilbreth, and Y. Alhassid, Phys. Rev. Lett. **124**, 090604 (2020); Phys. Rev. Lett. **125**, 043402 (2020).

[25] A. Richie-Halford, J. E. Drut, and A. Bulgac, Phys. Rev. Lett. **125**, 060403 (2020).

[26] E. Burovski, N. Prokof'ev, B. Svistunov, and M. Troyer, Phys. Rev. Lett. **96**, 160402 (2006).

[27] O. Goulko and M. Wingate, Phys. Rev. A **82**, 053621 (2010).

[28] Unbiased QMC methods typically face an exponential scaling of computational time with the number of fermions $\mathcal{N}$, hence limiting the accessible $\mathcal{N}$ despite tremendous efforts in various fields including condensed matter, chemistry, and lattice QCD [56]. Often the sign problem is eliminated using an approximate ansatz for the nodal surface [8, 44, 57] or for the entire wavefunction [57], although unbiased sign-free approaches are also being developed [25, 58]. The sign problem also plagues machine-learning approaches [59].

[29] T. Koponen, J. Kinnunen, J.-P. Martikainen, L. M. Jensen, and P. Törmä, New J. Phys. **8**, 179 (2006); T. K. Koponen, T. Paananen, J.-P. Martikainen, and P. Törmä, Phys. Rev. Lett. **99**, 120403 (2007); Y. L. Loh and N. Trivedi, Phys. Rev. Lett. **104**, 165302 (2010); P. Rosenberg, S. Chiesa, and S. Zhang, J. Phys.: Condens. Matter **27**, 225601 (2015).

[30] Y. L. Loh and N. Trivedi, *Theoretical Studies of Superconductor-Insulator Transitions,* in: *Conductor-Insulator Quantum Phase Transitions*, edited by V. Dobrosavljevic, N. Trivedi, and J. M. Valles (Oxford University Press, 2012).

[31] T.-L. Dao, M. Ferrero, A. Georges, M. Capone, and O. Parcollet, Phys. Rev. Lett. **101**, 236405 (2008); A. Koga and P. Werner, J. Phys. Soc. Jpn. **79**, 064401 (2010); E. Z. Kuchinskii, N. A. Kuleeva, and M. V. Sadovskii, JETP **127**, 753 (2018).

[32] R. A. Hart, P. M. Duarte, T.-L. Yang, X. Liu, T. Paiva, E. Khatami, R. T. Scalettar, N. Trivedi, D. A. Huse, and R. G. Hulet, Nature **519**, 211 (2015); A. Mazurenko, C. S. Chiu, G. Ji, M. F. Parsons, M. Kanász-Nagy, R. Schmidt, F. Grusdt, E. Demler, D. Greif, and M. Greiner, Nature **545**, 462 (2017); W. Xu, W. R. McGehee, W. N. Morong, and B. DeMarco, Nature Comm. **10**, 1588 (2019); P. T. Brown, E. Guardado-Sanchez, B. M. Spar, E. W. Huang, T. P. Devereaux, and W. S. Bakr, Nature Phys. **16**, 26 (2020); M. Gall, C. F. Chan, N. Wurz, and M. Köhl, Phys. Rev. Lett. **124**, 010403 (2020).

[33] R. Rossi, Phys. Rev. Lett. **119**, 045701 (2017).

[34] E. Kozik, K. Van Houcke, E. Gull, L. Pollet, N. Prokof'ev, B. Svistunov, and M. Troyer, Europhys. Lett. **90**, 10004 (2010); S. A. Kulagin, N. Prokof'ev, O. A. Starykh, B. Svistunov, and C. N. Varney, Phys. Rev. Lett. **110**, 070601 (2013); A. S. Mishchenko, N. Nagaosa, and N. Prokof'ev, Phys. Rev. Lett. **113**, 166402 (2014); J. Gukelberger, E. Kozik, L. Pollet, N. Prokof'ev, M. Sigrist, B. Svistunov, and M. Troyer, Phys. Rev. Lett. **113**, 195301 (2014); Y. Deng, E. Kozik, N. V. Prokof'ev, and B. V. Svistunov, Europhys. Lett. **110**, 57001 (2015); J. P. F. LeBlanc, A. E. Antipov, F. Becca, I. W. Bulik, G. K.-L. Chan, C.-M. Chung, Y. Deng, M. Ferrero, T. M. Henderson, C. A. Jiménez-Hoyos, E. Kozik, X.-W. Liu, A. J. Millis, N. V. Prokof'ev, M. Qin, G. E. Scuseria, H. Shi, B. V. Svistunov, L. F. Tocchio, I. S. Tupitsyn, S. R. White, S. Zhang, B.-X. Zheng, Z. Zhu, and E. Gull, Phys. Rev. X **5**, 041041 (2015); Y. Huang, K. Chen, Y. Deng, N. Prokof'ev, and B. Svistunov, Phys. Rev. Lett. **116**, 177203 (2016); I. S. Tupitsyn, A. S. Mishchenko, N. Nagaosa, and N. Prokof'ev, Phys. Rev. B **94**, 155145 (2016); I. S. Tupitsyn and N. V. Prokof'ev, Phys. Rev. Lett. **118**, 026403 (2017); W. Wu, M. Ferrero, A. Georges, and E. Kozik, Phys. Rev. B **96**, 041105(R) (2017); M. Motta, D. M. Ceperley, G. K.-L. Chan, J. A. Gomez, E. Gull, S. Guo, C. A. Jiménez-Hoyos, T. N. Lan, J. Li, F. Ma, A. J. Millis, N. V. Prokof'ev, U. Ray, G. E. Scuseria, S. Sorella, E. M. Stoudenmire, Q. Sun, I. S. Tupitsyn, S. R. White, D. Zgid, and S. Zhang, Phys. Rev. X **7**, 031059 (2017); J. Carlström and E. J. Bergholtz, Phys. Rev. B **98**, 241102(R) (2018); J. Carlström, Phys. Rev. B **97**, 075119 (2018); I. S. Tupitsyn and N. V. Prokof'ev, Phys. Rev. B **99**, 121113(R) (2019); K. Chen and K. Haule, Nature Comm. **10**, 3725 (2019); F. Šimkovic, J. P. F. LeBlanc, A. J. Kim, Y. Deng, N. V. Prokof'ev, B. V. Svistunov, and E. Kozik, Phys. Rev. Lett. **124**, 017003 (2020); A. J. Kim, F. Simkovic, and E. Kozik, Phys. Rev. Lett. **124**, 117602 (2020); C. Lenihan, A. J. Kim, F. Šimkovic, and E. Kozik, Phys. Rev. Lett. **126**, 105701 (2021); A. Taheridehkordi, S. H. Curnoe, and J. P. F. LeBlanc, Phys. Rev. B **102**, 045115 (2020); J. Vucicevic, P. Stipsic, and M. Ferrero, "Analytical solution for time-integrals in diagrammatic expansions: application to real-frequency diagrammatic monte carlo," arXiv:2011.08226; T. Schäfer, N. Wentzell, F. Simkovic, Y.-Y. He, C. Hille, M. Klett, C. J. Eckhardt, B. Arzhang, V. Harkov, F.-M. L. Régent, A. Kirsch, Y. Wang, A. J. Kim, E. Kozik, E. A. Stepanov, A. Kauch, S. Andergassen, P. Hansmann, D. Rohe, Y. M. Vilk, J. P. F. LeBlanc, S. Zhang, A. M. S. Tremblay, M. Ferrero, O. Parcollet, and A. Georges, "Tracking the footprints of spin fluctuations: A multi-method, multi-messenger study of the two-dimensional hubbard model," arXiv:2006.10769; A. S. Mishchenko, N. Nagaosa, and N. Prokof'ev, "Fermi blockade of the electron-phonon interaction: why strong coupling effects may not be seen in optimally doped high temperature superconductors," arXiv:2007.09888; A. Wietek, R. Rossi, F. Simkovic, M. Klett, P. Hansmann, M. Ferrero, E. M. Stoudenmire, T. Schäfer, and A. Georges, "Mott insulating states with competing orders in the triangular lattice Hubbard model," arXiv:2102.12904.

[35] K. Van Houcke, F. Werner, E. Kozik, N. Prokof'ev, B. Svistunov, M. J. H. Ku, A. T. Sommer, L. W. Cheuk, A. Schirotzek, and M. W. Zwierlein, Nature Phys. **8**, 366 (2012); R. Rossi, T. Ohgoe, K. Van Houcke, and F. Werner, Phys. Rev. Lett **121**, 130405 (2018); R. Rossi, T. Ohgoe, E. Kozik, N. Prokof'ev, B. Svistunov, K. Van Houcke, and F. Werner, Phys. Rev. Lett **121**, 130406 (2018).

[36] R. Rossi, F. Šimkovic, and M. Ferrero, Europhys. Lett. **132**, 11001 (2020).

[37] For an analogous discussion in the contect of the broken-symmetry phase of ϕ^4 theory, see M. Serone, G. Spada, and G. Villadoro, JHEP **5**, 47 (2019).

[38] R. Rossi and F. Šimkovic, *Fast Feynman Diagrammatics*, to be published.

[39] F. Šimkovic and R. Rossi, "Many-Configuration Markov-Chain Monte Carlo," arXiv:2102.05613.

[40] A. Rubtsov, arXiv:cond-mat/0302228; A. N. Rubtsov, V. V. Savkin, and A. I. Lichtenstein, Phys. Rev. B **72**, 035122 (2005).

[41] A. N. Rubtsov and A. I. Lichtenstein, JETP Lett. **80**, 61 (2004); E. Gull, A. J. Millis, A. I. Lichtenstein, A. N. Rubtsov, M. Troyer, and P. Werner, Rev. Mod. Phys. **83**, 349 (2011).

[42] F. Šimkovic and E. Kozik, Phys. Rev. B **100**, 121102(R) (2019).

[43] Y. Shin, C. Schunck, A. Schirotzek, and W. Ketterle, Nature **451**, 689 (2008); S. Nascimbène, N. Navon, K. J. Jiang, F. Chevy, and C. Salomon, Nature **463**, 1057 (2010); N. Navon, S. Nascimbène, F. Chevy, and C. Salomon, Science **328**, 729 (2010).

[44] S. Pilati and S. Giorgini, Phys. Rev. Lett. **100**, 030401 (2008).

[45] G. Sarma, J. Phys. Chem. Solids **24**, 1029 (1963).

[46] In this case, the diagrammatic series is generated by $H_\xi^{(\eta)} := H_0 + \xi\ (H^{(\eta)} - H_0)$. Accordingly, $\delta_{\rm sh}$ is given by $\langle O \rangle_{H_0} + (\Delta_0 - \eta)/U$.

[47] A. Z. Patashinskii and V. L. Pokrovskii, Zh. Eksp. Teor. Fiz. **64**, 1445 (1973) [Sov. Phys. JETP **37**, 4 (1973)]; E. Brézin and D. J. Wallace, Phys. Rev. B **7**, 1967 (1973).

[48] N. Dupuis, *private communication*; N. Dupuis, Phys. Rev. E **83**, 031120 (2011).

[49] J. Langer, Ann. Phys. **41**, 108 (1967); N. J. Gunther, D. J. Wallace, and D. A. Nicole, J. Phys. A **13**, 1755 (1980).

[50] Since one can go gradually from one phase to the other by slowly rotating the order parameter, the surface tension only grows with the bubble radius R as R^{d-2} in d dimensions, leading to $B(\xi) \sim 1/|1-\xi|^{d/2-1}$.

[51] Here the surface tension has the standard scaling R^{d-1}, hence $\mathcal{B}(\xi) \sim 1/|\xi_c - \xi|^{d-1}$.

[52] P. Fulde and R. Ferrell, Phys. Rev **135**, A550 (1964), A. I. Larkin and Y. N. Ovchinnikov, Zh. Eksp. Teor. Fiz **47**, 1136 (1964) [Sov. Phys. JETP **20**, 762 (1965)].

[53] F. Šimkovic, R. Rossi, and M. Ferrero, Phys. Rev. B **102**, 195122 (2020).

[54] A. Neumayr and W. Metzner, Phys. Rev. B **67**, 035112 (2003).

[55] A. Tichai, P. Arthuis, T. Duguet, H. Hergert, V. Somà, and R. Roth, Phys. Lett. B **786**, 195 (2018).

[56] S. Muroya, A. Nakamura, C. Nonaka, and T. Takaishi, Prog. Theor. Phys. **110**, 615 (2003); P. de Forcrand, PoS(LAT2009)010 ; G. H. Booth, A. J. W. Thom, and A. Alavi, J. Chem. Phys. **131**, 054106 (2009); T. Ma, L. Zhang, C.-C. Chang, H.-H. Hung, and R. T. Scalettar, Phys. Rev. Lett. **120**, 116601 (2018).

[57] D. M. Ceperley and B. J. Alder, Phys. Rev. Lett. **45**, 566 (1980); S. Zhang and H. Krakauer, Phys. Rev. Lett. **90**, 136401 (2003); D. Ceperley, Rev. Mineral. Geochem. **71**, 129 (2010); O. Juillet, A. Leprévost, J. Bonnard, and R. Frésard, J. Phys. A **50**, 175001 (2017); M. Motta and S. Zhang, WIREs Comput. Mol. Sci. **8**, e1364 (2018); M. Qin, C.-M. Chung, H. Shi, E. Vitali, C. Hubig, U. Schollwöck, S. R. White, and S. Zhang, Phys. Rev. X **10**, 031016 (2020); T. Ohgoe and M. Imada, Phys. Rev. Lett. **119**, 197001 (2017); T. Ohgoe, M. Hirayama, T. Misawa, K. Ido, Y. Yamaji, and M. Imada, Phys. Rev. B **101**, 045124 (2020).

[58] C. Berger, L. Rammelmüller, A. Loheac, F. Ehmann, J. Braun, and J. Drut, Phys. Rep. **892**, 1 (2021).

[59] T. Westerhout, N. Astrakhantsev, K. S. Tikhonov, M. I. Katsnelson, and A. A. Bagrov, Nature Comm. **11**, 1593 (2020); A. Szabó and C. Castelnovo, Phys. Rev. Research **2**, 033075 (2020).

Bibliography

[1] C. S. Alexander, G. Cao, V. Dobrosavljevic, S. McCall, J. E. Crow, E. Lochner, and R. P. Guertin. Destruction of the mott insulating ground state of ca_2ruo_4 by a structural transition. *Phys. Rev. B*, 60:R8422–R8425, Sep 1999.

[2] P. W. Anderson. Localized magnetic states in metals. *Phys. Rev.*, 124:41–53, Oct 1961.

[3] P. W. Anderson. Local moments and localized states. *Science*, 201(4353):307–316, 1978.

[4] Andrey E. Antipov, Qiaoyuan Dong, Joseph Kleinhenz, Guy Cohen, and Emanuel Gull. Currents and green's functions of impurities out of equilibrium: Results from inchworm quantum monte carlo. *Phys. Rev. B*, 95:085144, Feb 2017.

[5] Hideo Aoki, Naoto Tsuji, Martin Eckstein, Marcus Kollar, Takashi Oka, and Philipp Werner. Nonequilibrium dynamical mean-field theory and its applications. *Rev. Mod. Phys.*, 86:779–837, Jun 2014.

[6] Camille Aron, Cedric Weber, and Gabriel Kotliar. Impurity model for non-equilibrium steady states. *Phys. Rev. B*, 87:125113, Mar 2013.

[7] Daniel P. Arovas, Erez Berg, Steven A. Kivelson, and Srinivas Raghu. The Hubbard Model. *Annual Review of Condensed Matter Physics*, 13(1):239–274, 2022.

[8] Thomas Ayral and Olivier Parcollet. Mott physics and spin fluctuations: A unified framework. *Phys. Rev. B*, 92:115109, Sep 2015.

[9] Thomas Ayral and Olivier Parcollet. Mott physics and spin fluctuations: A functional viewpoint. *Phys. Rev. B*, 93:235124, Jun 2016.

[10] George A. Baker. Application of the padé approximant method to the investigation of some magnetic properties of the ising model. *Phys. Rev.*, 124:768–774, Nov 1961.

[11] J. Bauer and A. C. Hewson. Quasiparticle excitations and dynamic susceptibilities in the bcs-bec crossover. *Europhysics Letters*, 85(2):27001, jan 2009.

[12] Francoise Berthoud, Bruno Bzeznik, Nicolas Gibelin, Myriam Laurens, Cyrille Bonamy, Maxence Morel, and Xavier Schwindenhammer. *Estimation de l'empreinte carbone d'une heure. coeur de calcul.* PhD thesis, UGA-Université Grenoble Alpes; CNRS; INP Grenoble; INRIA, 2020.

[13] Corentin Bertrand, Daniel Bauernfeind, Philipp T. Dumitrescu, Marjan Maček, Xavier Waintal, and Olivier Parcollet. Quantum quasi monte carlo algorithm for out-of-equilibrium green functions at long times. *Phys. Rev. B*, 103:155104, Apr 2021.

[14] Corentin Bertrand, Serge Florens, Olivier Parcollet, and Xavier Waintal. Reconstructing nonequilibrium regimes of quantum many-body systems from the analytical structure of perturbative expansions. *Phys. Rev. X*, 9:041008, Oct 2019.

[15] Corentin Bertrand, Olivier Parcollet, Antoine Maillard, and Xavier Waintal. Quantum monte carlo algorithm for out-of-equilibrium green's functions at long times. *Phys. Rev. B*, 100:125129, Sep 2019.

[16] N. E. Bickers. Review of techniques in the large-n expansion for dilute magnetic alloys. *Rev. Mod. Phys.*, 59:845–939, Oct 1987.

[17] Andreas Björklund, Thore Husfeldt, Petteri Kaski, and Mikko Koivisto. Fourier meets möbius: Fast subset convolution. In *Proceedings of the Thirty-Ninth Annual ACM Symposium on Theory of Computing*, STOC '07, page 67–74, New York, NY, USA, 2007. Association for Computing Machinery.

[18] Immanuel Bloch. Ultracold quantum gases in optical lattices. *Nature physics*, 1(1):23–30, 2005.

[19] E. Brézin and D. J. Wallace. Critical behavior of a classical heisenberg ferromagnet with many degrees of freedom. *Phys. Rev. B*, 7:1967–1974, Mar 1973.

[20] C. Brezinski. Extrapolation algorithms and padé approximations: a historical survey. *Applied Numerical Mathematics*, 20(3):299–318, 1996.

[21] Henrik Bruus and Karsten Flensberg. *Many-body quantum theory in condensed matter physics: an introduction*. OUP Oxford, 2004.

[22] Ralf Bulla, Theo A. Costi, and Thomas Pruschke. Numerical renormalization group method for quantum impurity systems. *Rev. Mod. Phys.*, 80:395–450, Apr 2008.

[23] Evgeni Burovski, Nikolay Prokof'ev, Boris Svistunov, and Matthias Troyer. The fermi–hubbard model at unitarity. *New Journal of Physics*, 8(8):153, aug 2006.

[24] Massimo Campostrini, Martin Hasenbusch, Andrea Pelissetto, Paolo Rossi, and Ettore Vicari. Critical exponents and equation of state of the three-dimensional heisenberg universality class. *Phys. Rev. B*, 65:144520, Apr 2002.

[25] Hsing-Ta Chen, Guy Cohen, and David R. Reichman. Inchworm monte carlo for exact non-adiabatic dynamics. i. theory and algorithms. *The Journal of Chemical Physics*, 146(5):054105, 2017.

[26] Hsing-Ta Chen, Guy Cohen, and David R. Reichman. Inchworm monte carlo for exact non-adiabatic dynamics. ii. benchmarks and comparison with established methods. *The Journal of Chemical Physics*, 146(5):054106, 2017.

[27] Kun Chen and Kristjan Haule. A combined variational and diagrammatic quantum monte carlo approach to the many-electron problem. *Nature communications*, 10(1):3725, 2019.

[28] Agnieszka Cichy and Roman Micnas. The spin-imbalanced attractive hubbard model in d=3: Phase diagrams and bcs–bec crossover at low filling. *Annals of Physics*, 347:207–249, 2014.

[29] Lorenzo De Leo, Corinna Kollath, Antoine Georges, Michel Ferrero, and Olivier Parcollet. Trapping and Cooling Fermionic Atoms into Mott and Néel States. *Phys. Rev. Lett.*, 101:210403, Nov 2008.

[30] N. Dupuis. Infrared behavior in systems with a broken continuous symmetry: Classical o(n) model versus interacting bosons. *Phys. Rev. E*, 83:031120, Mar 2011.

[31] Martin Eckstein and Philipp Werner. Nonequilibrium dynamical mean-field calculations based on the noncrossing approximation and its generalizations. *Phys. Rev. B*, 82:115115, Sep 2010.

[32] J. Ehrlich and C. Honerkamp. Functional renormalization group for fermion lattice models in three dimensions: Application to the hubbard model on the cubic lattice. *Phys. Rev. B*, 102:195108, Nov 2020.

[33] Michael E. Fisher and Vladimir Privman. First-order transitions breaking o(n) symmetry: Finite-size scaling. *Phys. Rev. B*, 32:447–464, Jul 1985.

[34] L. Fratino, P. Sémon, M. Charlebois, G. Sordi, and A.-M. S. Tremblay. Signatures of the mott transition in the antiferromagnetic state of the two-dimensional hubbard model. *Phys. Rev. B*, 95:235109, Jun 2017.

[35] Arti Garg, H. R. Krishnamurthy, and Mohit Randeria. Bcs-bec crossover at $t = 0$: A dynamical mean-field theory approach. *Phys. Rev. B*, 72:024517, Jul 2005.

[36] R. Garioud, F. Šimkovic IV au2, R. Rossi, G. Spada, T. Schäfer, F. Werner, and M. Ferrero. Precise many-body simulations of antiferromagnetic phases using broken-symmetry perturbative expansions, 2022.

[37] Antoine Georges. The beauty of impurities: Two revivals of friedel's virtual bound-state concept. *Comptes Rendus Physique*, 17(3):430–446, 2016. Physique de la matière condensée au XXIe siècle: l'héritage de Jacques Friedel.

[38] Antoine Georges and Gabriel Kotliar. Hubbard model in infinite dimensions. *Phys. Rev. B*, 45:6479–6483, Mar 1992.

[39] Antoine Georges, Gabriel Kotliar, Werner Krauth, and Marcelo J. Rozenberg. Dynamical mean-field theory of strongly correlated fermion systems and the limit of infinite dimensions. *Rev. Mod. Phys.*, 68:13–125, Jan 1996.

[40] Pedro Gonnet, Stefan Güttel, and Lloyd N. Trefethen. Robust padé approximation via svd. *SIAM Review*, 55(1):101–117, 2013.

[41] E. V. Gorelik, I. Titvinidze, W. Hofstetter, M. Snoek, and N. Blümer. Néel Transition of Lattice Fermions in a Harmonic Trap: A Real-Space Dynamic Mean-Field Study. *Phys. Rev. Lett.*, 105:065301, Aug 2010.

[42] E. Gorelov, M. Karolak, T. O. Wehling, F. Lechermann, A. I. Lichtenstein, and E. Pavarini. Nature of the mott transition in ca_2ruo_4. *Phys. Rev. Lett.*, 104:226401, Jun 2010.

[43] Daniel Greif, Gregor Jotzu, Michael Messer, Rémi Desbuquois, and Tilman Esslinger. Formation and dynamics of antiferromagnetic correlations in tunable optical lattices. *Phys. Rev. Lett.*, 115:260401, Dec 2015.

[44] Markus Greiner, Olaf Mandel, Tilman Esslinger, Theodor W Hänsch, and Immanuel Bloch. Quantum phase transition from a superfluid to a mott insulator in a gas of ultracold atoms. *nature*, 415(6867):39–44, 2002.

[45] Kent Griffin and Michael J. Tsatsomeros. Principal minors, part i: A method for computing all the principal minors of a matrix. *Linear Algebra and its Applications*, 419(1):107–124, 2006.

[46] Emanuel Gull, Andrew J. Millis, Alexander I. Lichtenstein, Alexey N. Rubtsov, Matthias Troyer, and Philipp Werner. Continuous-time monte carlo methods for quantum impurity models. *Rev. Mod. Phys.*, 83:349–404, May 2011.

[47] Emanuel Gull, David R. Reichman, and Andrew J. Millis. Bold-line diagrammatic monte carlo method: General formulation and application to expansion around the noncrossing approximation. *Phys. Rev. B*, 82:075109, Aug 2010.

[48] N J Gunther, D J Wallace, and D A Nicole. Goldstone modes in vacuum decay and first-order phase transitions. *Journal of Physics A: Mathematical and General*, 13(5):1755, may 1980.

[49] Martin C. Gutzwiller. Effect of Correlation on the Ferromagnetism of Transition Metals. *Phys. Rev. Lett.*, 10:159–162, Mar 1963.

[50] Russell A. Hart, Pedro M. Duarte, Tsung-Lin Yang, Xinxing Liu, Thereza Paiva, Ehsan Khatami, Richard T. Scalettar, Nandini Trivedi, David A. Huse, and Randall G. Hulet. Observation of antiferromagnetic correlations in the Hubbard model with ultracold atoms. *Nature*, 519(7542):211–214, Mar 2015.

[51] K. Haule, S. Kirchner, J. Kroha, and P. Wölfle. Anderson impurity model at finite coulomb interaction u: Generalized noncrossing approximation. *Phys. Rev. B*, 64:155111, Sep 2001.

[52] K. Held. Electronic structure calculations using dynamical mean field theory. *Advances in Physics*, 56(6):829–926, 2007.

[53] Alexander Cyril Hewson. *The Kondo problem to heavy fermions*. Number 2. Cambridge university press, 1997.

[54] Daniel Hirschmeier, Hartmut Hafermann, Emanuel Gull, Alexander I. Lichtenstein, and Andrey E. Antipov. Mechanisms of finite-temperature magnetism in the three-dimensional hubbard model. *Phys. Rev. B*, 92:144409, Oct 2015.

[55] A. F. Ho, M. A. Cazalilla, and T. Giamarchi. Quantum simulation of the hubbard model: The attractive route. *Phys. Rev. A*, 79:033620, Mar 2009.

[56] J. Hubbard and Brian Hilton Flowers. Electron correlations in narrow energy bands. *Proc. R. Soc. London, Sect. A*, 276(1365):238–257, 1963.

[57] J. Hubbard and Brian Hilton Flowers. Electron correlations in narrow energy bands III. An improved solution. *Proc. R. Soc. London, Sect. A*, 281(1386):401–419, 1964.

[58] Fedor Šimkovic and Evgeny Kozik. Determinant monte carlo for irreducible feynman diagrams in the strongly correlated regime. *Phys. Rev. B*, 100:121102, Sep 2019.

[59] Fedor Šimkovic, Riccardo Rossi, and Michel Ferrero. Efficient one-loop-renormalized vertex expansions with connected determinant diagrammatic monte carlo. *Phys. Rev. B*, 102:195122, Nov 2020.

[60] Fedor Šimkovic IV. and Riccardo Rossi. Many-configuration markov-chain monte carlo, 2021.

[61] Fedor Šimkovic IV., Riccardo Rossi, Antoine Georges, and Michel Ferrero. Origin and fate of the pseudogap in the doped hubbard model, 2022.

[62] Sergei Iskakov and Emanuel Gull. Phase transitions in partial summation methods: Results from the three-dimensional hubbard model. *Phys. Rev. B*, 105:045109, Jan 2022.

[63] Fedor Šimkovic IV and Michel Ferrero. Fast principal minor algorithms for diagrammatic monte carlo. *Phys. Rev. B*, 105:125104, Mar 2022.

[64] Fedor Šimkovic IV, Riccardo Rossi, and Michel Ferrero. Two-dimensional hubbard model at finite temperature: Weak, strong, and long correlation regimes. *Phys. Rev. Res.*, 4:043201, Dec 2022.

[65] D. Jaksch, C. Bruder, J. I. Cirac, C. W. Gardiner, and P. Zoller. Cold bosonic atoms in optical lattices. *Phys. Rev. Lett.*, 81:3108–3111, Oct 1998.

[66] D. Jaksch and P. Zoller. The cold atom hubbard toolbox. *Annals of Physics*, 315(1):52–79, 2005. Special Issue.

[67] M. Jarrell. Hubbard model in infinite dimensions: A quantum monte carlo study. *Phys. Rev. Lett.*, 69:168–171, Jul 1992.

[68] Jason Kaye and Denis Golež. Low rank compression in the numerical solution of the nonequilibrium Dyson equation. *SciPost Phys.*, 10:091, 2021.

[69] Jason Kaye and Hugo U. R. Strand. A fast time domain solver for the equilibrium dyson equation, 2023.

[70] P. R. C. Kent, M. Jarrell, T. A. Maier, and Th. Pruschke. Efficient calculation of the antiferromagnetic phase diagram of the three-dimensional hubbard model. *Phys. Rev. B*, 72:060411, Aug 2005.

[71] Aaram J. Kim, Nikolay V. Prokof'ev, Boris V. Svistunov, and Evgeny Kozik. Homotopic action: A pathway to convergent diagrammatic theories. *Phys. Rev. Lett.*, 126:257001, Jun 2021.

[72] Jun Kondo. Resistance Minimum in Dilute Magnetic Alloys. *Progress of Theoretical Physics*, 32(1):37–49, 07 1964.

[73] E. Kozik, E. Burovski, V. W. Scarola, and M. Troyer. Néel temperature and thermodynamics of the half-filled three-dimensional hubbard model by diagrammatic determinant monte carlo. *Phys. Rev. B*, 87:205102, May 2013.

[74] E. Kozik, K. Van Houcke, E. Gull, L. Pollet, N. Prokof'ev, B. Svistunov, and M. Troyer. Diagrammatic monte carlo for correlated fermions. *Europhysics Letters*, 90(1):10004, apr 2010.

[75] Evgeny Kozik, Michel Ferrero, and Antoine Georges. Nonexistence of the luttinger-ward functional and misleading convergence of skeleton diagrammatic series for hubbard-like models. *Phys. Rev. Lett.*, 114:156402, Apr 2015.

[76] Francis Laliberté. *Fluctuations Supraconductrices Comme Source de L'effet Nernst Dans Un Cuprate Dopé en Électrons*. PhD thesis, Université de Sherbrooke, 2013.

[77] J.S. Langer. Theory of the condensation point. *Annals of Physics*, 281(1):941–990, 2000.

[78] Loïc Lannelongue, Jason Grealey, and Michael Inouye. Green algorithms: quantifying the carbon footprint of computation. *Advanced science*, 8(12):2100707, 2021.

[79] J. P. F. LeBlanc, Andrey E. Antipov, Federico Becca, Ireneusz W. Bulik, Garnet Kin-Lic Chan, Chia-Min Chung, Youjin Deng, Michel Ferrero, Thomas M. Henderson, Carlos A. Jiménez-Hoyos, E. Kozik, Xuan-Wen Liu, Andrew J. Millis, N. V. Prokof'ev, Mingpu Qin, Gustavo E. Scuseria, Hao Shi, B. V. Svistunov, Luca F. Tocchio, I. S. Tupitsyn, Steven R. White, Shiwei Zhang, Bo-Xiao Zheng, Zhenyue Zhu, and Emanuel Gull. Solutions of the two-dimensional hubbard model: Benchmarks and results from a wide range of numerical algorithms. *Phys. Rev. X*, 5:041041, Dec 2015.

[80] Connor Lenihan, Aaram J. Kim, Fedor Šimkovic IV., and Evgeny Kozik. Entropy in the non-fermi-liquid regime of the doped 2D hubbard model. *Phys. Rev. Lett.*, 126:105701, Mar 2021.

[81] Connor Lenihan, Aaram J. Kim, IV. Šimkovic, Fedor, and Evgeny Kozik. Evaluating second-order phase transitions with Diagrammatic Monte Carlo: Néel Transition in the doped three-dimensional Hubbard model. *arXiv e-prints*, page arXiv:2112.15209, December 2021.

[82] Jiajun Li, Camille Aron, Gabriel Kotliar, and Jong E. Han. Electric-field-driven resistive switching in the dissipative hubbard model. *Phys. Rev. Lett.*, 114:226403, Jun 2015.

[83] Alexandru Macridin, M. Jarrell, Thomas Maier, P. R. C. Kent, and Eduardo D'Azevedo. Pseudogap and antiferromagnetic correlations in the hubbard model. *Phys. Rev. Lett.*, 97:036401, Jul 2006.

[84] Marjan Maček, Philipp T. Dumitrescu, Corentin Bertrand, Bill Triggs, Olivier Parcollet, and Xavier Waintal. Quantum quasi-monte carlo technique for many-body perturbative expansions. *Phys. Rev. Lett.*, 125:047702, Jul 2020.

[85] Anne Matthies, Jiajun Li, and Martin Eckstein. Control of competing superconductivity and charge order by nonequilibrium currents. *Phys. Rev. B*, 98:180502, Nov 2018.

[86] Giordano Mattoni, Shingo Yonezawa, Fumihiko Nakamura, and Yoshiteru Maeno. Role of local temperature in the current-driven metal–insulator transition of ca_2ruo_4. *Phys. Rev. Mater.*, 4:114414, Nov 2020.

[87] Anton Mazurenko, Christie S Chiu, Geoffrey Ji, Maxwell F Parsons, Márton Kanász-Nagy, Richard Schmidt, Fabian Grusdt, Eugene Demler, Daniel Greif, and Markus Greiner. A cold-atom fermi–hubbard antiferromagnet. *Nature*, 545(7655):462–466, 2017.

[88] Rafael Medeiros. Utilisation du supercalculateur. `http://www.idris.fr/media/jean-zay/jean-zay-conso-heure-calcul.pdf`.

[89] Yigal Meir and Ned S. Wingreen. Landauer formula for the current through an interacting electron region. *Phys. Rev. Lett.*, 68:2512–2515, Apr 1992.

[90] William J Morokoff and Russel E Caflisch. Quasi-random sequences and their discrepancies. *SIAM Journal on Scientific Computing*, 15(6):1251–1279, 1994.

[91] Alice Moutenet. *Novel algorithms for strongly correlated quantum systems in and out of equilibrium.* Theses, Institut Polytechnique de Paris, July 2020.

[92] Alice Moutenet, Wei Wu, and Michel Ferrero. Determinant monte carlo algorithms for dynamical quantities in fermionic systems. *Phys. Rev. B*, 97:085117, Feb 2018.

[93] E Müller-Hartmann. Self-consistent perturbation theory of the anderson model: ground state properties. *Zeitschrift für Physik B Condensed Matter*, 57(4):281–287, 1984.

[94] Fumihiko Nakamura, Mariko Sakaki, Yuya Yamanaka, Sho Tamaru, Takashi Suzuki, and Yoshiteru Maeno. Electric-field-induced metal maintained by current of the mott insulator ca2ruo4. *Scientific reports*, 3(1):1–6, 2013.

[95] John W Negele. *Quantum many-particle systems.* CRC Press, 2018.

[96] Ryuji Okazaki, Yasuo Nishina, Yukio Yasui, Fumihiko Nakamura, Takashi Suzuki, and Ichiro Terasaki. Current-induced gap suppression in the mott insulator ca2ruo4. *Journal of the Physical Society of Japan*, 82(10):103702, 2013.

[97] Ivan Oseledets and Eugene Tyrtyshnikov. Tt-cross approximation for multidimensional arrays. *Linear Algebra and its Applications*, 432(1):70–88, 2010.

[98] Olivier Parcollet, Antoine Georges, Gabriel Kotliar, and Anirvan Sengupta. Overscreened multichannel SU(n) kondo model: Large-n solution and conformal field theory. *Phys. Rev. B*, 58:3794–3813, Aug 1998.

[99] AZ Patashinskii and VL Pokrovskii. Longitudinal susceptibility and correlations in degenerate systems. *Zh. Eksp. Teor. Fiz*, 64:1445, 1973.

[100] Francesco Peronaci, Marco Schiró, and Olivier Parcollet. Resonant thermalization of periodically driven strongly correlated electrons. *Phys. Rev. Lett.*, 120:197601, May 2018.

[101] Robert Peters and Norio Kawakami. Spin density waves in the hubbard model: A dmft approach. *Phys. Rev. B*, 89:155134, Apr 2014.

[102] Francesco Petocchi, Sophie Beck, Claude Ederer, and Philipp Werner. Hund excitations and the efficiency of mott solar cells. *Phys. Rev. B*, 100:075147, Aug 2019.

[103] R. Preuss, W. Hanke, C. Gröber, and H. G. Evertz. Pseudogaps and their interplay with magnetic excitations in the doped 2d hubbard model. *Phys. Rev. Lett.*, 79:1122–1125, Aug 1997.

[104] Rosario E. V. Profumo, Christoph Groth, Laura Messio, Olivier Parcollet, and Xavier Waintal. Quantum monte carlo for correlated out-of-equilibrium nanoelectronic devices. *Phys. Rev. B*, 91:245154, Jun 2015.

[105] Nikolai V. Prokof'ev and Boris V. Svistunov. Polaron problem by diagrammatic quantum monte carlo. *Phys. Rev. Lett.*, 81:2514–2517, Sep 1998.

[106] Nikolay Prokof'ev and Boris Svistunov. Bold diagrammatic monte carlo technique: When the sign problem is welcome. *Phys. Rev. Lett.*, 99:250201, Dec 2007.

[107] Cyril Proust and Louis Taillefer. The remarkable underlying ground states of cuprate superconductors. *Annual Review of Condensed Matter Physics*, 10(1):409–429, 2019.

[108] Mingpu Qin, Chia-Min Chung, Hao Shi, Ettore Vitali, Claudius Hubig, Ulrich Schollwöck, Steven R. White, and Shiwei Zhang. Absence of superconductivity in the pure two-dimensional hubbard model. *Phys. Rev. X*, 10:031016, Jul 2020.

[109] Mingpu Qin, Thomas Schäfer, Sabine Andergassen, Philippe Corboz, and Emanuel Gull. The Hubbard Model: A Computational Perspective. *Annual Review of Condensed Matter Physics*, 13(1):275–302, 2022.

[110] Alexis Reymbaut. *Universalité du crossover de Mott à demi-remplissage et effets de la répulsion coulombienne aux premiers voisins sur la dynamique supraconductrice des isolants de Mott dopés aux trous.* PhD thesis, Université de Sherbrooke, 2016.

[111] G. Rohringer, A. Toschi, A. Katanin, and K. Held. Critical properties of the half-filled hubbard model in three dimensions. *Phys. Rev. Lett.*, 107:256402, Dec 2011.

[112] R. Rossi, T. Ohgoe, K. Van Houcke, and F. Werner. Resummation of diagrammatic series with zero convergence radius for strongly correlated fermions. *Phys. Rev. Lett.*, 121:130405, Sep 2018.

[113] R. Rossi, N. Prokof'ev, B. Svistunov, K. Van Houcke, and F. Werner. Polynomial complexity despite the fermionic sign. *EPL (Europhysics Letters)*, 118(1):10004, apr 2017.

[114] Riccardo Rossi. Determinant diagrammatic monte carlo algorithm in the thermodynamic limit. *Phys. Rev. Lett.*, 119:045701, Jul 2017.

[115] Riccardo Rossi, Félix Werner, Nikolay Prokof'ev, and Boris Svistunov. Shifted-action expansion and applicability of dressed diagrammatic schemes. *Phys. Rev. B*, 93:161102, Apr 2016.

[116] Riccardo Rossi, Fedor Šimkovic, and Michel Ferrero. Renormalized perturbation theory at large expansion orders. *Europhysics Letters*, 132(1):11001, nov 2020.

[117] A. N. Rubtsov, M. I. Katsnelson, A. I. Lichtenstein, and A. Georges. Dual fermion approach to the two-dimensional hubbard model: Antiferromagnetic fluctuations and fermi arcs. *Phys. Rev. B*, 79:045133, Jan 2009.

[118] A.N. Rubtsov, M.I. Katsnelson, and A.I. Lichtenstein. Dual boson approach to collective excitations in correlated fermionic systems. *Annals of Physics*, 327(5):1320–1335, 2012.

[119] Andreas Rüegg, Emanuel Gull, Gregory A. Fiete, and Andrew J. Millis. Sum rule violation in self-consistent hybridization expansions. *Phys. Rev. B*, 87:075124, Feb 2013.

[120] Mariko Sakaki, Nobuo Nakajima, Fumihiko Nakamura, Yasuhisa Tezuka, and Takashi Suzuki. Electric-field-induced insulator–metal transition in ca2ruo4 probed by x-ray absorption and emission spectroscopy. *Journal of the Physical Society of Japan*, 82(9):093707, 2013.

[121] Anders W. Sandvik. Critical temperature and the transition from quantum to classical order parameter fluctuations in the three-dimensional heisenberg antiferromagnet. *Phys. Rev. Lett.*, 80:5196–5199, Jun 1998.

[122] T. Schäfer, A. A. Katanin, K. Held, and A. Toschi. Interplay of correlations and kohn anomalies in three dimensions: Quantum criticality with a twist. *Phys. Rev. Lett.*, 119:046402, Jul 2017.

[123] Thomas Schäfer, Nils Wentzell, Fedor Šimkovic, Yuan-Yao He, Cornelia Hille, Marcel Klett, Christian J. Eckhardt, Behnam Arzhang, Viktor Harkov, François-Marie Le Régent, Alfred Kirsch, Yan Wang, Aaram J. Kim, Evgeny Kozik, Evgeny A. Stepanov, Anna Kauch, Sabine Andergassen, Philipp Hansmann, Daniel Rohe, Yuri M. Vilk, James P. F. LeBlanc, Shiwei Zhang, A.-M. S. Tremblay, Michel Ferrero, Olivier Parcollet, and Antoine Georges. Tracking the footprints of spin fluctuations: A multimethod, multimessenger study of the two-dimensional hubbard model. *Phys. Rev. X*, 11:011058, Mar 2021.

[124] Ulrich Schollwöck. The density-matrix renormalization group in the age of matrix product states. *Annals of Physics*, 326(1):96–192, 2011. January 2011 Special Issue.

[125] J. R. Schrieffer and P. A. Wolff. Relation between the anderson and kondo hamiltonians. *Phys. Rev.*, 149:491–492, Sep 1966.

[126] Hao Shi and Shiwei Zhang. Symmetry in auxiliary-field quantum monte carlo calculations. *Phys. Rev. B*, 88:125132, Sep 2013.

[127] J. C. Slater. Magnetic effects and the hartree-fock equation. *Phys. Rev.*, 82:538–541, May 1951.

[128] G. Spada, R. Rossi, F. Simkovic, R. Garioud, M. Ferrero, K. Van Houcke, and F. Werner. High-order expansion around bcs theory, 2021.

[129] Rudolf Staudt, Michael Dzierzawa, and A Muramatsu. Phase diagram of the three-dimensional hubbard model at half filling. *The European Physical Journal B-Condensed Matter and Complex Systems*, 17(3):411–415, 2000.

[130] Gianluca Stefanucci and Robert Van Leeuwen. *Nonequilibrium many-body theory of quantum systems: a modern introduction*. Cambridge University Press, 2013.

[131] Julian Stobbe and Georg Rohringer. Consistency of potential energy in the dynamical vertex approximation. *Phys. Rev. B*, 106:205101, Nov 2022.

[132] Amir Taheridehkordi, S. H. Curnoe, and J. P. F. LeBlanc. Optimal grouping of arbitrary diagrammatic expansions via analytic pole structure. *Phys. Rev. B*, 101:125109, Mar 2020.

[133] C. Taranto, G. Sangiovanni, K. Held, M. Capone, A. Georges, and A. Toschi. Signature of antiferromagnetic long-range order in the optical spectrum of strongly correlated electron systems. *Phys. Rev. B*, 85:085124, Feb 2012.

[134] Leticia Tarruell and Laurent Sanchez-Palencia. Quantum simulation of the hubbard model with ultracold fermions in optical lattices. *Comptes Rendus Physique*, 19(6):365–393, 2018. Quantum simulation / Simulation quantique.

[135] A. Toschi, M. Capone, and C. Castellani. Energetic balance of the superconducting transition across the bcs—bose einstein crossover in the attractive hubbard model. *Phys. Rev. B*, 72:235118, Dec 2005.

[136] Leandro Tosi, Pablo Roura-Bas, Ana María Llois, and Luis O. Manuel. Effects of vertex corrections on diagrammatic approximations applied to the study of transport through a quantum dot. *Phys. Rev. B*, 83:073301, Feb 2011.

[137] Matthias Troyer and Uwe-Jens Wiese. Computational complexity and fundamental limitations to fermionic quantum monte carlo simulations. *Phys. Rev. Lett.*, 94:170201, May 2005.

[138] Kris Van Houcke, Evgeny Kozik, N. Prokof'ev, and B. Svistunov. Diagrammatic monte carlo. *Physics Procedia*, 6:95–105, 2010. Computer Simulations Studies in Condensed Matter Physics XXI.

[139] Kris Van Houcke, Félix Werner, and Riccardo Rossi. High-precision numerical solution of the fermi polaron problem and large-order behavior of its diagrammatic series. *Phys. Rev. B*, 101:045134, Jan 2020.

[140] J. Van Kranendonk and J. H. Van Vleck. Spin waves. *Rev. Mod. Phys.*, 30:1–23, Jan 1958.

[141] F. Werner, O. Parcollet, A. Georges, and S. R. Hassan. Interaction-Induced Adiabatic Cooling and Antiferromagnetism of Cold Fermions in Optical Lattices. *Phys. Rev. Lett.*, 95:056401, Jul 2005.

[142] Steven R. White. Density matrix formulation for quantum renormalization groups. *Phys. Rev. Lett.*, 69:2863–2866, Nov 1992.

[143] Steven R. White. Density-matrix algorithms for quantum renormalization groups. *Phys. Rev. B*, 48:10345–10356, Oct 1993.

[144] Alexander Wietek, Yuan-Yao He, Steven R. White, Antoine Georges, and E. Miles Stoudenmire. Stripes, antiferromagnetism, and the pseudogap in the doped hubbard model at finite temperature. *Phys. Rev. X*, 11:031007, Jul 2021.

[145] Alexander Wietek and Andreas M. Läuchli. Sublattice coding algorithm and distributed memory parallelization for large-scale exact diagonalizations of quantum many-body systems. *Phys. Rev. E*, 98:033309, Sep 2018.

[146] Kenneth G. Wilson. The renormalization group: Critical phenomena and the kondo problem. *Rev. Mod. Phys.*, 47:773–840, Oct 1975.

[147] Wei Wu, Michel Ferrero, Antoine Georges, and Evgeny Kozik. Controlling feynman diagrammatic expansions: Physical nature of the pseudogap in the two-dimensional hubbard model. *Phys. Rev. B*, 96:041105, Jul 2017.

[148] Wei Wu, Mathias S. Scheurer, Shubhayu Chatterjee, Subir Sachdev, Antoine Georges, and Michel Ferrero. Pseudogap and fermi-surface topology in the two-dimensional hubbard model. *Phys. Rev. X*, 8:021048, May 2018.

[149] Hao Xu, Chia-Min Chung, Mingpu Qin, Ulrich Schollwöck, Steven R. White, and Shiwei Zhang. Coexistence of superconductivity with partially filled stripes in the hubbard model, 2023.

[150] Susumu Yamada, Toshiyuki Imamura, and Masahiko Machida. High performance lobpcg method for solving multiple eigenvalues of hubbard model: Efficiency of communication avoiding neumann expansion preconditioner. In Rio Yokota and Weigang Wu, editors, *Supercomputing Frontiers*, pages 243–256, Cham, 2018. Springer International Publishing.

[151] Shiwei Zhang. 15 auxiliary-field quantum monte carlo for correlated electron systems. *Emergent Phenomena in Correlated Matter*, 2013.

ECOLE
DOCTORALE

Titre : Quand la théorie des perturbations devient non-perturbative : applications aux systèmes fortement corrélés

Mots clés : Physique numérique - Matière condensée - Systèmes fortement corrélés - Transition de phase - Algorithmes

Résumé : Les matériaux fortement corrélés révèlent des phénomènes physiques remarquables à basse température. Selon les paramètres externes, ils présentent des phases électroniques extrêmement différentes, allant d'ordres magnétiques isolants à une phase supraconductrice présentant une conductivité électrique infinie. La richesse de ces phénomènes physiques prend ses racines dans les interactions fortes qui impactent le comportement des électrons. Ces matériaux ne peuvent pas être compris par un traitement effectif à un seul corps. Pour décrire avec précision leurs propriétés, il faut résoudre le problème quantique à N corps. Il s'agit d'un problème complexe qui nécessite des approches numériques efficaces pour obtenir des résultats quantitativement précis. Dans cette thèse, nous abordons le développement de nouveaux algorithmes pour résoudre les systèmes fermioniques à fortes interactions.

Après avoir introduit les systèmes à fortes interactions, nous montrons que la théorie des perturbations est un outil puissant pour étudier le problème à N corps quantique. En considérant les interactions électroniques comme une perturbation du système sans interaction, nous exposons comment calculer de manière efficace, et jusqu'à des ordres élevés, la série perturbative qui peut être exprimée comme une somme de diagrammes de Feynman. Nous présentons l'algorithme CDet (Connected Determinants) qui nous permet d'atteindre des ordres de perturbation élevés. Nous dépassons l'une des principales limites de la théorie des perturbations en introduisant un changement de potentiel chimique qui brise une symétrie du système. Cette approche permet de décrire de façon perturbative la physique des phases ordonnées dans la limite thermodynamique. Ce nouvel algorithme est appliqué au modèle de Hubbard à moitié rempli et sur un réseau cubique. Il fournit une description quantitative de l'ordre de Néel à la fois près de la transition de phase et à basse température jusqu'au régime de couplage fort. Cette étude nous permet de détailler les limites de notre méthode et de présenter les outils numériques qui assurent une mise en œuvre efficace de l'algorithme CDet et une resommation précise des séries perturbatives. La version attractive de ce modèle présente une phase supraconductrice qui est décrite en adaptant notre approche d'expansion dans une phase à symétrie brisée.

Dans le dernier chapitre de cette thèse, nous nous intéressons aux systèmes à forte interaction et hors équilibre. Le problème hors équilibre dans les matériaux fortement corrélés est exceptionnellement difficile à résoudre exactement, et nous nous appuyons sur une approximation diagrammatique NCA (Non Crossing Approximation). Nous implémentons un solveur d'impuretés efficace et rapide en alternant entre les domaines en temps réel et en fréquence, dans la limite du régime permanent. Ce solveur nous permet de calculer les propriétés de transport dans des systèmes qui sont maintenus hors équilibre par un champ électrique extérieur.

Title : When perturbation theory becomes non-perturbative : applications to strongly-correlated systems

Keywords : Numerical physics - Condensed Matter - Strongly correlated materials - Phase transition - Algorithms

Abstract : Strongly correlated materials reveal remarkable physical phenomena at low temperatures. Depending on external parameters, they exhibit extremely different electronic phases, ranging from insulating magnetic orders to strong superconductivity with infinite electrical conductivity. The richness of these physical phenomena takes its roots in the strong interactions that impact heavily the behaviour of electrons. These materials can not be understood by an effective one-body treatment. To accurately describe these properties, one must solve the quantum many-body problem of interacting particles. This is a complex problem that requires numerical approaches to obtain quantitatively accurate results. In this thesis, we focus on the development of new algorithms to address strongly interacting fermionic systems.

After introducing strongly interacting systems, we show that the perturbation theory framework is a powerful tool for studying the many-body problem. By considering electronic interactions as a perturbation to the non-interacting system, we focus on computing efficiently, and up to high orders, the perturbation series, which can be expressed as sums of Feynman diagrams. We present the CDet (Connected Determinants) state-of-the-art algorithm which allows us to reach high perturbation orders. We overcome one of the main limitations of perturbation theory by introducing a novel chemical potential shift that breaks a symmetry. We show that this approach allows us to describe perturbatively the physics of ordered phases in the thermodynamic limit. We apply this new algorithm to the cubic half-filled Hubbard model and provide a quantitative description of the Néel order both near the phase transition and at low temperature up to the high coupling regime. This study enables us to detail the limitations to our method and to present the numerical tools that ensure an efficient implementation of the CDet algorithm and an accurate resummation of the resulting perturbative series. The attractive counterpart of this model shows a superconducting phase that can also be described by adapting our symmetry-breaking approach.

In the last chapter of this thesis we turn our attention to out-of- equilibrium interacting systems. The non-equilibrium interacting problem in real materials is extraordinarily difficult to solve exactly, and we rely on a diagrammatic approximation : the Non-Crossing-Approximation. We implement an efficient and fast impurity solver by alternating between the real-time and frequency domains in the steady-state limit. This solver allows us to compute transport properties in systems that are driven out-of-equilibrium by an external electric field.

Institut Polytechnique de Paris
91120 Palaiseau, France